

Chemical evolution from cores to disks

Chemical evolution from cores to disks

PROEFSCHRIFT

ter verkrijging van
de graad van Doctor aan de Universiteit Leiden,
op gezag van de Rector Magnificus prof. mr. P. F. van der Heijden,
volgens besluit van het College voor Promoties
te verdedigen op woensdag 21 oktober 2009
klokke 15.00 uur

door

Ruud Visser
geboren te Amersfoort
in 1983

Promotiecommissie

Promotor: Prof. dr. E. F. van Dishoeck

Overige leden: Prof. dr. H. V. J. Linnartz
Prof. dr. K. Kuijken
Dr. M. R. Hogerheijde
Prof. dr. G. A. Blake California Institute of Technology
Prof. dr. S. D. Doty Denison University
Prof. dr. E. A. Bergin University of Michigan
Dr. C. P. Dullemond Max-Planck-Institut für Astronomie

voor papa & mama

“Welcome the task that makes you go beyond yourself.”

– Frank McGee

Inhoudsopgave

1	Introduction	1
1.1	From ancient astronomy to modern astrochemistry	2
1.2	Low-mass star formation and the role of chemistry	4
1.3	Planets, comets and meteorites	8
1.4	Chemical models	10
1.4.1	Historical development and reaction types	10
1.4.2	Solution methods	12
1.5	This thesis	14
2	The chemical history of molecules in circumstellar disks	
	I: Ices	19
2.1	Introduction	21
2.2	Model	22
2.2.1	Envelope	23
2.2.2	Disk	25
2.2.3	Star	28
2.2.4	Temperature	30
2.2.5	Accretion shock	30
2.2.6	Model parameters	31
2.2.7	Adsorption and desorption	32
2.3	Results	33
2.3.1	Density profiles and infall trajectories	34
2.3.2	Temperature profiles	36
2.3.3	Gas and ice abundances	37
2.3.4	Temperature histories	44
2.4	Discussion	45
2.4.1	Model parameters	45
2.4.2	Complex organic molecules	49
2.4.3	Mixed CO-H ₂ O ices	52
2.4.4	Implications for comets	53
2.4.5	Limitations of the model	54
2.5	Conclusions	55
	Appendix: Disk formation efficiency	56
3	The chemical history of molecules in circumstellar disks	
	II: Gas-phase species	59
3.1	Introduction	61
3.2	Collapse model	63

3.2.1	Step-wise summary	63
3.2.2	Differences with Chapter 2	64
3.2.3	Radiation field	65
3.3	Chemical network	66
3.3.1	Photodissociation and photoionisation	67
3.3.2	Gas-grain interactions	67
3.4	Results from the pre-collapse phase	70
3.5	Results from the collapse phase	72
3.5.1	One single parcel	72
3.5.2	Other parcels	79
3.6	Chemical history versus local chemistry	88
3.7	Discussion	97
3.7.1	Caveats	97
3.7.2	Comets	98
3.7.3	Collapse models: 1D versus 2D	102
3.8	Conclusions	102
4	Sub-Keplerian accretion onto circumstellar disks	105
4.1	Introduction	107
4.2	Equations	109
4.3	Size and mass of the disk	111
4.4	Gas-ice ratios	112
4.5	Crystalline silicates	114
4.5.1	Observations and previous model results	114
4.5.2	New model results	115
4.5.3	Discussion and future work	120
4.6	Conclusions	122
5	The photodissociation and chemistry of CO isotopologues: applications to interstellar clouds and circumstellar disks	123
5.1	Introduction	125
5.2	Molecular data	126
5.2.1	Band positions and identifications	127
5.2.2	Rotational constants	130
5.2.3	Oscillator strengths	131
5.2.4	Lifetimes and predissociation probabilities	132
5.2.5	Atomic and molecular hydrogen	134
5.3	Depth-dependent photodissociation	134
5.3.1	Default model parameters	134
5.3.2	Unshielded photodissociation rates	135
5.3.3	Shielding by CO, H ₂ and H	135
5.3.4	Continuum shielding by dust	137
5.3.5	Uncertainties	138
5.4	Excitation temperature and Doppler width	139

5.4.1	Increasing $T_{\text{ex}}(\text{CO})$	139
5.4.2	Increasing $b(\text{CO})$	142
5.4.3	Increasing $T_{\text{ex}}(\text{H}_2)$ or $b(\text{H}_2)$	142
5.4.4	Grid of T_{ex} and b	143
5.5	Shielding function approximations	146
5.5.1	Shielding functions on a grid of $N(\text{CO})$ and $N(\text{H}_2)$	146
5.5.2	Comparison between the full model and the approximations	147
5.6	Chemistry of CO: astrophysical implications	151
5.6.1	Translucent clouds	151
5.6.2	Photon-dominated regions	159
5.6.3	Circumstellar disks	162
5.7	Conclusions	166
6	PAH chemistry and IR emission from circumstellar disks	169
6.1	Introduction	171
6.2	PAH model	172
6.2.1	Characterisation of PAHs	172
6.2.2	Photoprocesses	173
6.2.3	Absorption cross sections	176
6.2.4	Electron recombination and attachment	177
6.2.5	Hydrogen addition	179
6.2.6	PAH growth and destruction	179
6.2.7	Other chemical processes	180
6.3	Disk model	182
6.3.1	Computational code	182
6.3.2	Template disk with PAHs	183
6.4	Results	183
6.4.1	PAH chemistry	183
6.4.2	PAH emission	186
6.4.3	Other PAHs	190
6.4.4	Spatial extent of the PAH emission	190
6.4.5	Sensitivity analysis	191
6.4.6	T Tauri stars	193
6.4.7	Comparison with observations	194
6.5	Conclusions	194
	Nederlandse samenvatting	197
	Literatuur	204
	Publicaties	219
	Curriculum vitae	221
	Nawoord	223

Introduction

1

1.1 From ancient astronomy to modern astrochemistry

Mankind has ever been fascinated with the stars. Dating back to the most ancient of times, human life has been governed by the endless cycles of day and night and of winter, spring, summer and fall. Already in the early Stone Age, people must have seen a relationship between the rising and setting of the Sun on the one hand, and dark turning into light turning back into dark on the other hand. Having established the Sun as the cause of light and warmth, it is a logical next step to wonder whether other objects in the sky could equally influence life on Earth. As George Forbes wrote in his book *History of Astronomy* (1909), “this led to a search for other signs in the heavens. If the appearance of a comet was sometimes noted simultaneously with the death of a great ruler, or an eclipse with a scourge of plague, these might well be looked upon as causes in the same sense that the veering or backing of the wind is regarded as a cause of fine or foul weather.”

With today’s knowledge, it is easy to say that comets, eclipses and most other astronomical phenomena do not altogether affect our lives as much as our ancestors believed. Nonetheless, their suppositions led them to keep detailed records of anything remarkable taking place in the sky. Clay tablets surviving from Babylonia show that people were keeping track of solar eclipses at least as far back as 1062 B.C. (Cowell 1905). In China, c. 2450 B.C., the emperor Zhuanxu apparently saw a conjunction of Mercury, Mars, Saturn and Jupiter on the same day that the Moon was in conjunction with the Sun (Chambers 1889, Hail & Leavens 1940). The preferential east-west and north-south alignment of graves and bodies in burial sites from the late Stone Age suggests that mankind was engaged in primitive astronomy as early as 4500 B.C. (Schmidt-Kaler & Schlosser 1984).

If the Babylonians laid the foundations for modern astronomy, it was the Greek who started building in earnest. From around 600 B.C. onwards, scholars like Thales, Pythagoras, Anaxagoras, Plato and Eratosthenes performed many revolutionary measurements and observations, and devised many equally revolutionary theories about the Earth and the Moon, the planets, and the Sun and the stars (Lewis 1862). The most prolific of the Greek astronomers was Hipparchus (c. 190–120 B.C.), regarded by Forbes (1909) as the founder of observational astronomy. Amongst other contributions, he compiled the first comprehensive star catalogue and discovered the precession of the Earth’s axis. Another key figure from the classical period is the Roman Ptolemy, who, around 150 A.D., wrote one of the first textbooks on astronomy. Known as the *Almagest* or the *Great Treatise*, it contained a summary of the astronomical knowledge then available, including a detailed model of the motions of the Sun, the planets and the stars.

Hipparchus, Ptolemy and all astronomers before them were mostly concerned with the motions of the stars and the planets, and not so much with their physical nature. After all, astronomy as a science was born out of a desire to be able to predict signs in the skies that might announce a good harvest or the start of a war. In 1608, almost a millennium and a half after Ptolemy’s *Almagest*, the three Dutchmen Hans Lippershey, Zacharias Janssen and Jacob Metius invented the telescope (van Helden 2009). This allowed Galileo Galilei (1564–1642) to embark on a whole new kind of astronomy. Suddenly, the Sun was known to have dark spots on its surface, Venus to have phases, Jupiter to have moons, and the Milky Way to consist of countless individual stars (Drake 1978).

Galileo's observations supported the heliocentric theory published by Nicolaus Copernicus in his 1543 work *De Revolutionibus Orbium Coelestium*, and scientists were now gradually accepting the idea of a spherical Earth orbiting the Sun in a vast expanse. This inevitably led to questions about the nature of the space between the planets and the stars. Sir Francis Bacon appears to have been the first to publish on this topic. In his *Descriptio Globi Intellectualis* (1653), he wrote, "Another question is, *what is contained in the interstellar spaces?* For they are either empty, as Gilbert thought; or filled with a body which is to the stars what air is to flame (. . .); or filled with a body homogeneous with the stars themselves, lucid and almost empyreal, but in a less degree (. . .)."¹ Despite Bacon's excellent ideas – his third option is remarkably close to the truth – it was not until the early 20th century that astronomers widely started to think of interstellar space as a very dilute gas. The first strong evidence of interstellar material came with the discovery of a very narrow calcium absorption line towards δ Orionis, which Hartmann (1904) concluded had to be due to a cloud of calcium gas located somewhere between Earth and this star. Independent of him, Kapteyn (1909) theorised that "interstellar space must contain, at every moment, a considerable amount of gas," based on the coronal gas expelled by the Sun and, presumably, other stars. The "dark markings of the sky" observed by Barnard (1919) provided further evidence of interstellar material, as did spectroscopic observations by Heger (1919), Beals (1936) and Dunham (1937a,b) and theoretical considerations by Birkeland (1913) and Thorndike (1930).

Now that astronomers knew there was an interstellar medium (ISM), they set out to identify its chemical composition. The observations so far had established the presence of Na, K, Ca⁺, Ti⁺ and other metal atoms and ions.² It was soon suggested the ISM might also contain simple molecules (Eddington 1926, Russell 1935, Swings 1937, Saha 1937), and this hypothesis was confirmed by the detections of CH (Swings & Rosenfeld 1937), CN (McKellar 1940) and CH⁺ (Douglas & Herzberg 1941). Astrochemistry had arrived.

The advent of radio and microwave astronomy in the 1960s, followed by infrared astronomy in the late 1970s, provided a great boost for this fledgling area of science. By the time Neil Armstrong set foot on the Moon, the detection of OH, NH₃, H₂O and H₂CO had increased the number of confirmed interstellar molecules to seven (Weinreb 1963, Cheung et al. 1968, 1969, Snyder et al. 1969). Seven more were known within a year and a half, including two of the most abundant ones: H₂ and CO (Carruthers 1970, Wilson et al. 1970). The 50th and 100th space molecules were detected in 1978 (NO, by Liszt & Turner) and 1992 (SO⁺, by Turner). Meanwhile, strong evidence had arisen for the ubiquitous presence of a class of much larger molecules known as polycyclic aromatic hydrocarbons or PAHs (Fig. 1.1; Gillett et al. 1973, Puget & Leger 1989, Allamandola et al. 1989, Tielens 2008), although as of yet no individual members of this class have been

¹ The quote comes from Bacon's collected and translated works, edited by Spedding, Ellis and Heath. The possibility of space being empty refers to William Gilbert's hypothesis in his *De Magnete* (1600; translated by Mottelay) that "the space above the earth's exhalations is a vacuum."

² Worth mentioning here is nebulium or nebulum, an element conjured up by Sir William Huggins in the 1860s to designate, as Clerke (1898) put it, "the exotic *world-stuff* originating the chief nebular ray at λ 5007 [and] its companion at λ 4959." Nebulium continued to be considered a common component of the ISM until Bowen (1928) showed that the lines at 5007 and 4959 Å were in fact due to doubly ionised oxygen, prompting Russell (1932) to quip that "nebulium [had] thus very literally vanished into thin air".

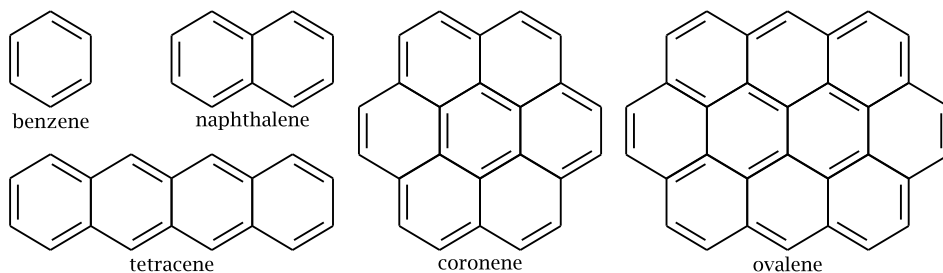


Figure 1.1 – A selection of polycyclic aromatic hydrocarbons (PAHs): benzene (C_6H_6), naphthalene ($C_{10}H_8$), tetracene ($C_{18}H_{12}$), coronene ($C_{24}H_{12}$) and ovalene ($C_{32}H_{14}$). Each corner represents a carbon atom; hydrogen atoms are not drawn.

firmly identified. The counter of interstellar and circumstellar molecules and molecular ions currently stands at 162 (Woon 2009), and astrochemistry has firmly established itself as an important field of research.³

1.2 Low-mass star formation and the role of chemistry

The ISM is now understood to consist of several components (Field et al. 1969, McKee & Ostriker 1977, Ferrière 2001). By volume, the top three are the hot ionised medium (particle density of 10^{-4} – 10^{-2} cm^{-3} , temperature of 10^6 – 10^7 K), the warm ionised medium (0.2 – 0.5 cm^{-3} , 8000 K) and the warm neutral medium (0.2 – 0.5 cm^{-3} , 6000–10000 K), together accounting for 95–99%. Most of the remaining volume is taken up by the cold neutral medium (20 – 50 cm^{-3} , 50–100 K). The densest ISM component, with a fractional volume of less than 1%, are the molecular clouds (10^2 – 10^6 cm^{-3} , 10–20 K). They are of particular importance for this thesis, as they are the birthplace of new stars.

Molecular clouds range in diameter from a few to maybe 10 or 20 pc and have a mass between 10^3 and 10^4 M_{\odot} (Cambrésy 1999). They tend to be irregularly shaped and their density distribution is far from homogeneous. Embedded in molecular clouds are so-called clumps with typical densities of 10^3 – 10^4 cm^{-3} and typical diameters of 0.3–3 pc (Loren 1989, Williams et al. 1994). The clumps in turn harbour the so-called cores, whose densities are another order of magnitude higher and whose diameters are another order of magnitude smaller (Motte et al. 1998, Jijina et al. 1999, Caselli et al. 2002). The temperature in all these substructures is about 10 K (Bergin & Tafalla 2007).

Supported by pressure, turbulence and magnetic fields, cloud cores usually survive for a few 10^5 to possibly several 10^6 yr. They consist of a mixture of gas and tiny dust grains (radius of about 0.1 μm) in a mass ratio of 1 to 0.01, or a number ratio of 1 to 10^{-12} (Spitzer

³ The list of 162 molecules includes various isomers, but no isotopologues. It contains no PAHs except the tentatively detected benzene (C_6H_6). It also contains other tentative and disputed detections such as glycine (NH_2CH_2COOH) and 1,3-dihydroxyacetone ($CO(CH_2OH)_2$).

1954, Kimura et al. 2003).⁴ An active chemistry is already taking place during this stage. First of all, the initially atomic gas – inherited from the more diffuse ISM out of which the cloud coalesced – is transformed into simple molecules like CO, OH and N₂. Because of the low temperature and moderately high density, most of these molecules freeze out onto the dust. The resulting ice mantles offer the possibility for additional chemical reactions, leading for example to CO₂, CH₄, H₂O, H₂CO and CH₃OH (Watanabe & Kouchi 2002, Ioppolo et al. 2008, 2009, Fuchs et al. 2009).

The various physical and chemical stages involved in the formation of low-mass stars are illustrated in Fig. 1.2. Point 0 represents the cold phase of the static cloud core. As described in more detail in the rest of this section, the formation of a star at the centre of the core is initially accompanied by a warm-up of the surrounding material. At a later stage, when a dense disk is formed around the star, the temperature decreases again in some areas. The range of physical conditions encountered throughout the star-formation process results in a complex chemical evolution of both the gas and the dust.

The collapse of the core under its own gravity is initiated by the loss of turbulent or magnetic support. Material starts falling in towards the centre along trajectories such as the one drawn in Fig. 1.2. The core is gradually warmed up by gravitational contraction, accretion shocks and, eventually, nuclear fusion in the protostar. Volatile species such as CO, CH₄ and N₂ now evaporate from the grains (van Dishoeck et al. 1993, Aikawa et al. 2001, Jørgensen et al. 2002, 2004, 2005, Lee et al. 2004) and this also affects the gas-phase abundances of other species (Chapter 3). The warm-up to 20–40 K further drives a rich grain-surface chemistry (Garrod & Herbst 2006, Garrod et al. 2008, Öberg et al. 2009a; see also the review by Herbst & van Dishoeck 2009). The remaining ice molecules may not be volatile enough at these temperatures to evaporate, but they are mobile enough to diffuse more rapidly across the surface and react with each other. This leads to the formation of so-called first-generation complex organic molecules like HCOOH and HCOOCH₃ at point 1 in Fig. 1.2.

As shown by Benson & Myers (1989) and Goodman et al. (1993), cloud cores rotate at a rate of 10^{-14} – 10^{-13} s⁻¹. Angular momentum must be conserved throughout the collapse and this results in the formation of a disk around the protostar (Cassen & Moosman 1981, Terebey et al. 1984). Another feature that appears at roughly the same time is a bipolar jet, launched along the core's rotation axis from close to the protostar (Shu et al. 1991, Bally et al. 2007). The jets are probably another mechanism to remove excess angular momentum, but their precise origin remains poorly understood (Ray et al. 2007). They carve out a bipolar cavity in the remnant core material, which at this stage is usually called the envelope. Bipolar cavities have been observed for many protostars (Padgett et al. 1999, Arce & Sargent 2006).

The interaction between the envelope and the circumstellar disk is only understood in the most general terms: material falls in from large radii, hits the disk at some point, and is absorbed by it. It is still an open question whether the accretion from the envelope occurs predominantly onto the inner parts or the outer parts of the disk. The two-dimensional

⁴ The canonical mass ratio of 0.01 is actually the mass ratio between the dust and the hydrogen gas. The mass ratio between the dust and the total gas is 0.007 (Zhukovska et al. 2008).

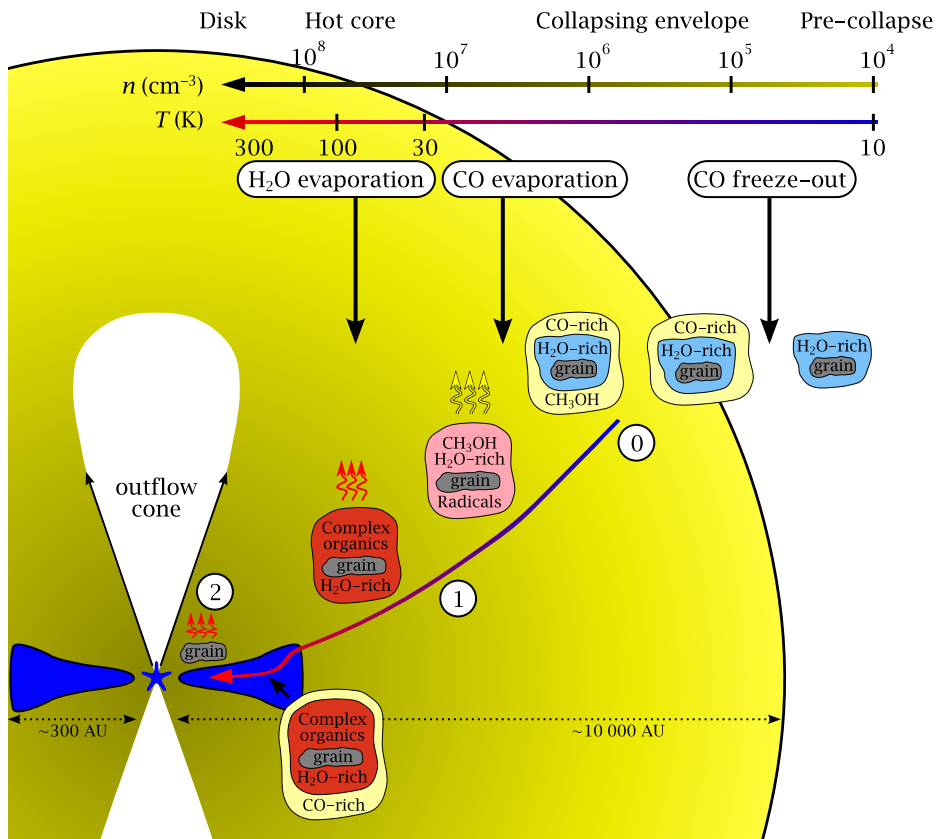


Figure 1.2 – Schematic representation of low-mass star formation and some of the chemistry involved, as reviewed by Herbst & van Dishoeck (2009). CO freezes out before the onset of collapse and is partially hydrogenated to CH_3OH (point 0). As the core warms up during the collapse, CO and other volatiles evaporate and first-generation complex organic molecules are formed on the grains (point 1). Conservation of angular momentum results in the formation of a circumstellar disk, where the temperature may become low enough for CO to freeze out again. In the hot inner region of the core and the disk, the entire ice mantle evaporates and high-temperature reactions in the gas phase lead to a second generation of complex organics (point 2).

(2D) axisymmetric hydrodynamical simulations of Brinch et al. (2008a,b) suggest the latter. As the disk gets thicker (i.e., more vertically extended), material from the envelope would have to flow across the surface of the disk in order to accrete onto the inner part. Brinch et al. showed that this does not typically happen. Instead, most material hits the disk near its outer edge. We also see a lot of envelope material hitting the outer parts of the disk in our semi-analytical collapse model, but there is still a fair amount (up to 50%) that makes its way to the inner parts of the disk and accretes there (Fig. 1.3; see also Fig.

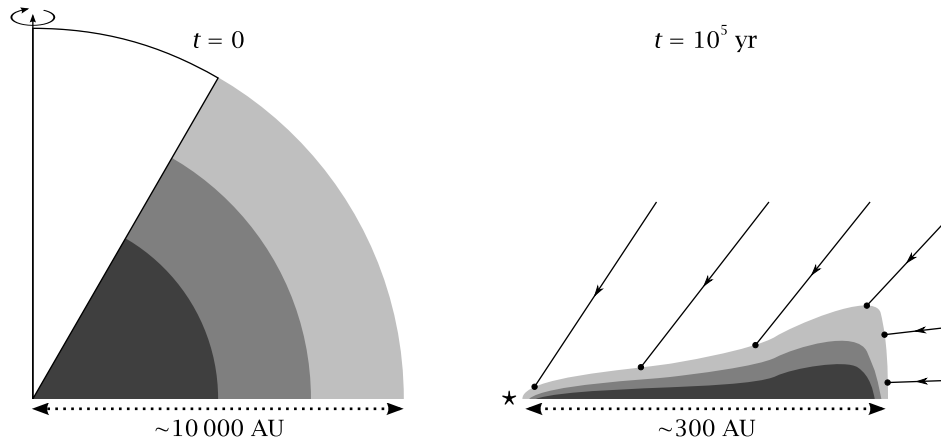


Figure 1.3 – Cartoon view of the layered accretion in one quadrant of our collapse model, based on Fig. 2.7 from Chapter 2. The outer parts of the original cloud core (left) end up as the surface layers of the circumstellar disk (right). The white part of the core is roughly the part that disappears into the outflow. The arrows illustrate the flow of material onto the disk.

4.2 in Chapter 4). Both the hydrodynamical simulations of Brinch et al. and our semi-analytical model result in layered accretion: the inner parts of the original cloud core end up near the midplane of the disk, and the outer parts of the core end up near the surface of the disk (Fig. 1.3; see Chapter 2 for details). Whether this is indeed what happens in reality remains to be confirmed by observations and 3D models.

Depending on initial conditions like the mass of the core and its rotation rate, the disk formed around the protostar can grow as large as 1000 AU (Andrews & Williams 2007b). Its density is several orders of magnitude higher than that of the core – in the inner parts, 10^{12} cm^{-3} is not unusual. Because of the wide range of physical conditions present throughout the disk, there are several distinct chemical regimes (Fig. 1.4). The midplane is shielded from direct irradiation, so the temperature may drop to 10 K or less. The volatile species that evaporated during the initial stages of the collapse now freeze out again onto the cold dust (see also Fig. 1.2, between points 1 and 2). Closer to the surface of the disk, the physical conditions are very different: the density is only 10^6 cm^{-3} or less, the temperature easily exceeds 100 K, and there is a strong UV field from the protostar. Ices cannot survive in such an environment and the first-generation complex organics formed at earlier times are liberated into the gas phase (point 2 in Fig. 1.2). There they can participate in a hot-core chemistry to form a second generation of complex organics (Herbst & van Dishoeck 2009). The same can happen with infalling material that passes through the hot inner part of the remnant envelope.

The entire collapse phase typically lasts a few 10^5 yr. The envelope gradually dissipates towards the end of that period and we are left with a pre-main sequence star surrounded by a circumstellar disk. Depending on the mass of star, it is known in this stage

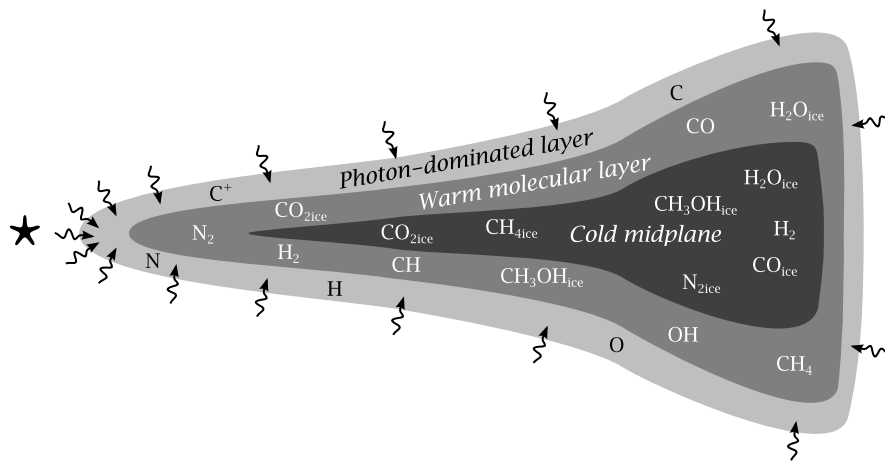


Figure 1.4 – Schematic representation of the three chemical regimes in a circumstellar disk: the photon-dominated layer (irradiated by the protostar and the interstellar UV field), the warm molecular layer, and the cold midplane. Typical species for each regime are indicated.

as a T Tauri ($< 2 M_{\odot}$) or Herbig Ae/Be star ($2\text{--}8 M_{\odot}$). The gaseous part of the disk disappears over a period of about 10 Myr by photoevaporation and ongoing accretion onto the star (Hollenbach et al. 2000, Haisch et al. 2001). During that time, its chemistry can roughly be divided into the three regimes shown in Fig. 1.4 (Bergin et al. 2007). It is as yet unknown whether the chemical composition of the disk is purely a result of the physical conditions during the T Tauri or Herbig Ae/Be stage, or whether the disk contains some kind of chemical history from the collapse phase. This is one of the key questions addressed in this thesis.

1.3 Planets, comets and meteorites

The evolution of the dust in the disk is governed by two processes: settling towards the midplane and coagulation into larger grains (Weidenschilling 1980, Miyake & Nakagawa 1995, Dullemond & Dominik 2004b, D’Alessio et al. 2006, Dullemond et al. 2007a, Lommen et al. 2007, 2009; see also the reviews by Natta et al. 2007 and Dominik et al. 2007). Together this may eventually lead to the formation of comets and planets. Whether planets are formed in all circumstellar disks is still an open question. It is also not yet clear how exactly planets are formed: two mechanisms have been proposed (core accretion and gravitational instabilities), but neither of them can be ruled out based on current observations (Matsuo et al. 2007, Lissauer & Stevenson 2007, Durisen et al. 2007).

Regardless of the details of how planets are formed, their initial chemical composition is inherited from the disk. This is also true for comets, and it is these objects in

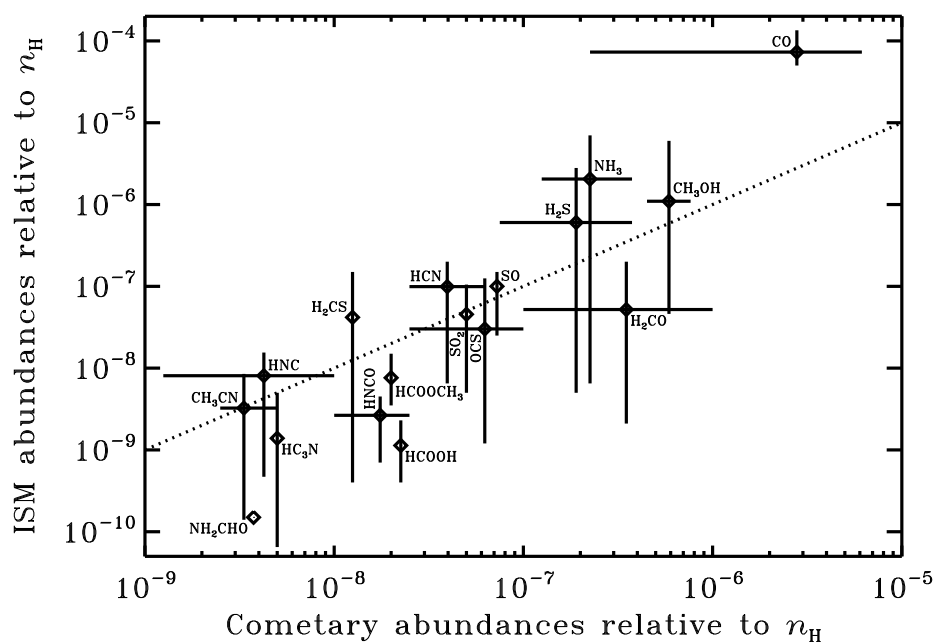


Figure 1.5 – Molecular abundances in comets (Halley, Hale-Bopp, Hyakutake, Lee, C/1999 S4 and Ikeya-Zhang) compared to those in ISM sources (IRAS 16293–2422 (warm inner envelope), L1157, W3(H₂O), G34.3+0.15, Orion Hot Core and Orion Compact Ridge) as provided by Bockelée-Morvan et al. (2000, 2004) and Schöier et al. (2002). The error bars indicate the spread between sources; errors from individual measurements are not included. The dashed line represents a one-to-one correspondence between cometary and ISM abundances and is not a fit to the data.

our own solar system that provide the most direct probe of the chemistry of the pre-solar nebula (Bockelée-Morvan et al. 2000). Spectroscopic studies of comet C/1995 O1 (Hale-Bopp) revealed a chemical composition that is remarkably similar to that of interstellar ices, hot cores and bipolar outflows, suggesting that the cometary ices were formed in the ISM and underwent little processing in the solar nebula. However, observations of a dozen other comets show abundance variations of at least an order of magnitude for CO, H₂CO, CH₃OH, HNC, H₂S and S₂, as well as smaller variations for other species (Bockelée-Morvan et al. 2004, Kobayashi et al. 2007). In Fig. 1.5, the abundances from the six comets 1P/Halley, Hale-Bopp, C/1996 B2 (Hyakutake), C/1999 H1 (Lee), C/1999 S4 (LINEAR) and 153P/Ikeya-Zhang are compared against those in the embedded protostar IRAS 16293–2422 (warm inner envelope), the bipolar outflow L1157, and the four hot cores W3(H₂O), G34.3+0.15, Orion HC and Orion CR (Bockelée-Morvan et al. 2000, 2004, Schöier et al. 2002). On the one hand, it shows the general correspondence between cometary and ISM abundances. On the other hand, it shows that the abundances can vary

greatly from one comet to the next. These different chemical compositions may be explained by assuming that the comets were formed in different parts of the solar nebula. If that is indeed the case, there must have been some degree of chemical processing between the ISM and the formation of the cometary nuclei. Two-dimensional collapse models such as the one presented in this thesis may help to clarify exactly how chemically pristine the cometary material is and where the mutual differences come from.

Meteorites provide another set of clues about the physical and chemical conditions in the early solar system. For example, Clayton et al. (1973) measured the abundances of the rare oxygen isotopes ^{17}O and ^{18}O in meteorites and found that they could not be explained with normal low-temperature isotope enhancement reactions alone.⁵ Recently, this so-called oxygen isotope anomaly has been interpreted as evidence for isotope-selective photoprocesses in the solar nebula – more specifically, for the selective photodissociation of C^{16}O , C^{17}O and C^{18}O (Clayton 2002, Lyons & Young 2005, Lee et al. 2008). If true, this would put strong constraints on the ambient UV intensity in the solar neighbourhood around 5 Gyr ago.

1.4 Chemical models

1.4.1 Historical development and reaction types

Chemical models play a pivotal role in interpreting abundances derived from spectroscopic observations. One of the first such models was constructed at Leiden Observatory in 1946 by Kramers & ter Haar and was targeted at CH and CH^+ , two of the first three molecules detected in the ISM (Sect. 1.1). Other early chemical modelling studies were undertaken by Bates & Spitzer (1951) and Solomon & Klemperer (1972). The latter used a network consisting of 22 monatomic and diatomic species linked by 34 reactions. They obtained good quantitative agreement with the observations of Herbig (1968) of CH and CN along the line of sight towards the star ζ Ophiuchi, but they could not reproduce the abundance of CH^+ . As observations identified ever more complex species over the years, so chemical networks have expanded. The latest versions of the two most popular networks – UMIST06 and osu_03_2008 – contain about 450 species and 4500 reactions (Woodall et al. 2007, Hersant et al. 2009).⁶ However, there are still many scientific questions that can be answered with only a few dozen species and a few hundred reactions (see, for example, Chapters 5 and 6).

The reactions in an astrochemical network can be categorised into several types. Table 1.1 lists the types used in modern networks like UMIST06 and osu_03_2008. The first 14 reaction types belong exclusively to the gas phase; types 15–18 describe gas-grain

⁵ For a set of isotopologues, the zero-point vibrational energy decreases with increasing mass. Therefore, the abundances of heavy isotopologues like H_2^{17}O and H_2^{18}O are enhanced at low temperature relative to the lighter isotopologue H_2^{16}O .

⁶ These numbers do not include recent developments like grain-surface chemistry (Hasegawa et al. 1992, Garrod et al. 2008) or hydrocarbon anions (Millar et al. 2007, Walsh et al. 2009), which would make the networks even larger. Adding isotopes like D or ^{13}C would also greatly expand the size of the network.

Table 1.1 – Reaction types in current astrochemical models.^a

Number	Type ^b	Example
1	<i>neutral-neutral</i>	$\text{OH} + \text{O} \rightarrow \text{O}_2 + \text{H}$
2	<i>ion-neutral</i>	$\text{CH}_2^+ + \text{H}_2 \rightarrow \text{CH}_3^+ + \text{H}$
3	<i>charge exchange</i>	$\text{CH} + \text{C}^+ \rightarrow \text{CH}^+ + \text{C}$
4	mutual neutralisation	$\text{C}^+ + \text{H}^- \rightarrow \text{C} + \text{H}$
5	<i>dissociative recombination</i>	$\text{CH}^+ + \text{e}^- \rightarrow \text{C} + \text{H}$
6	<i>radiative recombination</i>	$\text{CH}^+ + \text{e}^- \rightarrow \text{CH} + h\nu$
7	associative detachment	$\text{N} + \text{H}^- \rightarrow \text{NH} + \text{e}^-$
8	<i>radiative association</i>	$\text{C} + \text{H}_2 \rightarrow \text{CH}_2 + h\nu$
9	<i>photodissociation</i>	$\text{CO} + h\nu \rightarrow \text{C} + \text{O}$
10	<i>photoionisation</i>	$\text{C} + h\nu \rightarrow \text{C}^+ + \text{e}^-$
11	cosmic-ray dissociation	$\text{H}_2 + \zeta \rightarrow \text{H}^+ + \text{H}^-$
12	<i>cosmic-ray ionisation</i>	$\text{H}_2 + \zeta \rightarrow \text{H}_2^+ + \text{e}^-$
13	cosmic-ray–induced photodissociation	$\text{CO} + \zeta-h\nu \rightarrow \text{C} + \text{O}$
14	cosmic-ray–induced photoionisation	$\text{C} + \zeta-h\nu \rightarrow \text{C}^+ + \text{e}^-$
15	adsorption (or freeze-out)	$\text{CO} \rightarrow \text{CO}_{\text{ice}}$
16	desorption (or evaporation)	$\text{CO}_{\text{ice}} \rightarrow \text{CO}$
17	grain-surface hydrogenation	$\text{O}_{\text{ice}} + \text{H} \rightarrow \text{OH}_{\text{ice}}$
18	grain-surface radical-radical	$\text{CHO}_{\text{ice}} + \text{OH}_{\text{ice}} \rightarrow \text{HCOOH}_{\text{ice}}$

^a Based on Woodall et al. (2007). All species are in the gas phase unless indicated otherwise. The symbols $h\nu$, ζ and $\zeta-h\nu$ indicate a photon, a cosmic ray and a cosmic-ray–induced photon, respectively.

^b Reaction types in italics were already included in the model by Solomon & Klemperer (1972).

interactions and grain-surface reactions. It is interesting to note that of the fourteen gas-phase reaction types in Table 1.1, nine were already included by Solomon & Klemperer (1972) in their chemical model. A reaction type of particular importance to this thesis is photodissociation. It is one of the key processes controlling the abundances during the collapse phase in Chapter 3 and it sets a lower limit to the size of circumstellar PAHs in Chapter 6. It plays an even larger role in Chapter 5, which is entirely about the selective photodissociation of CO isotopologues.

Photodissociation can take place in several ways (van Dishoeck 1987, 1988, Kirby & van Dishoeck 1988), two of which are illustrated in Fig. 1.6. For most simple species, the main channel is direct photodissociation. Absorption of a UV or visible photon brings the molecule from the electronic ground state into a repulsive excited state. Spontaneous emission back to the ground state is a slow process, so essentially all absorptions result in photodissociation. The corresponding cross section is a continuous function peaking at the vertical excitation energy. Another possible mechanism is predissociation: the molecule is first excited from the ground state into a bound upper state and then crosses over into a repulsive state. This is the dominant dissociation mechanism for CO and its isotopologues (Chapter 5). The predissociation cross section consists of a series of discrete peaks, corresponding to the vibrational levels of the bound upper state.

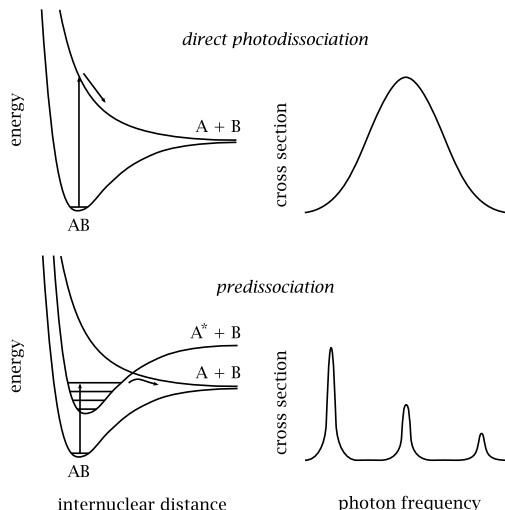


Figure 1.6 – Schematic potential energy curves and cross sections for direct photodissociation (top) and predissociation (bottom) of a diatomic molecule AB, after van Dishoeck (1988).

For molecules with a large number of atoms, such as PAHs (Fig. 1.1), the density of vibrational levels at each electronic state becomes high enough to form a quasi-continuum. When a PAH absorbs a UV or visible photon and is excited to an upper electronic state, it rapidly crosses over into the vibrational quasi-continuum of the electronic ground state (Léger et al. 1988, 1989). From here, it relaxes back to a low vibrational level by radiative decay. As long as the internal energy of the PAH exceeds a certain threshold value, there is the possibility of losing a hydrogen atom or a carbon fragment (Le Page et al. 2001). In the strong radiation fields in the inner parts of the disk and the envelope, the PAH may absorb a second photon before its internal energy falls back below the dissociation threshold. Multi-photon absorptions keep the PAH at high internal energy, thus greatly increasing the effective photodissociation rate (Chapter 6).

1.4.2 Solution methods

Mathematically, a network of chemical reactions results in a system of ordinary differential equations (ODEs). Each species i is formed by a certain number of reactions (say, m_f) and it is destroyed by a certain number of other reactions (say, m_d). Hence, the time derivative of the number density (n_i in cm^{-3}) is

$$\frac{dn_i}{dt} = \sum_{j=1}^{m_f} R_{f,j} - \sum_{j=1}^{m_d} R_{d,j}, \quad (1.1)$$

with $R_{f,j}$ and $R_{d,j}$ the rates (in $\text{cm}^{-3} \text{s}^{-1}$) of the individual formation and destruction reactions. If a reaction involves two reactants with number densities n_1 and n_2 , its rate is of

the form

$$R = kn_1n_2. \quad (1.2)$$

This is the case for reaction types 1–8, 17 and 18 from Table 1.1. For types 9–16, where there is only one reactant, the rate is of the form

$$R = kn_1. \quad (1.3)$$

Because of the low densities in most astronomical objects of interest to chemical modellers, reactions with three reactants are very slow and are not included in the standard networks. However, they start to become important in the innermost regions of circumstellar disks.

The variable k in Eqs. (1.2) and (1.3) is the so-called rate coefficient. Rate coefficients are obtained most reliably by measuring the reaction in controlled conditions in a laboratory – ideally at a range of conditions, so that it can be established quantitatively how the coefficient depends for example on temperature. Another good method is to derive the coefficient from quantum chemical state-to-state calculations. However, both methods are time-consuming, so many coefficients in current networks are based on extrapolations or chemical kinetic theories, and some of them are no more than educated guesses.

Given a set of species, reactions and rate coefficients, there are two ways of solving for the abundances: find an equilibrium or follow the evolution of the abundances in time. The two methods are now illustrated with a very simple system consisting of only two species (CO gas and CO ice, with number densities n_{gas} and n_{ice}) linked by two reactions (freeze-out and evaporation, with rates R_{des} and R_{ads}), similar to what is used in Chapter 2. The rate coefficients depend on the temperature T and the gas density n_{H} ; we approximate them as

$$k_{\text{ads}} = (1 \times 10^{-18} \text{ cm}^3 \text{ K}^{-1/2} \text{ s}^{-1}) n_{\text{H}} \sqrt{T}, \quad (1.4)$$

$$k_{\text{des}} = (1 \times 10^{12} \text{ s}^{-1}) \exp\left(-\frac{855 \text{ K}}{T}\right), \quad (1.5)$$

after Charnley et al. (2001) and Bisschop et al. (2006).

If we are interested in the equilibrium abundances at a given T and n_{H} , we have to solve the equations

$$\begin{cases} \text{d}n_{\text{gas}}/\text{d}t = k_{\text{des}}n_{\text{ice}} - k_{\text{ads}}n_{\text{gas}} = 0 \\ \text{d}n_{\text{ice}}/\text{d}t = k_{\text{ads}}n_{\text{gas}} - k_{\text{des}}n_{\text{ice}} = 0 \end{cases} \quad (1.6)$$

under the condition of conservation of mass. Setting the total CO abundance to 10^{-4} relative to n_{H} , this is simply expressed as

$$n_{\text{gas}} + n_{\text{ice}} = 10^{-4} n_{\text{H}}. \quad (1.7)$$

The equilibrium solution then becomes

$$n_{\text{gas}} = \frac{10^{-4} n_{\text{H}} k_{\text{des}}}{k_{\text{ads}} + k_{\text{des}}}, \quad n_{\text{ice}} = 10^{-4} n_{\text{H}} - n_{\text{gas}}. \quad (1.8)$$

The procedure is essentially the same for a full chemical network: set the time derivatives of all individual abundances to zero and ensure conservation of mass. However, an analytical solution can generally not be derived for a full network. Instead, the problem must be solved with a numerical procedure like the Newton-Raphson routine (Press et al. 1992).

Solving for the equilibrium abundances is usually fine if the physical conditions are constant, although one always has to check that the object of interest is old enough to reach chemical equilibrium. If that is not the case, or if the physical conditions change on timescales shorter than the chemical timescale, one has to solve the abundances time-dependently with an integration package like VODE (Brown et al. 1989). Starting from some initial values, the abundances are evolved in small time steps Δt up to a pre-determined final time. Turning back to our CO system, we could for example begin with all CO as ice and ask how long it takes to evaporate at $n_{\text{H}} = 10^4 \text{ cm}^{-3}$ and $T = 18 \text{ K}$. We could also simulate the warm-up phase during the collapse of a cloud core by starting at 10 K and increasing the temperature at a typical rate of 0.01 K yr^{-1} . If we couple this to a physical model of the collapse to get a relationship between the temperature and the distance from the protostar, we could then say *where* CO evaporates. Finally, we could add other molecules to the mix and expand the simple freeze-out/evaporation scheme to a full chemical network. In essence, this is what we do in Chapters 2 and 3.

1.5 This thesis

The central theme of this thesis is the chemical evolution during the formation of low-mass stars and their surrounding disks. Although the initial stages of the collapsing cloud core are well described by spherically symmetric models, this is no longer possible once the disk is formed. So far, the chemistry during the collapse phase has only been studied up to the point that the disk is formed or on large scales where spherical symmetry can still be safely assumed ($> 1000 \text{ AU}$). In this thesis we present the first physical-chemical model that follows the entire core collapse and disk formation process in two dimensions.

In the preceding sections we introduced several open questions related to low-mass star formation and the chemical evolution of the material involved. The most important ones addressed in this thesis are:

- Does material from the envelope accrete predominantly on the inner or on the outer parts of the disk?
- How does the chemical composition of the gas and dust change from the envelope to the disk?
- Is the chemical composition of a T Tauri or Herbig Ae/Be disk purely a result of in situ processes or does it retain some signature of the collapse phase?
- What fraction of the cometary ices is truly pristine?
- What is the origin of the chemical diversity of comets?

The first three chapters of this thesis deal with our 2D collapse model. To begin with, Chapter 2 contains a full description of the model. We couple the analytical collapse solu-

tions of Shu (1977), Cassen & Moosman (1981) and Terebey et al. (1984) to the model of Lynden-Bell & Pringle (1974) for a viscously evolving circumstellar disk. The size and luminosity of the central sources evolve according to Adams & Shu (1986) and Young & Evans (2005). We define a standard set of initial conditions (core mass, sound speed and rotation rate) and find that the resulting density and velocity profiles show good agreement with those from more detailed hydrodynamical simulations (Yorke & Bodenheimer 1999, Brinch et al. 2008a,b). The temperature is a very important input parameter for the chemistry, so we compute it with a full radiative transfer method (Dullemond & Dominik 2004a) at a series of time intervals. The semi-analytical nature of our model allows us to easily change the initial conditions and we obtain density, velocity and temperature profiles for a small grid of parameters.

As a first illustration of the full chemistry, we look at the freeze-out and evaporation of CO and H₂O. We calculate infall trajectories originating from several thousand points in the cloud core to see how material flows towards the star and the disk. The density and temperature along each trajectory provide the input for evolving the gas and ice abundances of CO and H₂O, resulting in 2D profiles of the gas-to-ice ratios in the disk and remnant envelope.

In Chapter 4, we revisit one particular physical aspect of our collapse model: the sub-Keplerian velocity at which material accretes onto the disk. This problem was studied previously by Cassen & Moosman (1981) and Hueso & Guillot (2005), but not in the context of a 2D model. We derive a new solution for the radial velocities inside the disk and show that it does not strongly affect the results from the preceding chapter. However, it does offer new insights into the related question of why the dust in circumstellar disks is more crystalline than in the ISM. We rerun the models of Dullemond et al. (2006a) and obtain a better match with observed crystalline abundances in disks.

We couple our 2D collapse model – including the new correction for sub-Keplerian accretion – to a full gas-phase chemical network in Chapter 3 to analyse the abundances of several major oxygen-, carbon- and nitrogen-bearing species. We describe the evolution of the abundances along one specific infall trajectory and show that most changes can be traced back to key chemical processes like the evaporation of CO or the photodissociation of H₂O. In turn, these key processes relate back to physical events like the increase in temperature or UV flux at some point along the trajectory. Material ending up in other parts of the disk encounters different physical conditions and we show how that affects the abundances of certain species. Finally, we seek to answer whether the disks around T Tauri and Herbig Ae/Be stars retain some signature of the collapse-phase chemistry, or if their chemical composition is fully determined by in situ processing. To that end, we evolve the abundances obtained at the end of the collapse for another 1 Myr in a static disk model to see how much they still change.

Having discussed the gas-phase chemistry and the dust mineralogy, we turn to the question of isotopes in Chapter 5. We derive an extensive update to the CO photodissociation model of van Dishoeck & Black (1988) using new laboratory data. The model includes not only the regular isotopes ¹²C and ¹⁶O, but also the less abundant ¹³C, ¹⁷O and ¹⁸O. We discuss the effect of the temperature on the isotope-selective photodissociation rates and we couple the photodissociation model to a small chemical network to

analyse the abundance of CO and its isotopologues as a function of depth into diffuse clouds, photon-dominated regions and circumstellar disks. A long-standing puzzle in our own solar system is the anomalous oxygen isotope ratio found in meteorites. Our results support the recent hypothesis by Lyons & Young (2005) that the anomalous ratio is due to CO photodissociation in the solar nebula.

The final chapter of this thesis targets the chemistry of yet another class of compounds: polycyclic aromatic hydrocarbons or PAHs. We adapt the chemistry models of Le Page et al. (2001) and Weingartner & Draine (2001) and the excitation model of Draine & Li (2007) to find the dominant charge and hydrogenation states of PAHs in disks around T Tauri and Herbig Ae/Be stars. We explicitly calculate where in the disk PAHs are photodissociated, taking into account the possibility of multi-photon absorption events. The 2D abundance profiles thus obtained are coupled to a radiative transfer package (Dullemond & Dominik 2004a) to simulate spatially resolved spectra. Finally, we compare the predicted spatial extent of the PAH features to observations by van Boekel et al. (2004), Habart et al. (2006) and Geers et al. (2007) to determine the size of the PAHs responsible for the observed emission.

Each of the Chapters 2–6 closes with a summary of the conclusions that we draw from our model results and the comparison with observations and other models. We present here the main conclusions from this thesis.

- Our two-dimensional semi-analytical collapse model produces realistic density and velocity profiles, allowing us to track the chemistry all the way from pre-stellar cores to circumstellar disks. Combined with full radiative transfer to get temperatures and UV fluxes, this makes it an excellent tool to study the chemical evolution during low-mass star formation (Chapters 2 and 3).
- Both CO and H₂O freeze out before the onset of collapse. H₂O remains frozen throughout the collapse phase, except when it gets into the inner 5–10 AU of a disk. From there, it may move outwards again to colder regions as the disk expands to conserve angular momentum. CO rapidly evaporates once the collapse starts, although some of it is likely to be trapped in the H₂O ice. In the coldest parts of a disk (< 18 K), all CO freezes out again (Chapters 2 and 3).
- The chemistry during the collapse of a cloud core and the formation of a disk is dominated by a small number of key chemical processes that are activated by changes in the physical conditions. Examples of these key processes are the evaporation of CO, CH₄ and H₂O at approximately 18, 22 and 100 K, and the photodissociation of CH₄ and H₂O in the vicinity of the outflow wall. The photodissociation of CO requires a stellar temperature of at least 7000 K or a colder star with excess UV emission (Chapter 3).
- Because of the short dynamical timescales, the chemistry does not reach equilibrium at any time during the collapse. The chemical composition of the disk at the end of the collapse phase is therefore primarily a product of the physical conditions at earlier times. Additional work is required to determine if any chemical signatures from the collapse phase survive into the T Tauri or Herbig Ae/Be stages (Chapter 3).

- The material from which solar-system comets are formed must be of mixed origins. Our collapse model predicts a large degree of chemical processing towards the comet-forming zone in the disk. The observed fractions of crystalline silicates in comets are also indicative of strong processing. However, strong processing cannot explain why the chemical composition of cometary ices so closely resembles that of interstellar ices. The detections of amorphous silicates in comets also point at the presence of unprocessed material. Hence, it would seem that comets were formed partially from processed material and partially from pristine material (Chapters 3 and 4).
- The chemical diversity between individual comets is likely a result of them having formed at different locations in the solar nebula. The physical conditions in a disk change in time, so if two comets were formed several 10^4 or 10^5 yr apart, their chemical compositions would also be different (Chapter 3).
- It is important to take the vertical structure of a disk into account when computing the infall trajectories. The outer parts of a disk can intercept material and keep it from accreting onto the disk at much smaller radii, as it would if the disk is treated as completely flat (Chapters 2–4).
- Thermal annealing followed by outward radial mixing is responsible for at least part of the crystalline silicates observed in circumstellar disks (Chapter 4).
- The CO photodissociation rate obtained with our new model is 30% higher than the old value. The dissociation of $C^{17}O$ and $^{13}C^{17}O$ shows almost exactly the same depth dependence as that of $C^{18}O$ and $^{13}C^{18}O$, respectively, so ^{17}O and ^{18}O are equally fractionated with respect to ^{16}O . The level of fractionation is higher for cold gas than it is for warm gas (Chapter 5).
- Isotope fractionation in circumstellar disks through the photodissociation of CO in the surface layers requires a far-UV component in the irradiating spectrum. The interstellar radiation field is sufficient for this purpose. Our model supports the hypothesis that the photodissociation of CO is responsible for the anomalous ^{17}O and ^{18}O abundances in meteorites (Chapter 5).
- PAH emission from circumstellar disks is extended on a scale similar to the size of the disks. Neutral and positively ionised PAHs contribute to the emission in roughly equal amounts. Based on the spatial extent, the observed emission originates mostly from PAHs with a size of at least 100 carbon atoms. Smaller PAHs are efficiently destroyed by the stellar UV field in the inner ~ 30 AU of a disk (Chapter 6).

Although our two-dimensional semi-analytical collapse model is an important step forwards in the study of the chemical evolution during low-mass star formation, many questions still remain unanswered. With regards to the model itself, we have only undertaken some basic tests against observations. One of the first challenges now is to couple the model to a radiative transfer package to predict spectral lines and compare them to observational data. The start of science operations with the Herschel Space Observatory later this year and with the Atacama Large Millimeter/submillimeter Array (ALMA) in

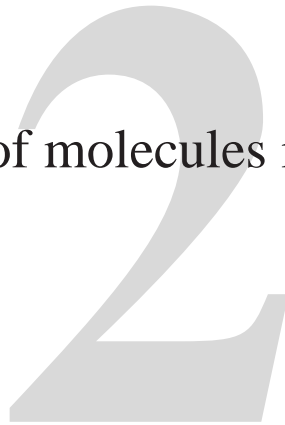
2011 offers both exciting possibilities and additional challenges. For example, the unprecedented spatial resolution of ALMA may well require a revision of the physics in the inner parts of the disk and envelope.

Given the semi-analytical nature of our model, some physical aspects had to be simplified. The bipolar outflow is only included in an ad-hoc fashion and we may be underestimating how much material it sweeps up and out of the system. Another simplification involves the amount of core material that becomes involved in the collapse. We currently let the entire core accrete onto the star and disk, but recent interferometric observations call this into question (Jørgensen et al. 2007). In both cases, the final disk mass and temperature would be different, and some of the chemistry would change as well.

On the chemical side, the treatment of photoprocesses currently involves several approximations in the way the shape of the irradiating spectrum is taken into account. Also, grain-surface processes are still largely unexplored. They have to be added to our network if we want to reproduce the observed abundances of methanol and more complex organic molecules. If amino acids and other biologically important species are formed in circumstellar disks, it is likely that this happens on grain surfaces, or that this at least requires precursor molecules formed on grains. In either case, grain-surface chemistry promises to be important as astronomers worldwide continue to unravel the history of our solar system in general and the origins of life on Earth in particular.

The chemical history of molecules in circumstellar disks

I: Ices



R. Visser, E. F. van Dishoeck, S. D. Doty and C. P. Dullemond
Astronomy & Astrophysics, 2009, 495, 881

Abstract

Context. Many chemical changes occur during the collapse of a molecular cloud core to form a low-mass star and the surrounding disk. One-dimensional models have been used so far to analyse these chemical processes, but they cannot properly describe the incorporation of material into disks.

Aims. The goal of this chapter is to understand how material changes chemically as it is transported from the cloud to the star and the disk. Of special interest is the chemical history of the material in the disk at the end of the collapse.

Methods. We present a two-dimensional, semi-analytical model that, for the first time, follows the chemical evolution from the pre-stellar core to the protostar and circumstellar disk. The model computes infall trajectories from any point in the cloud core and tracks the radial and vertical motion of material in the viscously evolving disk. It includes a full time-dependent radiative transfer treatment of the dust temperature, which controls much of the chemistry. We explore a small parameter grid to understand the effects of the sound speed and the mass and rotation rate of the core. The freeze-out and evaporation of carbon monoxide (CO) and water (H₂O), as well as the potential for forming complex organic molecules in ices, are considered as important first steps towards illustrating the full chemistry.

Results. Both species freeze out towards the centre before the collapse begins. Pure CO ice evaporates during the infall phase and readsorbs in those parts of the disk that cool below the CO desorption temperature of ~ 18 K. H₂O remains solid almost everywhere during the infall and disk formation phases and evaporates within ~ 10 AU of the star. Mixed CO-H₂O ices are important in keeping some solid CO above 18 K and in explaining the presence of CO in comets. Material that ends up in the planet- and comet-forming zones of the disk (~ 5 –30 AU from the star) is predicted to spend enough time in a warm zone (several 10^4 yr at a dust temperature of 20–40 K) during the collapse to form first-generation complex organic species on the grains. The dynamical timescales in the hot inner envelope (hot core or hot corino) are too short for abundant formation of second-generation molecules by high-temperature gas-phase chemistry.

2.1 Introduction

The formation of low-mass stars and their planetary systems is a complex event, spanning several orders of magnitude in temporal and spatial scales, and involving a wide variety of physical and chemical processes. Thanks to observations, theory and computer simulations, the general picture of low-mass star formation is now understood (see reviews by Shu et al. 1987, di Francesco et al. 2007, Klein et al. 2007, White et al. 2007 and Dullemond et al. 2007b). An instability in a cold molecular cloud core leads to gravitational collapse. Rotation and magnetic fields cause a flattened density structure early on, which evolves into a circumstellar disk at later times. The protostar continues to accrete matter from the disk and the remnant envelope, while also expelling matter in a bipolar pattern. Grain growth in the disk eventually leads to the formation of planets, and as the remaining dust and gas disappear, a mature solar system emerges. While there has been ample discussion in the literature on the origin and evolution of grains in disks (see reviews by Natta et al. 2007 and Dominik et al. 2007 or the discussion in Chapter 4), little attention has so far been paid to the chemical history of the more volatile material in a two- or three-dimensional setting.

Chemical models are required to understand the observations and develop the simulations (see reviews by Ceccarelli et al. 2007, Bergin et al. 2007 and Bergin & Tafalla 2007). The chemistry in pre-stellar cores is relatively easy to model, because the dynamics and the temperature structure are simpler before the protostar is formed than afterwards. A key result from the pre-stellar core models is the depletion of many carbon-bearing species towards the centre of the core (Bergin & Langer 1997, Lee et al. 2004).

The next step in understanding the chemical evolution during star formation is to model the chemistry during the collapse phase (Ceccarelli et al. 1996, Rodgers & Charnley 2003, Doty et al. 2004, Lee et al. 2004, Garrod & Herbst 2006, Aikawa et al. 2008, Garrod et al. 2008). All of the collapse chemistry models so far are one-dimensional, and thus necessarily ignore the circumstellar disk. As the protostar turns on and heats up the surrounding material, all models agree that frozen-out species return to the gas phase if the dust temperature surpasses their evaporation temperature. The higher temperatures can further drive a hot-core-like chemistry, and complex molecules may be formed if the infall timescales are long enough.

If the model is expanded into a second dimension and the disk is included, the system gains a large reservoir where infalling material from the cloud can be stored for a long time (at least several 10^4 yr) before accreting onto the star. This can lead to further chemical enrichment, especially in the warmer parts of the disk (Aikawa et al. 1997, 2008, Aikawa & Herbst 1999, Willacy & Langer 2000, van Zadelhoff et al. 2003, Rodgers & Charnley 2003). The interior of the disk is shielded from direct irradiation by the star, so it is colder than the disk's surface and the remnant envelope. Hence, molecules that evaporated as they fell in towards the star may freeze out again when they enter the disk. This was first shown quantitatively by Brinch et al. (2008b, hereafter BWH08) using a two-dimensional hydrodynamical simulation.

In addition to observations of nearby star-forming regions, the comets in our own solar system provide a unique probe into the chemistry that takes place during star and planet

formation. The bulk composition of the cometary nuclei is believed to be mostly pristine, closely reflecting the composition of the pre-solar nebula (Bockelée-Morvan et al. 2004). However, large abundance variations have been observed between individual comets and these remain poorly understood (Kobayashi et al. 2007). Two-dimensional chemical models may shed light on the cometary chemical diversity.

Two molecules of great astrophysical interest are carbon monoxide (CO) and water (H₂O). They are the main reservoirs of carbon and oxygen and control much of the overall chemistry. CO is an important precursor for more complex molecules; for example, solid CO can be hydrogenated to formaldehyde (H₂CO) and methanol (CH₃OH) at low temperatures (Watanabe & Kouchi 2002, Fuchs et al. 2009). In turn, these two molecules form the basis of even larger organic species like methyl formate (HCOOCH₃; Garrod & Herbst 2006, Garrod et al. 2008). The key role of H₂O in the formation of life on Earth and potentially elsewhere is evident. If the entire formation process of low-mass stars and their planets is to be understood, a thorough understanding of these two molecules is essential.

This chapter is the first in a series of publications aiming to model the chemical evolution from the pre-stellar core to the disk phase in two dimensions, using a simplified, semi-analytical approach for the dynamics of the collapsing envelope and the disk, but including detailed radiative transfer for the temperature structure. The model follows individual parcels of material as they fall in from the cloud core into the disk. The gaseous and solid abundances of CO and H₂O are calculated for each infalling parcel to obtain global gas-ice profiles. The semi-analytical nature of the model allows for an easy exploration of physical parameters like the core's mass and rotation rate, or the effective sound speed. Tracing the temperature history of the infalling material provides a first clue into the formation of more complex species. The model also offers some insight into the origin of the chemical diversity in comets.

Section 2.2 contains a full description of the model. Results are presented in Sect. 2.3 and discussed in a broader astrophysical context in Sect. 2.4. Finally, conclusions are drawn in Sect. 2.5.

2.2 Model

The physical part of our two-dimensional axisymmetric model describes the collapse of an initially spherical, isothermal, slowly rotating cloud core to form a star and circumstellar disk. The collapse dynamics are taken from Shu (1977, hereafter S77), including the effects of rotation as described by Cassen & Moosman (1981, hereafter CM81) and Terebey et al. (1984, hereafter TSC84). Infalling material hits the equatorial plane inside the centrifugal radius to form a disk, whose further evolution is constrained by conservation of angular momentum (Lynden-Bell & Pringle 1974). Some properties of the star and the disk are adapted from Adams & Shu (1986) and Young & Evans (2005, hereafter YE05). Magnetic fields are not included in our model. They are unlikely to affect the chemistry directly and their main physical effect (causing a flattened density distribution; Galli & Shu 1993) is already accounted for by the rotation of the core.

Our model is an extension of the one used by Dullemond et al. (2006a) to study the crystallinity of dust in circumstellar disks (see also Chapter 4). That model was purely one-dimensional; our model treats the disk more realistically as a two-dimensional structure.

2.2.1 Envelope

The cloud core (or envelope) is taken to be a uniformly rotating singular isothermal sphere at the onset of collapse. It has a solid-body rotation rate Ω_0 and an r^{-2} density profile (S77):

$$\rho_0(r) = \frac{c_s^2}{2\pi G r^2}, \quad (2.1)$$

where G is the gravitational constant and c_s the effective sound speed. Throughout this thesis, r is used for the spherical radius and R for the cylindrical radius. Setting the outer radius at r_{env} , the total mass of the core is

$$M_0 = \frac{2c_s^2 r_{\text{env}}}{G}. \quad (2.2)$$

After the collapse is triggered at the centre, an expansion wave (or collapse front) travels outwards at the sound speed (S77, TSC84). Material inside the expansion wave falls in towards the centre to form a protostar. The infalling material is deflected towards the gravitational midplane by the core's rotation. It first hits the midplane inside the centrifugal radius (where gravity balances angular momentum; CM81), resulting in the formation of a circumstellar disk (Sect. 2.2.2).

The dynamics of a collapsing singular isothermal sphere were computed by S77 in terms of the non-dimensional variable $x = r/c_s t$, with t the time after the onset of collapse. In this self-similar description, the head of the expansion wave is always at $x = 1$. The density and radial velocity are given by the non-dimensional variables \mathcal{A} and v , respectively. (S77 used α for the density, but our model already uses that symbol for the viscosity in Sect. 2.2.2.) These variables are dimensionalised through

$$\rho(r, t) = \frac{\mathcal{A}(x)}{4\pi G t^2}, \quad (2.3)$$

$$u_r(r, t) = c_s v(x). \quad (2.4)$$

Values for \mathcal{A} and v are tabulated in S77.

CM81 and TSC84 analysed the effects of slow uniform rotation on the S77 collapse solution, with the former focussing on the flow onto the protostar and the disk and the latter on what happens farther out in the envelope. In the axisymmetric TSC84 description, the density and infall velocities depend on the time, the radius and the polar angle:

$$\rho(r, \theta, t) = \frac{\mathcal{A}(x, \theta, \tau)}{4\pi G t^2}, \quad (2.5)$$

$$u_r(r, \theta, t) = c_s v(x, \theta, \tau), \quad (2.6)$$

where $\tau = \Omega_0 t$ is the non-dimensional time. The polar velocity is given by

$$u_\theta(r, \theta, t) = c_s w(x, \theta, \tau). \quad (2.7)$$

We solved the differential equations from TSC84 numerically to obtain solutions for \mathcal{A} , v and w .

The TSC84 solution breaks down around $x = \tau^2$, so the CM81 solution is used inside of this point. A streamline through a point (r, θ) effectively originated at an angle θ_0 in this description:

$$\frac{\cos \theta_0 - \cos \theta}{\sin^2 \theta_0 \cos \theta_0} - \frac{R_c}{r} = 0, \quad (2.8)$$

where R_c is the centrifugal radius,

$$R_c(t) = \frac{1}{16} c_s m_0^3 t^3 \Omega_0^2, \quad (2.9)$$

with m_0 a numerical factor equal to 0.975. The CM81 radial and polar velocity are

$$u_r(r, \theta, t) = -\sqrt{\frac{GM}{r}} \sqrt{1 + \frac{\cos \theta}{\cos \theta_0}}, \quad (2.10)$$

$$u_\theta(r, \theta, t) = \sqrt{\frac{GM}{r}} \sqrt{1 + \frac{\cos \theta}{\cos \theta_0}} \frac{\cos \theta_0 - \cos \theta}{\sin \theta}, \quad (2.11)$$

and the CM81 density is

$$\rho(r, \theta, t) = -\frac{\dot{M}}{4\pi r^2 u_r} \left[1 + 2 \frac{R_c}{r} P_2(\cos \theta_0) \right]^{-1}, \quad (2.12)$$

where P_2 is the second-order Legendre polynomial and $\dot{M} = m_0 c_s^3 / G$ is the total accretion rate from the envelope onto the star and disk (S77, TSC84). The primary accretion phase ends when the outer shell of the envelope reaches the star and disk. This point in time ($t_{\text{acc}} = M_0 / \dot{M}$) is essentially the beginning of the T Tauri or Herbig Ae/Be phase, but it does not yet correspond to a typical T Tauri or Herbig Ae/Be object (see Sect. 2.3.2).

The TSC84 and CM81 solutions do not reproduce the cavities created by the star's bipolar outflow, so they have to be put in separately. Outflows have been observed in two shapes: conical and curved (Padgett et al. 1999). Both can be characterised by the outflow opening angle, γ , which grows with the age of the object. Arce & Sargent (2006) found a linear relationship in log-log space between the age of a sample of 17 young stellar objects and their outflow opening angles. Some explanations exist for the outflow widening in general, but it is not yet understood how $\gamma(t)$ depends on parameters like the initial cloud core mass and the sound speed. It is likely that the angle depends on the relative age of the object rather than on the absolute age.

The purpose of our model is not to include a detailed description of the outflow cavity. Instead, the outflow is primarily included because of its effect on the temperature profiles (Whitney et al. 2003). Its opening angle is based on the fit by Arce & Sargent (2006)

to their Fig. 5, but it is taken to depend on t/t_{acc} rather than t alone. The outflow is also kept smaller, which brings it closer to the Whitney et al. angles. Its shape is taken to be conical. With the resulting formula,

$$\log \frac{\gamma(t)}{\text{deg}} = 1.5 + 0.26 \log \frac{t}{t_{\text{acc}}}, \quad (2.13)$$

the opening angle is always 32° at $t = t_{\text{acc}}$. The numbers in Eq. (2.13) are poorly constrained; however, the details of the outflow (both size and shape) do not affect the temperature profiles strongly, so this introduces no major errors in the chemistry results. The outflow cones are filled with a constant mass of $0.002M_0$ at a uniform density, which decreases to $10^3\text{--}10^4 \text{ cm}^{-3}$ at t_{acc} depending on the model parameters. The outflow effectively removes about 1% of the initial envelope mass.

2.2.2 Disk

The rotation of the envelope causes the infalling material to be deflected towards the midplane, where it forms a circumstellar disk. The disk initially forms inside the centrifugal radius (CM81), but conservation of angular momentum quickly causes the disk to spread beyond this point. The evolution of the disk is governed by viscosity, for which our model uses the common α prescription (Shakura & Sunyaev 1973). This gives the viscosity coefficient ν as

$$\nu(R, t) = \alpha c_{s,d} H. \quad (2.14)$$

The sound speed in the disk, $c_{s,d} = \sqrt{kT_m/\mu m_p}$ (with k the Boltzmann constant, m_p the proton mass and μ the mean molecular mass of 2.3 nuclei per hydrogen molecule), is different from the sound speed in the envelope, c_s , because the midplane temperature of the disk, T_m , varies as described in Hueso & Guillot (2005). The other variable from Eq. (2.14) is the scale height:

$$H(R, t) = \frac{c_{s,d}}{\Omega_k}, \quad (2.15)$$

where Ω_k is the Keplerian rotation rate:

$$\Omega_k(R, t) = \sqrt{\frac{GM_*}{R^3}}, \quad (2.16)$$

with M_* the stellar mass (Eq. (2.29)). The viscosity parameter α is kept constant at 10^{-2} (Dullemond et al. 2007b, Andrews & Williams 2007b).

Solving the problem of advection and diffusion yields the radial velocities inside the disk (Dullemond et al. 2006a, Lynden-Bell & Pringle 1974):

$$u_R(R, t) = -\frac{3}{\Sigma \sqrt{R}} \frac{\partial}{\partial R} (\Sigma \nu \sqrt{R}). \quad (2.17)$$

The surface density Σ evolves as

$$\frac{\partial \Sigma(R, t)}{\partial t} = -\frac{1}{R} \frac{\partial}{\partial R} (\Sigma R u_R) + S, \quad (2.18)$$

where the source function S accounts for the infall of material from the envelope:

$$S(R, t) = 2N\rho u_z, \quad (2.19)$$

with u_z the vertical component of the envelope velocity field (Eqs. (2.6), (2.7), (2.10) and (2.11)). The factor 2 accounts for the envelope accreting onto both sides of the disk and the normalisation factor N ensures that the overall accretion rate onto the star and the disk is always equal to \dot{M} . Both ρ and u_z in Eq. (2.19) are to be computed at the disk-envelope boundary, which is defined at the end of this section.

As noted by Hueso & Guillot (2005), the infalling envelope material enters the disk with a sub-Keplerian rotation rate, so, by conservation of angular momentum, it would tend to move a bit farther inwards. Not taking this into account would artificially generate angular momentum, causing the disk to take longer to accrete onto the star. As a consequence the disk has, at any given point in time, too high a mass and too large a radius. Hueso & Guillot solved this problem by modifying Eq. (2.19) to place the material directly at the correct radius. However, this causes an undesirable discontinuity in the infall trajectories. Instead, our model adds a small extra component to Eq. (2.17) for $t < t_{\text{acc}}$:

$$u_R(R, t) = -\frac{3}{\Sigma\sqrt{R}}\frac{\partial}{\partial R}(\Sigma v\sqrt{R}) - \eta_t\sqrt{\frac{GM}{R}}. \quad (2.20)$$

The functional form of the extra term derives from the CM81 solution. A constant value of 0.002 for η_t is found to reproduce very well the results of Hueso & Guillot. It also provides a good match with the disk masses from Yorke & Bodenheimer (1999), YE05 and BWH08, whose models cover a wide range of initial conditions. The problem of sub-Keplerian accretion is addressed in more detail in Chapter 4. There, we derive a more rigorous solution and show that it does not affect the gas-ice results from the current chapter in a significant way.

The disk's inner radius is determined by the evaporation of dust as it gets heated above a critical temperature by the stellar radiation (e.g., YE05):

$$R_i(t) = \sqrt{\frac{L_*}{4\pi\sigma T_{\text{evap}}^4}}, \quad (2.21)$$

where σ is the Stefan-Boltzmann constant. The dust evaporation temperature, T_{evap} , is set to 2000 K. Taking an alternative value of 1500 or even 1200 K has no effect on our results. The stellar luminosity, L_* , is discussed in Sect. 2.2.3. Inward transport of material at R_i leads to accretion from the disk onto the star:

$$\dot{M}_{\text{d}\rightarrow*} = -2\pi R_i u_R \Sigma, \quad (2.22)$$

with the radial velocity, u_R , and the surface density, Σ , taken at R_i . The disk gains mass from the envelope at a rate $\dot{M}_{\text{e}\rightarrow\text{d}}$, so the disk mass evolves as

$$M_{\text{d}}(t) = \int_0^t (\dot{M}_{\text{e}\rightarrow\text{d}} - \dot{M}_{\text{d}\rightarrow*}) dt'. \quad (2.23)$$

We adopt a Gaussian profile for the vertical structure of the disk (Shakura & Sunyaev 1973):

$$\rho(R, z, t) = \rho_c \exp\left(-\frac{z^2}{2H^2}\right), \quad (2.24)$$

with z the height above the midplane. The scale height comes from Eq. (2.15) and the midplane density is

$$\rho_c(R, t) = \frac{\Sigma}{H\sqrt{2\pi}}. \quad (2.25)$$

Along with the radial motion (Eq. (2.20), taken to be independent of z), material also moves vertically in the disk, as it must maintain the Gaussian profile at all times. To see this, consider a parcel of material that enters the disk at time t at coordinates R and z into a column with scale height H and surface density Σ . The column of material below the parcel is

$$\int_0^z \rho(R, \zeta, t) d\zeta = \frac{1}{2}\Sigma \operatorname{erf}\left(\frac{z}{H\sqrt{2}}\right), \quad (2.26)$$

where erf is the error function. At a later time t' , the entire column has moved to R' and has a scale height H' and a surface density Σ' . The same amount of material must still be below the parcel:

$$\frac{1}{2}\Sigma' \operatorname{erf}\left(\frac{z'}{H'\sqrt{2}}\right) = \frac{1}{2}\Sigma \operatorname{erf}\left(\frac{z}{H\sqrt{2}}\right). \quad (2.27)$$

Rearranging gives the new height of the parcel, z' :

$$z'(R', t') = H' \sqrt{2} \operatorname{erf}^{-1}\left[\frac{\Sigma}{\Sigma'} \operatorname{erf}\left(\frac{z}{H\sqrt{2}}\right)\right], \quad (2.28)$$

where erf^{-1} is the inverse of the error function. In the absence of vertical mixing, our description leads to purely laminar flow.

The location of the disk-envelope boundary (needed, e.g., in Eq. (2.19)) is determined in two steps. First, the surface is identified where the density due to the disk (Eq. (2.24)) equals that due to the envelope (Eqs. (2.5) and (2.12)). In order for accretion to take place at a given point P_1 on the surface, it must be intersected by an infall trajectory. Due to the geometry of the surface, such a trajectory might also intersect the disk at a larger radius P_2 (Fig. 2.1). Material flowing in along that trajectory accretes at P_2 instead of P_1 . Hence, the second step in determining the disk-envelope boundary consists of raising the surface at “obstructed points” like P_1 to an altitude where accretion can take place. The source function is then computed at that altitude. Physically, this can be understood as follows: the region directly above the obstructed points becomes less dense than what it would be in the absence of a disk, because the disk also prevents material from reaching there. The lower density above the disk reduces the downward pressure, so the disk puffs up and the disk-envelope boundary moves to a higher altitude.

The infall trajectories in the vicinity of the disk are very shallow, so the bulk of the material accretes at the outer edge. Because the disk quickly spreads beyond the centrifugal radius, much of the accretion occurs far from the star. In contrast, accretion in

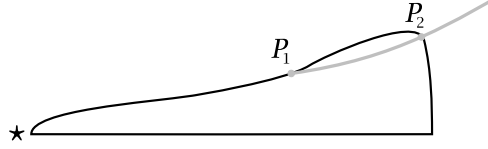


Figure 2.1 – Schematic view of the disk-envelope boundary in the upper right quadrant of the (R, z) plane. The black line indicates the surface where the density due to the disk equals that due to the envelope. The grey line is the infall trajectory that would lead to point P_1 . However, it already intersects the disk at point P_2 , so no accretion is possible at P_1 . The disk-envelope boundary is therefore raised at P_1 until it can be reached freely by an infall trajectory.

one-dimensional collapse models occurs at or inside of R_c (see also Chapter 4). Our results are consistent with the hydrodynamical work of BWH08, where most of the infalling material also hits the outer edge of a rather large disk. The large accretion radii lead to weaker accretion shocks than commonly assumed (Sect. 2.2.5).

2.2.3 Star

The star gains material from the envelope and from the disk, so its mass evolves as

$$M_*(t) = \int_0^t (\dot{M}_{e \rightarrow *} + \dot{M}_{d \rightarrow *}) dt'. \quad (2.29)$$

The protostar does not come into existence immediately at the onset of collapse; it is preceded by the first hydrostatic core (FHC; Masunaga et al. 1998, Boss & Yorke 1995). Our model follows YE05 and takes a lifetime of 2×10^4 yr and a size of 5 AU for the FHC, independent of other parameters. After this stage, a rapid transition occurs from the large FHC to a protostar of a few R_\odot :

$$R_* = (5 \text{ AU}) \left(1 - \sqrt{\frac{t - 20\,000 \text{ yr}}{100 \text{ yr}}} \right) + R_*^{\text{PS}} \quad 20\,000 < t \text{ (yr)} < 20\,100, \quad (2.30)$$

where R_*^{PS} (ranging from 2 to 5 R_\odot) is the protostellar radius from Palla & Stahler (1991). For $t > 2.01 \times 10^4$ yr, R_* equals R_*^{PS} . Our results are not sensitive to the exact values used for the size and lifetime of the FHC or the duration of the FHC-protostar transition.

The star's luminosity, L_* , consists of two terms: the accretion luminosity, $L_{*,\text{acc}}$, dominant at early times, and the luminosity due to gravitational contraction and deuterium burning, L_{phot} . The accretion luminosity comes from Adams & Shu (1986):

$$L_{*,\text{acc}}(t) = L_0 \left\{ \frac{1}{6u_*} \left[6u_* - 2 + (2 - 5u_*) \sqrt{1 - u_*} \right] + \frac{\eta_*}{2} \left[1 - (1 - \eta_d) \mathcal{M}_d \right] \left[1 - (1 - \eta_d) \sqrt{1 - u_*} \right] \right\}, \quad (2.31)$$

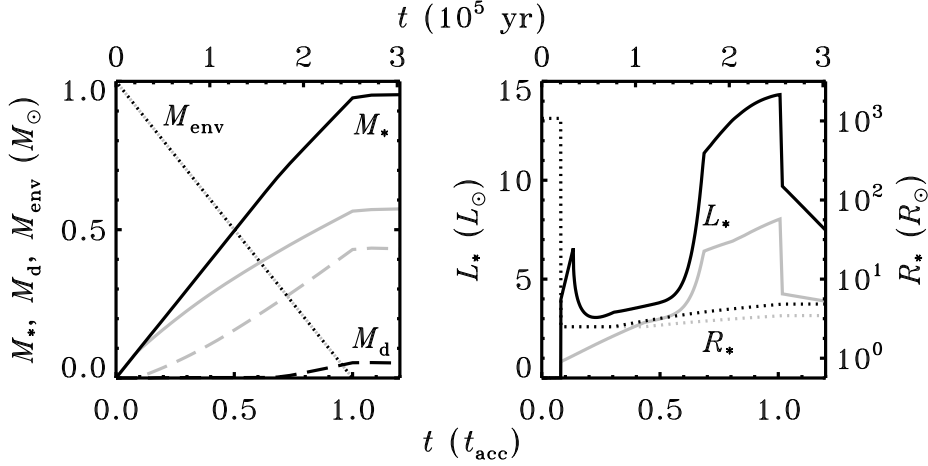


Figure 2.2 – Evolution of the mass of the envelope, star and disk (left panel) and the luminosity (solid lines) and radius (dotted lines) of the star (right panel) for our standard model (black lines) and our reference model (grey lines).

where $L_0 = GM\dot{M}/R_*$ (with $M = M_* + M_{\text{d}}$ the total accreted mass), $u_* = R_*/R_{\text{c}}$, and

$$\mathcal{M}_{\text{d}} = \frac{1}{3} u_*^{1/3} \int_{u_*}^1 \frac{\sqrt{1-u}}{u^{4/3}} du. \quad (2.32)$$

Analytical solutions exist for the asymptotic cases of $u_* \approx 0$ and $u_* \approx 1$. For intermediate values, the integral must be solved numerically. The efficiency parameters η_* and η_{d} in Eq. (2.31) have values of 0.5 and 0.75 for a $1 M_\odot$ envelope (YE05). The photospheric luminosity is adopted from D’Antona & Mazzitelli (1994), using YE05’s method of fitting and interpolating, including a time difference of $0.38 t_{\text{acc}}$ (equal to the free-fall time) between the onset of $L_{*,\text{acc}}$ and $L_{*,\text{phot}}$ (Myers et al. 1998). The sum of these two terms, $L_*(t) = L_{*,\text{acc}} + L_{*,\text{phot}}$, gives the total stellar luminosity.

Figure 2.2 shows the evolution of the stellar mass, luminosity and radius for our standard case of $M_0 = 1.0 M_\odot$, $c_{\text{s}} = 0.26 \text{ km s}^{-1}$ and $\Omega_0 = 10^{-14} \text{ s}^{-1}$, and our reference case of $M_0 = 1.0 M_\odot$, $c_{\text{s}} = 0.26 \text{ km s}^{-1}$ and $\Omega_0 = 10^{-13} \text{ s}^{-1}$ (Sect. 2.2.6). The transition from the FHC to the protostar at $t = 2 \times 10^4 \text{ yr}$ is clearly visible in the R_* and L_* profiles. At $t = t_{\text{acc}}$, there is no more accretion from the envelope onto the star, so the luminosity decreases sharply.

The masses of the disk and the envelope are also shown in Fig. 2.2. Our disk mass of $0.43 M_\odot$ at $t = t_{\text{acc}}$ in the reference case is in excellent agreement with the value of $0.4 M_\odot$ found by BWH08 for the same parameters.

2.2.4 Temperature

The envelope starts out as an isothermal sphere at 10 K and it is heated up from the inside after the onset of collapse. Using the star as the only photon source, we compute the dust temperature in the disk and envelope with the axisymmetric three-dimensional radiative transfer code RADMC (Dullemond & Dominik 2004a). Because of the high densities throughout most of the system, the gas and dust are expected to be well coupled, and the gas temperature is set equal to the dust temperature. Cosmic-ray heating of the gas is included implicitly by setting a lower limit of 8 K in the dust radiative transfer results. As mentioned in Sect. 2.2.1, the presence of the outflow cones has some effect on the temperature profiles (Whitney et al. 2003). This is discussed further in Sect. 2.3.2.

2.2.5 Accretion shock

The infall of high-velocity envelope material into the low-velocity disk causes a J-type shock. The temperature right behind the shock front can be much higher than what it would be due to the stellar photons. Neufeld & Hollenbach (1994) calculated in detail the relationship between the pre-shock velocities and densities (u_s and n_s) and the maximum grain temperature reached after the shock ($T_{d,s}$). A simple formula, valid for $u_s < 70 \text{ km s}^{-1}$, can be extracted from their Fig. 13:

$$T_{d,s} \approx (104 \text{ K}) \left(\frac{n_s}{10^6 \text{ cm}^{-3}} \right)^{0.21} \left(\frac{u_s}{30 \text{ km s}^{-1}} \right)^p \left(\frac{a_{gr}}{0.1 \mu\text{m}} \right)^{-0.20}, \quad (2.33)$$

with a_{gr} the grain radius. The exponent p is 0.62 for $u_s < 30 \text{ km s}^{-1}$ and 1.0 otherwise.

The pre-shock velocities and densities are highest at early times, when accretion occurs close to the star and all ices would evaporate anyway. Important for our purposes is the question whether the dust temperature due to the shock exceeds that due to stellar heating. If all grains have a radius of $0.1 \mu\text{m}$, as assumed in our model, this is not the case for any of the material in the disk at t_{acc} for either our standard or our reference model (Fig. 2.3, cf. Simonelli et al. 1997).

In reality, the dust spans a range of sizes, extending down to a radius of about $0.005 \mu\text{m}$. Small grains are heated more easily; $0.005\text{-}\mu\text{m}$ dust reaches a shock temperature almost twice as high as does $0.1\text{-}\mu\text{m}$ dust (Eq. (2.33)). This is enough for the shock temperature to exceed the radiative heating temperature in part of the sample in Fig. 2.3. However, this has no effect on the CO and H₂O gas-ice ratios. In those parcels where shock heating becomes important for small grains, the temperature from radiative heating lies already above the CO evaporation temperature of about 18 K and the shock temperature remains below 60 K, which is not enough for H₂O to evaporate. Hence, shock heating is not included in our model.

H₂O may also be removed from the grain surfaces in the accretion shock through sputtering (Tielens et al. 1994, Jones et al. 1994). The material that makes up the disk at the end of the collapse in our standard model experiences a shock of at most 8 km s^{-1} . At that velocity, He⁺, the most important ion for sputtering, carries an energy of 1.3 eV.

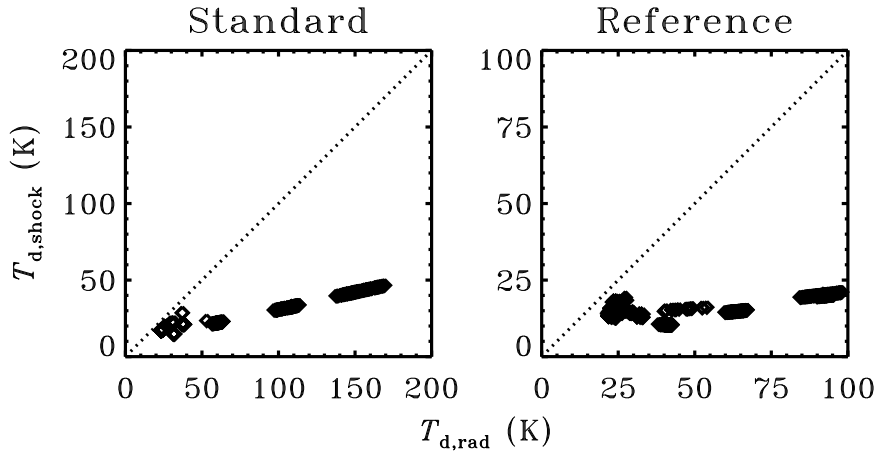


Figure 2.3 – Dust temperature due to the accretion shock (vertical axis) and stellar radiation (horizontal axis) at the point of entry into the disk for $0.1\text{-}\mu\text{m}$ grains in a sample of several hundred parcels in our standard (left) and reference (right) models. These parcels occupy positions from $R = 1$ to 300 AU in the disk at t_{acc} . Note the different scales between the two panels.

However, a minimum of 2.2 eV is required to remove H_2O (Bohdansky et al. 1980), so sputtering is unimportant for our purposes.

Some of the material in our model is heated to more than 100 K during the collapse (Fig. 2.12) or experiences a shock strong enough to induce sputtering. This material normally ends up in the star before the end of the collapse, but mixing may keep some of it in the disk. The possible consequences are discussed briefly in Sect. 2.4.4.

2.2.6 Model parameters

The standard set of parameters for our model corresponds to Case J from Yorke & Bodenheimer (1999), except that the solid-body rotation rate is reduced from 10^{-13} to 10^{-14} s^{-1} to produce a more realistic disk mass of $0.05 M_{\odot}$, consistent with observations (e.g., Andrews & Williams 2007a,b). The envelope has an initial mass of $1.0 M_{\odot}$ and a radius of 6700 AU, and the effective sound speed is 0.26 km s^{-1} .

The original Case J (with $\Omega_0 = 10^{-13}$ s^{-1}), which was also used in BWH08, is used here as a reference model to enable a direct quantitative comparison of the results with an independent method. This case results in a much higher disk mass of $0.43 M_{\odot}$. Although such high disk masses are not excluded by observations and theoretical arguments (Hartmann et al. 2006), they are considered less representative of typical young stellar objects than the disks of lower mass.

The parameters M_0 , c_s and Ω_0 are changed in one direction each to create a 2^3 parameter grid. The two values for Ω_0 , 10^{-14} and 10^{-13} s^{-1} , cover the range of rotation rates

Table 2.1 – Summary of the parameter grid used in our model.^a

Case ^b	Ω_0 (s^{-1})	c_s (km s^{-1})	M_0 (M_\odot)	t_{acc} (10^5 yr)	τ_{ads} (10^5 yr)	M_{d} (M_\odot)
1	10^{-14}	0.19	1.0	6.3	14.4	0.22
2	10^{-14}	0.19	0.5	3.2	3.6	0.08
3 (std)	10^{-14}	0.26	1.0	2.5	2.3	0.05
4	10^{-14}	0.26	0.5	1.3	0.6	0.001
5	10^{-13}	0.19	1.0	6.3	14.4	0.59
6	10^{-13}	0.19	0.5	3.2	3.6	0.25
7 (ref)	10^{-13}	0.26	1.0	2.5	2.3	0.43
8	10^{-13}	0.26	0.5	1.3	0.6	0.16

^a Ω_0 : solid-body rotation rate; c_s : effective sound speed; M_0 : initial core mass; t_{acc} : accretion time; τ_{ads} : adsorption timescale for H_2O at the edge of the initial core; M_{d} : disk mass at t_{acc} .

^b Case 3 is our standard parameter set and Case 7 is our reference set.

observed by Goodman et al. (1993). The other variations are chosen for their opposite effect: a lower sound speed gives a more massive disk, and a lower initial core mass gives a less massive disk. The full model is run for each set of parameters to analyse how the chemistry can vary between different objects. The parameter grid is summarised in Table 2.1. Our standard set is Case 3 and our reference set is Case 7.

Table 2.1 also lists the accretion time and the adsorption timescale for H_2O at the edge of the initial core. For comparison, Evans et al. (2009) found a median timescale for the embedded phase (Class 0 and I) of $5.4 \times 10^5 \text{ yr}$ from observations. It should be noted that the end point of our model (t_{acc}) is not yet representative of a typical T Tauri disk (see Sect. 2.3.2). Nevertheless, it allows an exploration of how the chemistry responds to plausible changes in the environment.

2.2.7 Adsorption and desorption

The adsorption and desorption of CO and H_2O are solved in a Lagrangian frame. When the time-dependent density, velocity and temperature profiles have been calculated, the envelope is populated by a number of parcels of material (typically 12 000) at $t = 0$. They fall in towards the star or disk according to the velocity profiles. The density and temperature along each parcel’s infall trajectory are used as input to solve the adsorption-desorption balance. Both species start fully in the gas phase. The envelope is kept static for $3 \times 10^5 \text{ yr}$ before the onset of collapse to simulate the pre-stellar core phase. This is the same value as used by Rodgers & Charnley (2003) and BWH08, and it is consistent with recent observations by Enoch et al. (2008). The amount of gaseous material left over near the end of the pre-collapse phase is also consistent with observations, which show that the onset of H_2O ice formation is around an A_V of 3 mag (Whittet et al. 2001). In six of our eight parameter sets, the adsorption timescales of H_2O at the edge of the cloud core are shorter than the combined collapse and pre-collapse time (Table 2.1), so all H_2O

is expected to freeze out before entering the disk. Because of the larger core size, the adsorption timescales are much longer in Cases 1 and 5, and some H₂O may still be in the gas phase when it reaches the disk.

No chemical reactions are included other than adsorption and thermal desorption, so the total abundance of CO and H₂O in each parcel remains constant. The adsorption rate in cm⁻³ s⁻¹ is taken from Charnley et al. (2001):

$$R_{\text{ads}}(X) = (4.55 \times 10^{-18} \text{ cm}^3 \text{ K}^{-1/2} \text{ s}^{-1}) n_{\text{H}} n_{\text{g}}(X) \sqrt{\frac{T_{\text{g}}}{M(X)}}, \quad (2.34)$$

where n_{H} is the total hydrogen density, T_{g} the gas temperature, $n_{\text{g}}(X)$ the gas-phase abundance of species X and $M(X)$ its molecular weight. The numerical factor assumes unit sticking efficiency, a grain radius of 0.1 μm and a grain abundance x_{gr} of 10^{-12} with respect to H₂.

The thermal desorption of CO and H₂O is a zeroth-order process:

$$R_{\text{des}}(X) = (1.26 \times 10^{-21} \text{ cm}^2) n_{\text{H}} f(X) \nu(X) \exp\left[-\frac{E_{\text{b}}(X)}{kT_{\text{d}}}\right], \quad (2.35)$$

where T_{d} is the dust temperature and

$$f(X) = \min\left[1, \frac{n_{\text{s}}(X)}{N_{\text{b}} n_{\text{gr}}}\right], \quad (2.36)$$

with $n_{\text{s}}(X)$ the solid abundance of species X and $N_{\text{b}} = 10^6$ the typical number of binding sites per grain. The numerical factor in Eq. (2.35) assumes the same grain properties as in Eq. (2.34). The pre-exponential factor, $\nu(X)$, and the binding energy, $E_{\text{b}}(X)/k$, are set to $7 \times 10^{26} \text{ cm}^{-2} \text{ s}^{-1}$ and 855 K for CO and to $1 \times 10^{30} \text{ cm}^{-2} \text{ s}^{-1}$ and 5773 K for H₂O (Fraser et al. 2001, Bisschop et al. 2006).

Using a single $E_{\text{b}}(\text{CO})$ value means that all CO evaporates at the same temperature. This would be appropriate for a pure CO ice, but not for a mixed CO-H₂O ice as is likely to form in reality. During the warm-up phase, part of the CO is trapped inside the H₂O ice until the temperature becomes high enough for the H₂O to evaporate. Recent laboratory experiments suggest that CO desorbs from a CO-H₂O ice in several discrete steps (Collings et al. 2004; Fayolle et al. in prep.). We simulate this in some model runs with four ‘‘flavours’’ of CO ice, each with a different $E_{\text{b}}(\text{CO})$ value (Viti et al. 2004). For each flavour, the desorption is assumed to be zeroth order. The four-flavour model is summarised in Table 2.2.

2.3 Results

Results are presented in this section for our standard and reference models (Cases 3 and 7) as described in Sect. 2.2.6. These cases are compared to the other parameter sets in Sect. 2.4.1. The appendix at the end of this chapter describes a formula to estimate the

Table 2.2 – Binding energies and desorbing fractions for the four-flavour CO evaporation model.^a

Flavour	$E_b(\text{CO})/k$ (K) ^b	Fraction ^c
1	855	0.350
2	960	0.455
3	3260	0.130
4	5773	0.065

^a Based on Viti et al. (2004).

^b The rates for Flavours 1–3 are computed from Eq. (2.35) with $X = \text{CO}$. The rate for Flavour 4 is equal to the H_2O desorption rate.

^c Fractions of adsorbing CO: 35% of all adsorbing CO becomes Flavour 1, and so on.

disk formation efficiency, defined as M_d/M_0 at the end of the collapse phase, based on a fit to our model results. The results from this section are partially revisited in Chapters 3 and 4, where we use a different solution to the problem of sub-Keplerian accretion.

2.3.1 Density profiles and infall trajectories

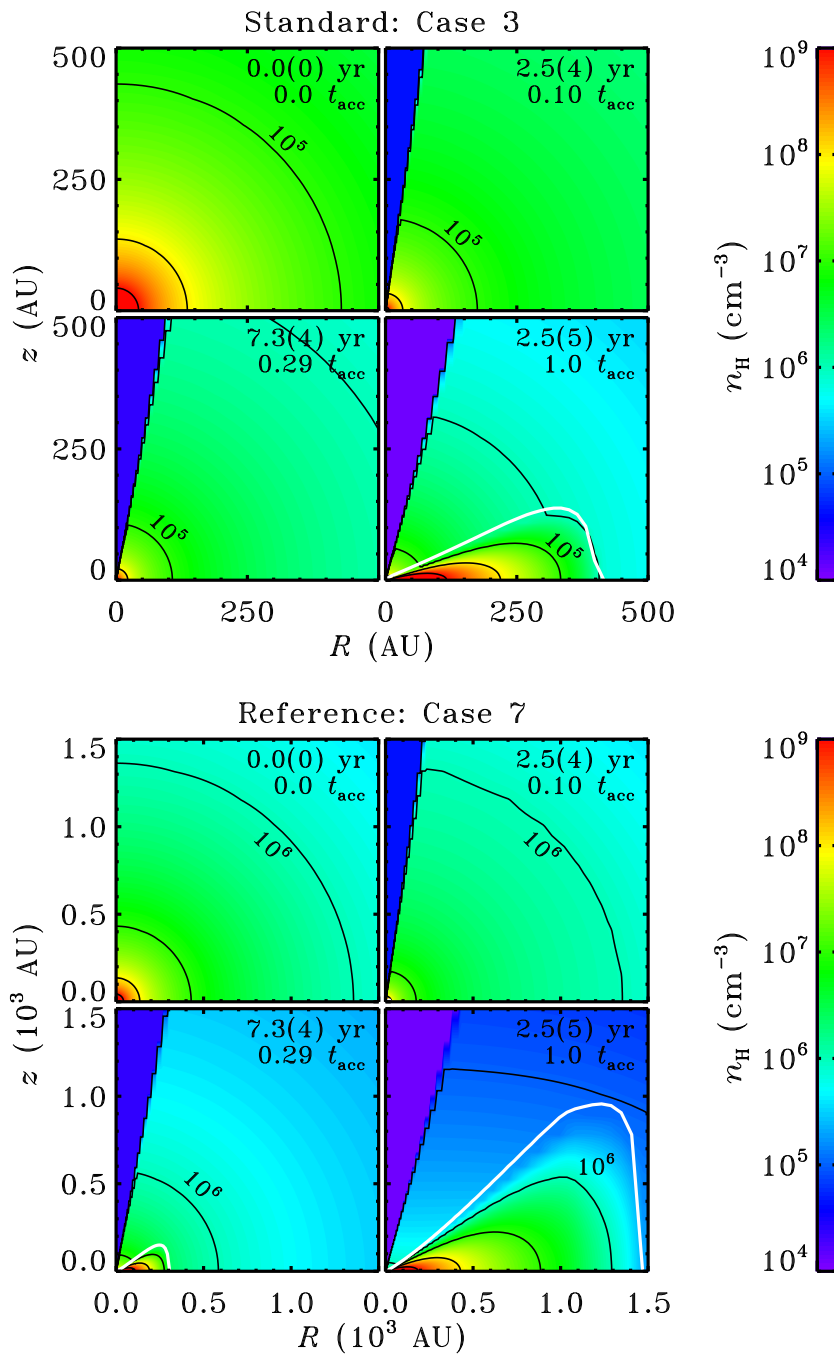
In our standard model (Case 3), the envelope collapses in 2.5×10^5 yr to give a star of $0.94 M_\odot$ and a disk of $0.05 M_\odot$. The remaining $0.01 M_\odot$ has disappeared through the bipolar outflow. The centrifugal radius in our standard model at t_{acc} is 4.9 AU, but the disk has spread to 400 AU at that time due to angular momentum redistribution. The densities in the disk are high: more than 10^9 cm^{-3} at the midplane inside of 120 AU (Fig. 2.4, top) and more than 10^{14} cm^{-3} near 0.3 AU. The corresponding surface densities of the disk are 2.0 g cm^{-2} at 120 AU and 660 g cm^{-2} at 0.3 AU.

Due to the higher rotation rate, our reference model (Case 7) gets a much higher disk mass: $0.43 M_\odot$. This value is consistent with the mass of $0.4 M_\odot$ reported by BWH08. Overall, the reference densities from our semi-analytical model (Fig. 2.4, bottom) compare well with those from their more realistic hydrodynamical simulations; the differences are generally less than a factor of two.

In both cases, the disk first emerges at 2×10^4 yr, when the FHC contracts to become the protostar, but it is not until a few 10^4 yr later that the disk becomes visible on the scale of Fig. 2.4. The regions of high density ($n_{\text{H}} > 10^5\text{--}10^6 \text{ cm}^{-3}$) are still contracting at that time, but the growing disks eventually cause them to expand again.

Material falls in along nearly radial streamlines far out in the envelope and deflects towards the midplane closer in. When a parcel enters the disk, it follows the radial motion

Figure 2.4 – Total density at four time steps for our standard model (Case 3; top) and our reference model (Case 7; bottom). The notation $a(b)$ denotes $a \times 10^b$. The density contours increase by factors of ten going inwards; the 10^5-cm^{-3} contours are labelled in the standard panels and the 10^6-cm^{-3} contours in the reference panels. The white curves indicate the surface of the disk as defined in Sect. 2.2.2 (only visible in three panels). Note the different scale between the two sets of panels.



caused by the viscous evolution and accretion of more material from the envelope. At any time, conservation of angular momentum causes part of the disk to move inwards and part of it to move outwards. An individual parcel entering the disk may move out for some time before going farther in. This takes the parcel through several density and temperature regimes, which may affect the gas-ice ratios or the chemistry in general. The back-and-forth motion occurs especially at early times, when the entire system changes more rapidly than at later times. The parcel motions are visualised in Figs. 2.5 and 2.6, where infall trajectories are drawn for 24 parcels ending up at one of eight positions at t_{acc} : at the midplane or near the surface at radial distances of 10, 30, 100 and 300 AU. Only parcels entering the disk before $t \approx 2 \times 10^5$ yr in our standard model or $t \approx 1 \times 10^5$ yr in our reference model undergo the back-and-forth motion. The parcels ending up near the midplane all enter the disk earlier than the ones ending up at the surface.

Accretion from the envelope onto the disk occurs in an inside-out fashion. Because of the geometry of the disk (Fig. 2.1), a lot of the material enters near the outer edge and prevents the older material from moving farther out. Our flow inside the disk is purely laminar, so some material near the midplane does move outwards underneath the newer material at higher altitudes.

Because of the low rotation rate in our standard model, the disk does not really begin to build up until 1.5×10^5 yr ($0.6 t_{\text{acc}}$) after the onset of collapse. In addition, most of the early material to reach the disk makes it to the star before the end of the accretion phase, so the disk at t_{acc} consists only of material from the edge of the original cloud core (Fig. 2.7, top).

The disk in our reference model, however, begins to form right after the FHC-protostar transition at 2×10^4 yr. As in the standard model, a layered structure is visible in the disk, but it is more pronounced here. At the end of the collapse, the midplane consists mostly of material that was originally close to the centre of the envelope (Fig. 2.7, bottom). The surface and outer parts of the disk are made up primarily of material from the outer parts of the envelope. This was also reported by BWH08.

2.3.2 Temperature profiles

When the star turns on at 2×10^4 yr, the envelope quickly heats up and reaches more than 100 K inside of 10 AU. As the disk grows, its interior is shielded from direct irradiation and the midplane cools down again. At the same time, the remnant envelope material above the disk becomes less dense and warmer. As in Whitney et al. (2003), the outflow has some effect on the temperature profile. Photons emitted into the outflow can scatter and illuminate the disk from the top, causing a higher disk temperature beyond $R \approx 200$ AU than if there were no outflow cone. At smaller radii, the disk temperature is lower than in a no-outflow model. Without the outflow, the radiation would be trapped in the inner envelope and inner disk, increasing the temperature at small radii.

At $t = t_{\text{acc}}$ in our standard model, the 100- and 18-K isotherms (where H_2O and pure CO evaporate) intersect the midplane at 20 and 2000 AU (Fig. 2.8, top). The disk in our reference model is denser and therefore colder: it reaches 100 and 18 K at 5 and 580 AU on the midplane (Fig. 2.8, bottom). Our radiative transfer method is a more rigorous way

to obtain the dust temperature than the diffusion approximation used by BWH08, so our temperature profiles are more realistic than theirs.

Compared to typical T Tauri disk models (e.g., D’Alessio et al. 1998, 1999, 2001), our standard disk at t_{acc} is warmer. It is 81 K at 30 AU on the midplane, while the closest model from the D’Alessio catalogue is 28 K at that point. If our model is allowed to run beyond t_{acc} , part of the disk accretes further onto the star. At $t = 4 t_{\text{acc}}$ (1 Myr), the disk mass goes down to $0.03 M_{\odot}$. The luminosity of the star decreases during this period (D’Antona & Mazzitelli 1994), so the disk cools down: the midplane temperature at 30 AU is now 42 K. Meanwhile, the dust is likely to grow to larger sizes, which would further decrease the temperatures (D’Alessio et al. 2001). Hence, it is important to realise that the normal end point of our models does not represent a “mature” T Tauri star and disk as typically discussed in the literature.

2.3.3 Gas and ice abundances

Our two species, CO and H₂O, begin entirely in the gas phase. They freeze out during the static pre-stellar core phase from the centre outwards due to the density dependence of Eq. (2.34). After the pre-collapse phase of 3×10^5 yr, only a few tenths of per cent of each species is still in the gas phase at 3000 AU. About 30% remains in the gas phase at the edge of the envelope.

Up to the point where the disk becomes important and the system loses its spherical symmetry, our model gives the same results as the one-dimensional collapse models: the temperature quickly rises to a few tens of K in the collapsing region, driving most of the CO into the gas phase, but keeping H₂O on the grains.

As the disk grows in mass, it provides an increasingly large body of material that is shielded from the star’s radiation, and that is thus much colder than the surrounding envelope. However, the disk in our standard model never gets below 18 K before the end of the collapse (Sect. 2.3.2), so CO remains in the gas phase (Fig. 2.9, top). Note that trapping of CO in the H₂O ice is not taken into account here; this possibility is discussed in Sect. 2.4.3.

The disk in our reference model is more massive and therefore colder. After about 5×10^4 yr, the outer part drops below 18 K. CO arriving in this region readsorbs onto the grains (Fig. 2.10, top). Another 2×10^5 yr later, at $t = t_{\text{acc}}$, 19% of all CO in the disk is in solid form. Moving out from the star, the first CO ice is found at the midplane at 400 AU. The solid fraction gradually increases to unity at 600 AU. At $R = 1000$ AU, nearly all CO is solid up to an altitude of 170 AU. The solid and gaseous CO regions meet close to the 18-K surface. The densities throughout most of the disk are high enough that once a parcel of material goes below the CO desorption temperature, all CO rapidly disappears from the gas. The exception to this rule occurs at the outer edge, near 1500 AU, where the adsorption and desorption timescales are longer than the dynamical timescales of the infalling material. Small differences between the trajectories of individual parcels then cause some irregularities in the gas-ice profile.

The region containing gaseous H₂O is small at all times during the collapse. At $t = t_{\text{acc}}$, the snow line (the transition of H₂O from gas to ice) lies at 15 AU at the midplane

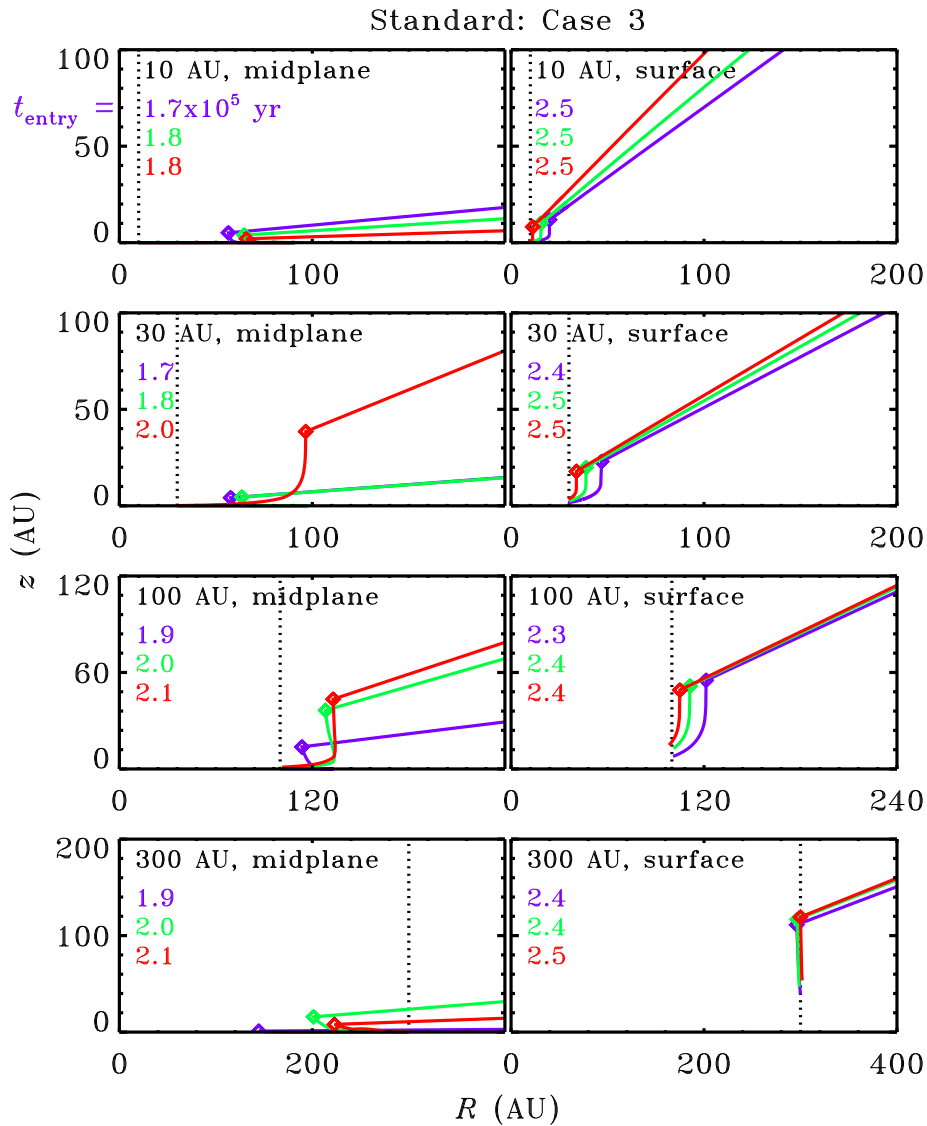


Figure 2.5 – Infall trajectories for parcels in our standard model (Case 3) ending up at the midplane (left) or near the surface (right) at radial positions of 10, 30, 100 and 300 AU (dotted lines) at $t = t_{\text{acc}}$. Each panel contains trajectories for three parcels, which are illustrative for material ending up at the given location. Trajectories are only drawn up to $t = t_{\text{acc}}$. Diamonds indicate where each parcel enters the disk; the time of entry is given in units of 10^5 yr. Note the different scales between some panels.

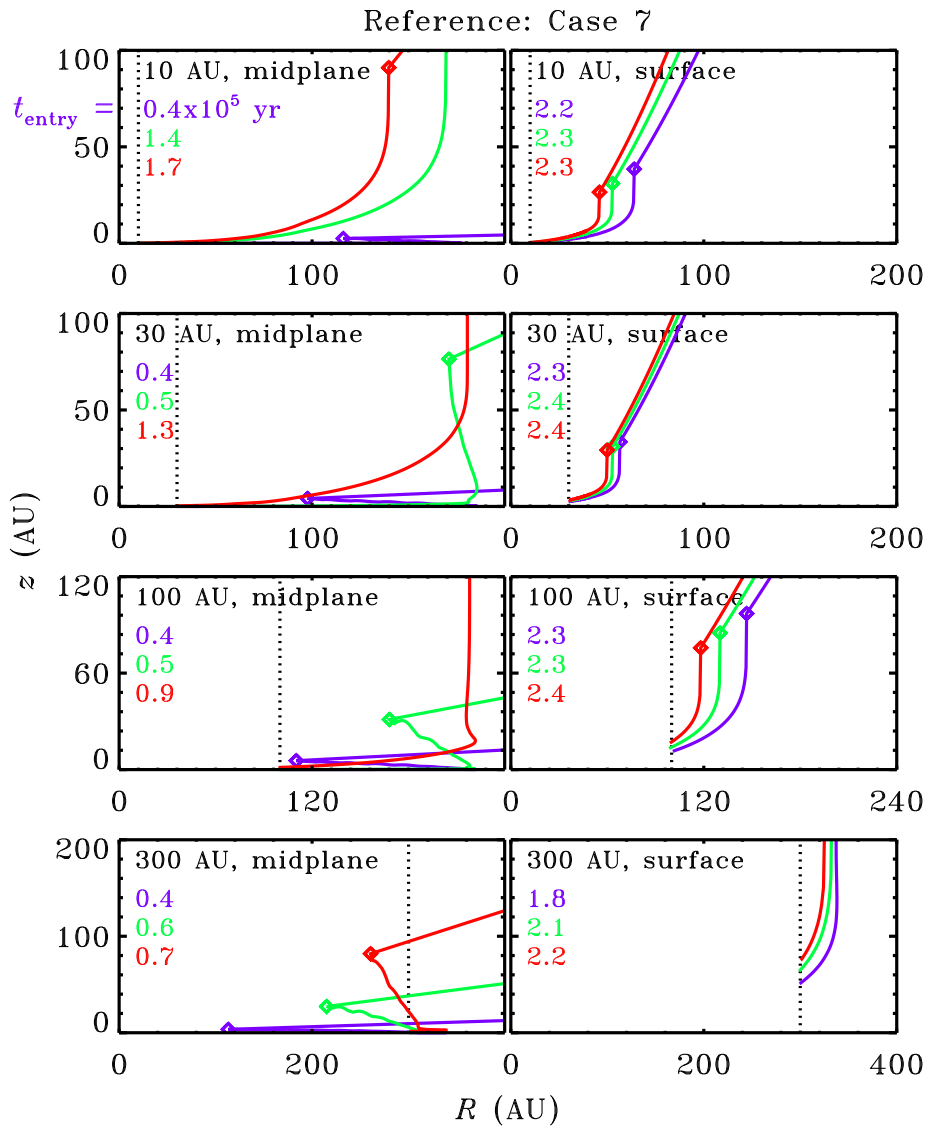


Figure 2.6 – Same as Fig. 2.5, but for our reference model (Case 7).

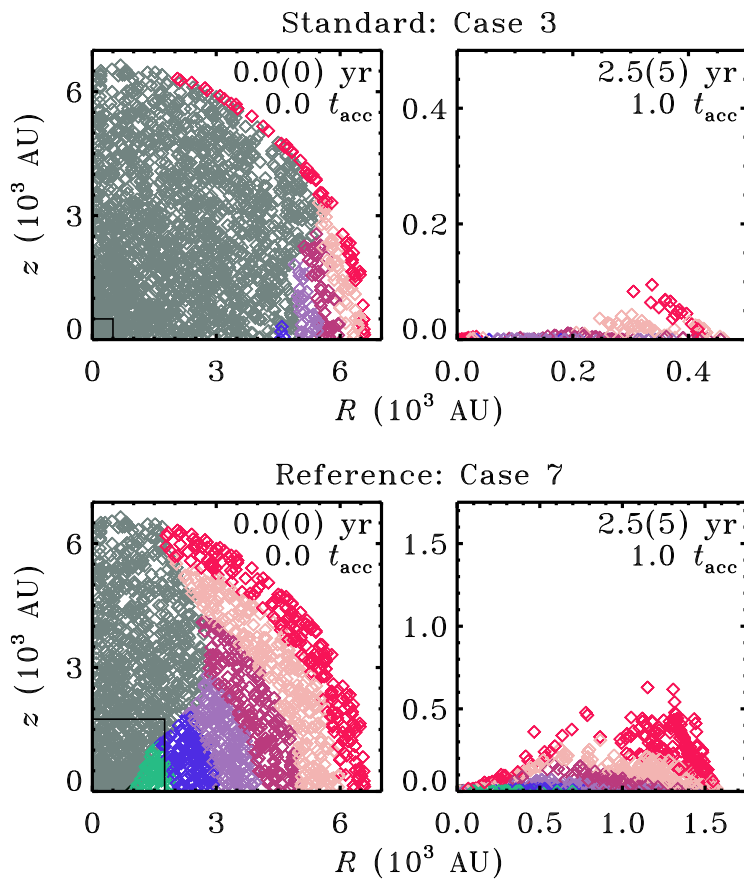
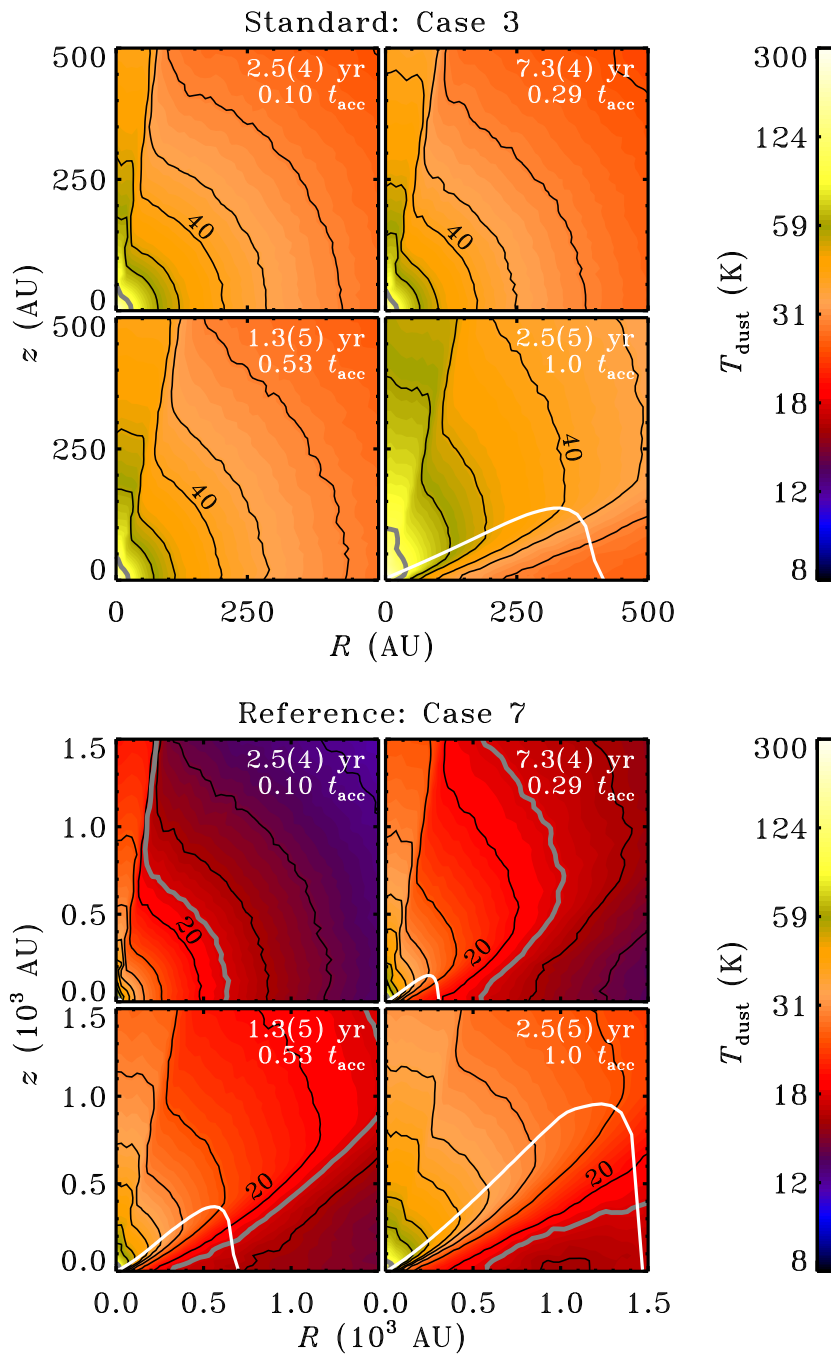


Figure 2.7 – Position of parcels of material in our standard model (Case 3; top) and our reference model (Case 7; bottom) at the onset of collapse ($t = 0$) and at the end of the collapse phase ($t = t_{\text{acc}}$). The parcels are coloured according to their initial position. The layered accretion is most pronounced in our reference model. The grey parcels from $t = 0$ end up in the star or disappear in the outflow. Note the different spatial scale between the two panels of each set; the small boxes in the left panels indicate the scales of the right panels.

Figure 2.8 – Dust temperature, as in Fig. 2.4. Contours are drawn at 100, 60, 50, 40, 35, 30, 25, 20, 18, 16, 14 and 12 K. The 40- and 20-K contours are labelled in the standard and reference panels, respectively. The 18- and 100-K contours are drawn in grey. The white curves indicate the surface of the disk as defined in Sect. 2.2.2 (only visible in four panels).



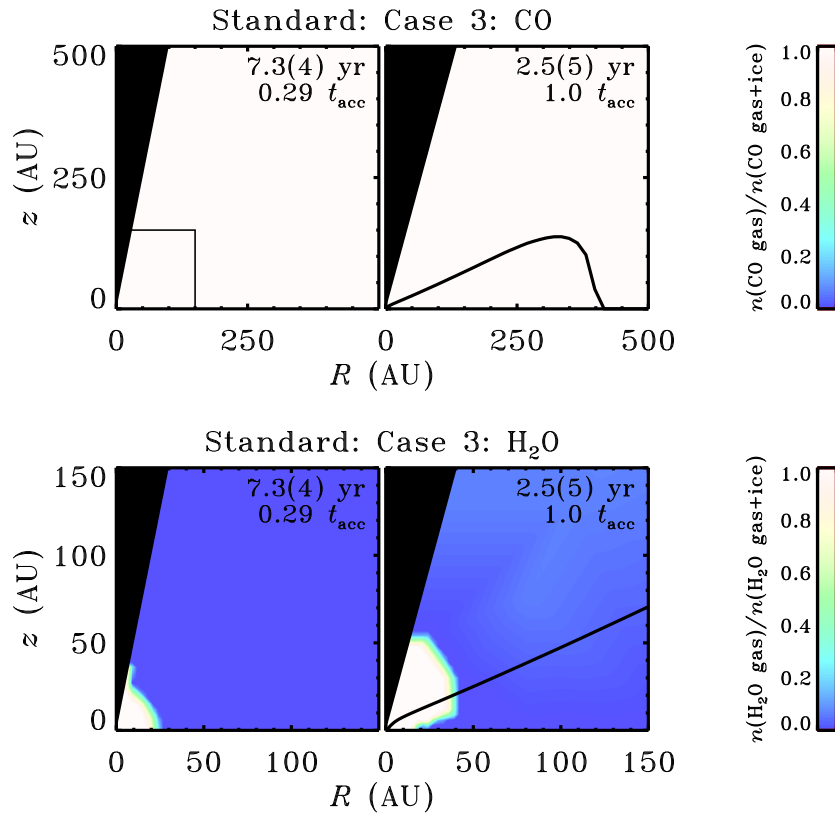


Figure 2.9 – Gaseous CO as a fraction of the total CO abundance (top) and idem for H₂O (bottom) at two time steps for our standard model (Case 3). The black curves indicate the surface of the disk (only visible in two panels). The black area near the pole is the outflow, where no abundances are computed. Note the different spatial scale between the two panels of each set; the small box in the left CO panel indicates the scale of the H₂O panels.

in our standard model (Fig. 2.9, bottom). The surface of the disk holds gaseous H₂O out to $R = 41$ AU, and overall 13% of all H₂O in the disk is in the gas phase. This number is much lower in the colder disk of our reference model: only 0.4%. The snow line now lies at 7 AU and gaseous H₂O can be found out to 17 AU in the disk’s surface layers (Fig. 2.10, bottom).

Using the adsorption-desorption history of all the individual infalling parcels, the original envelope can be divided into several chemical zones. This is trivial for our standard model. All CO in the disk is in the gas phase and it has the same qualitative history: it freezes out before the onset of collapse and quickly evaporates as it falls in. H₂O also freezes out initially and only returns to the gas phase if it reaches the inner disk.

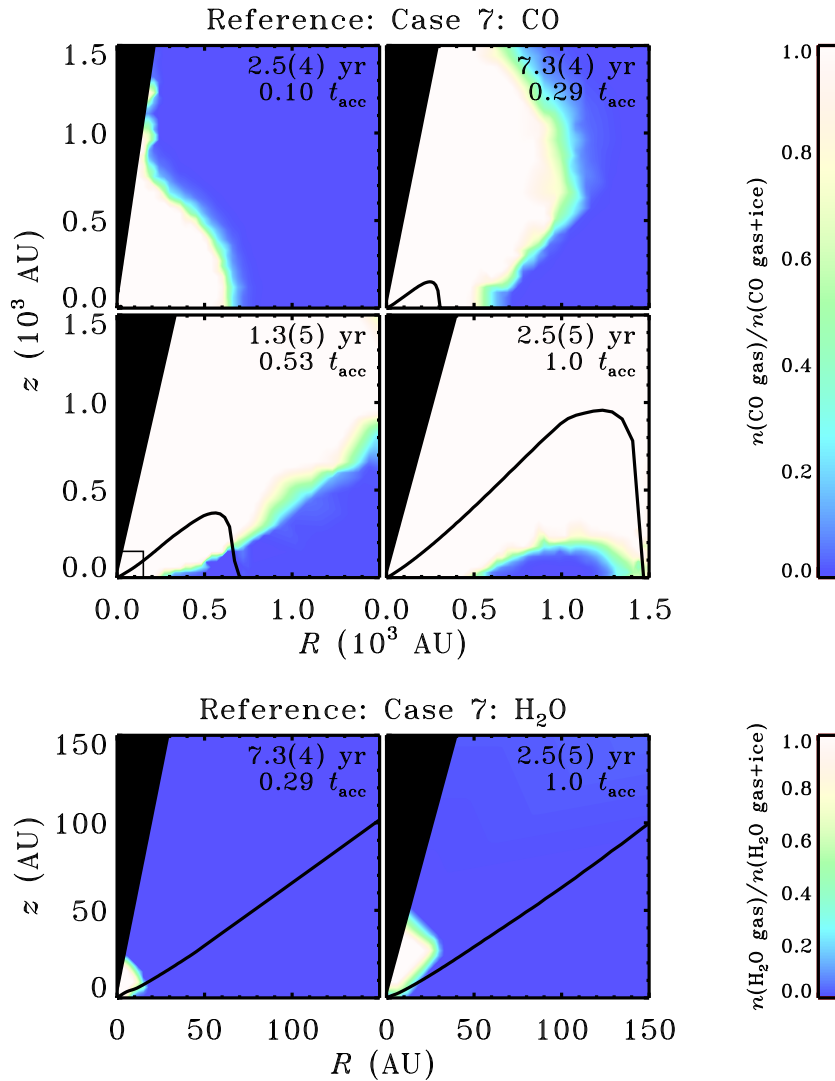


Figure 2.10 – Same as Fig. 2.9, but for our reference model (Case 7). The CO gas fraction is plotted on a larger scale and at two additional time steps.

Our reference model has the same general H₂O adsorption-desorption history, but it shows more variation for CO, as illustrated in Fig. 2.11. For the red parcels in that figure, more than half of the CO always remains on the grains after the initial freeze-out phase. On the other hand, more than half of the CO comes off the grains during the collapse for

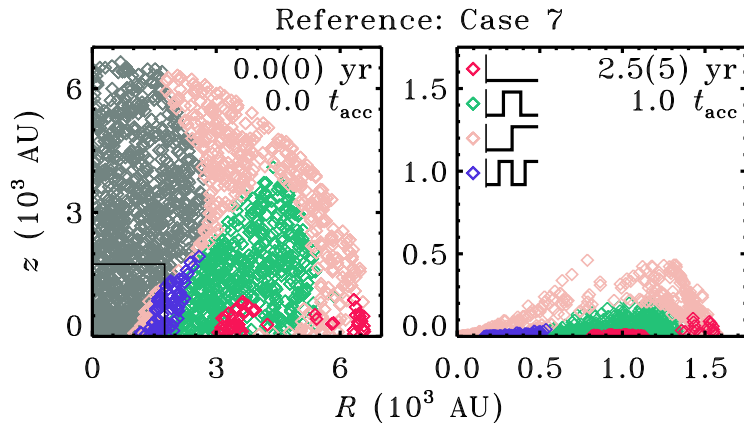


Figure 2.11 – Same as Fig. 2.7, but only for our reference model (Case 7) and with a different colour scheme to denote the CO adsorption-desorption behaviour. In all parcels, CO adsorbs during the pre-collapse phase. Red parcels: CO remains adsorbed; green parcels: CO desorbs and readsorbs; pink parcels: CO desorbs and remains desorbed; blue parcels: CO desorbs, readsorbs and desorbs once more. The fraction of gaseous CO in each type of parcel as a function of time is indicated schematically in the inset in the right panel. The grey parcels from $t = 0$ end up in the star or disappear in the outflow. In our standard model (Case 3), all CO in the disk at the end of the collapse phase is in the gas phase and it all has the same qualitative adsorption-desorption history, equivalent to the pink parcels.

the green parcels, but it freezes out again inside the disk. The pink parcels, ending up in the inner disk or in the upper layers, remain warm enough to keep CO off the grains once it first evaporates. The blue parcels follow a more erratic temperature profile, with CO evaporating, readsorbing and evaporating a second time. This is related to the back-and-forth motion of some material in the disk (Fig. 2.6).

2.3.4 Temperature histories

The proximity of the CO and H₂O gas-ice boundaries to the 18- and 100-K surfaces indicates that the temperature is primarily responsible for the adsorption and desorption. At $n_{\text{H}} = 10^6 \text{ cm}^{-3}$, adsorption and desorption of CO are equally fast at $T_{\text{d}} = 18 \text{ K}$ (a timescale of $9 \times 10^3 \text{ yr}$). For a density a thousand times higher or lower, the dust temperature only has to increase or decrease by 2–3 K to maintain $k_{\text{ads}} = k_{\text{des}}$.

The exponential temperature dependence in the desorption rate (Eq. (2.35)) also holds for other species than CO and H₂O, as well as for the rates of some chemical reactions. Hence, it is useful to compute the temperature history for infalling parcels that occupy a certain position at t_{acc} . Figures 2.12 and 2.13 show these histories for the parcels from Figs. 2.5 and 2.6. These parcels end up at the midplane or near the surface of the disk at radial distances of 10, 30, 100 and 300 AU. Parcels ending up inside of 10 AU have

a temperature history very similar to those ending up at 10 AU, except that the final temperature of the former is higher.

Each panel in Figs. 2.12 and 2.13 contains the history of three parcels ending up close to the desired position. The qualitative features are the same for all parcels. The temperature is low while a parcel remains far out in the envelope. As it falls in with an ever higher velocity, there is a temperature spike as it traverses the inner envelope, followed by a quick drop once it enters the disk. Inward radial motion then leads to a second temperature rise; because of the proximity to the star, this one is higher than the first. For most parcels in Figs. 2.12 and 2.13, the second peak does not occur until long after t_{acc} . In all cases, the shock encountered upon entering the disk is weak enough that it does not heat the dust to above the temperature caused by the stellar photons (Fig. 2.3).

Based on the temperature histories, the gas-ice transition at the midplane would lie inside of 10 AU for H₂O and beyond 300 AU for CO in both our models. This is indeed where they were found to be in Sect. 2.3.3. The transition for a species with an intermediate binding energy, such as H₂CO, is then expected to be between 10 and 100 AU, if its abundance can be assumed constant throughout the collapse.

The dynamical timescales of the infalling material before it enters the disk are between 10^4 and 10^5 yr. The timescales decrease as it approaches the disk, due to the rapidly increasing velocities. Once inside the disk, the material slows down again and the dynamical timescales return to 10^4 – 10^5 yr. The adsorption timescales for CO and H₂O are initially a few 10^5 yr, so they exceed the dynamical timescale before entering the disk. Depletion occurs nonetheless because of the pre-collapse phase of 3×10^5 yr. The higher densities in the disk cause the adsorption timescales to drop to 100 yr or less. If the temperature approaches (or crosses) the desorption temperature for CO or H₂O, the corresponding desorption timescale becomes even shorter than the adsorption timescale. Overall, the timescales for these specific chemical processes (adsorption and desorption) in the disk are shorter by a factor of 1000 or more than the dynamical timescales.

At some final positions, there is a wide spread in the time that the parcels spend at a given temperature. This is especially true for parcels ending up near the midplane inside of 100 AU in our reference model. All of the midplane parcels ending up near 10 AU exceed 18 K during the collapse; the first one does so at 3.5×10^4 yr after the onset of collapse, the last one at 1.6×10^5 yr. Hence, some parcels at this final position spend more than twice as long above 18 K than others. This does not appear to be relevant for the gas-ice ratio, but it is important for the formation of more complex species (Garrod & Herbst 2006, Garrod et al. 2008). This is discussed in more detail in Sect. 2.4.2.

2.4 Discussion

2.4.1 Model parameters

When the initial conditions of our model are modified (Sect. 2.2.6), the qualitative chemistry results do not change. In Cases 3, 4 and 8, the entire disk at t_{acc} is warmer than 18 K, and it contains no solid CO. In the other cases, the disk provides a reservoir of

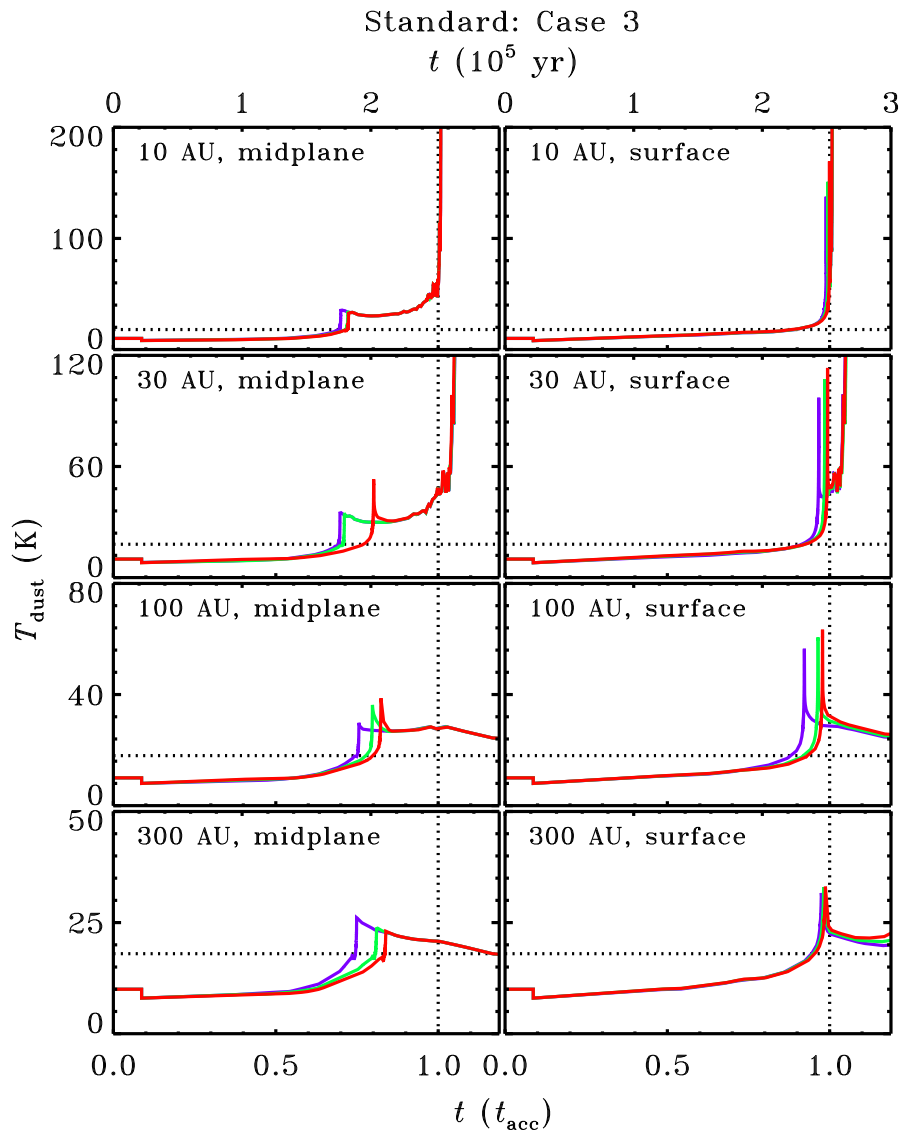


Figure 2.12 – Temperature history for parcels in our standard model (Case 3) ending up at the midplane (left) or near the surface (right) at radial positions of 10, 30, 100 and 300 AU at $t = t_{\text{acc}}$. The colours correspond to Fig. 2.5. The dotted lines are drawn at $T_{\text{d}} = 18$ K and $t = t_{\text{acc}}$. Note the different vertical scales between some panels.

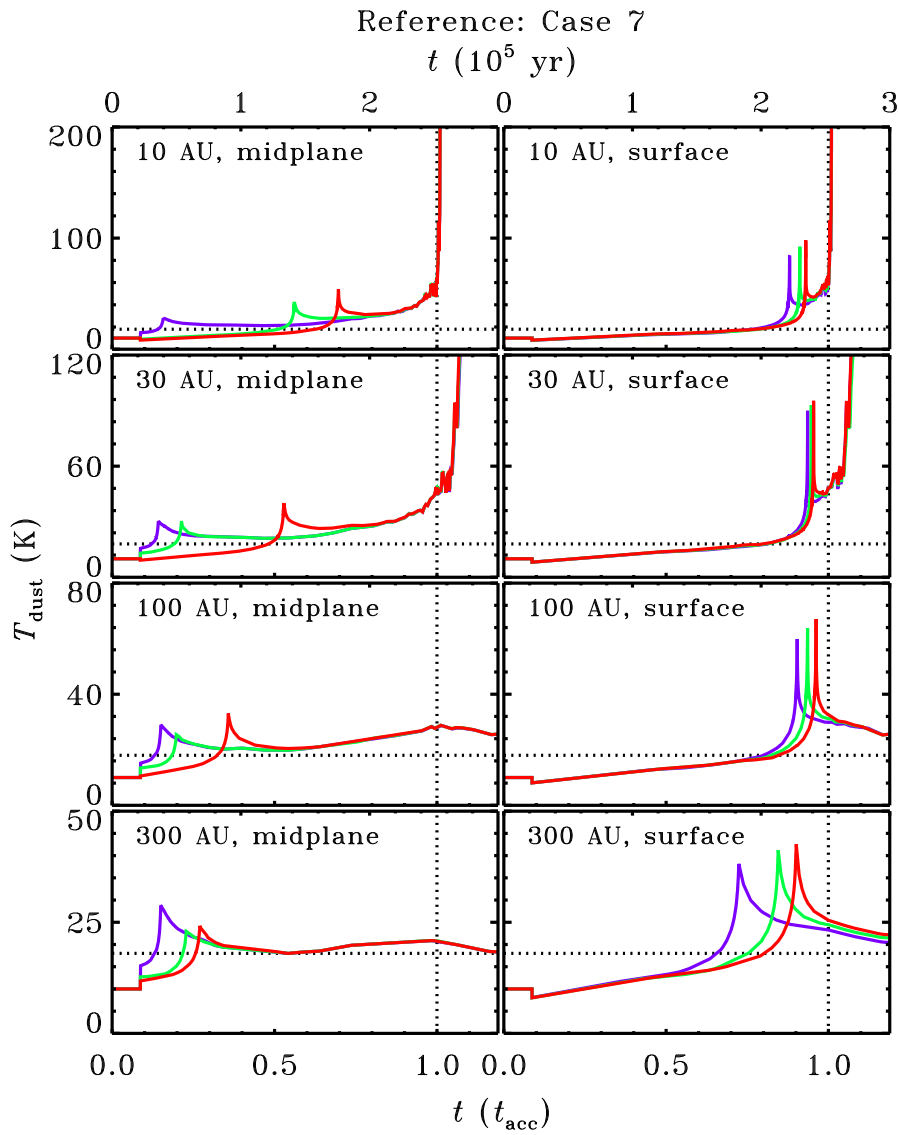


Figure 2.13 – Same as Fig. 2.12, but for our reference model (Case 7). The colours correspond to Fig. 2.6.

relatively cold material where CO, which evaporates early on in the collapse, can return to the grains. H₂O can only desorb in the inner few AU of the disk and remnant envelope.

Figures 2.14 and 2.15 show the density and dust temperature at t_{acc} for each parameter set; our standard and reference models are the two panels on the second row (Case 3 and 7). Several trends are visible:

- With a lower sound speed (Cases 1, 2, 5 and 6), the overall accretion rate (\dot{M}) is smaller so the accretion time increases ($t_{\text{acc}} \propto c_s^{-3}$). The disk can now grow larger and more massive. In our standard model, the disk is $0.05 M_{\odot}$ at t_{acc} and extends to about 400 AU radially. Decreasing the sound speed to 0.19 km s^{-1} (Case 1) results in a disk of $0.22 M_{\odot}$ and nearly 2000 AU. The lower accretion rate also reduces the stellar luminosity. These effects combine to make the disk colder in the low- c_s cases.
- With a lower rotation rate (Cases 1–4), the infall occurs in a more spherically symmetric fashion. Less material is captured in the disk, which remains smaller and less massive. From our reference to our standard model, the disk mass goes from 0.43 to $0.05 M_{\odot}$ and the radius from 1400 to 400 AU. The stronger accretion onto the star causes a higher luminosity. Altogether, this makes for a small, relatively warm disk in the low- Ω_0 cases.
- With a lower initial mass (Cases 2, 4, 6 and 8), there is less material to end up on the disk. The density profile is independent of the mass in a Shu-type collapse (Eq. (2.1)), so the initial mass is lowered by taking a smaller envelope radius. The material from the outer parts of the envelope is the last to accrete and is therefore more likely to end up in the disk. If the initial mass is halved relative to our standard model (as in Case 4), the resulting disk is only $0.001 M_{\odot}$ and 1 AU. Our reference disk goes from $0.43 M_{\odot}$ and 1400 AU to $0.16 M_{\odot}$ and 600 AU (Cases 7 and 8). The luminosity at t_{acc} is lower in the high- M_0 cases and the cold part of the disk ($T_d < 18 \text{ K}$) has a somewhat larger relative size.

Dullemond et al. (2006a) noted that accretion occurs closer to the star for a slowly rotating core than for a fast rotating core, resulting in a larger fraction of crystalline dust in the former case. The same effect is seen here, but overall the accretion takes place farther from the star than in Dullemond et al. (2006a). This is due to our taking into account the vertical structure of the disk. Our gaseous fractions in the low- Ω_0 disks are higher than in the high- Ω_0 disks (consistent with a higher crystalline fraction), but not because material enters the disk closer to the star. Rather, as mentioned above, the larger gas content comes from the higher temperatures throughout the disk. A more detailed discussion of the crystallinity in disks can be found in Chapter 4.

Combining the density and the temperature, the fractions of cold ($T_d < 18 \text{ K}$), warm ($T_d > 18 \text{ K}$) and hot ($T_d > 100 \text{ K}$) material in the disk can be computed. The warm and hot fractions are listed in Table 2.3 along with the fractions of gaseous CO and H₂O in the disk at t_{acc} . Across the parameter grid, 23–100% of the CO is in the gas, along with 0.3–100% of the H₂O. This includes Case 4, which only has a disk of $0.0014 M_{\odot}$. If that one is omitted, at most 13% of the H₂O in the disk at t_{acc} is in the gas. The gaseous H₂O fractions for Cases 1, 2, 6, 7 and 8 (at most a few per cent) are quite uncertain, because the

Table 2.3 – Summary of properties at $t = t_{\text{acc}}$ for our parameter grid.^a

Case	$M_{\text{d}}/M^{\text{b}}$	$f_{\text{warm}}^{\text{c}}$	$f_{\text{hot}}^{\text{c}}$	$f_{\text{gas}}(\text{CO})^{\text{d}}$	$f_{\text{gas}}(\text{H}_2\text{O})^{\text{d}}$
1	0.22	0.69	0.004	0.62	0.028
2	0.15	0.94	0.035	0.93	0.020
3 (std)	0.05	1.00	0.17	1.00	0.13
4	0.003	1.00	1.00	1.00	1.00
5	0.59	0.15	0.0001	0.23	0.11
6	0.50	0.34	0.0004	0.27	0.02
7 (ref)	0.43	0.83	0.003	0.81	0.004
8	0.33	1.00	0.028	1.00	0.003

^a These results are for the one-flavour CO desorption model.

^b The fraction of the disk mass with respect to the total accreted mass ($M = M_* + M_{\text{d}}$).

^c The fractions of warm ($T_{\text{d}} > 18$ K) and hot ($T_{\text{d}} > 100$ K) material with respect to the entire disk. The warm fraction also includes material above 100 K.

^d The fractions of gaseous CO and H₂O with respect to the total amounts of CO and H₂O in the disk.

model does not have sufficient resolution in the inner disk to resolve these small amounts. They may be lower by up to a factor of ten or higher by up to a factor of three.

There is good agreement between the fractions of warm material and gaseous CO. In Case 5, about a third of the CO gas at t_{acc} is gas left over from the initial conditions, due to the long adsorption timescale for the outer part of the cloud core. This is also the case for the majority of the gaseous H₂O in Cases 1, 5 and 6. For the other parameter sets, f_{hot} and $f_{\text{gas}}(\text{H}_2\text{O})$ are the same within the error margins. Overall, the results from the parameter grid show once again that the adsorption-desorption balance is primarily determined by the temperature, and that the adsorption-desorption timescales are usually shorter than the dynamical timescales.

By comparing the fraction of gaseous material at the end of the collapse to the fraction of material above the desorption temperature, the history of the material is disregarded. For example, some of the cold material was heated above 18 K during the collapse, and CO desorbed before re-adsorbing inside the disk. This may affect the CO abundance if the model is expanded to include a full chemical network. In that case, the results from Table 2.3 only remain valid if the CO abundance is mostly constant throughout the collapse. The same caveat holds for H₂O. This point is explored in more detail in Chapter 3.

2.4.2 Complex organic molecules

A full chemical network, including grain-surface reactions, is required to analyse the gas and ice abundances of more complex species. While this will be a topic for a future publication, the current CO and H₂O results, combined with recent other work, can already provide some insight.

Complex organic species can be divided into two categories: first-generation species that are formed on the grain surfaces during the initial warm-up to ~ 40 K, and second-

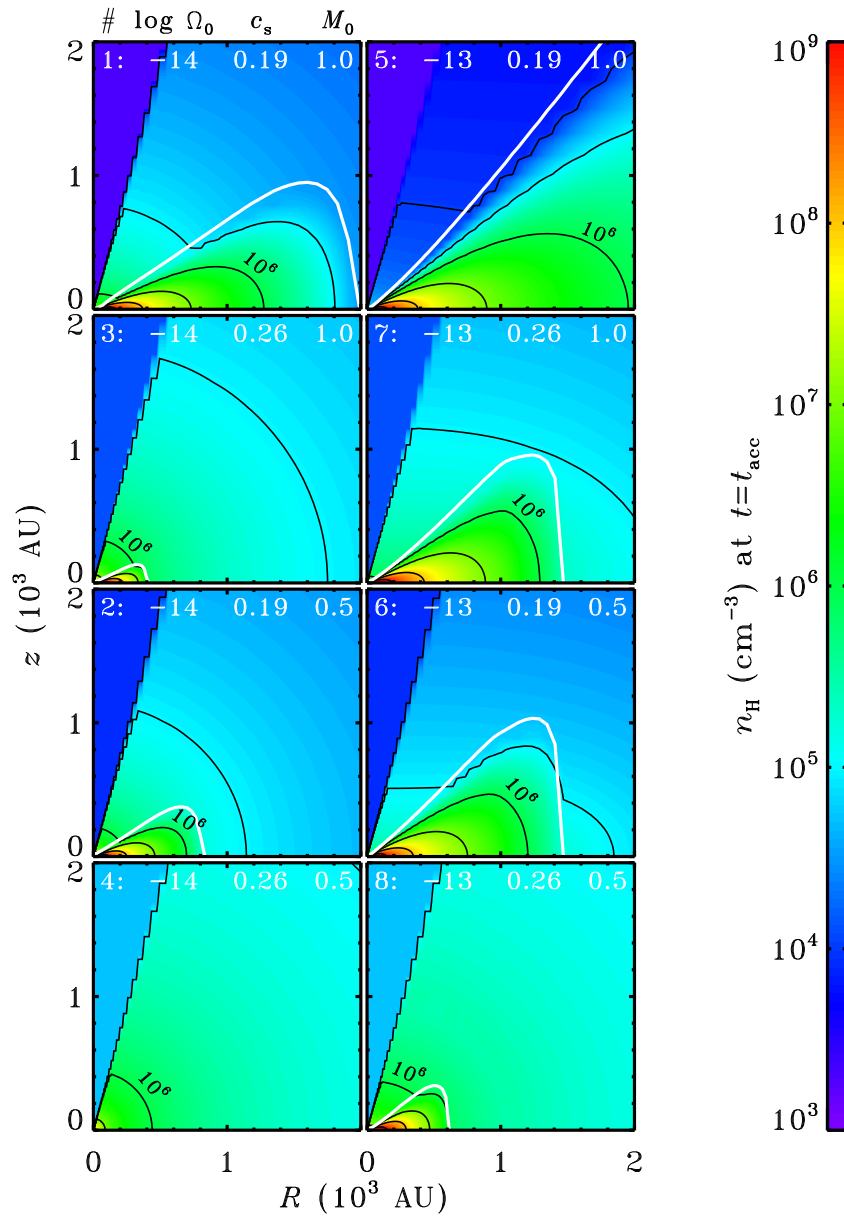


Figure 2.14 – Total density at $t = t_{\text{acc}}$ for our parameter grid (Table 2.1). The rotation rates ($\log \Omega_0$ in s^{-1}), sound speeds (km s^{-1}) and initial masses (M_\odot) are indicated. The contours increase by factors of ten going inwards; the 10^6-cm^{-3} contour is labelled in each panel. The white curves indicate the surfaces of the disks; the disk for Case 4 is too small to be visible.

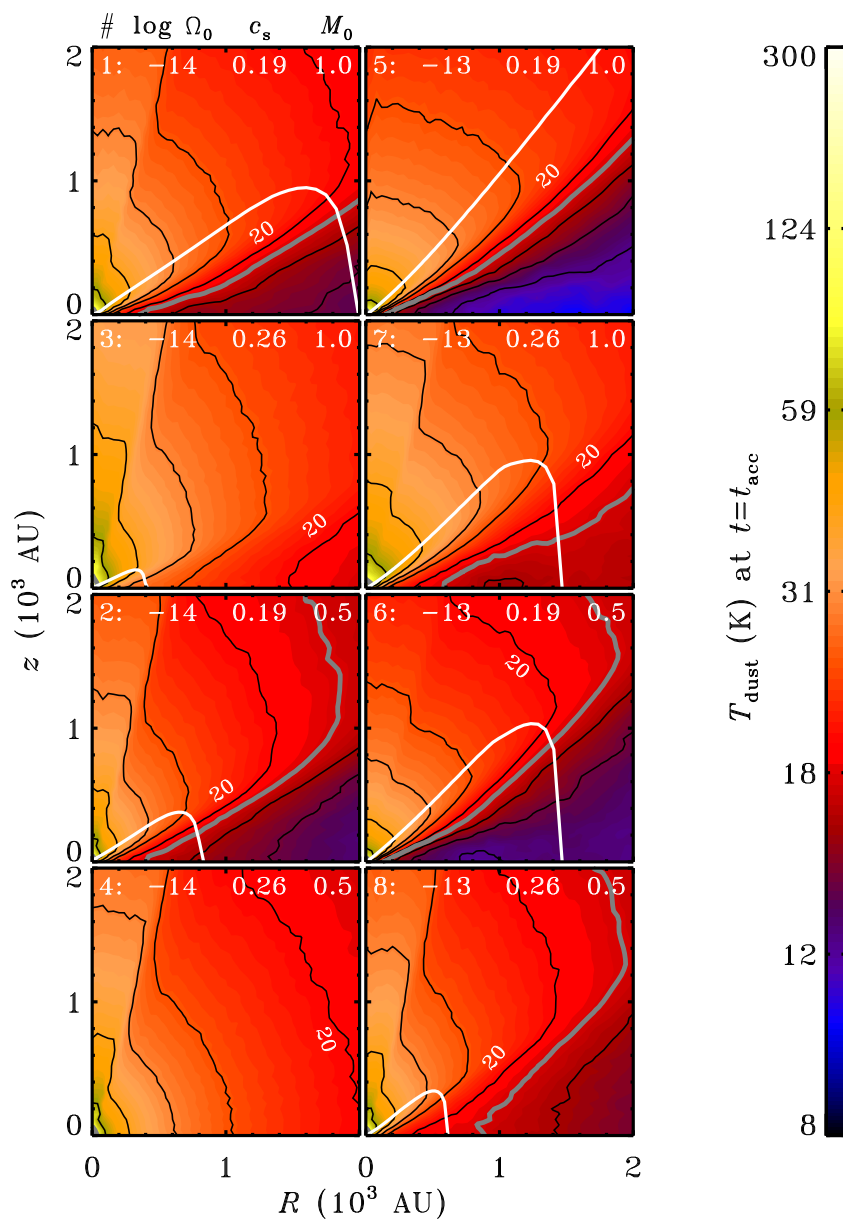


Figure 2.15 – Dust temperature, as in Fig. 2.14. The temperature contours are drawn at 100, 60, 40, 30, 25, 20, 18, 16, 14 and 12 K from the centre outwards. The 20-K contour is labelled in each panel and the 18-K contours are drawn as grey lines.

generation species that are formed in the warm gas phase when the first-generation species have evaporated (Herbst & van Dishoeck 2009). Additionally, CH₃OH may be considered a zeroth-generation complex organic because it is already formed efficiently during the pre-collapse phase (Garrod & Herbst 2006). Its gas-ice ratio should be similar to that of H₂O, due to the similar binding energies.

Larger first-generation species such as methyl formate (HCOOCH₃) can be formed on the grains if material spends at least several 10⁴ yr at 20–40 K. The radicals involved in the surface formation of HCOOCH₃ (HCO and CH₃O) are not mobile enough at lower temperatures and are not formed efficiently enough at higher temperatures. A low surface abundance of CO (at temperatures above 18 K) does not hinder the formation of HCOOCH₃: HCO and CH₃O are formed from reactions of OH and H with H₂CO, which is already formed at an earlier stage and which does not evaporate until ~40 K (Garrod & Herbst 2006). Cosmic-ray-induced photons are available to form OH from H₂O even in the densest parts of the disk and envelope (Shen et al. 2004).

As shown in Sect. 2.3.4, many of the parcels ending up near the midplane inside of ~300 AU in our standard model spend sufficient time in the required temperature regime to allow for efficient formation of HCOOCH₃ and other complex organics. Once formed, these species are likely to assume the same gas-ice ratios as H₂O and the smaller organics. They evaporate in the inner 10–20 AU, so in the absence of mixing, complex organics would only be observable in the gas phase close to the star. The Atacama Large Millimeter/submillimeter Array (ALMA), currently under construction, will be able to test this hypothesis.

The gas-phase route towards complex organics involves the hot inner envelope ($T_d > 100$ K), also called the hot core or hot corino in the case of low-mass protostars (Ceccarelli 2004, Bottinelli et al. 2004, 2007). Most of the ice evaporates here and a rich chemistry can take place if material spends at least several 10³ yr in the hot core (Charnley et al. 1992). However, the material in the hot inner envelope in our model is essentially in freefall towards the star or the inner disk, and its transit time of a few 100 yr is too short for complex organics to be formed abundantly (see also Schöier et al. 2002). Additionally, the total mass in this region is very low: about a per cent of the disk mass. In order to explain the observations of second-generation complex molecules, there has to be some mechanism to keep the material in the hot core for a longer time. Alternatively, it has recently been suggested that molecules typically associated with hot cores may in fact form on the grain surfaces as well (Garrod et al. 2008).

2.4.3 Mixed CO-H₂O ices

In the results presented in Sect. 2.3, all CO was taken to desorb at a single temperature. In a more realistic approach, some of it would be trapped in the H₂O ice and desorb at higher temperatures. This was simulated with four “flavours” of CO ice, as summarised in Table 2.2. With our four-flavour model, the global gas-ice profiles are mostly unchanged. All CO is frozen out in the sub-18 K regions and it fully desorbs when the temperature goes above 100 K. Some 10 to 20% remains in the solid phase in areas of intermediate temperature. In our standard model, the four-flavour variety has 15% of all CO in the disk

at t_{acc} on the grains, compared to 0% in the one-flavour variety. In our reference model, the solid fraction increases from 19 to 33%.

The grain-surface formation of H_2CO , CH_3OH , HCOOCH_3 and other organics should not be very sensitive to these variations. H_2CO and CH_3OH are already formed abundantly before the onset of collapse, when the one- and four-flavour models predict equal amounts of solid CO. H_2CO is then available to form HCOOCH_3 (via the intermediates HCO and CH_3O) during the collapse. The higher abundance of solid CO at 20–40 K in the four-flavour model could slow down the formation of HCOOCH_3 somewhat, because CO destroys the OH needed to form HCO (Garrod & Herbst 2006). H_2CO evaporates around 40 K, so HCOOCH_3 cannot be formed efficiently anymore above that temperature. On the other hand, if a multiple-flavour approach is also employed for H_2CO , some of it remains solid above 40 K, and HCOOCH_3 can continue to be produced. Overall, then, the multiple-flavour desorption model is not expected to cause large variations in the abundances of these organic species compared to the one-flavour model.

2.4.4 Implications for comets

Comets in our solar system are known to be abundant in CO and they are believed to have formed between 5 and 30 AU in the circumsolar disk (Bockelée-Morvan et al. 2004, Kobayashi et al. 2007). However, the dust temperature in this region at the end of the collapse is much higher than 18 K for all of our parameter sets. This raises the question of how solid CO can be present in the comet-forming zone.

One possible answer lies in the fact that even at $t = t_{\text{acc}}$, our objects are still very young. As noted in Sect. 2.3.2, the disks cool down as they continue to evolve towards “mature” T Tauri systems. Given the right set of initial conditions, this may bring the temperature below 18 K inside of 30 AU. However, there are many T Tauri disk models in the literature where the temperature at those radii remains well above the CO evaporation temperature (e.g., D’Alessio et al. 1998, 2001). Specifically, models of the minimum-mass solar nebula (MMSN) predict a dust temperature of ~ 40 K at 30 AU (Lecar et al. 2006).

A more plausible solution is to turn to mixed ices. At the temperatures computed for the comet-forming zone of the MMSN, 10–20% of all CO may be trapped in the H_2O ice. Assuming typical CO- H_2O abundance ratios, this is entirely consistent with observed cometary abundances (Bockelée-Morvan et al. 2004).

Large abundance variations are possible for more complex species, due to the different densities and temperatures at various points in the comet-forming zone in our model, as well as the different density and temperature histories for material ending up at those points. This seems to be at least part of the explanation for the chemical diversity observed in comets. Our current model is extended in Chapter 3 to include a full gas-phase chemical network to analyse these variations and compare them against cometary abundances.

The desorption and readsorption of H_2O in the disk-envelope boundary shock has been suggested as a method to trap noble gases in the ice and include them in comets (Owen et al. 1992, Owen & Bar-Nun 1993). As shown in Sects. 2.2.5 and 2.3.4, a number of parcels in our standard model are heated to more than 100 K just prior to entering

the disk. However, these parcels end up in the disk's surface. Material that ends up at the midplane, in the comet-forming zone, never gets heated above 50 K. Vertical mixing, which is ignored in our model, may be able to bring the noble-gas-containing grains down into the comet-forming zone.

Another option is episodic accretion, resulting in temporary heating of the disk (Sect. 2.4.5). In the subsequent cooling phase, noble gases may be trapped as the ices reform. The alternative of trapping the noble gases already in the pre-collapse phase is unlikely. This requires all the H₂O to start in the gas phase and then freeze out rapidly. However, in reality (contrary to what is assumed in our model) it is probably formed on the grain surfaces by hydrogenation of atomic oxygen, which would not allow for trapping of noble gases.

2.4.5 Limitations of the model

The physical part of our model is known to be incomplete and this may affect the chemical results. For example, our model does not include radial and vertical mixing. Semenov et al. (2006) and Aikawa (2007) recently showed that mixing can enhance the gas-phase CO abundance in the sub-18 K regions of the disk. Similarly, there could be more H₂O gas if mixing is included. This would increase the fractions of CO and H₂O gas listed in Table 2.3. The gas-phase abundances can also be enhanced by allowing for photodesorption of the ices in addition to the thermal desorption considered here (Shen et al. 2004, Öberg et al. 2007, 2009b,c). Mixing and photodesorption can each increase the total amount of gaseous material by up to a factor of two. The higher gas-phase fractions are mostly found in the regions where the temperature is a few degrees below the desorption temperature of CO or H₂O.

Accretion from the envelope onto the star and disk occurs in our model at a constant rate \dot{M} until all of the envelope mass is gone. However, the lack of widespread red-shifted absorption seen in interferometric observations suggests that the infall may stop already at an earlier time (Jørgensen et al. 2007). This would reduce the disk mass at t_{acc} . The size of the disk is determined by the viscous evolution, which would probably not change much. Hence, if accretion stops or slows down before t_{acc} , the disk would be less dense and therefore warmer. It would also reduce the fraction of disk material where CO never desorbed, because most of that material comes from the outer edge of the original cloud core (Fig. 2.11). Both effects would increase the gas-ice ratios of CO and H₂O.

Our results are also modified by the likely occurrence of episodic accretion (Kenyon & Hartmann 1995, Evans et al. 2009). In this scenario, material accretes from the disk onto the star in short bursts, separated by intervals where the disk-to-star accretion rate is a few orders of magnitude lower. The accretion bursts cause luminosity flares, briefly heating up the disk before returning to an equilibrium temperature that is lower than in our models. This may produce a disk with a fairly large ice content for most of the time, which evaporates and reabsorbs after each accretion episode. The consequences for complex organics and the inclusion of various species in comets are unclear.

2.5 Conclusions

This chapter presents the first results from a two-dimensional, semi-analytical model that simulates the collapse of a molecular cloud core to form a low-mass protostar and its surrounding disk. The model follows individual parcels of material from the core into the star or disk and also tracks their motion inside the disk. It computes the density and temperature at each point along these trajectories. The density and temperature profiles are used as input for a chemical code to calculate the gas and ice abundances for carbon monoxide (CO) and water (H₂O) in each parcel, which are then transformed into global gas-ice profiles. Material ending up at different points in the disk spends a different amount of time at certain temperatures. These temperature histories provide a first look at the chemistry of more complex species. The main results from this chapter are as follows:

- Both CO and H₂O freeze out towards the centre of the core before the onset of collapse. As soon as the protostar turns on, a fraction of the CO rapidly evaporates, while H₂O remains on the grains. CO returns to the solid phase when it cools below 18 K inside the disk. Depending on the initial conditions, this may be in a small or a large fraction of the disk (Sect. 2.3.3).
- All parcels that end up in the disk have the same qualitative temperature history (Fig. 2.12). There is one temperature peak just before entering the disk, when material traverses the inner envelope, and a second one (higher than the first) when inward radial motion brings the parcel closer to the star. In some cases, this results in multiple desorption and adsorption events during the parcel's infall history (Sect. 2.3.4).
- Material that originates near the midplane of the initial core remains at lower temperatures than does material originating from closer to the poles. As a result, the chemical content of the material from near the midplane is less strongly modified during the collapse than the content of material from other regions (Fig. 2.11). The outer part of the disk contains the chemically most pristine material, where at most only a small fraction of the CO ever desorbed (Sect. 2.3.3).
- A higher sound speed results in a smaller and warmer disk, with larger fractions of gaseous CO and H₂O at the end of the envelope accretion. A lower rotation rate has the same effect. A higher initial mass results in a larger and colder disk, and smaller gaseous CO and H₂O fractions (Sect. 2.4.1).
- The infalling material generally spends enough time in a warm zone (20–40 K) for first-generation complex organic species to be formed abundantly on the grains (Fig. 2.12). Large differences can occur in the density and temperature histories for material ending up at various points in the disk. These differences allow for spatial abundance variations in the complex organics across the entire disk. This appears to be at least part of the explanation for the cometary chemical diversity (Sects. 2.4.2 and 2.4.4).
- Complex second-generation species are not formed abundantly in the warm inner envelope (the hot core or hot corino) in our model, due to the combined effects of the dynamical timescales and low mass fraction in that region (Sect. 2.4.2).
- The temperature in the disk's comet-forming zone (5–30 AU from the star) lies well above the CO desorption temperature, even if effects of grain growth and continued

disk evolution are taken into account. Observed cometary CO abundances can be explained by mixed ices: at temperatures of several tens of K, as predicted for the comet-forming zone, CO can be trapped in the H₂O ice at a relative abundance of a few per cent (Sect. 2.4.4).

Appendix: Disk formation efficiency

The results from our parameter grid can be used to derive the disk formation efficiency, η_{df} , as a function of the sound speed, c_s , the solid-body rotation rate, Ω_0 , and the initial core mass, M_0 . This efficiency can be defined as the fraction of M_0 that is in the disk at the end of the collapse phase ($t = t_{\text{acc}}$) or as the mass ratio between the disk and the star at that time. The former is used in this appendix.

In order to cover a wider range of initial conditions, the physical part of our model was run on a 9^3 grid. The sound speed was varied from 0.15 to 0.35 km s⁻¹, the rotation rate from $10^{-14.5}$ to $10^{-12.5}$ s⁻¹ and the initial core mass from 0.1 to 2.1 M_\odot . The resulting η_{df} at $t = t_{\text{acc}}$ were fitted to

$$\eta_{\text{df}} = \frac{M_{\text{d}}}{M_0} = g_1 + g_2 \left[\frac{\log(\Omega_0/\text{s}^{-1})}{-13} \right] \quad (2.37)$$

with

$$g_1 = k_1 + k_2 \left[\frac{\log(\Omega_0/\text{s}^{-1})}{-13} \right]^{q_1} + k_3 \left[\frac{c_s}{0.2 \text{ km s}^{-1}} \right]^{q_2} + k_4 \left[\frac{M_0}{M_\odot} \right]^{q_3}, \quad (2.38)$$

$$g_2 = k_5 + k_6 \left[\frac{\log(\Omega_0/\text{s}^{-1})}{-13} \right] + k_7 \left[\frac{c_s}{0.2 \text{ km s}^{-1}} \right] + k_8 \left[\frac{M_0}{M_\odot} \right]. \quad (2.39)$$

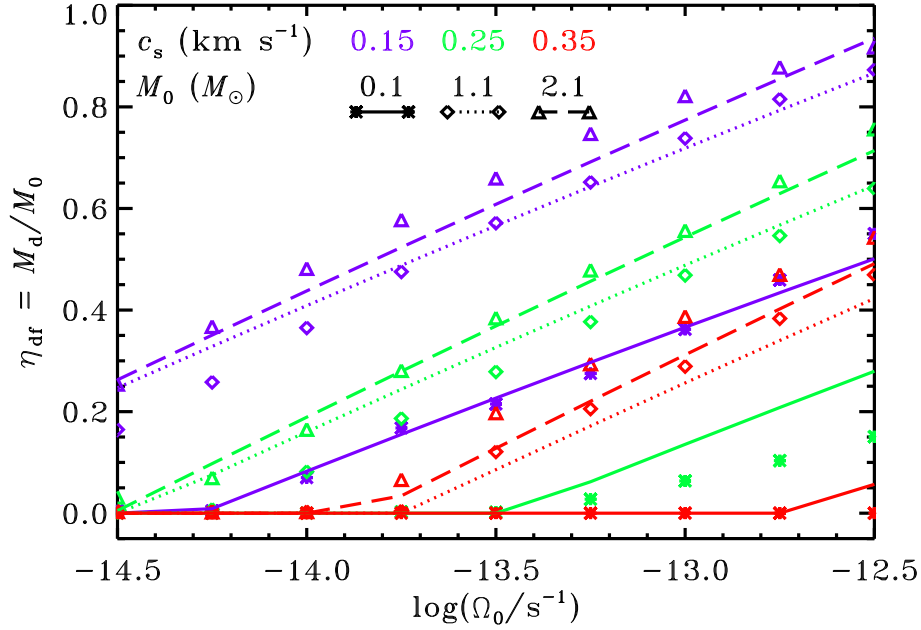
Equation (2.37) can give values lower than 0 or larger than 1. In those cases, it should be interpreted as being 0 or 1.

The best-fit values for the coefficients k_i and the exponents q_i are listed in Table 2.4. The absolute and relative difference between the best fit and the model data have a root mean square (rms) of 0.04 and 5%. The largest absolute and relative difference are 0.20 and 27%. The fit is worst for a high core mass, a low sound speed and an intermediate rotation rate, as well as for a low core mass, an intermediate to high sound speed and a high rotation rate.

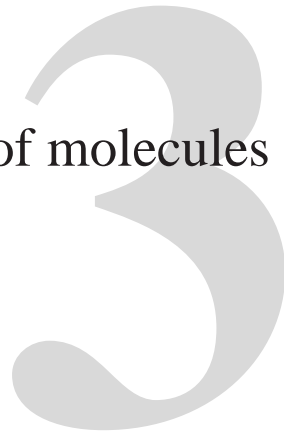
Figure 2.16 shows the disk formation efficiency as a function of the rotation rate, including the fit from Eq. (2.37). The efficiency is roughly a quadratic function in $\log \Omega_0$, but due to the narrow dynamic range of this variable, the fit appears as straight lines. Furthermore, the efficiency is roughly a linear function in c_s and a square root function in M_0 .

Table 2.4 – Coefficients and exponents for the best fit for the disk formation efficiency.

Coefficient	Value	Coefficient	Value	Exponent	Value
k_1	2.08	k_5	-0.106	q_1	0.236
k_2	0.020	k_6	-1.539	q_2	0.255
k_3	0.035	k_7	-0.470	q_3	0.537
k_4	0.914	k_8	-0.344		

**Figure 2.16** – Disk formation efficiency as a function of the solid-body rotation rate. The model values are plotted as symbols and the fit from Eq. (2.37) as lines. The different values of the sound speed are indicated by colours and the different values of the initial core mass are indicated by symbols and line types, with the solid lines corresponding to the asterisks, the dotted lines to the diamonds and the dashed lines to the triangles.

The chemical history of molecules in circumstellar disks II: Gas-phase species



R. Visser, S. D. Doty and E. F. van Dishoeck
to be submitted

Abstract

Context. The chemical composition of a molecular cloud changes dramatically as it collapses to form a low-mass protostar and circumstellar disk. Two-dimensional (2D) chemodynamical models are required to properly study this process.

Aims. The goal of this work is to follow, for the first time, the chemical evolution in two dimensions all the way from a pre-stellar cloud into a circumstellar disk. Of special interest is the question whether the chemical composition of the disk is a result of chemical processing during the collapse phase, or whether it is determined by in situ processing after the disk has formed.

Methods. We combine a semi-analytical method to get 2D axisymmetric density and velocity structures with detailed radiative transfer calculations to get temperature profiles and UV fluxes. Material is followed in from the cloud to the disk and a full gas-phase chemistry network – including freeze-out onto and evaporation from cold dust grains – is evolved along these trajectories. The abundances thus obtained are compared to the results from a static disk model and to cometary observations.

Results. The chemistry during the collapse phase is dominated by a few key processes, such as the evaporation of CO or the photodissociation of H₂O. Depending on the physical conditions encountered along specific trajectories, some of these processes are absent. At the end of the collapse phase, the disk can thus be divided into zones with different chemical histories. The disk is found not to be in chemical equilibrium at the end of the collapse. We argue that comets must be formed from material with different chemical histories: some of it is strongly processed, some of it remains pristine. Variations between individual comets are possible if they formed at different positions or times in the solar nebula. The chemical zones in the disk and the mixed origin of the cometary material arise from the 2D nature of our model.

3.1 Introduction

The formation of a low-mass protostar out of a cold molecular cloud is accompanied by large-scale changes in the chemical composition of the constituent gas and dust. Pre-stellar cloud cores are cold (~ 10 K), moderately dense ($\sim 10^4$ – 10^6 cm $^{-3}$), and irradiated only by the ambient interstellar radiation field (see reviews by Shu et al. 1987, di Francesco et al. 2007 and Bergin & Tafalla 2007). As the core starts to collapse, several mechanisms act to heat up the material, such as gravitational contraction, accretion shocks and, eventually, radiation produced by nuclear fusion in the protostar. The inner few hundred AU of the core flatten out to form a circumstellar disk, where planets may be formed at a later stage (see review by Dullemond et al. 2007b). The density in the interior of the disk, especially at small radii, is several orders of magnitude higher than the density of the pre-stellar core. Meanwhile, the protostar infuses the disk with high fluxes of ultraviolet and X-ray photons. The chemical changes arising from these evolving physical conditions have been analysed by various groups with one-dimensional models (see reviews by Ceccarelli et al. 2007, Bergin et al. 2007 and Bergin & Tafalla 2007). However, two-dimensional models are required to properly describe the formation of the circumstellar disk and the chemical processes taking place inside it.

This chapter follows the preceding chapter in a series of publications aiming to model the chemical evolution from pre-stellar cores to circumstellar disks in two dimensions. Chapter 2 contains a detailed description of our semi-analytical model and an analysis of the gas and ice abundances of carbon monoxide (CO) and water (H₂O). We found that most CO evaporates during the infall phase and freezes out again in those parts of the disk that are colder than 18 K. The much higher binding energy of H₂O keeps it in solid form at all times, except within ~ 10 AU of the star. Based on the time that the infalling material spends at dust temperatures between 20 and 40 K, first-generation complex organic species were predicted to form abundantly on the grain surfaces according to the scenario of Garrod & Herbst (2006) and Garrod et al. (2008).

The current chapter extends the chemical analysis to a full gas-phase network, including freeze-out onto and evaporation from dust grains, as well as basic grain-surface hydrogenation reactions. Combining semi-analytical density and velocity structures with detailed temperature profiles from full radiative transfer calculations, our aim is to bridge the gap between 1D chemical models of collapsing cores and 1+1D or 2D chemical models of mature T Tauri and Herbig Ae/Be disks. One of the key questions is whether the chemical composition of such disks is mainly a result of chemical processing during the collapse or whether it is determined by in situ processing after the disk has formed.

As reviewed by di Francesco et al. (2007) and Bergin & Tafalla (2007), the chemistry of pre-stellar cores is well understood. Because of the low temperatures and the moderately high densities, a lot of molecules are observed to be depleted from the gas by freezing out onto the cold dust grains. The main ice constituent is H₂O, showing abundances of $\sim 10^{-4}$ relative to H₂ (Tielens et al. 1991, van Dishoeck 2004). Other abundant ices are CO₂ (30–35% of H₂O; Pontoppidan et al. 2008b) and CO (5–100% of H₂O; Jørgensen et al. 2005, Pontoppidan 2006). Correspondingly, the observed gas-phase abundances of H₂O, CO and CO₂ in pre-stellar cores are low (Snell et al. 2000, Ashby et al. 2000, Bergin

& Snell 2002, Bacmann et al. 2002). Nitrogen-bearing species like N_2 and NH_3 are generally less depleted than carbon- and oxygen-bearing ones (Rawlings et al. 1992, Tafalla et al. 2002, 2004), probably because they require a longer time to be formed in the gas and therefore have not yet had a chance to freeze out (di Francesco et al. 2007). The observed depletion factors are well reproduced with 1D chemical models (Bergin & Langer 1997, Lee et al. 2004).

The collapse phase is initially characterised by a gradual warm-up of the material, resulting in the evaporation of the ice species according to their respective binding energies (van Dishoeck et al. 1993, van Dishoeck & Blake 1998, Boogert et al. 2000, van der Tak et al. 2000a, Aikawa et al. 2001, Jørgensen et al. 2002, 2004, 2005, Jørgensen 2004). The higher temperatures also drive a rich chemistry, especially if it gets warm enough to evaporate H_2O and organic species like CH_3OH and $HCOOCH_3$ (Blake et al. 1987, Millar et al. 1991, Charnley et al. 1992). Going back to the late 1970s, the chemical evolution during the collapse phase has been studied with purely spherical models (Gerola & Glassgold 1978, Leung et al. 1984, Ceccarelli et al. 1996, Rodgers & Charnley 2003, Doty et al. 2004, Lee et al. 2004, Garrod & Herbst 2006, Aikawa et al. 2008, Garrod et al. 2008). They are successful at explaining the observed abundances at scales of several thousand AU, where the envelope is still close to spherically symmetric, but they cannot make the transition from the 1D spherically symmetric envelope to the 2D axisymmetric circumstellar disk.

Recently, van Weeren et al. (2009) followed the chemical evolution within the framework of a 2D hydrodynamical simulation and obtained a reasonable match with observations. However, their primary focus was still on the envelope, not on the disk. Nevertheless, they showed how important it is to treat the chemical evolution during low-mass star formation as more than a simple 1D process.

Once the phase of active accretion from the envelope comes to an end, the circumstellar disk settles into a comparatively static situation (Bergin et al. 2007, Dullemond et al. 2007a). Observationally, we are now in the T Tauri and Herbig Ae/Be stages, and some simple molecules have been detected in these objects (Dutrey et al. 1997, Kastner et al. 1997, Qi et al. 2003, Thi et al. 2004, Lahuis et al. 2006). They have also received a lot of attention with 2D models, showing for example that disks can be divided vertically into three chemical layers: a cold zone near the midplane, a warm molecular layer at intermediate altitudes, and a photon-dominated region at the surface (Aikawa et al. 1996, 1997, 2002, 2008, Aikawa & Herbst 1999, 2001, Willacy & Langer 2000, van Zadelhoff et al. 2003, Rodgers & Charnley 2003, Jonkheid et al. 2004, Semenov et al. 2006, Woitke et al. 2009). However, as noted above, the chemical connection between the early 1D stages of low-mass star formation and the 2D circumstellar disks at later stages remains an unsolved puzzle.

This chapter aims to provide the first steps towards solving this puzzle by following the chemical evolution all the way from a pre-stellar cloud core to a circumstellar disk in two spatial dimensions. The physical and chemical models are described in Sects. 3.2 and 3.3. We briefly discuss the chemistry during the pre-collapse phase in Sect. 3.4 before turning to the collapse itself in Sect. 3.5. There, we first follow the chemistry in detail along a trajectory terminating at one particular position in the disk, and then

generalise those results to material ending up at other positions. In Sect. 3.6, we compare the abundances resulting from the collapse to in situ processing in a static disk. Finally, we discuss some caveats and the implications of our results for the origin of comets in Sect. 3.7. Conclusions are drawn in Sect. 3.8.

3.2 Collapse model

3.2.1 Step-wise summary

Our semi-analytical collapse model is described in detail in Chapter 2; it consists of several steps, summarised in Fig. 3.1. We start with a singular isothermal sphere characterised by a total mass M_0 , an effective sound speed c_s , and a uniform rotation rate Ω_0 . As soon as the collapse starts, at $t = 0$, the rotation causes the infalling material to be deflected towards the equatorial midplane. This breaks the spherical symmetry, so we run the entire model as a two-dimensional axisymmetric system. The 2D density and velocity profiles follow the solutions of Shu (1977), Cassen & Moosman (1981) and Terebey et al. (1984) for an inside-out collapse with rotation. After the disk is first formed at the midplane, it evolves by ongoing accretion from the collapsing core and by viscous spreading to conserve angular momentum (Shakura & Sunyaev 1973, Lynden-Bell & Pringle 1974).

Taking the 2D density profiles from step 2, and adopting the appropriate size and luminosity for the protostar (Adams & Shu 1986, Young & Evans 2005), the next step consists of computing the dust temperature at a number of time steps. We do this with the radiative transfer code RADMC (Dullemond & Dominik 2004a), which takes a 2D axisymmetric density profile but follows photons in all three dimensions. The RADMC code also computes the full radiation spectrum at each point in the axisymmetric disk and remnant envelope, as required for the photon-driven reactions in our chemical network (Sects. 3.2.3 and 3.3.1). The gas temperature is set equal to the dust temperature throughout the disk and the envelope. This is a poor assumption in the surface of the disk and the

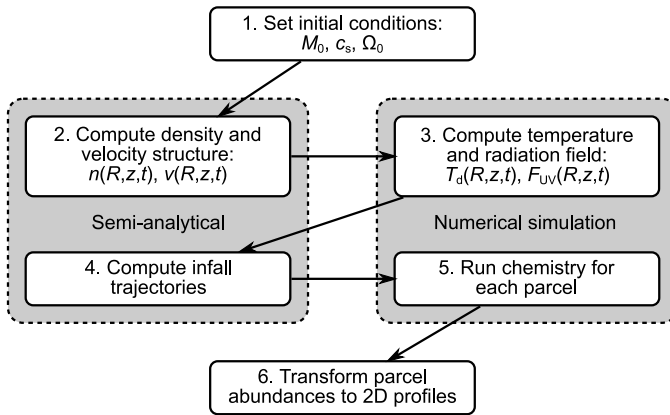


Figure 3.1 – Step-wise summary of our 2D axisymmetric collapse model. Steps 2 and 4 are semi-analytical, while steps 3 and 5 consist of detailed numerical simulations.

inner parts of the envelope (Kamp & Dullemond 2004, Jonkheid et al. 2004, Woitke et al. 2009), the consequences of which are addressed in Sect. 3.7.1.

Given the dynamical nature of the collapse, it is easiest to solve the chemistry in a Lagrangian frame. In Chapter 2, we populated the envelope with several thousand parcels at $t = 0$ and followed them in towards the disk and star. We now take an alternative approach where we define a regular grid of parcels at the end of the collapse and follow the parcels backwards in time to their position at $t = 0$. Since we are usually interested in the abundance profiles at the end of the collapse, when the disk is fully formed, it has many advantages to have a regular grid of parcels at that time rather than at the beginning. In either case, step 4 of the model produces a set of infall trajectories with densities, temperatures and UV intensities as a function of time and position. These data are required for the next step: solving the time-dependent chemistry for each individual parcel. Although the parcels are followed backwards in time to get their trajectories, we compute the chemistry in the normal forward direction. The last step of our model consists of transforming the abundances from the individual parcels back into 2D axisymmetric profiles at whatever time steps we are interested in.

In Chapter 2, the model was run for a grid of initial conditions. In the current chapter, the analysis is limited to our standard set of parameters: $M_0 = 1.0 M_{\odot}$, $c_s = 0.26 \text{ km s}^{-1}$ and $\Omega_0 = 10^{-14} \text{ s}^{-1}$. Section 3.7.2 contains a brief discussion on how the results may change for other parameter values.

3.2.2 Differences with Chapter 2

The current version of the model contains several improvements over the version used in Chapter 2. Most importantly, it now correctly treats the problem of sub-Keplerian accretion onto a 2D disk. It has long been known that material falling onto the disk along an elliptic orbit has sub-Keplerian angular momentum, so it exerts a torque on the disk that results in an inward push. Several solutions are available (e.g., Cassen & Moosman 1981, Hueso & Guillot 2005), but these are not suitable for our 2D model. The ad-hoc solution from Chapter 2 provided the appropriate qualitative physical correction, namely increasing the inward radial velocity of the disk material, but it did not properly conserve angular momentum. We now use a new, fully consistent solution, derived directly from the equations for the conservation of mass and angular momentum. It is described in detail in Chapter 4, where it is also shown that it results in disks that are typically a factor of a few smaller than those obtained with the original model. The new disks are a few degrees colder in the inner part and warmer in the outer part, which may further affect the chemistry.

Other changes to the model include the definition of the disk-envelope boundary and the shape of the outflow cavity. In Chapter 2, the disk-envelope boundary was defined as the surface where the density of the infalling envelope material equals that of the disk. Instead, we now take the surface where the ram pressure of the infalling material equals the thermal pressure of the disk (see Chapter 4). This provides a more physically correct description of where material becomes part of the disk. The outflow cavity now has curved walls rather than straight ones, consistent with both observations and theoretical

predictions (Velusamy & Langer 1998, Cantó et al. 2008). The outflow wall is described by

$$z = (0.191 \text{ AU}) \left(\frac{t}{t_{\text{acc}}} \right)^{-3} \left(\frac{R}{\text{AU}} \right)^{1.5}, \quad (3.1)$$

with R and z in spherical coordinates and $t_{\text{acc}} = M_0/\dot{M}$ the time required for the entire envelope to accrete onto the star and disk. The t^{-3} dependence is chosen so that the outflow starts very narrow and becomes increasingly wide as the collapse proceeds. The full opening angle at t_{acc} is 33.6° at $z = 1000 \text{ AU}$ and 15.9° at $z = 10\,000 \text{ AU}$.

3.2.3 Radiation field

Photodissociation and photoionisation by ultraviolet (UV) radiation are important processes in the hot inner core and in the surface layers of the disk. The temperature and luminosity of the protostar evolve as described in Chapter 2, so neither the strength nor the spectral shape of the radiation it emits are constant in time. In addition, the spectral shape changes as the radiation passes through the disk and remnant envelope. Hence, we cannot simply take the photorates from the interstellar medium and scale them according to the integrated UV flux at each spatial grid point.

The most accurate way to obtain the time- and location-dependent photorates is to multiply the cross section for each reaction by the UV field at each grid point. The latter can be computed from 2D radiative transfer at high spectral resolution. As this is too computationally demanding, several approximations have to be made. First of all, we assume the wavelength-dependent attenuation of the radiation field by the dust in the disk and envelope can be represented by a single factor γ for each reaction. The rate coefficient for a given photoreaction at spatial coordinates r and θ and at time t can then be expressed as

$$k_{\text{ph}}(r, \theta, t) = k_{\text{ph}}^* \left(\frac{r}{R_*} \right)^{-2} e^{-\gamma A_V}, \quad (3.2)$$

with A_V the visual extinction towards that point. The unshielded rate coefficient is calculated at the stellar surface (k_{ph}^*) by multiplying the cross section of the reaction by the blackbody flux at the effective temperature of the protostar. The term $(r/R_*)^{-2}$ accounts for the geometrical dilution of the radiation from the star across a distance r . The factor γ is discussed in Sect. 3.3.1.

In order to apply Eq. (3.2), we need the extinction towards each point. In a 1D model, this can simply be done by integrating the total hydrogen number density from the star to a point r and converting the resulting column density to a visual extinction. This approach has been extended to 2D circumstellar disk models by dividing the disk into annuli, each irradiated only from the top and bottom (e.g., Aikawa & Herbst 1999, Jonkheid et al. 2004). Such a 1+1D method is poorly suited to our model, which always has infalling envelope material right above and below the disk. Instead, we compute an average UV flux for each spatial grid point at a number of time steps and compare it to the flux that would be obtained in the case of zero attenuation. The difference gives us an effective extinction for each point.

Table 3.1 – Elemental abundances: $x(X) = n(X)/n_{\text{H}}$.

Species	Abundance	Species	Abundance	Species	Abundance
H ₂	5.00(-1)	Na	2.25(-9)	Cl	1.00(-9)
He	9.75(-2)	Mg	1.09(-8)	Ar	3.80(-8)
C	7.86(-5)	Al	3.10(-8)	Ca	2.20(-8)
N	2.47(-5)	Si	2.74(-9)	Cr	4.90(-9)
O	1.80(-4)	P	2.16(-10)	Fe	2.74(-9)
Ne	1.40(-6)	S	9.14(-8)	Ni	1.80(-8)

The first step in this procedure is to run the Monte Carlo radiative transfer package RADMC (Dullemond & Dominik 2004a) at a low spectral resolution of one frequency point per eV. The large number of photons propagated through the grid (typically 10^5) ensures that we get a statistical sampling of the possible trajectories leading to each point. The specific UV fluxes thus obtained for a point (r, θ, t) are integrated from 6 to 13.6 eV to get the average flux (F_{UV}). This flux is lower than that at the stellar surface because of geometrical dilution and attenuation by dust. Denoting the flux at the stellar surface as F_{UV}^* , we can express the effects of dilution and attenuation as

$$F_{\text{UV}}(r, \theta) = F_{\text{UV}}^0 e^{-\tau_{\text{UV,eff}}} = F_{\text{UV}}^* \left(\frac{r}{R_*} \right)^{-2} e^{-\tau_{\text{UV,eff}}}. \quad (3.3)$$

The effective UV extinction, $\tau_{\text{UV,eff}}$, is converted to the visual extinction A_{V} through the standard relationship $A_{\text{V}} = \tau_{\text{UV,eff}}/3.02$. The unattenuated UV flux, F_{UV}^0 , can also be expressed as a scaling factor relative to the average flux in the interstellar medium (ISM): $\chi = F_{\text{UV}}^0/F_{\text{ISM}}$, with $F_{\text{ISM}} = 8 \times 10^7 \text{ cm}^{-2} \text{ s}^{-1}$ (Draine 1978).

3.3 Chemical network

The basis of our chemical network is the UMIST06 database (Woodall et al. 2007) as modified by Bruderer et al. (2009), except that we do not include X-ray chemistry. The cosmic-ray ionisation rate of H₂ is set to $5 \times 10^{-17} \text{ s}^{-1}$ (van der Tak et al. 2000b, Doty et al. 2004, Dalgarno 2006). The network contains 162 neutral species, 251 cations and six anions, built up out of 18 elements. We take a fully atomic composition as the starting point, except that hydrogen starts as H₂. Elemental abundances are adopted from Aikawa et al. (2008), with additional values from Bruderer et al. (2009). The latter are reduced by a factor of 100 from the original undepleted values to account for the incorporation of these heavy elements into the dust grains. Table 3.1 lists the elemental abundances relative to the total hydrogen nucleus density: $n_{\text{H}} = n(\text{H}) + 2n(\text{H}_2)$.

In order to set the chemical composition at the onset of collapse ($t = 0$), we evolve the initially atomic gas for a period of 1 Myr at $n_{\text{H}} = 8 \times 10^4 \text{ cm}^{-3}$ and $T_{\text{g}} = T_{\text{d}} = 10 \text{ K}$. The extinction during this pre-collapse phase is set to 100 mag to disable all photoprocesses, except for a minor contribution from cosmic-ray-induced photons. The resulting solid

and gas-phase abundances are consistent with those observed in pre-stellar cores (e.g., Bergin et al. 2000, di Francesco et al. 2007), and we take them as the initial condition for the collapse phase for all infalling parcels. In the remainder of this chapter, $t = 0$ always refers to the onset of collapse, following the 1 Myr pre-collapse phase here described.

3.3.1 Photodissociation and photoionisation

Photodissociation and photoionisation by UV radiation are important processes in the inner disk and inner envelope. Their rates are given by Eq. (3.2) using the extinction from Eq. (3.3). The extinction factor γ from Eq. (3.2) depends on the spectral shape of the radiation field, but it is not feasible to include this dependence in detail. Instead, we use the molecule-specific values tabulated for a 4000 K blackbody by van Dishoeck et al. (2006). The unshielded rates at the stellar surface (k_{ph}^*) are calculated with the cross sections from our freely available database, compiled from Lee (1984), van Dishoeck (1988), Roberge et al. (1991), Huebner et al. (1992), van Dishoeck et al. (2006) and van Hemert & van Dishoeck (2008).¹ The final output of this procedure consists of a 3D array (time and two spatial coordinates) with rate coefficients for each photoreaction. When computing the infall trajectories for individual parcels (step 4 in Fig. 3.1), we perform a linear interpolation to get the rate coefficients at all points along each trajectory.

The photodissociation of H_2 and CO requires some special treatment. Both processes occur exclusively through discrete absorption lines, so self-shielding plays an important role. The amount of shielding for H_2 is a function of the H_2 column density; for CO, it is a function of both the CO and the H_2 column density, because some CO lines are shielded by H_2 lines. The effective UV extinction from Eq. (3.3) can be converted to a total hydrogen column density through $A_V = \tau_{\text{UV,eff}}/3.02$ and $N_{\text{H}} = 1.59 \times 10^{21} A_V \text{ cm}^{-2}$ (Diplas & Savage 1994). Assuming that most hydrogen along each photon path is in molecular form, we simply set $N(\text{H}_2) = 0.5N_{\text{H}}$ to get the effective H_2 column density towards each spatial grid point. Equation (37) from Draine & Bertoldi (1996) then gives the amount of self-shielding for H_2 . The unshielded dissociation rate is computed according to the one-line approximation from van Dishoeck (1987), scaled so that the rate is $4.5 \times 10^{-11} \text{ s}^{-1}$ in the standard Draine (1978) field. For CO, we use the new shielding functions and cross sections from Chapter 5. Effective CO column densities are derived from the H_2 column densities by assuming an average $N(\text{CO})/N(\text{H}_2)$ ratio of 10^{-5} . Since both H_2 and CO require absorption of photons shortwards of 1100 \AA , their dissociation rates are greatly reduced at $T_* \approx 4000 \text{ K}$ compared with the Draine field (see also van Zadelhoff et al. 2003). During the collapse, this results in a zone where molecules like H_2O and CH_4 are photodissociated, while H_2 and CO remain intact (Sect. 3.5.1).

3.3.2 Gas-grain interactions

We allow all neutral species other than H, H_2 and the three noble gases to freeze out onto the dust according to Charnley et al. (2001). In cold, dense environments – such as our

¹ <http://www.strw.leidenuniv.nl/~ewine/photo>

model cores before the onset of collapse – observations show H₂O, CO and CO₂ to be the most abundant ices (Gibb et al. 2004, Boogert et al. 2008). Of these three, H₂O and CO₂ are mixed together, but most CO is found to reside in a separate layer (Pontoppidan et al. 2003, 2008b). As the temperature rises during the collapse, the ices evaporate according to their binding energy. However, the presence of non-volatile species like H₂O prevents the more volatile species like CO and CO₂ from evaporating entirely: some CO and CO₂ gets trapped in the H₂O ice (Sandford & Allamandola 1988, Hasegawa & Herbst 1993, Collings et al. 2004). In Chapter 2, we showed that this is required to explain the presence of CO in solar-system comets.

Incorporating ice trapping in a chemical network is a non-trivial task. The approach of Viti et al. (2004) was primarily designed to reproduce the temperature-programmed desorption (TPD) experiments from Collings et al. (2004). It works for astrophysical models where the temperature is increasing monotonically, but as shown in Chapter 2, the infalling material in our collapse model goes through periods of decreasing temperature as well. We could still apply the Viti et al. method to a “network” consisting of only CO and H₂O (Chapter 2), but applying it to the full network currently used consistently leads to numerical instabilities. In addition, recent experiments by Fayolle et al. (in prep.) show that the amount of trapping depends on the ice thickness and the volatile-to-H₂O mixing ratio. Collings et al. performed all their experiments at the same thickness and the same mixing ratio, so the amount of trapping in the model of Viti et al. is independent of these properties.

We ignore trapping for now and treat desorption of all species according to the zeroth-order rate equation

$$R_{\text{thdes}}(X) = 4\pi a_{\text{gr}}^2 n_{\text{gr}} f(X) \nu(X) \exp\left[-\frac{E_b(X)}{kT_d}\right], \quad (3.4)$$

where T_d is the dust temperature, $a_{\text{gr}} = 0.1 \mu\text{m}$ the typical grain radius, and $n_{\text{gr}} = 10^{-12} n_{\text{H}}$ the grain number density. The canonical pre-exponential factor, ν , for *first-order* desorption is $2 \times 10^{12} \text{ s}^{-1}$ (Sandford & Allamandola 1993). We multiply this by the number of binding sites per unit grain surface ($8 \times 10^{14} \text{ cm}^{-2}$ for our $0.1 \mu\text{m}$ grains, assuming 10^6 binding sites per grain) to get a *zeroth-order* pre-exponential factor of $2 \times 10^{27} \text{ cm}^{-2} \text{ s}^{-1}$. This value is used for all ice species, with the exception of the four listed in Table 3.2. The binding energies of species other than those four are set to the values tabulated by Sandford & Allamandola (1993) and Aikawa et al. (1997). Species for which the binding energy is unknown are assigned the binding energy *and* the pre-exponential factor of H₂O. The dimensionless factor f in Eq. (3.4) ensures that each species desorbs according to its abundance in the ice, and changes the overall desorption behaviour from zeroth to first order when there is less than one monolayer of ice:

$$f(X) = \frac{n_s(X)}{\max(n_{\text{ice}}, N_b n_{\text{gr}})}, \quad (3.5)$$

with $N_b = 10^6$ the typical number of binding sites per grain and n_{ice} the total number density (per unit volume of cloud or disk) of all ice species combined. We briefly discuss in Sect. 3.7.1 how our results might change if we include trapping.

Table 3.2 – Pre-exponential factors and binding energies for selected species in our network.

Species	ν (cm ⁻² s ⁻¹)	E_b/k (K)	Reference
H ₂ O	1×10^{30}	5773	Fraser et al. (2001)
CO	7×10^{26}	855	Bisschop et al. (2006)
N ₂	8×10^{25}	800	Bisschop et al. (2006)
O ₂	7×10^{26}	912	Acharyya et al. (2007)

In addition to thermal desorption, our model includes desorption induced by UV photons. Laboratory experiments on the photodesorption of H₂O, CO and CO₂ all produce a yield of $Y \approx 10^{-3}$ molecules per grain per incident UV photon (Westley et al. 1995a,b, Öberg et al. 2007, 2009b), while the yield for N₂ is an order of magnitude lower (Öberg et al. 2009c). Classical dynamics calculations predict a somewhat lower yield of 4×10^{-4} for H₂O (Andersson et al. 2006, Andersson & van Dishoeck 2008). The yields depend to some extent on properties like the dust temperature and the ice thickness, but this has little effect on chemical models (Öberg et al. 2009b). Hence, we take a constant yield of 10^{-3} for H₂O, CO and CO₂, and of 10^{-4} for N₂. For all other ice species in our network, whose photodesorption yields have not yet been determined experimentally or theoretically, we also take a yield of 10^{-3} . The photodesorption rate then becomes

$$R_{\text{phdes}}(X) = \pi a_{\text{gr}}^2 n_{\text{gr}} f(X) Y(X) F_{\text{UV}}^0 e^{-\tau_{\text{UV,eff}}}, \quad (3.6)$$

with f the same factor as for thermal desorption. The unattenuated UV flux (F_{UV}^0) and the effective UV extinction ($\tau_{\text{UV,eff}}$) follow from Eq. (3.3). Photodesorption occurs even in strongly shielded regions because of cosmic-ray-induced photons. We incorporate this effect by setting a lower limit of 10^4 cm⁻² s⁻¹ to F_{UV}^0 (Shen et al. 2004).

The chemical reactions in our model are not entirely limited to the gas phase. As usual, the network includes the grain-surface formation of H₂ (Black & van Dishoeck 1987). Inspired by Bergin et al. (2000) and Hollenbach et al. (2009), it also includes the hydrogenation of C to CH₄, N to NH₃, O to H₂O, and S to H₂S. The hydrogenation is done one H atom at a time and is always in competition with thermal and photon-induced desorption. The formation of CH₄, NH₃, H₂O and H₂S does not have to start with the respective atom freezing out. For instance, CH freezing out from the gas is also subject to hydrogenation on the grain surface. The rate of each hydrogenation step is taken to be the adsorption rate of H from the gas multiplied by the probability that the H atom finds the atom or molecule X to hydrogenate:

$$R_{\text{hydro}}(X) = \pi a_{\text{gr}}^2 n_{\text{gr}} n(\text{H}) f'(X) \sqrt{\frac{8kT_{\text{g}}}{\pi m_{\text{p}}}} \quad (3.7)$$

with T_{g} the gas temperature. The factor f' serves a similar purpose as the factor f in Eqs. (3.4) and (3.6). Since the hydrogenation is assumed to be near-instantaneous as soon as the H atom meets X before X desorbs, X is assumed to reside always near the top layer of the ice. Hence, we are not interested in the abundance of solid X relative to the

total amount of ice (as in f), but in its abundance relative to the other species that can be hydrogenated:

$$f'(X) = \frac{n_s(X)}{\max(n_{\text{hydro}}, N_b n_{\text{gr}})}, \quad (3.8)$$

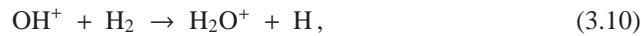
with n_{hydro} the sum of the solid abundances of the eleven species X : C, CH, CH₂, CH₃, N, NH, NH₂, O, OH, S and SH. The main effect of this hydrogenation scheme is to build up an ice mixture of simple saturated molecules during the pre-collapse phase, as is found observationally (Tielens et al. 1991, Gibb et al. 2004, Tafalla et al. 2004, van Dishoeck 2004, Öberg et al. 2008).

Grain-surface hydrogenation is known to occur for more species than just the eleven included here. For example, CO can be hydrogenated to form H₂CO and CH₃OH (Watanabe & Kouchi 2002, Fuchs et al. 2009). Grains also play an important role in the formation of more complex species (Garrod & Herbst 2006, Garrod et al. 2008, Öberg et al. 2009a). However, none of these reactions can be implemented as easily as the hydrogenation of C, N, O and S. In addition, the main focus of this chapter is on simple molecules whose abundances can be well explained with conventional gas-phase chemistry. Therefore, we are safe in ignoring the more complex grain-surface reactions.

3.4 Results from the pre-collapse phase

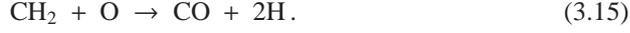
This section, together with the next two, contains the results from the gas-phase chemistry in our collapse model. First we briefly discuss what happens during the pre-collapse phase. The chemistry during the collapse is analysed in detail for one particular parcel in Sect. 3.5.1 and then generalised to others in Sect. 3.5.2. Finally, we compare the collapse chemistry to a static disk model in Sect. 3.6. The results in this section are all consistent with available observational constraints on pre-stellar cores (e.g., Bergin et al. 2000, di Francesco et al. 2007).

During the 1.0 Myr pre-collapse phase, the initially atomic oxygen gradually freezes out and is hydrogenated to H₂O ice. Meanwhile, H₂ is ionised by cosmic rays and the resulting H₂⁺ reacts with H₂ to give H₃⁺. This sets off the following chain of oxygen chemistry:

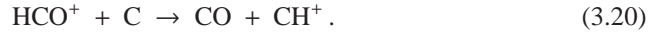
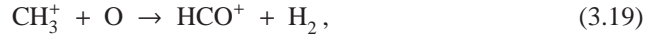
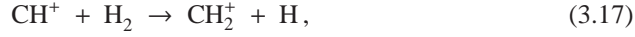
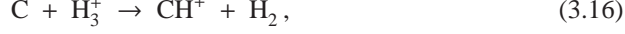


The O₂ thus produced freezes out for the most part. At the onset of collapse, the four major oxygen reservoirs are H₂O ice (44%), CO ice (34%), O₂ ice (16%) and NO ice (3%).

The oxygen chemistry is tied closely to the carbon chemistry through CO. It is initially formed in the gas phase from CH₂, which in turn is formed from atomic C:



Another early pathway from C to CO is powered by H₃⁺ and goes through an HCO⁺ intermediate:

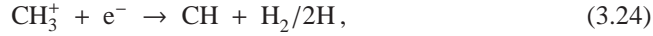


The formation of CO through these two pathways accounts for most of the pre-collapse processing of carbon: at $t = 0$, 82% of all carbon has been converted into CO, of which 97% has frozen out onto the grains. Most of the remaining carbon is present as CH₄ ice (14% of all C), formed from the rapid grain-surface hydrogenation of atomic C.

The initial nitrogen chemistry consists mostly of converting atomic N into NH₃, N₂ and NO. The first of these is formed on the grains after freeze-out of N, in the same way that H₂O and CH₄ are formed from adsorbed O and C. We find two pathways leading to N₂. The first one starts with the cosmic-ray dissociation of H₂:



The other pathway couples the nitrogen chemistry to the carbon chemistry. It starts with Reactions (3.16)–(3.18) to form CH₃⁺, followed by



The nitrogen chemistry is also tied to the oxygen chemistry, forming NO out of N and OH:



with OH formed by Reaction (3.12). Nearly all of the N₂ and NO formed during the pre-collapse phase freezes out. At $t = 0$, solid N₂, solid NH₃ and solid NO account for 41, 32 and 22% of all nitrogen.

3.5 Results from the collapse phase

3.5.1 One single parcel

The collapse-phase chemistry is run for the standard set of model parameters from Chapter 2: $M_0 = 1.0 M_\odot$, $c_s = 0.26 \text{ km s}^{-1}$ and $\Omega_0 = 10^{-14} \text{ s}^{-1}$. We first discuss the chemistry in detail for one particular infalling parcel of material. It starts near the edge of the cloud core, at 6710 AU from the center and 48.8° degrees from the z axis. Its trajectory terminates at $t = t_{\text{acc}}$ at $R = 6.3 \text{ AU}$ and $z = 2.4 \text{ AU}$, about 0.2 AU below the surface of the disk. The physical conditions encountered along the trajectory (χ , n_{H} , T_{d} and A_{V}) are plotted in Fig. 3.2. This figure also shows the abundances of the main oxygen-, carbon- and nitrogen-bearing species. The right four panels are regular plots as function of R : the coordinate along the midplane. The infall velocity of the parcel increases as it gets closer to the star, so the physical conditions and chemical abundances change ever more rapidly at later times. Hence, the left panel of each row is plotted as a function of $t_{\text{acc}} - t$: the time before the end of the collapse phase. In each individual panel, the parcel essentially moves from right to left.

A schematic overview of the parcel’s chemical evolution is presented in Fig. 3.3. It shows the infall trajectory of the parcel and the abundances of several species at four points along the trajectory. The physical conditions and the key reactions controlling those abundances are also listed. Most abundance changes for individual species are related to one specific chemical event, such as the evaporation of CO or the photodissociation of H_2O . The remainder of this subsection discusses the abundance profiles from Fig. 3.2 and explains them in the context of Fig. 3.3.

3.5.1.1 Oxygen chemistry

At the onset of collapse ($t = 0$), the main oxygen reservoir is solid H_2O at an abundance of 8×10^{-5} relative to n_{H} . The abundance remains constant until the parcel gets to point C in Fig. 3.3, where the temperature is high enough for the H_2O ice to evaporate. The parcel is now located close to the outflow wall, so the stellar UV field is only weakly attenuated ($A_{\text{V}} = 0.7 \text{ mag}$). Hence, the evaporating H_2O is immediately photodissociated into H and OH, which in turn is dissociated into O and a second H atom. At $R = 17 \text{ AU}$ (23 AU inside of point C), the dust temperature is 150 K and all solid H_2O is gone. Moving in further, the parcel enters the surface layers of the disk and is quickly shielded from the stellar radiation ($A_{\text{V}} = 10\text{--}20 \text{ mag}$). The temperature decreases at the same time to 114 K, allowing some H_2O ice to reform. The final abundance at t_{acc} (point D) is 4×10^{-8} .

The dissociative recombination of H_3O^+ (formed by Reactions (3.9)–(3.11)) initially maintains H_2O in the gas at an abundance of 7×10^{-8} . Following the sharp increase in the overall gas density at $t = 2.1 \times 10^5 \text{ yr}$ (Fig. 3.2), the freeze-out rate increases and the gas-phase H_2O abundance goes down to 3×10^{-10} at point A in Fig. 3.3. Moving on towards point B, the evaporation of O_2 from the grains enables a new H_2O formation route:





followed by Reactions (3.10) and (3.11) to give H_3O^+ , which recombines with an electron to give H_2O . The H_2O abundance thus increases to 3×10^{-9} at $R = 300$ AU. Farther in, at point C, solid H_2O comes off the grains as described above. However, photodissociation keeps the gas-phase abundance from growing higher than $\sim 10^{-7}$. Once all H_2O ice is gone at $R = 17$ AU, the gas-phase abundance can no longer be sustained at 10^{-7} and it drops to 3×10^{-12} . Some H_2O is eventually reformed as the parcel gets into the disk and is shielded from the stellar radiation, producing a final abundance of 2×10^{-11} relative to n_{H} .

Another main oxygen reservoir at $t = 0$ is solid O_2 , with an abundance of 1×10^{-5} . The corresponding gas-phase abundance is 4×10^{-7} . O_2 gradually continues to freeze out until it reaches a minimum gas-phase abundance of 3×10^{-10} just inside of point A. The temperature at that time is 19 K, enough for O_2 to slowly start evaporating thermally. The gas-phase abundance is up by a factor of ten by the time the dust temperature reaches 23 K, about halfway between points A and B. The evaporation is 99% complete as the parcel reaches $R = 460$ AU, about 140 AU inside of point B. The gas-phase abundance remains stable at 1×10^{-5} for the next few hundred years. Then, as the parcel gets closer to the outflow wall and into a region of lower extinction, the photodissociation of O_2 sets in and its abundance decreases to 2×10^{-8} at point C. The evaporation and photodissociation of H_2O at that point enhances the abundances of OH and O, which react with each other to replenish some O_2 . As soon as all the H_2O ice is gone, this O_2 production channel quickly disappears and the O_2 abundance drops to 1×10^{-11} . Finally, when the parcel enters the top of the disk, O_2 is no longer photodissociated and its abundance goes back up to 4×10^{-8} at point D.

The abundance of gas-phase OH starts at 3×10^{-7} . Its main formation pathway is initially the dissociative recombination of H_3O^+ (Reaction (3.12)), and its main destructors are O, N and H_3^+ . The increase in total density at 2.1×10^5 yr speeds up the destruction reactions, and the OH abundance drops to 3×10^{-10} at point B. The evaporation of solid OH then briefly increases the gas-phase abundance to 1×10^{-8} . When all of the OH has evaporated at $R = 300$ AU, the gas-phase abundance goes down again to 5×10^{-10} over the next 150 AU. As the parcel continues towards and past point C, the OH abundance is boosted to a maximum of 1×10^{-6} by the photodissociation of H_2O . The high abundance lasts only briefly, however. As the last of the H_2O evaporates and gets photodissociated, OH can no longer be formed as efficiently, and it is itself photodissociated. At the end of the collapse, the OH abundance is $\sim 10^{-14}$.

The fifth main oxygen-bearing species is atomic O itself. Its abundance is 7×10^{-7} at $t = 0$ and 1×10^{-4} at $t = t_{\text{acc}}$, accounting for respectively 0.4 and 56% of the total amount of free oxygen. Starting from $t = 0$, the O abundance remains constant during the first 2.0×10^5 yr of the collapse phase. The increasing overall density then speeds up the reactions with OH (forming O_2) and H_3^+ (forming OH^+), as well as the desorption onto the grains, and the O abundance decreases to a minimum of 2×10^{-8} just before point A. The abundance goes back up thanks to the evaporation of CO and, at point B, of O_2 and

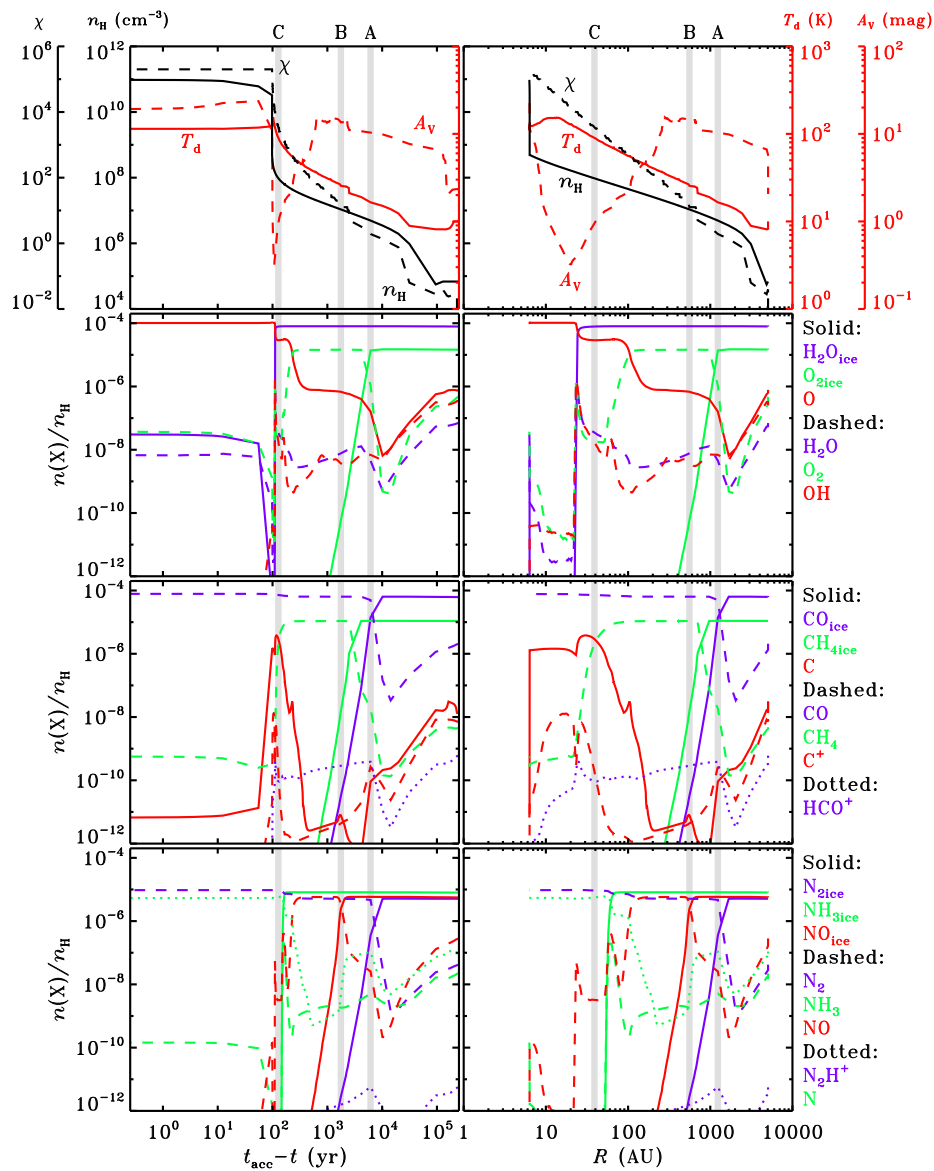


Figure 3.2 – Physical conditions (χ , n_{H} , T_{d} and A_{v}) and abundances of the main oxygen-, carbon- and nitrogen-bearing species for the single parcel from Sect. 3.5.1, as function of time before the end of the collapse (left) and as function of horizontal position (right). The grey bars correspond to the points A, B and C from Fig. 3.3. Note that in each panel, the parcel moves from right to left.

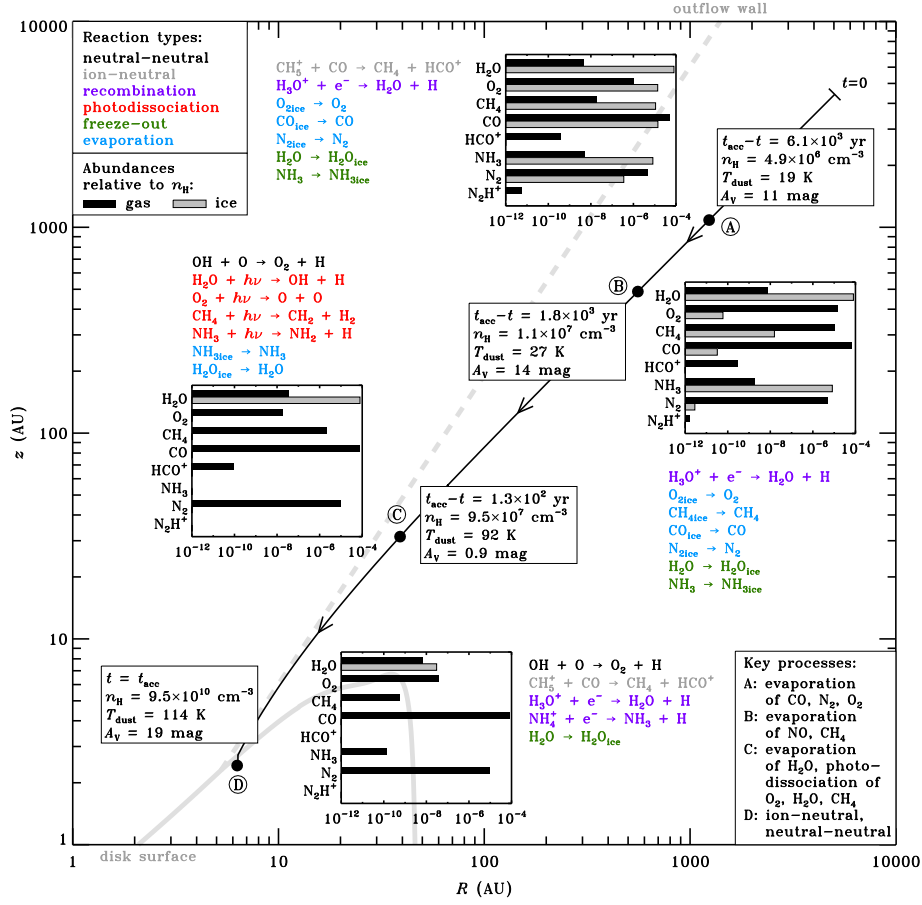


Figure 3.3 – Overview of the chemistry along the infall trajectory of the single parcel from Sect. 3.5.1. The solid and dashed grey lines denote the surface of the disk and the outflow wall, both at $t = t_{\text{acc}} = 2.52 \times 10^5$ yr. Physical conditions, abundances (black bars: gas; grey bars: ice) and key reactions are indicated at four points (A, B, C and D) along the trajectory. The key processes governing the overall chemistry at each point are listed in the bottom right. The type of each reaction is indicated by colour, as listed in the top left.

NO, with O formed from the following reactions:

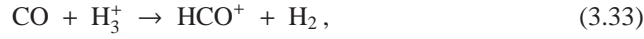


Heading on towards point C, the photodissociation of O_2 , NO and H_2O further drives up the amount of atomic O to the aforementioned final abundance of 1×10^{-4} .

3.5.1.2 Carbon chemistry

With solid and gas-phase abundances of 6×10^{-5} and 2×10^{-6} relative to n_H , CO is the main form of free carbon at the onset of collapse. CO is a very stable molecule and its chemistry is straightforward. The freeze-out process started during the pre-collapse phase continues up to $t = 2.4 \times 10^5$ yr, a few thousand years prior to reaching point A in Fig. 3.3, where the dust temperature of 18 K results in CO evaporating again. As the parcel continues its inward journey and is heated up further, all solid CO rapidly disappears and the gas-phase abundance goes up to 6×10^{-5} at point B. During the remaining part of the infall trajectory, the other main carbon-bearing species (e.g., C, CH, CH_2 , C_2 and HCO^+) are all largely converted into CO. At the end of the collapse (point D), 99.8% of the available carbon is locked up in CO. It also contains for 44% of the available oxygen.

The protonated form of CO, HCO^+ , starts the collapse phase at an abundance of 6×10^{-10} relative to n_H , or 3×10^{-4} relative to $n(CO)$. It is in equilibrium with CO via the two reactions



It is possible to derive a simple analytical estimate of the HCO^+ -CO abundance ratio. As shown by Lepp et al. (1987), the H_3^+ density does not depend strongly on the total gas density. We find $n(H_3^+) \approx 1 \times 10^{-4} \text{ cm}^{-3}$ along the entire trajectory, except for the part outside point A, where most CO is frozen out and therefore unable to destroy H_3^+ . If the cosmic-ray ionisation rate is changed from our current value of $5 \times 10^{-17} \text{ s}^{-1}$, the H_3^+ density would change proportionally. The electron abundance is roughly constant at 3×10^{-8} relative to n_H . Denoting the rate coefficients for Reactions (3.33) and (3.34) as k_f and k_b , and assuming HCO^+ and CO to be in mutual equilibrium, we get

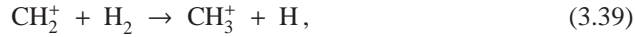
$$k_f n(CO) n(H_3^+) \approx k_b n(HCO^+) n(e^-). \quad (3.35)$$

Substituting $n(H_3^+) = 1 \times 10^{-4} \text{ cm}^{-3}$, $n(e^-) = 3 \times 10^{-8} n_H$, $k_f = 1.7 \times 10^{-9} \text{ cm}^3 \text{ s}^{-1}$ (Kim et al. 1975) and $k_b = 2.4 \times 10^{-7} (T_g/300 \text{ K})^{-0.69} \text{ cm}^3 \text{ s}^{-1}$ (Mitchell 1990), this rearranges to

$$\frac{n(HCO^+)}{n(CO)} \approx 5 \times 10^{-4} \left(\frac{n_H}{10^4 \text{ cm}^{-3}} \right)^{-1} \left(\frac{T_g}{30 \text{ K}} \right)^{0.69}. \quad (3.36)$$

The overall density increases by six orders of magnitude along the entire trajectory, while the temperature changes only by one, so the HCO^+ -CO abundance ratio should be roughly inversely proportional to the density. Our full chemical simulation confirms this relationship to within an order of magnitude throughout the collapse. However, the ratio comes out about a factor of ten larger than what is predicted by Eq. (3.36). The HCO^+ abundance reaches a final value at t_{acc} of 8×10^{-13} relative to n_H , or 1×10^{-8} relative to $n(CO)$.

The second most abundant carbon-bearing ice at the onset of collapse is CH_4 , at 1×10^{-5} with respect to n_{H} . The gas-phase abundance of CH_4 begins at 4×10^{-9} , about a factor of 2500 lower. At point A, the evaporation of CO provides the first increase in $x(\text{CH}_4)$ through a chain of reactions starting with the formation of C^+ from CO. The successive hydrogenation of C^+ produces CH_5^+ , which reacts with another CO molecule to form CH_4 :



The CH_4 ice evaporates at point B, bringing the gas-phase abundance up to 1×10^{-5} . So far, the abundances of CH_4 and CO are well coupled. The link is broken when the parcel reaches point C, where CH_4 is photodissociated, but CO is not. This difference arises from the fact that CO can only be dissociated by photons shortwards of 1076 Å, while CH_4 can be dissociated out to 1450 Å (Chapter 5). The 5300 K blackbody spectrum emitted by the protostar at this time is not powerful enough at short wavelengths to cause significant photodissociation of CO. CH_4 , on the other hand, is quickly destroyed. Its final abundance at point D is 6×10^{-10} .

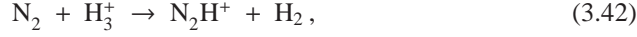
Neutral and ionised carbon show the same trends in their abundance profiles, with the former always more abundant by a few per cent to a few orders of magnitude. Both start the collapse phase at $\sim 10^{-8}$ relative to n_{H} . The increase in total density at 2.1×10^5 yr speeds up the destruction reactions (mainly by OH and O_2 for C and by OH and H_2 for C^+), so the abundances go down to $x(\text{C}) = 4 \times 10^{-10}$ and $x(\text{C}^+) = 5 \times 10^{-11}$ just outside point A. This is where CO begins to evaporate, and as a result, the C and C^+ abundances increase again. As the parcel continues to fall in towards point B, the evaporation of O_2 and NO and the increasing total density cause a second drop in C and C^+ . Once again, though, the drop is of a temporary nature. Moving on towards point C, the parcel gets exposed to the stellar UV field. The photodissociation of CH_4 leads – via intermediate CH, CH_2 or CH_3 – to neutral C, part of which is ionised to also increase the C^+ abundance. Finally, at point D, the photoprocesses no longer play a role, so the C and C^+ abundances go back down. Their final values relative to n_{H} are 7×10^{-12} and $\sim 10^{-14}$.

3.5.1.3 Nitrogen chemistry

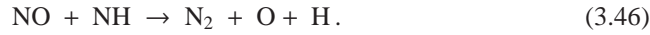
The most common nitrogen-bearing species at $t = 0$ is solid N_2 , with an abundance of 5×10^{-6} . The corresponding gas-phase abundance is 4×10^{-8} . The evolution of N_2 parallels that of CO, because they have similar binding energies and are both very stable molecules (Bisschop et al. 2006). N_2 continues to freeze out slowly until it gets near point A in Fig. 3.3, where the grain temperature of ~ 18 K causes all N_2 ice to evaporate. The

gas-phase N_2 remains intact along the rest of the infall trajectory and its final abundance is 1×10^{-5} , accounting for 77% of all nitrogen.

The parallels between CO and N_2 extend to their respective protonated forms, HCO^+ and N_2H^+ . An approximate equilibrium exists between N_2 and N_2H^+ through the reactions



The recombination of N_2H^+ also has a product channel of NH and N (Geppert et al. 2004), but this still results in N_2 being reformed through the additional reactions



Assuming that the recombination of N_2H^+ eventually results in the formation of N_2 most of the time, we repeat the method outlined for the HCO^+ -CO abundance ratio to derive the expected relationship

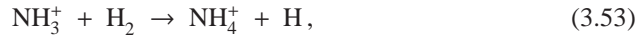
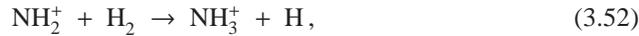
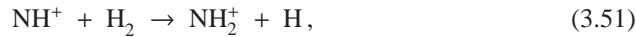
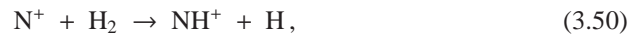
$$\frac{n(\text{N}_2\text{H}^+)}{n(\text{N}_2)} \approx 5 \times 10^{-4} \left(\frac{n_{\text{H}}}{10^4 \text{ cm}^{-3}} \right)^{-1} \left(\frac{T_{\text{g}}}{30 \text{ K}} \right)^{0.51}. \quad (3.47)$$

The results from the full chemical model show that within an order of magnitude, the N_2H^+ - N_2 abundance ratio is indeed inversely proportional to the overall density and follows the prediction from Eq. (3.47). In the previous subsection, the ratio between HCO^+ and CO was also found to be roughly inversely proportional to the density (Eq. (3.36)). An important difference between N_2H^+ and HCO^+ arises from the reaction



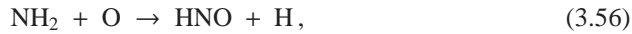
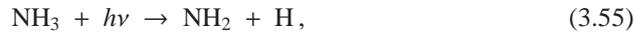
which transforms some N_2H^+ into HCO^+ as soon as CO evaporates. This reaction is responsible for the drop in N_2H^+ right after point A.

The second largest nitrogen reservoir at the onset of collapse is NH_3 , with solid and gas-phase abundances of 8×10^{-6} and 2×10^{-8} . The gas-phase abundance receives a short boost at point A due to the evaporation of N_2 , followed by



The binding energy of NH_3 is intermediate to that of O_2 and H_2O , so it evaporates between points B and C. Like H_2O , NH_3 is photodissociated upon evaporation. As the last of the NH_3 ice leaves the grains at $R = 50$ AU (10 AU outside of point C), the gas-phase reservoir is no longer replenished and $x(\text{NH}_3)$ drops to $\sim 10^{-14}$. Some NH_3 is eventually reformed as the parcel gets into the disk, and the final abundance at point D is 1×10^{-10} relative to n_{H} .

With an abundance of 6×10^{-6} , solid NO is the third major initial nitrogen reservoir. Gaseous NO is a factor of twenty less abundant at $t = 0$: 3×10^{-7} . The NO gas is gradually destroyed prior to reaching point A by continued freeze-out and reactions with H^+ and H_3^+ . It experiences a brief gain at point A from the evaporation of OH and its subsequent reaction with N to give NO and H. As the parcel continues to point B, the solid NO begins to evaporate and the gas-phase abundance rises to 6×10^{-6} . Photodissociation reactions then set in around $R = 100$ AU and the NO abundance goes back down to 6×10^{-9} . The evaporation and photodissociation of NH_3 cause a brief spike in the NO abundance through the reactions



The evaporation of the last of the NH_3 ice at $R = 50$ AU eliminates this channel and the NO gas abundance decreases to 3×10^{-9} at point C. NO is now mainly sustained by the reaction between OH and N. As described above, the OH abundance drops sharply at $R = 17$ AU, and the NO abundance follows suit. The final abundance at point D is $\sim 10^{-14}$.

The last nitrogen-bearing species from Fig. 3.2 is atomic N itself. It starts at an abundance of 1×10^{-7} and slowly freezes out to an abundance of 2×10^{-8} just before reaching point A. At point A, N_2 evaporates and is partially converted to N_2H^+ by Reaction (3.42). The dissociative recombination of N_2H^+ mostly reforms N_2 , but, as noted above, there is also a product channel of NH and N. The N abundance jumps back to 1×10^{-7} and remains nearly constant at that value until the parcel reaches point B, where NO evaporates and reacts with N to produce N_2 and O (Reaction (3.45)). This reduces $x(\text{N})$ to a minimum of 5×10^{-10} between points B and C. Moving in further, the parcel gets exposed to the stellar UV field, and NO and NH_3 are photodissociated to bring the N abundance to a final value of 5×10^{-6} relative to n_{H} . As such, it accounts for 22% of all nitrogen at the end of the collapse.

3.5.2 Other parcels

At the end of the collapse ($t = t_{\text{acc}}$), the parcel from Sect. 3.5.1 (hereafter called our reference parcel) is located at $R = 6.3$ AU and $z = 2.4$ AU, about 0.2 AU below the surface of the disk. As shown in Fig. 3.3, its trajectory passes close to the outflow wall, through a region of low extinction. This results in the photodissociation or photoionisation of

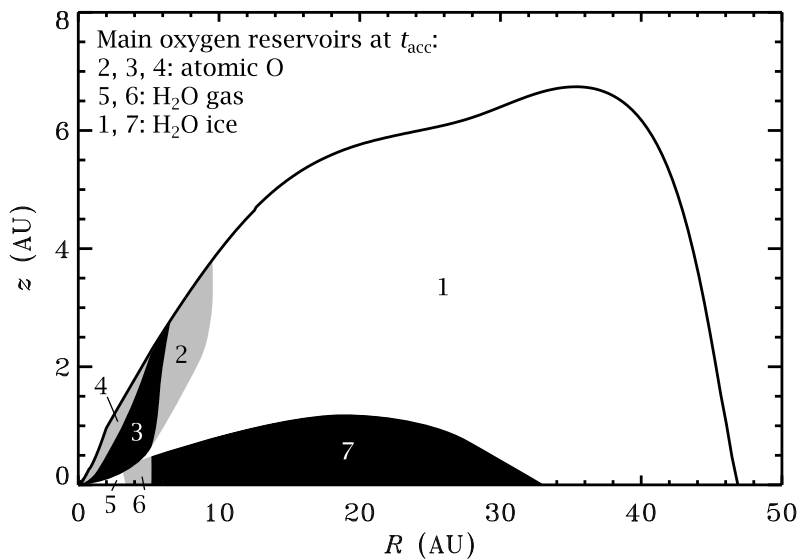


Figure 3.4 – Schematic view of the history of H₂O gas and ice throughout the disk. The main oxygen reservoir at t_{acc} is indicated for each zone; the histories are described in the text. Note the disproportionality of the R and z axes.

many species. At the same time, the parcel experiences dust temperatures of up to 150 K (Fig. 3.2), well above the evaporation temperature of H₂O and all other non-refractory species in our network. Material that ends up in other parts of the disk encounters different physical conditions during the collapse and therefore undergoes a different chemical evolution. This subsection shows how the absence or presence of some key chemical processes, related to certain physical conditions, affects the chemical history of the entire disk. Table 3.3 lists the abundances of selected species at four points in the disk at t_{acc} . Two-dimensional abundance profiles representing the entire disk’s chemical composition are presented in Sect. 3.6.

3.5.2.1 Oxygen chemistry

The main oxygen reservoir at the onset of collapse is H₂O ice (Sect. 3.4). Its abundance remains constant at 1×10^{-4} in our reference parcel until it gets to point C in Fig. 3.3, where it evaporates from the dust and is immediately photodissociated. When the parcel enters the disk, some H₂O is reformed to produce final gas-phase and solid abundances of $\sim 10^{-8}$ relative to n_{H} (Sect. 3.5.1.1).

Figure 3.4 shows the disk at t_{acc} , divided into seven zones according to different chemical evolutionary schemes for H₂O. The material in **zone 1** is the only material in the disk in which H₂O never evaporates during the collapse, because the temperature never gets high enough. The abundance is constant throughout zone 1 at t_{acc} at $\sim 1 \times 10^{-4}$ (see also

Table 3.3 – Abundances of selected species (relative to n_{H}) at $t = t_{\text{acc}}$ at four positions in the disk (two on the midplane, two at the surface).

Species	$R = 6 \text{ AU},$ $z = 0.0 \text{ AU}$	$R = 24 \text{ AU},$ $z = 0.0 \text{ AU}$	$R = 6 \text{ AU},$ $z = 2.0 \text{ AU}$	$R = 24 \text{ AU},$ $z = 6.0 \text{ AU}$
Zones ^a	7, 5, 8	7, 5, 8	2, 2, 5	1, 1, 2
H ₂ O	5(-7)	1(-12)	1(-8)	4(-9)
H ₂ O ice	1(-4)	1(-4)	7(-8)	8(-5)
O ₂	1(-6)	6(-8)	1(-7)	1(-5)
O ₂ ice	<1(-12)	<1(-12)	<1(-12)	<1(-12)
O	1(-6)	1(-6)	1(-4)	8(-7)
OH	2(-11)	<1(-12)	<1(-12)	9(-10)
CO	7(-5)	7(-5)	8(-5)	6(-5)
CO ice	<1(-12)	<1(-12)	<1(-12)	<1(-12)
CH ₄	7(-8)	1(-7)	2(-9)	1(-5)
CH ₄ ice	<1(-12)	<1(-12)	<1(-12)	<1(-12)
HCO ⁺	1(-12)	5(-11)	3(-12)	4(-12)
C	<1(-12)	<1(-12)	9(-12)	<1(-12)
C ⁺	<1(-12)	<1(-12)	<1(-12)	<1(-12)
N ₂	1(-5)	1(-5)	1(-5)	5(-6)
N ₂ ice	<1(-12)	<1(-12)	<1(-12)	<1(-12)
NH ₃	5(-10)	2(-10)	4(-10)	8(-6)
NH ₃ ice	<1(-12)	5(-9)	<1(-12)	5(-8)
NO	1(-8)	5(-10)	<1(-12)	6(-6)
NO ice	<1(-12)	<1(-12)	<1(-12)	<1(-12)
N ₂ H ⁺	<1(-12)	<1(-12)	<1(-12)	<1(-12)
N	5(-11)	1(-9)	5(-6)	4(-11)

^a The H₂O, CH₄ and NH₃ zones from Figs. 3.4, 3.7 and 3.9 in which each position is located.

Table 3.3). For the material ending up in the other six zones, H₂O evaporates at some point during the collapse phase. **Zone 2** contains our reference parcel, so its H₂O history has already been described. The total H₂O abundance (gas and ice combined) at t_{acc} is $\sim 10^{-8}$ at the top of zone 2 and $\sim 10^{-6}$ at the bottom. The gas-ice ratio goes from ~ 1 at the top to $\sim 10^{-6}$ at the bottom.

The H₂O history of **zone 3** is the same as that of zone 2, except that it finishes with a gas-ice ratio larger than unity. In both cases H₂O evaporates and is photodissociated prior to entering the disk (point C in Fig. 3.3), and it partially reforms inside the disk (point D). Parcels ending up in **zone 4** also undergo the evaporation and photodissociation of H₂O. However, the low extinction in zone 4 against the stellar UV radiation prevents H₂O from reforming like it does in zones 2 and 3.

The material in **zone 5** has a rather different history from that in zones 2–4 because it enters the disk at an earlier time: between $t = 1.3 \times 10^5$ and 2.3×10^5 yr. The material in

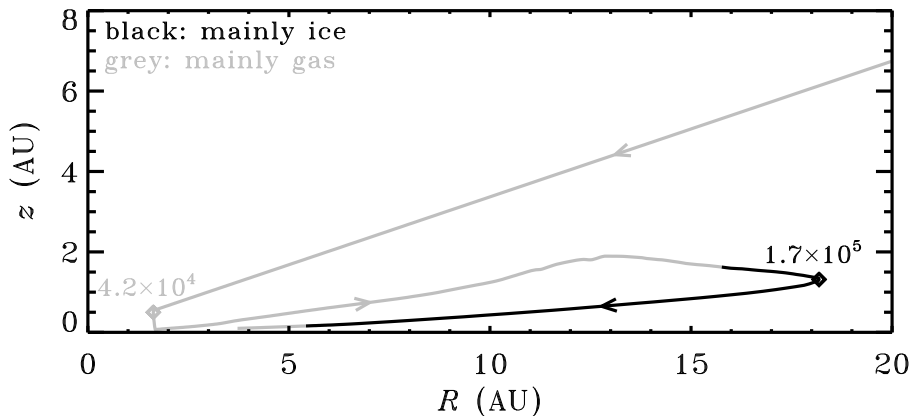


Figure 3.5 – Infall trajectory for a parcel ending up in zone 6 from Fig. 3.4, showing where H₂O is predominantly present as ice (black) or gas (grey). The two diamonds mark the time in years after the onset of collapse.

zones 2–4 all accretes after $t = 2.4 \times 10^5$ yr. The infall trajectories terminating in zone 5 do not pass close enough to the outflow wall or the inner disk surface for photoprocesses to play a role. All H₂O in zone 5 is in the gas phase at t_{acc} (abundance: 1×10^{-4}) because it lies inside the disk’s snow line. The evaporation of H₂O ice does not occur until the material actually crossed the snow line. Prior to that point, the temperature never gets high enough for H₂O to leave the grains.

Moving to **zones 6 and 7**, we find material that accretes even earlier: at $t = 4 \times 10^4$ yr. The disk at that time is only 2 AU large and several 100 K hot, so the ice mantles are completely removed. Instead of carrying on towards the star, this material remains part of the disk and is transported outwards to conserve angular momentum. Figure 3.5 shows the path followed by one particular parcel terminating in zone 6. As indicated by the initial grey portion of the line, H₂O has already evaporated (at $R = 25$ AU, not shown) before entering the young disk. The parcel cools down during the outward part of the trajectory and H₂O returns to the solid phase. At $t = 1.7 \times 10^5$ yr, the parcel starts moving inwards again and comes close enough to the protostar for H₂O to evaporate a second time. Other parcels ending up in zone 6 have similar trajectories and the same qualitative H₂O history. The parcels ending up in zone 7 also have H₂O evaporating during the initial infall and freezing out again during the outward part of the trajectory. However, they do not terminate close enough to the protostar for H₂O to desorb a second time. Therefore, most H₂O in zone 7 at t_{acc} is on the grains.

Our model is not the first one in which part of the disk contains H₂O that evaporated and reabsorbed. Lunine et al. (1991), Owen et al. (1992) and Owen & Bar-Nun (1993) argued that the accretion shock at the surface of the disk is strong enough for H₂O to evaporate. However, based on the model of Neufeld & Hollenbach (1994), we showed in

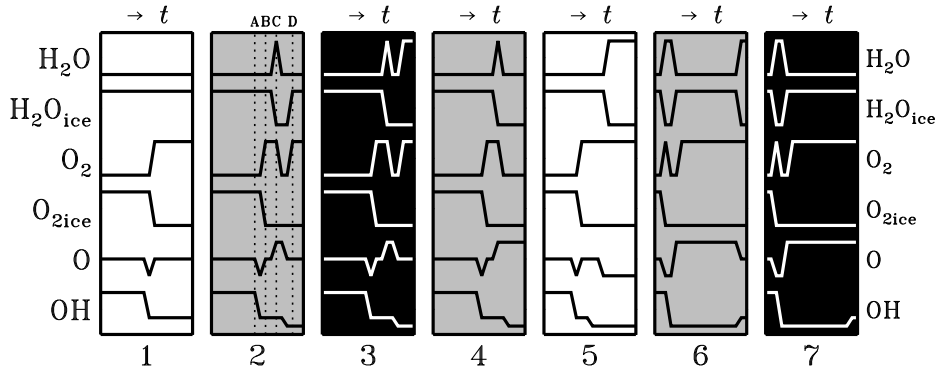


Figure 3.6 – Qualitative evolution of some abundances towards the seven zones with different H_2O histories from Fig. 3.4. The horizontal axes show the time (increasing from left to right) and are non-linear. The position of points A, B, C and D from Fig. 3.3 is indicated for zone 2, which contains our reference parcel.

Chapter 2 that most of the disk material does not pass through a shock that heats the dust to 100 K or more. Moreover, the material that does get shock-heated to that temperature accretes close enough to the star that the stellar radiation already heats it to more than 100 K. Hence, including the accretion shock explicitly in our model would at most result in minor changes to the chemistry.

As discussed in Sect. 3.5.1.1, H_2O controls part of the oxygen chemistry along the infall trajectory of our reference parcel, and it does the same thing for other parcels. Figure 3.6 presents a schematic view of the chemical evolution of six oxygen-bearing species towards each of the seven zones from Fig. 3.4. The abundances are indicated qualitatively as high, intermediate or low. The horizontal axes (time, increasing from left to right) are non-linear and only indicate the order in which various events take place.

For material ending up in **zone 1**, H_2O never evaporates, but O_2 does. OH is initially relatively abundant but most of it disappears when the overall density increases and the reactions with O, N and H_3^+ become faster. The abundance of atomic O experiences a drop at the same time, but it goes back up shortly after due to the evaporation of CO, O_2 and NO followed by Reactions (3.30)–(3.32). O_2 also evaporates on its way to **zones 2, 3 and 4** and because it passes through an area of low extinction, it is subsequently photodissociated. This, together with the photodissociation of OH and H_2O , causes an increase in the abundance of atomic O. Zones 2 and 3 are sufficiently shielded against the stellar UV field, so O_2 is reformed at the end of the trajectory. This does not happen in the less extinguished zone 4.

Material ending up in **zone 5** has the same qualitative history for gas-phase and solid O_2 as has material ending up in zone 1. The evolution of atomic O initially also shows the same pattern, but it experiences a second drop as the total density becomes even higher than it does for zone 1. The higher density also causes an additional drop in the

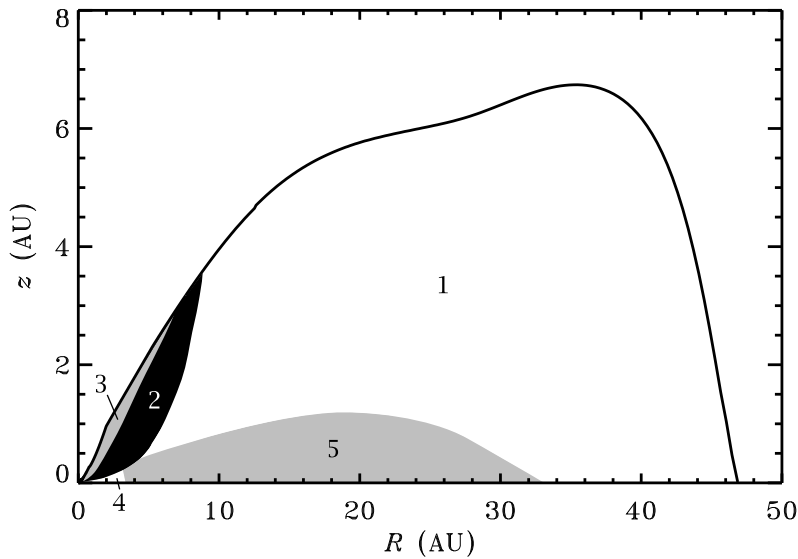


Figure 3.7 – As Fig. 3.4, but for CH_4 gas and ice. The main carbon reservoir at t_{acc} is CO gas throughout the disk.

OH abundance. En route towards **zones 6 and 7**, O_2 evaporates and is photodissociated during the early accretion onto the small disk. It is reformed during the outward part of the trajectory and survives until t_{acc} . Atomic O is also relatively abundant along most of the trajectory, although always one or two orders of magnitude below O_2 . In zone 6, the O abundance decreases at the end due to the reaction with evaporating CH_3 , producing H_2CO and H. Zone 7 does not get warm enough for CH_3 to evaporate, so O remains intact.

3.5.2.2 Carbon chemistry

The two main carbon reservoirs at the onset of collapse are CO ice and CH_4 ice (Sect. 3.4). Their binding energies are relatively low (855 and 1080 K), so they evaporate throughout the core soon after the collapse begins (Sect. 3.5.1.2). For our reference parcel, the main difference between the evolution of CO and CH_4 is the photodissociation of the latter (near point C in Fig. 3.3) while the former remains intact. Following our approach for H_2O , we can divide the disk at t_{acc} into several zones according to different chemical evolution scenarios for CO. However, the entire disk has the same qualitative CO history: apart from evaporating early on in the collapse phase, CO does not undergo any processing (cf. Chapter 2). Hence, we divide the disk according to the evolution of CH_4 instead (Fig. 3.7).

For material that ends up in **zone 1**, the only chemical process for CH_4 is the evaporation during the initial warm-up of the core. It is not photodissociated at any point

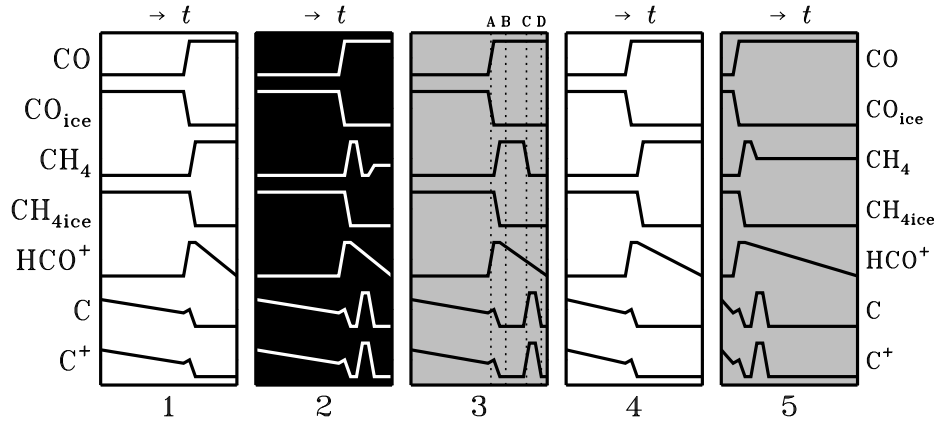


Figure 3.8 – As Fig. 3.6, but for the five zones with different CH_4 histories from Fig. 3.7.

during the collapse, nor does it freeze out again or react significantly with other species. Material ending up closer to the star, in **zones 2 and 3**, is sufficiently irradiated by the stellar UV/visible field for CH_4 to be photodissociated. Zone 3, which contains our reference parcel, is hardly shielded from the stellar flux and the final CH_4 abundance is only a few 10^{-10} . The stronger extinction towards zone 2 allows CH_4 to be reformed at a final abundance of 10^{-9} – 10^{-7} relative to n_{H} (Table 3.3).

Zone 4 contains material that accretes onto the disk several 10^4 yr earlier than does the material in zones 2 and 3. It always remains well shielded from the stellar radiation, so the only processing of CH_4 is the evaporation during the early parts of the collapse. The CH_4 history of zones 1 and 4 is thus qualitatively the same. The last zone, **zone 5**, consists of material that accretes around $t = 4 \times 10^4$ yr and is subsequently transported outwards to conserve angular momentum (Fig. 3.5). CH_4 in this material evaporates before entering the young disk and is photodissociated as it gets within a few AU of the protostar. The resulting atomic C is mostly converted into CO and remains in that form for the rest of the trajectory. Hence, even though the extinction decreases again when the parcel moves outwards, no CH_4 is reformed.

The evolution of the abundances of CH_4 gas and ice, CO gas and ice, HCO^+ , C and C^+ towards each of the five zones is plotted schematically in Fig. 3.8. As noted in Sect. 3.5.1.2, the HCO^+ abundance follows the CO abundance at a ratio that is roughly inversely proportional to the overall density. Hence, the HCO^+ evolution is qualitatively the same towards each zone: it reaches a maximum abundance of a few 10^{-10} when CO evaporates and gradually disappears as the density increases along the rest of the infall trajectories. The most complex history amongst these seven carbon-bearing species is found in C and C^+ . Towards all five zones, they are initially destroyed by reactions with H_2 , O_2 and OH. Some C and C^+ is reformed when CO evaporates (at point A in Fig. 3.3), but the subsequent evaporation of O_2 and OH causes the abundances to decrease again. En route

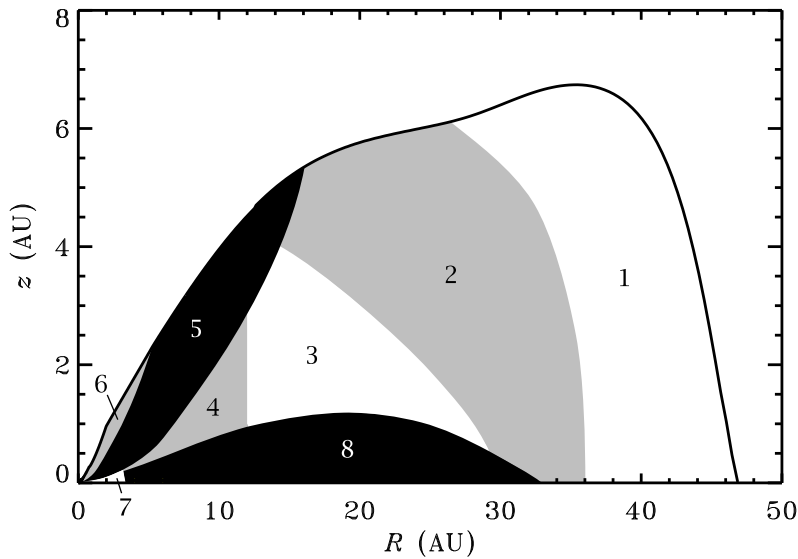


Figure 3.9 – As Fig. 3.4, but for NH_3 gas and ice. The main nitrogen reservoir at t_{acc} is N_2 gas throughout the disk.

to zones 2, 3 and 5, the photodissociation of CH_4 leads to a second increase in C and C^+ , followed by a third and final decrease when the parcel moves into a more shielded area.

3.5.2.3 Nitrogen chemistry

Most nitrogen at the onset of collapse is in the form of solid N_2 (41%), solid NH_3 (32%) and solid NO (22%). The evolution of N_2 during the collapse is the same as that of CO , except for a minor difference in the binding energy. Both species evaporate shortly after the collapse begins and remains in the gas phase throughout the rest of the simulation. Neither one is photodissociated because they need UV photons shortwards of 1100 \AA , and the protostar is not hot enough to provide those.

The evolution of NH_3 shows a lot more variation, as illustrated in Fig. 3.9. The disk at t_{acc} is divided into eight zones with different NH_3 histories. No processing occurs towards **zone 1**: the temperature never exceeds the 73 K required for NH_3 to evaporate, so it simply remains on the grains the whole time. Material ending up in **zone 2** does get heated above 73 K, so NH_3 evaporates. However, it freezes out again at the end of the trajectory because zone 2 itself is not warm enough to sustain gaseous NH_3 . The final solid NH_3 abundance in zones 1 and 2 is about 8×10^{-6} relative to n_{H} (Table 3.3).

NH_3 ending up in **zone 3** also evaporates from the grains just before entering the disk. It is then destroyed by UV photons (only for material that ends up inside of 15 AU in zone 3) and by HCO^+ (for all material in zone 3). Towards the end of the trajectory, some NH_3 is reformed from the dissociative recombination of NH_4^+ and this immediately freezes out

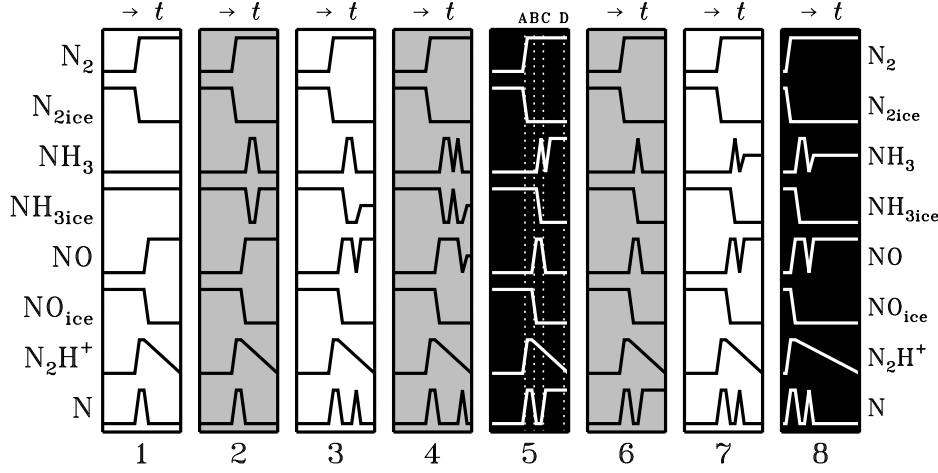


Figure 3.10 – As Fig. 3.6, but for the eight zones with different NH_3 histories from Fig. 3.9.

to produce a final solid NH_3 abundance of 10^{-10} – 10^{-8} . **Zone 4** has the same history, except that there is an additional adsorption-desorption cycle before the destruction by photons and HCO^+ .

Our standard parcel ends up in **zone 5**; its NH_3 evolution is mainly characterised by photodissociation above the disk and reformation inside it (Sect. 3.5.1.3). As is the case for zones 2–4, NH_3 evaporates when it gets to within about 200 AU of the star, halfway between points B and C in Fig. 3.3. It is immediately photodissociated, but some NH_3 is reformed once the material is shielded from the stellar radiation. The reformed NH_3 remains in the gas phase. No reformation takes place in the less extinguished **zone 6**, which otherwise has the same NH_3 history as does zone 5.

Material ending up in **zone 7** does not pass close enough to the outflow wall for NH_3 to be photodissociated upon evaporation. Instead, NH_3 is mainly destroyed by HCO^+ and attains a final abundance of $\sim 10^{-9}$. Lastly, **zone 8** contains again the material that accretes onto the disk at an early time and then moves outwards to conserve angular momentum. Its NH_3 evaporates already before reaching the disk and is subsequently dissociated by the stellar UV field. As the material moves away from the star and is shielded from its radiation, some NH_3 is reformed out of NH_4^+ to a final abundance of $\sim 10^{-10}$.

The abundances of N_2H^+ and atomic N are largely controlled by the evolution of N_2 and NH_3 , as shown schematically in Fig. 3.10. In all parcels, regardless of where they end up, N_2H^+ is mainly formed out of N_2 and H_3^+ , so its abundance goes up when N_2 evaporates shortly after the onset of collapse. It gradually disappears again as the collapse proceeds due to the inverse relationship between the overall density and the N_2H^+ - N_2 ratio (Eq. (3.47)). The atomic N abundance at the onset of collapse is 1×10^{-7} . It increases when N_2 evaporates and decreases again a short while later when NO evaporates (Sect. 3.5.1.3). For material that ends up in zones 1 and 2, the N abundance is mostly constant

for the rest of the collapse at a value of 10^{-13} (inner part of zone 2) to 10^{-10} (outer part of zone 1). Material that ends up in the other six zones is exposed to enough UV radiation for NO and NH_3 to be photodissociated, so there is a second increase in atomic N. Zones 3, 4, 7 and 8 are sufficiently shielded at t_{acc} to reform some or all NO and NH_3 , and the N abundance finishes low. Less reformation is possible in zones 5 and 6, so they have a relatively large amount of atomic N at the end of the collapse phase.

3.5.2.4 Mixing

Given the dynamical nature of circumstellar disks, the zonal distribution presented in the preceding subsections may offer too simple a picture of the chemical composition. For one thing, there are as yet no first principles calculations of the processes responsible for the viscous transport in disks. The radial velocity equation used in our model (see Chapter 4) is suitable as a zeroth-order description, but cannot explain important observational features like episodic accretion (Kenyon & Hartmann 1995, Evans et al. 2009). The radial velocity profile in real disks is probably much more chaotic, so there would be more mixing between adjacent zones. Hence, both the shapes and the locations of the zones are likely to be different from what is shown in Figs. 3.4, 3.7 and 3.9. A larger degree of mixing would also make the borders between the zones more diffuse than they are in our simple schematic representation. Nevertheless, the general picture from this section offers a plausible description of the chemical history towards different parts of the disk. Spectroscopic observations at AU resolution, for example with the upcoming Atacama Large Millimeter/submillimeter Array (ALMA), are required to determine to what extent this picture holds in reality.

3.6 Chemical history versus local chemistry

Section 3.5 contains many examples of abundances increasing or decreasing on short timescales of less than a hundred years (see, e.g., Fig. 3.2). It appears that the abundances respond rapidly to the changing physical conditions as material falls in supersonically through the inner envelope and accretes onto the disk. However, this does not necessarily mean that the abundances are always in equilibrium. In this section we explore the question as to whether the disk is in chemical equilibrium at the end of the collapse, or if its chemical composition is a non-equilibrium solution to the conditions encountered during the collapse phase. To that end, we evolve the chemistry for an additional 1 Myr beyond t_{acc} . We keep the density, temperature, UV flux and extinction constant at the values they have at t_{acc} , and we also keep all parcels of material at the same position. Clearly, this is a purely hypothetical scenario. In reality, the disk would change in many ways after t_{acc} : it spreads in size (see Chapter 4), the surface layers become more strongly irradiated, the temperature changes, the dust coagulates into planetesimals, gas is photoevaporated from the surface layers, and so on. All of these processes have the potential to affect the chemical composition. However, they would also interfere with our attempt to determine whether the disk is in chemical equilibrium at t_{acc} . This question is most easily addressed

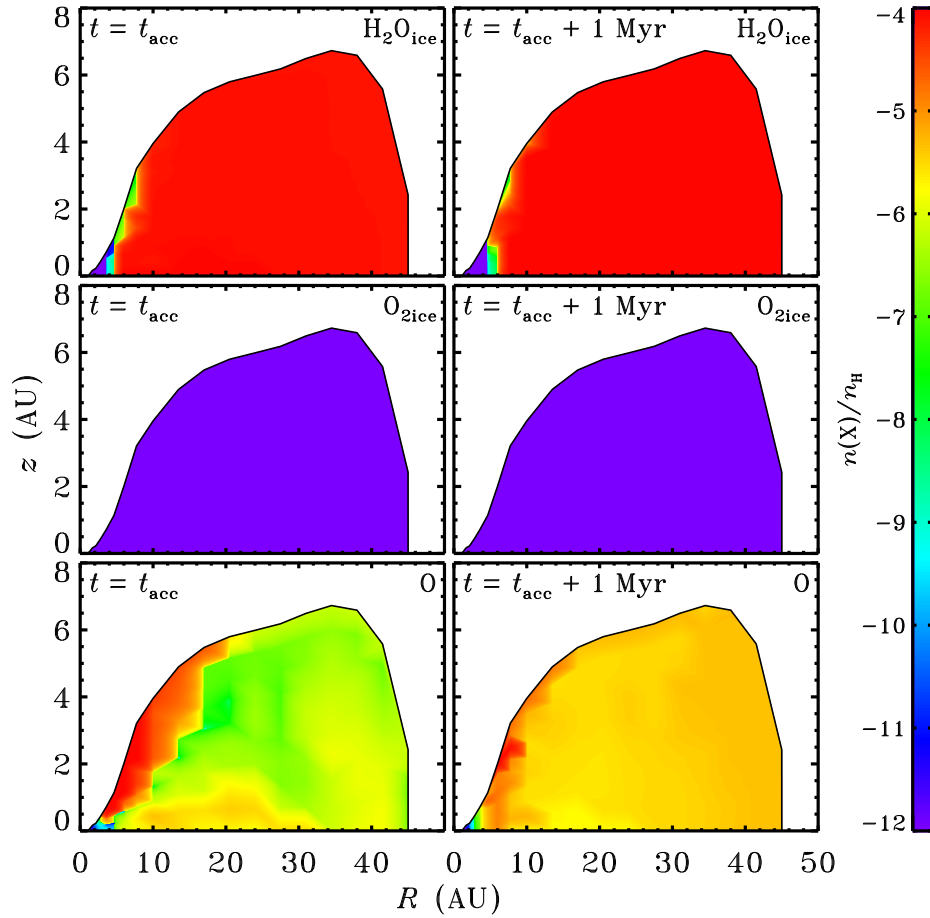


Figure 3.11 – Abundances of H₂O ice, O₂ ice and gaseous atomic O throughout the disk at the end of the collapse phase ($t = t_{\text{acc}}$) and after an additional static post-collapse phase of 1 Myr.

by evolving the chemistry for an additional period of time at constant conditions, hence we ignore all of the physical changes that would normally occur during the post-collapse phase.

The abundance profiles for the oxygen-, carbon- and nitrogen-bearing species from the previous sections are plotted in Figs. 3.11–3.17. In each case, the left panel corresponds to the end of the collapse phase ($t = t_{\text{acc}}$) and the right panel to the end of the static 1 Myr post-collapse phase ($t = t_{\text{acc}} + 1 \text{ Myr}$). Abundances of less than 10^{-12} are unreliable in our chemical code, so lower values are not plotted. Hence, the purple areas in the figures should be interpreted as upper limits.

The 21 species in Figs. 3.11–3.17 can be divided into two categories: those whose

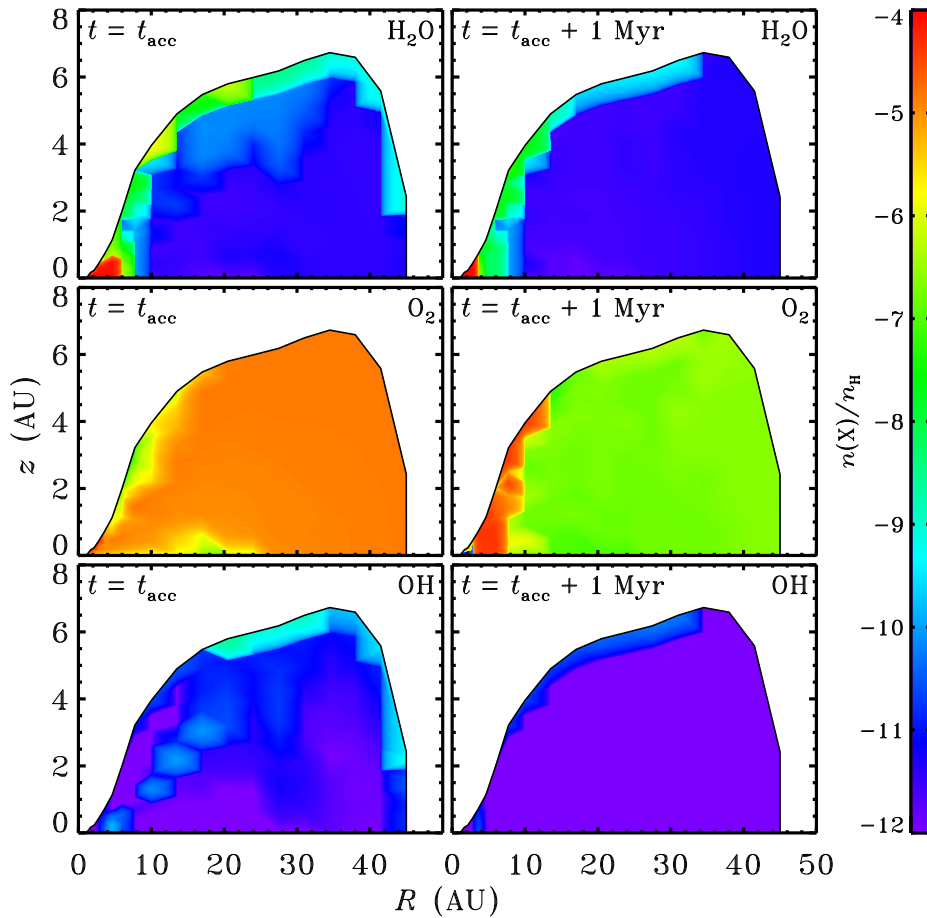


Figure 3.12 – As Fig. 3.11, for gaseous H_2O , O_2 and OH .

abundance profile changes during the post-collapse phase, and those whose abundance profile remains practically the same. Members of the former category are O_2 , OH , CH_4 , NH_3 and NO (all gaseous), NH_3 ice, and atomic O and N . The thirteen species in the “unchanged” category are H_2O gas and ice, O_2 ice, CO gas and ice, CH_4 ice, C , C^+ , N_2 gas and ice, NO ice, HCO^+ and N_2H^+ . The individual gas and ice abundances are summed in Fig. 3.18. The total H_2O , CO and N_2 abundances do not change significantly during the post-collapse phase, while the total O_2 , CH_4 , NH_3 and NO abundances change by more than two orders of magnitude in a fairly large part of the disk.

There are two areas in the disk where the abundances generally change the least: near the surface out to $R \approx 10$ AU, and at the midplane between ~ 5 and ~ 25 AU. In the first area, the chemistry is dominated by fast photoprocesses, allowing the abundances to reach

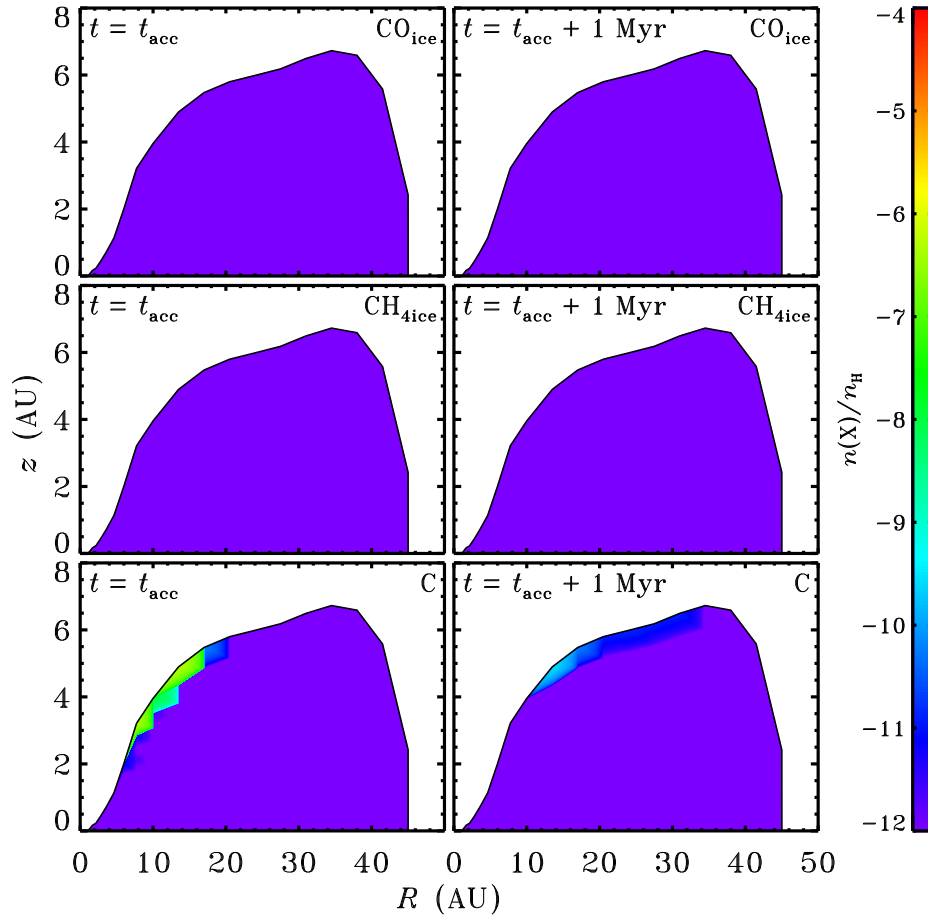


Figure 3.13 – As Fig. 3.11, for CO ice, CH₄ ice and gaseous atomic C.

equilibrium on short timescales. The second area, near the midplane, is the densest part of the disk and therefore has high collision frequencies and short chemical timescales. In addition, this part of the disk is populated by material that accreted at an early time (Fig. 3.5). The physical conditions it encountered during the rest of the collapse phase were relatively constant, aiding in establishing chemical equilibrium.

Outside these two “equilibrium areas”, one of the key processes during the post-collapse phase is the conversion of gas-phase oxygen-bearing species into H₂O, which subsequently freezes out. Because H₂O ice already is one the main oxygen reservoirs at t_{acc} throughout most of the disk, its abundance only increases by about 20% during the rest of the simulation (Fig. 3.11). These 20% represent 10% of the total oxygen budget and correspond to 2×10^{-5} oxygen nuclei per hydrogen nucleus. One of the species converted

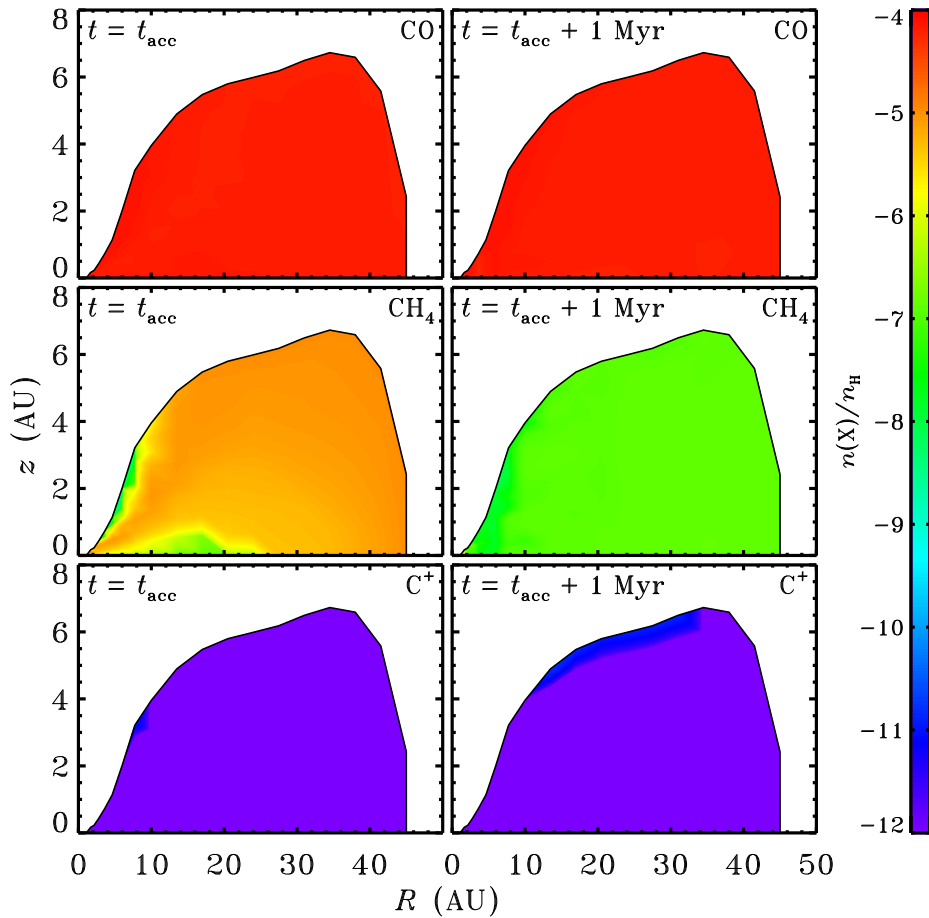
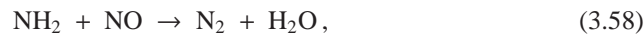


Figure 3.14 – As Fig. 3.11, for gaseous CO, CH₄ and C⁺.

into H₂O ice is NO, which reacts with NH₂ through



followed by adsorption of H₂O onto the dust. This reaction is responsible for the post-collapse destruction of gas-phase NO outside the two “equilibrium areas”, as well as for the small increase (~20%) in gas-phase N₂ (Fig. 3.16). NO is the main destructor of atomic N via



so the conversion of NO into H₂O also explains the increased N abundance from Fig.

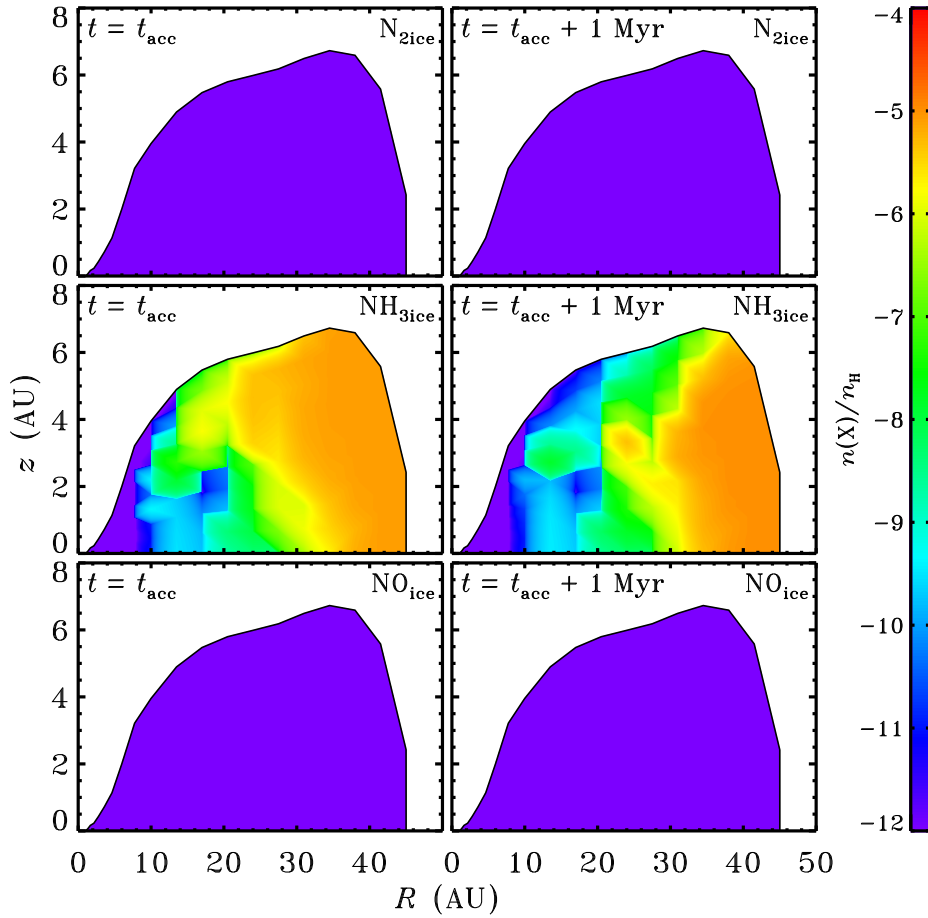


Figure 3.15 – As Fig. 3.11, for N_2 ice, NH_3 ice and NO ice.

3.17. The NH_2 required for Reaction (3.58) is formed from NH_3 :



The gas-phase reservoir of NH_3 is continuously fed by evaporation of NH_3 ice, so Reactions 3.60, 3.61 and 3.58 effectively transform all NH_3 into N_2 (Figs. 3.15 and 3.16).

Two other species that are destroyed in the post-collapse phase are gaseous O_2 and CH_4 (Figs. 3.12 and 3.14). O_2 is ionised by cosmic rays to produce O_2^+ , which then reacts with CH_4 :



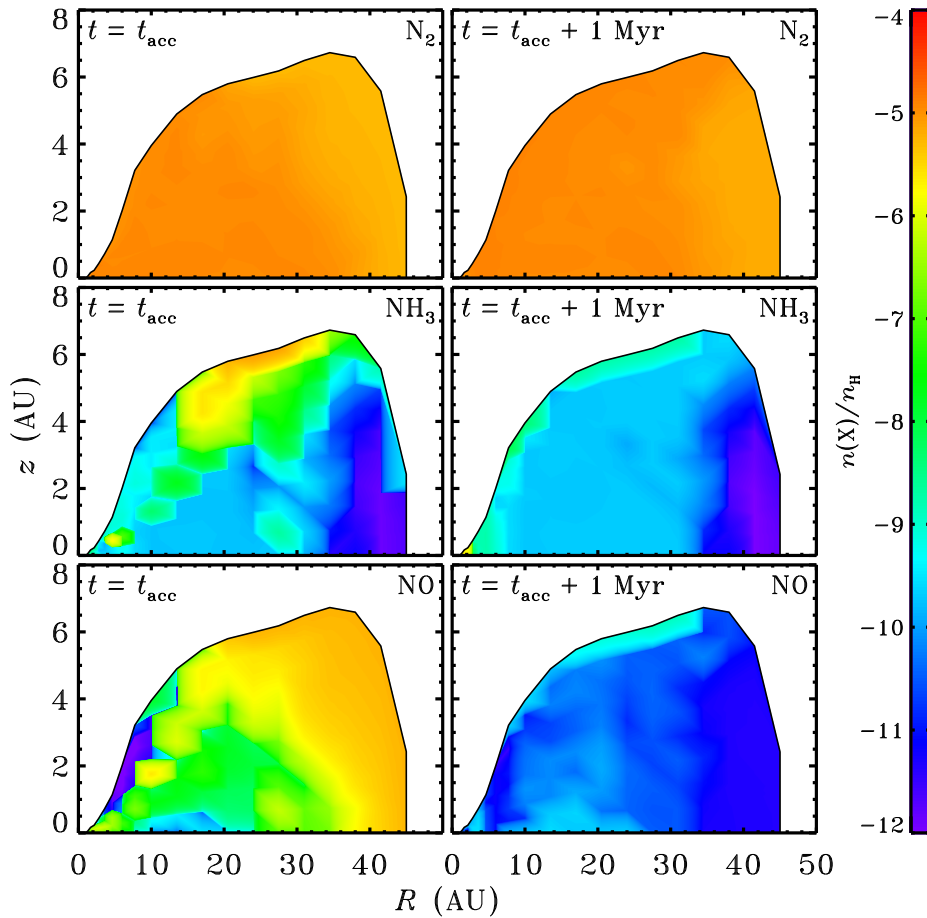
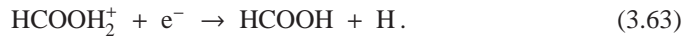


Figure 3.16 – As Fig. 3.11, for gaseous N_2 , NH_3 and NO .



The formic acid ($HCOOH$) freezes out, thus acting as a sink for both carbon and oxygen. At $t = t_{\text{acc}} + 1 \text{ Myr}$, the solid $HCOOH$ abundance is 3×10^{-6} , accounting for 3% of all oxygen and 4% of all carbon. The presence of such a sink is a common feature of disk chemistry models. Gas-phase species are processed by He^+ and H_3^+ until they form a species whose evaporation temperature is higher than the dust temperature. This is $HCOOH$ in our case, but it could also be carbon-chain molecules like C_2H_2 or C_3H_4 (Aikawa & Herbst 1999). Another important post-collapse sink reaction in our model is the freeze-out of HNO . At t_{acc} , OH is primarily formed by



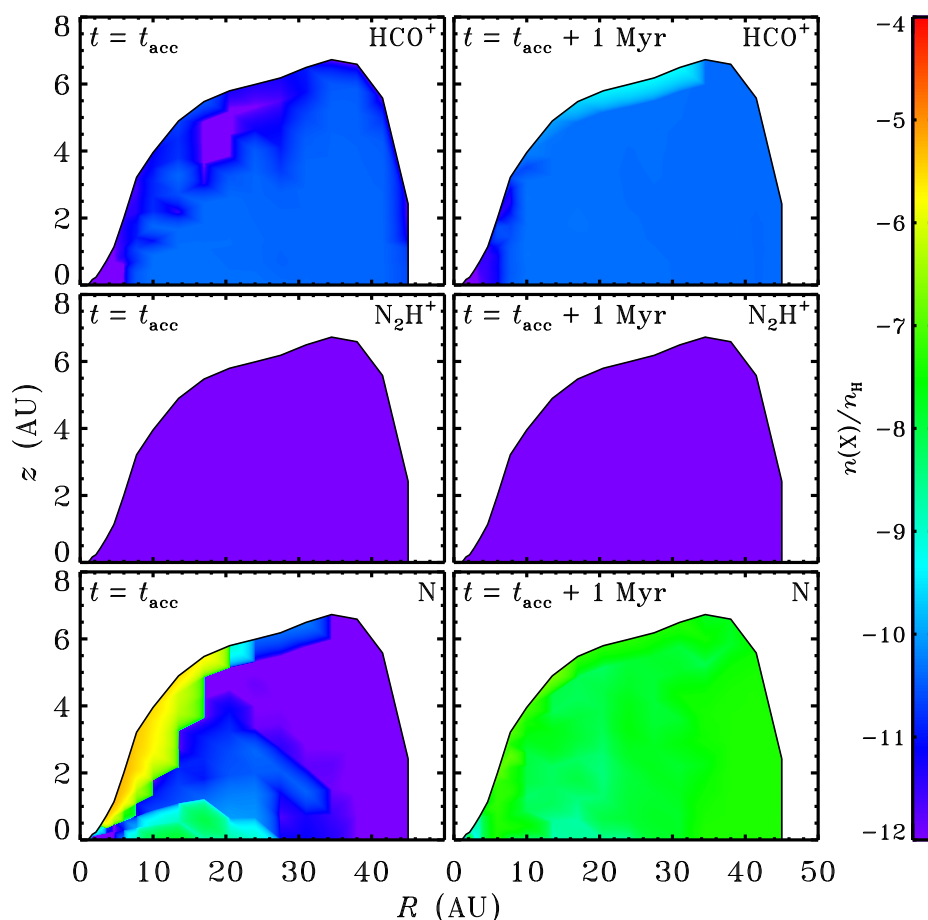


Figure 3.17 – As Fig. 3.11, for HCO⁺, N₂H⁺ and atomic N.

throughout most of the disk. This reaction is also one of the main destruction channels for atomic O. Hence, the gradual freeze-out of HNO after t_{acc} leads to a decrease in OH and an increase in O (Figs. 3.11 and 3.12). Also contributing to the higher O abundance is the fact that OH itself is an important destructor of O through Reaction (3.13).

The post-collapse chemistry described here is merely meant as an illustration of what might take place in a real circumstellar disk after the main accretion phase comes to an end. Depending on how the disk continues to evolve physically, other reactions may become more important than the ones listed above. However, it is clear that, in general, the disk is not in chemical equilibrium at t_{acc} . Figures 3.11–3.18 show several examples of abundances changing by a few orders of magnitude. Even the two “equilibrium areas” (near the surface out to 10 AU and from 5 to 25 AU at the midplane) are not truly in

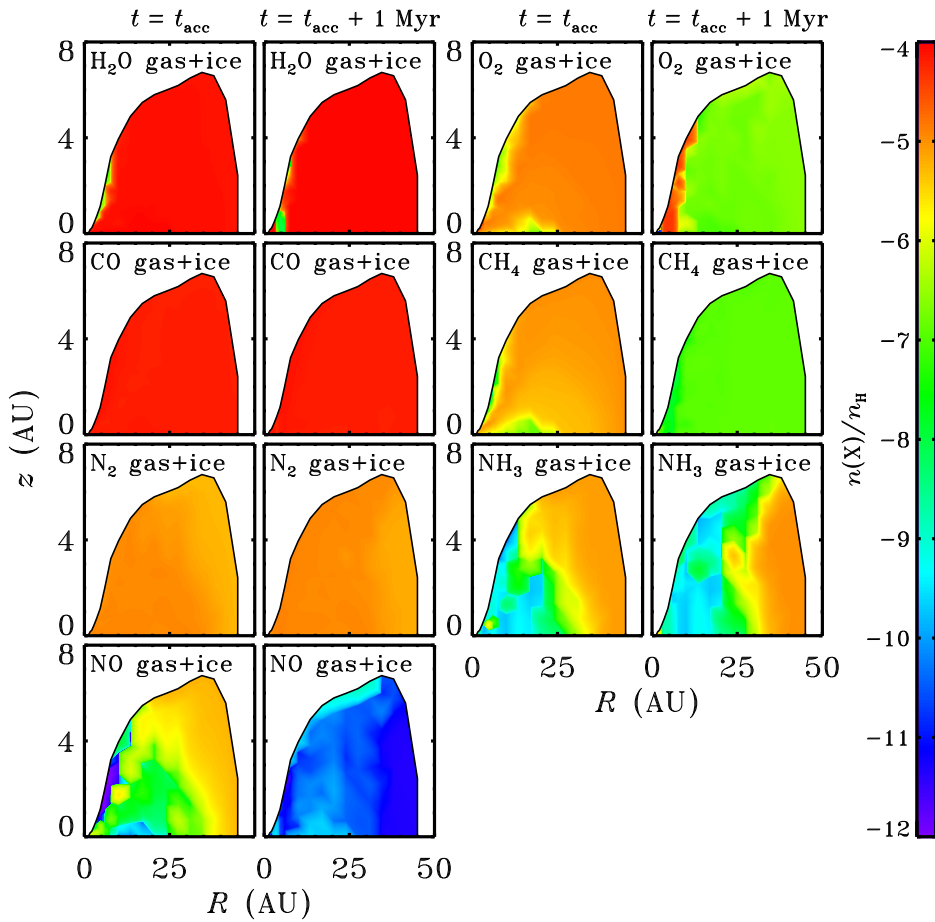


Figure 3.18 – Abundances of total H₂O, O₂, CO, CH₄, N₂, NH₃ and NO (gas and ice combined) throughout the disk at the end of the collapse phase ($t = t_{\text{acc}}$) and after an additional 1 Myr post-collapse phase ($t = t_{\text{acc}} + 1 \text{ Myr}$).

chemical equilibrium. For example, at 20 AU on the midplane, the abundances of solid HCOOH, C₂O, C₃O and CH₃OH increase by factors of 10 to 25 during the post-collapse processing.

As the disk evolves from the end of the collapse phase to a mature T Tauri disk, it spreads to larger radii. At the same time, material continues to accrete onto the protostar and gas is evaporated from the surface layers by the stellar radiation field. Altogether, this results in lower gas densities and longer chemical timescales. It is therefore unlikely that the gas will ever reach chemical equilibrium, as is indeed confirmed by chemical models

of T Tauri disks (Fegley 2000). Hence, some signature of the collapse-phase chemistry may survive into later stages. This will be the topic of a future publication.

3.7 Discussion

3.7.1 Caveats

Several caveats were mentioned in the preceding sections, which we briefly discuss here. First of all, our model does not calculate the gas temperature explicitly, but simply sets it equal to the dust temperature. This approach is valid for the interior of the disk (optically thick to UV radiation), but it breaks down in the surface layers and in the inner parts of the envelope (Kamp & Dullemond 2004, Jonkheid et al. 2004, Woitke et al. 2009). The chemistry in these optically thin regions is mostly controlled by photoprocesses and ion-molecule reactions, neither of which depend strongly on temperature. One aspect that would be affected is the gas-phase production of H₂O through the reactions



which have activation barriers of 3100 and 1700 K, respectively (Natarajan & Roth 1987, Oldenberg et al. 1992). Hence, our model probably underestimates the amount of H₂O in the surface of the disk. Other than that, increasing the gas temperature to a more realistic value is unlikely to change the chemical results. Taking a higher gas temperature might change some of the physical structure. It would increase the pressure of the disk, thus pushing up the disk-envelope boundary and possibly changing the spatial distribution of where material accretes onto the disk. However, the bulk of the accretion currently takes place in optically thick regions, so only a small fraction of the infalling material would be affected.

The shape of the stellar spectrum may have larger chemical consequences. Right now, we simply take a blackbody spectrum at the effective stellar temperature. Our star never gets hotter than 5800 K, which is not enough to produce UV photons of sufficient energy to dissociate CO and H₂. Many T Tauri stars are known to have a UV excess, which *would* allow CO and H₂ to be photodissociated. The stronger UV flux would also enhance the photoionisation of atomic C, probably resulting in C⁺ being the dominant form of carbon between points C and D in Fig. 3.3. In turn, this would boost the production of carbon-chain species like C₂S and HC₃N. As soon as the material enters the disk and is shielded again from the stellar radiation, C⁺ is converted back into C and CO. However, some signature of the temporary high C⁺ abundance may survive.

The third caveat has to do with the trapping of volatile species like CO, CH₄ and N₂ in the H₂O ice matrix. We argued in Chapter 2 that trapping of CO is required to explain the observed abundances of CO in comets. In the full chemical network from the current chapter, trapping of CO and other volatiles would reduce their gas-phase abundances, which in turn may reduce their controlling role in the gas-phase chemistry. However, the

trapped fraction is never more than 30% (Viti et al. 2004, Fayolle et al. in prep.; see also Gibb et al. 2004), so their gas-phase abundances remain high compared to other species. Hence, CO, CH₄, N₂, O₂ and NO are still likely to control the gas-phase chemistry even if they are partially trapped on the dust grains.

3.7.2 Comets

The chemical composition of cometary ices shows many similarities to that of sources in the ISM, but the abundance of a given species may vary by more than an order of magnitude from one comet to the next (A'Hearn et al. 1995, Bockelée-Morvan et al. 2000, 2004, Schöier et al. 2002, Ehrenfreund et al. 2004, Disanti & Mumma 2008). Both points are illustrated in Fig. 3.19, where the abundances of several species in the comets 1P/Halley, C/1995 O1 (Hale-Bopp), C/1996 B2 (Hyakutake), C/1999 H1 (Lee), C/1999 S4 (LINEAR) and 153P/Ikeya-Zhang are plotted against the abundances in the embedded protostar IRAS 16293–2422 (warm inner envelope), the bipolar outflow L1157, and the four hot cores W3(H₂O), G34.3+0.15, Orion HC and Orion CR. Each point is characterised by the mean value from the available sources (the diamonds) and the total spread in measurements (the error bars). Uncertainties from individual measurements are not shown. The dotted line marks the theoretical relationship where the ISM abundances equal the cometary abundances. The data generally follow this line, suggesting that the material ending up in comets underwent little chemical processing from the ISM. However, the plot also shows variations of at least an order of magnitude in the cometary abundances for CO, H₂CO, CH₃OH, HNC, H₂S and S₂, as well as smaller variations for other species. These different chemical compositions may be explained by assuming that the comets were formed in different parts of the solar nebula. If that is indeed the case, there must have been some degree of chemical processing between the ISM and the cometary nuclei. Another point to note is that the elemental nitrogen abundance in comets is at least a factor of three lower than that in the ISM (Wyckoff et al. 1991, Jessberger & Kissel 1991, Bockelée-Morvan et al. 2000). Although the reason for this deficiency remains unclear, it does also point at a certain degree of chemical processing.

Comets are thought to have formed at the gravitational midplane of the circumsolar disk, between 5 and 30 AU from the young Sun (Bockelée-Morvan et al. 2004, Kobayashi et al. 2007). In our model disk, the 5–30 AU range happens to be almost exactly the area containing material that accreted at an early time (4×10^4 yr after the onset of collapse) and stayed in the disk for the remainder of the collapse phase (Fig. 3.5). As discussed in Sect. 3.5.2, this material undergoes a larger degree of chemical processing than any other material in the disk, due to its accreting close to the star. If comets are entirely formed out of such material, it is hard to reconcile the large degree of processing with the observed similarities between cometary and ISM abundances. It requires that either the abundances of observed cometary species actually remain constant throughout the collapse, or that they return to ISM values after the material reaches its final position. In this section we argue that neither scenario is likely to be true, and that the similarity between cometary and ISM abundances in fact results from mixing unprocessed material from other parts of the disk into the comet-forming zone.

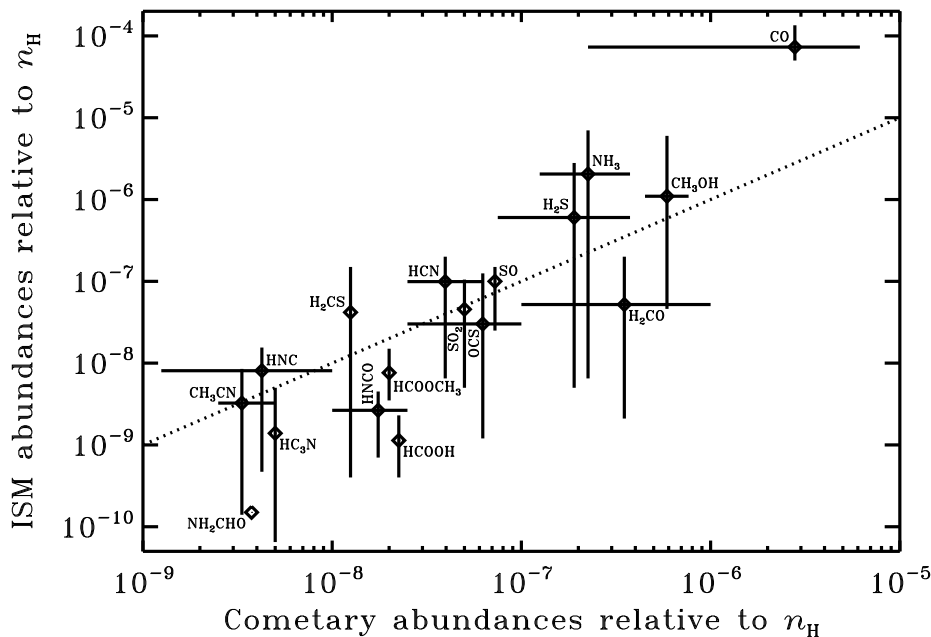


Figure 3.19 – Molecular abundances in comets (Halley, Hale-Bopp, Hyakutake, Lee, C/1999 S4 and Ikeya-Zhang) compared to those in ISM sources (IRAS 16293–2422 (warm inner envelope), L1157, W3(H₂O), G34.3+0.15, Orion Hot Core and Orion Compact Ridge) as provided by Bockelée-Morvan et al. (2000, 2004) and Schöier et al. (2002). The error bars indicate the spread between sources; errors from individual measurements are not included. The dashed line represents a one-to-one correspondence between cometary and ISM abundances and is not a fit to the data.

Figures 3.20 and 3.21 compare the cometary abundances from Bockelée-Morvan et al. (2000, 2004) to the abundances from our model at the end of the collapse phase. The horizontal error bars show again the spread in abundances between individual comets. In Fig. 3.20, the vertical error bars show the spread across our entire disk; in Fig. 3.21, they show the spread in the 5–30 AU region at the midplane. For all species, the gas and ice abundances from the model are summed and displayed as one.

The disk-wide abundances tend to cluster around the theoretical one-to-one relationship indicated by the dotted line. Two notable exceptions are CH₃OH and HCOOCH₃. Both of them are known to require grain-surface chemistry to get the correct abundance, and this is not included in our model. The spread in model abundances is at least six orders of magnitude, but given the wide range of physical conditions that are sampled, such a large spread is to be expected. The 5–30 AU abundances from Fig. 3.21 show less variation – between one and four orders of magnitude – but still take on a wider range of values than do the cometary abundances. More importantly, the 5–30 AU data show no

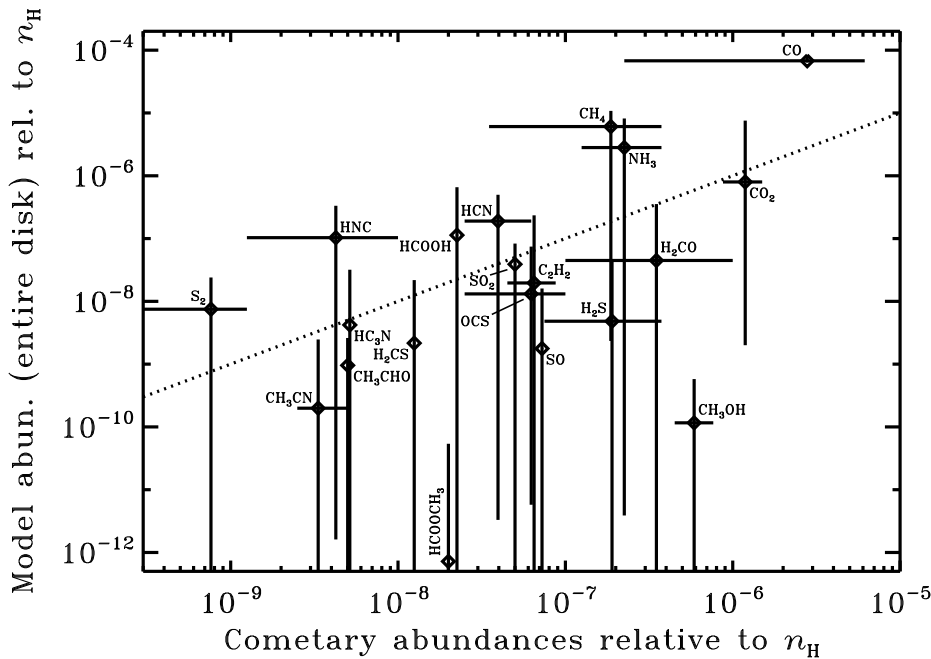


Figure 3.20 – As Fig. 3.19, but comparing the cometary abundances to those in our model at $t = t_{\text{acc}}$. The vertical black lines indicate the spread across the entire disk. For all species, the gas and ice abundances from the model are summed and displayed as one.

correlation with the comet data. There is no indication from Sect. 3.6 that post-collapse processing brings the abundances back to near-ISM values. Hence, the midplane material between 5 and 30 AU in our model does not appear to be analogous to the material from which the solar-system comets originated.

How plausible is the large degree of chemical processing for material that ends up in the comet-forming zone? The amount of processing is a direct result of the range of physical conditions encountered along a given infall trajectory, which in turn depends mostly on how close to the protostar the trajectory gets. We intentionally keep the physics in our model as simple as possible, so a trajectory like the one drawn in Fig. 3.5 may not be fully realistic. On the other hand, the back-and-forth motion results from the well-known concept of conservation of angular momentum. As the inner parts of the disk accrete onto the star, the outer parts must move out to maintain the overall angular momentum. They may be pushed inwards again at a later time if a sufficient amount of mass is accreted from the envelope at larger radii. This happens in our simple model, but also in the hydrodynamical simulations of Brinch et al. (2008a,b).

If we accept the possibility of back-and-forth motion, the question remains as to how close to the star the material gets before moving out to colder parts of the disk. Our

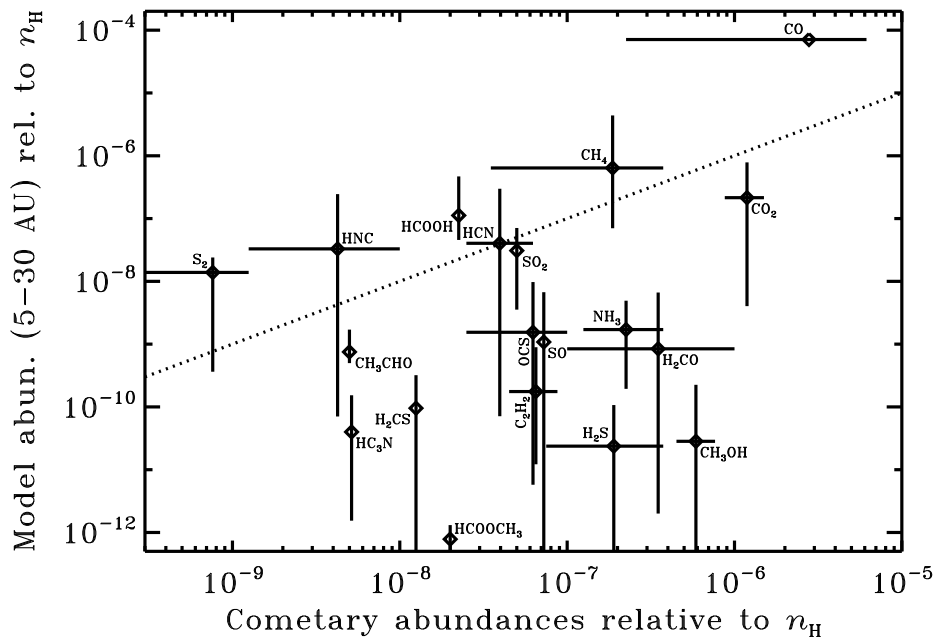


Figure 3.21 – As Fig. 3.19, but comparing the cometary abundances to those in our model at $t = t_{acc}$. The vertical black lines indicate the spread in the comet-forming region: at the midplane, between 5 and 30 AU from the star.

new solution to the problem of sub-Keplerian accretion (see Chapter 4) results in radial velocity profiles that are different from the ones in Chapter 2. With the old profiles, all material that accretes inside of the snow line always remains inside of the snow line. We therefore did not get any material in the comet-forming zone in which H_2O had evaporated and reabsorbed onto the grains. As shown in Fig. 3.5, we do get this with our current model. However, it is not a universal outcome for all initial physical conditions. If we run the new model on the parameter grid from Chapter 2, there are three cases (out of eight) where material accretes inside of the snow line and then moves out beyond it. The dividing factor appears to be a ratio of 0.2 between the disk mass at $t = t_{acc}$ and the core mass at $t = 0$. For larger ratios, material that accretes inside of the snow line always remains there.

The presence of crystalline silicate dust in disks provides a strong argument in favour of trajectories like the one from Fig. 3.5. Observations show crystalline fractions at $R \approx 10$ AU that are significantly larger than what is found in the ISM (Bouwman et al. 2001, 2008, van Boekel et al. 2005). Amorphous silicates can be crystallised by thermal annealing if they get close enough to the star to be heated to at least 800 K. The disk is less than 100 K at 10 AU, so the crystalline dust is formed at smaller radii than where it is ob-

served. We argue in Chapter 4 that the need to conserve angular momentum results in the outward transport of enough material to explain the observed crystalline fractions at 10 AU. Moreover, crystalline dust has been detected in several comets, including 1P/Halley, C/1995 01 (Hale-Bopp) and 81P/Wild 2, providing direct evidence that part of their constituent material has been heated to temperatures well above the evaporation temperature of H₂O (Bregman et al. 1987, Campins & Ryan 1989, Wooden et al. 1999, Keller et al. 2006).

If Halley, Hale-Bopp, Wild 2 and other comets contain crystalline silicates, they must also contain ices that underwent a large degree of chemical processing. Likewise, the presence of amorphous silicates in comets is indicative of chemically unprocessed ices. Hence, we conclude that the material from which comets are formed must be of mixed origins: some of it accreted close to the star and was heated to high temperatures, while another part accreted at larger radii and remained cold. Within the context of our model, this requires that material from beyond $R = 30$ AU is radially mixed into the comet-forming zone between 5 and 30 AU. Alternatively, vertical mixing may bring relatively pristine material from higher altitudes down into the comet-forming zone at the mid-plane. As for the chemical variations between individual comets, our model shows many examples of abundances changing with position or with time. The variations can thus be explained by having the comets form at different positions in the circumsolar disk, or at different times during the disk's lifetime.

3.7.3 Collapse models: 1D versus 2D

The model presented here and in Chapter 2 is the first one to follow the entire core collapse and disk formation process in two spatial dimensions. Some of our conclusions were previously drawn in other studies on the basis of 1D models. For example, it was already known that the collapse-phase chemistry is dominated by a few key chemical processes and that the collapsing core never attains chemical equilibrium (e.g., Doty et al. 2002, 2004, Rodgers & Charnley 2003, Lee et al. 2004, Aikawa et al. 2008). The 1D models cannot follow the infalling material all the way into the disk, so the zones with different chemical histories from Sect. 3.6 appear for the first time in our 2D model. Another new feature is the back-and-forth motion inside the disk, allowing material to accrete inside of the snow line and then move out to colder regions. This offers new insights into the chemical origin of cometary nuclei.

3.8 Conclusions

This chapter describes the two-dimensional chemical evolution during the collapse of a molecular cloud core to form a low-mass star and a circumstellar disk. The model is the same as used in Chapter 2, except for the improvements described in Chapter 4. The density and velocity profiles throughout the core and the disk are computed semi-analytically. We use a full radiative transfer method for the dust temperature and the radiation field. The chemistry is computed with a full gas-phase network, including adsorption and des-

orption from dust grains, as well as basic hydrogenation reactions on the grain surfaces. Starting from realistic initial conditions, we evolve the chemistry in parcels of material terminating at a range of positions in the disk. Special attention is paid to parcels ending up in the comet-forming zone. The conclusions from this chapter are as follows:

- The chemistry during the collapse phase is controlled by a small number of key chemical processes, each of which is activated by changes in the physical conditions. The evaporation of CO, CH₄ and H₂O at approximately 18, 22 and 100 K is one set of such key processes. Another set is the photodissociation of CH₄ and H₂O (Sect. 3.5.1).
- At the end of the collapse phase, the disk can be divided into several zones with different chemical histories. The different histories are related to the presence or absence of the aforementioned key processes along various infall trajectories. Spectroscopic observations at high spatial resolution are required to determine whether this zonal division really exists, or if it is smoothed out by mixing (Sect. 3.5.2).
- Part of the material that accretes onto the disk at early times is transported outwards to conserve angular momentum, and may remain in the disk for the rest of the collapse phase. It is heated to well above 100 K as it accretes close to the star, so H₂O and all other non-refractory species evaporate from the grains. They freeze out again when the material cools down during the subsequent outward transport (Sect. 3.5.2).
- When the chemistry is evolved for an additional 1 Myr at fixed physical conditions after the end of the collapse phase, the abundances of most species change throughout the disk. Hence, the disk is not in chemical equilibrium at the end of the collapse. Instead, its chemical composition is mainly a result of the physical conditions during the collapse phase. A robust feature of the post-collapse processing is the partial conversion of gaseous CH₄ into larger species like HCOOH or C₃H₄, which subsequently freeze out because of their higher binding energy (Sect. 3.6).
- Material that ends up in the comet-forming zone undergoes a large degree of chemical processing, including the evaporation and readsorption of H₂O and species trapped in the H₂O ice. This is consistent with the presence of crystalline silicates in comets. However, it is inconsistent with the chemical similarities observed between comets and ISM sources, which are indicative of little processing. Hence, it appears that the cometary material is of mixed origins: part of it was strongly processed, and part of it was not. The chemical variations observed between individual comets suggest they were formed at different positions or times in the solar nebula. Fully pristine ices only appear in the upper and outer parts of this particular disk model (Sect. 3.7.2).

Sub-Keplerian accretion onto circumstellar disks



R. Visser and C. P. Dullemond
to be submitted

Abstract

Context. Models of the formation, evolution and photoevaporation of circumstellar disks are an essential ingredient in many theories of the formation of planetary systems. The ratio of disk mass over stellar mass in the circumstellar phase of a disk is for a large part determined by the angular momentum of the original cloud core from which the system was formed. While full 3D or 2D axisymmetric hydrodynamical models of accretion onto the disk will automatically treat all aspects of angular momentum, this is not so trivial for 1D viscous disk models.

Aims. Since 1D disk models are still very useful for long-term evolutionary modelling of disks with relatively little numerical effort, we wish to investigate how the 2D nature of accretion affects the formation and evolution of the disk in such models. A proper treatment of this problem also requires a correction for the sub-Keplerian velocity at which accretion takes place.

Methods. We develop an update of our 1+1D time-dependent disk formation and evolution model that properly treats the sub-Keplerian accretion of matter onto the disk. The model also accounts for the effects of the vertical extent of the disk on the infall trajectories.

Results. The disks produced with the new method are smaller than those obtained previously, but their mass is mostly unchanged. The new disks are a few degrees warmer in the outer parts, so they contain less solid CO. Otherwise, the results for ices are unaffected. The 2D treatment of the accretion results in material accreting at larger radii, so a smaller fraction comes close enough to the star for amorphous silicates to be thermally annealed into crystalline form. The lower crystalline abundances thus predicted correspond more closely to the abundances found observationally. We argue that thermal annealing followed by radial mixing must be responsible for at least part of the observed crystalline material.

4.1 Introduction

With the enormous increase in the amount of high-quality observational data of circumstellar disks in the last few years, a picture is now gradually emerging of how these objects evolve in time (Jørgensen et al. 2007, Looney et al. 2007, Lommen et al. 2008, Sicilia-Aguilar et al. 2009). They form during the collapse of a pre-stellar cloud core, undergo a number of accretion events (FU Orionis and EX Lupi outbursts), live for 3 to 10 Myr, and, shortly before they are destroyed, open up huge gaps visible in the dust continuum and sometimes also in gas lines (D'Alessio et al. 2005, Goto et al. 2006, Brittain et al. 2007, Ratzka et al. 2007, Brown et al. 2008, Pontoppidan et al. 2008a). These physical changes are echoed in the evolution of their chemical composition and dust properties. Pre-stellar cores contain mostly simple hydrides, radicals and other small molecules, largely frozen out onto the cold dust grains (Bergin & Langer 1997, Lee et al. 2004). A fully formed circumstellar disk is predicted to contain a much richer chemical mixture with a wide variety of complex organic molecules (Rodgers & Charnley 2003, Aikawa et al. 2008), although only simple organics have been observed so far (Lahuis et al. 2006, Carr & Najita 2008, Salyk et al. 2008). The dust by this time has grown from less than a micron to millimetres and centimetres, and part of it has evolved from an amorphous to a crystalline structure (Bouwman et al. 2001, 2008, van Boekel et al. 2005, Natta et al. 2007, Lommen et al. 2007, 2009, Watson et al. 2009, Olofsson et al. 2009). Crystalline silicate dust is observed down to temperatures of 100 K, well below the threshold of 800 K required to convert amorphous silicates into crystalline form. One of the central questions of this chapter is how much silicate material comes close enough to the star to be crystallised. We also investigate how the crystalline silicates end up so far outside of the hot inner disk where they appear to be formed.

One way to answer these questions is to construct detailed models of the evolution of circumstellar disks based on our current understanding of the physics of these objects, and then compare to the available observational data. However, it would require extraordinarily heavy computations to run a model that does justice to all physical processes known to be involved. A circumstellar disk ranges from a few stellar radii to hundreds of AU, and lasts for several million years. A full model would therefore have to resolve hundreds of millions of inner orbits, and span some five orders of magnitude on a spatial scale. Moreover, an accurate radiative transfer method is required to properly compute the temperatures. All this is clearly too demanding. Most multidimensional hydrodynamical simulations therefore solve sub-problems that only capture part of the disk, or only evolve over a limited time. Even these models, though, require days or weeks of CPU time for a single set of parameters.

An alternative approach is to parameterise most of the physics in some form, and treat the disk evolution as a simpler one-dimensional (1D) time-dependent problem. One assumes axisymmetry and integrates the density vertically to obtain the surface density Σ , which is now only a function of the radial coordinate R and the time t . These kinds of models go back to the pioneering work by Shakura & Sunyaev (1973) and Lynden-Bell & Pringle (1974). In order to use these models throughout the disk's lifetime, some way must be found to also include the birth phase of the disk in a reasonably realistic

way. Two-dimensional axisymmetric hydrodynamical models of disk formation show the presence of a stand-off shock that decelerates the supersonically infalling matter as it approaches the disk from above and below (e.g., Tscharnuter 1987, Yorke et al. 1993, Neufeld & Hollenbach 1994). The structure of this stand-off shock is clearly multidimensional in the outer regions, but may be approximated in a simpler manner in the inner regions (Nakamoto & Nakagawa 1994). Hueso & Guillot (2005) constructed a 1D disk evolution model with such an approximation and used it to analyse two T Tauri stars. This showed that simple models of disk formation and evolution can be very powerful and yield valuable insight into the evolutionary stage of young stellar objects. Similar models have also been used to analyse the statistics of the accretion rates measured in pre-main-sequence stars (Dullemond et al. 2006b, Vorobyov & Basu 2008).

Another problem addressed with these 1D parameterised models is the origin, evolution and transport of gas and dust in circumstellar disks. For instance, Dullemond et al. (2006a, hereafter DAW06) suggested that the initial outward expansion of the disk during the disk formation phase (observationally the Class 0/I phase) may be very effective in transporting thermally processed dust to the outer parts of the disk. Based on that work, one would expect to find a number of disks with nearly 100% crystalline dust. However, no such extremely crystalline disks are observed (Bouwman et al. 2008, Watson et al. 2009). This is one of the issues addressed in this chapter.

In Chapter 2, we showed yet another application of 1D disk evolution models. We followed the envelope material from thousands of AU inwards, through the accretion shock and into the disk, to analyse when ices evaporate and recondense on the grains. Since much of the interesting physics happens in the outer regions of the disk (several hundred AU), where the accretion shock no longer has a simple 1D shape, some way had to be found to include the 2D axisymmetric nature of this region without having to resort to a full-scale multidimensional hydrodynamical simulation. Our recipe was to construct a semi-2D disk model, i.e., to generate the 2D density structure $\rho(R, z, t)$ (where z is the vertical coordinate away from the midplane) out of the 1D surface density $\Sigma(R, t)$ using the disk temperature to compute the scale height at every radius. The accretion onto the disk was then modelled by following infalling matter on ballistic supersonic trajectories until its density equals the density of the disk. This yields a 2D axisymmetric shape of the stand-off shock that is similar to that obtained by full 2D axisymmetric hydrodynamical models (Yorke et al. 1993, Brinch et al. 2008a). However, it is not trivial to link this type of multidimensional infall structure back to the 1D disk evolution model. The main obstacle is that a substantial fraction of the matter does not really fall onto the disk's *surface* but onto the disk's *outer edge*, i.e., it accretes from the side instead of from the top. Moreover, this matter will rotate with a very sub-Keplerian velocity. If this is not treated in some way, the total angular momentum balance of the system is violated, potentially leading to very wrong estimates of the evolution of the disk mass with time. We devised an ad-hoc solution to this problem in Chapter 2 (Eq. (2.20)), which gave reasonable results but did not properly conserve angular momentum. We derive a more rigorous solution in the current chapter.

The problem of sub-Keplerian accretion onto a disk is not studied here for the first time. It has long been known that material falling in an elliptic orbit onto the surface of

the disk has sub-Keplerian angular momentum, even in the case of infinitely flat disks. When mixing with the disk material, which is in Keplerian rotation, a torque is exerted that pushes the disk material in towards the star. Cassen & Moosman (1981) described this problem and solved it elegantly. For disks without internal torque and with small vertical extent, they found an analytical solution for the disk surface density as a function of time, and they also presented numerical results for viscous disks. Hueso & Guillot (2005) derived an alternative solution: they simply calculated the radius for which the specific angular momentum of the infalling matter is Keplerian, and inserted the matter into the disk at that radius. This is not unreasonable, because one may assume that the material, after it hits the surface of the disk, will first adjust its own orbit before it mixes with the disk material below. It may be argued that as long as the angular momentum budget is not violated, the disk evolution is not much affected by the precise treatment. However, if one wishes to follow the radial motion and mixing of certain chemical species or types of dust, this may depend more sensitively on the way the angular momentum problem is treated.

In this chapter we add a consistent treatment of sub-Keplerian semi-2D accretion to a 1D model for the formation and viscous evolution of a disk (Sect. 4.2). Some basic disk properties arising from the new treatment are discussed in Sect. 4.3, and the results from Chapter 2 are briefly revisited in Sect. 4.4. The dust crystallisation results from DAW06 are re-evaluated in Sect. 4.5, and finally conclusions are drawn in Sect. 4.6.

4.2 Equations

The model describes the formation and evolution of a circumstellar disk inside a collapsing cloud core. The disk's surface density is governed by two processes: accretion of material from the envelope and viscosity-driven diffusion. This requires the continuity equation

$$\frac{\partial(\Sigma R)}{\partial t} + \frac{\partial(\Sigma R u_R)}{\partial R} = RS, \quad (4.1)$$

with u_R the radial velocity and S the source function that accounts for accretion from the envelope. In addition to conservation of mass, ensured by Eq. (4.1), there must be conservation of angular momentum (Lynden-Bell & Pringle 1974):

$$\frac{\partial(\Sigma \Omega_K R^3)}{\partial t} + \frac{\partial(\Sigma \Omega_K R^3 u_R)}{\partial R} = \frac{\partial}{\partial R} \left(\Sigma \nu R^3 \frac{\partial \Omega_K}{\partial R} \right) + S \Omega_K R^3, \quad (4.2)$$

with Ω_K the Keplerian rotation rate. We employ the α description (Shakura & Sunyaev 1973) for the viscosity, so the viscosity coefficient ν is given by

$$\nu(R, t) = \frac{\alpha k T_m}{\mu m_p \Omega_K}, \quad (4.3)$$

with T_m the midplane temperature and μ the mean molecular mass of 2.3 nuclei per hydrogen molecule.

In the last term in Eq. (4.2), belonging to the accreting material, the rotation rate Ω is smaller than Ω_K . If accretion *would* occur with the Keplerian velocity, Eq. (4.2) can be solved to give the expression for u_R used by DAW06. Working from that solution, two methods have been used in the recent literature to correct for the sub-Keplerian velocity of the accreting material. Hueso & Guillot (2005) and DAW06 modified the source function so that all incoming material accretes at the exact radius where its angular momentum equals that of the disk. One might picture this as a quick redistribution of material in the top layers of the disk after accretion initially occurred in a sub-Keplerian manner. A disadvantage of this method is that it introduces a discontinuity in the infall trajectories: upon accretion onto the disk, material instantaneously jumps to a smaller radius. Hence, in Chapter 2 we chose to modify the expression for the radial velocity instead of that for the source function, taking

$$u_R(R, t) = -\frac{3}{\Sigma \sqrt{R}} \frac{\partial}{\partial R} (\Sigma \nu \sqrt{R}) - \eta_r \sqrt{\frac{GM_*}{R}}, \quad (4.4)$$

with M_* the stellar mass and η_r a parameter with a constant value of 0.002. While this method has the desired effect of transporting material to smaller radii without discontinuities, it does not properly conserve angular momentum.

As an alternative to these two methods, Eq. (4.2) can also be solved more generally for the case that $\Omega < \Omega_K$, giving

$$u_R(R, t) = -\frac{3}{\Sigma \sqrt{R}} \frac{\partial}{\partial R} (\Sigma \nu \sqrt{R}) - \frac{2RS}{\Sigma} \frac{\Omega_K - \Omega}{\Omega_K}. \quad (4.5)$$

Expressions for Ω (or, rather, for the azimuthal velocity) may be found in Cassen & Moosman (1981) and Terebey et al. (1984). Equations (4.1) and (4.5), together with the standard expressions for S (e.g., Chapter 2), now describe a fully continuous solution to the evolution of the surface density with proper conservation of angular momentum. A physical interpretation of Eq. (4.5) is provided in Sect. 4.3.

The boundary between the disk and the envelope was computed in Chapter 2 as the surface where the density from both was the same. Here, we take instead the surface where the ram pressure of the infalling gas equals the thermal gas pressure from the disk:

$$\rho_{\text{env}} u^2 = \frac{kT \rho_{\text{disk}}}{\mu m_p} \quad (4.6)$$

with u the velocity of the infalling material. The use of the isobaric surface as the disk-envelope boundary instead of the isopycnic surface can have some effect on the model results, but, as shown in the next sections, the effects of the new treatment of the sub-Keplerian accretion are usually much larger. In the remainder of this chapter, we exclusively use the new method presented in this section. The rest of the model is described by DAW06 and in Chapter 2.

4.3 Size and mass of the disk

The net effect of the rightmost terms in Eqs. (4.4) and (4.5) is the same: to provide an additional inward flux of matter. However, the radial dependence of the additional flux is different. In the old method (Eq. (4.4)), it was largest at the inner edge of the disk because of the $R^{-1/2}$ proportionality. In the new method, on the other hand, it is strongest at the *outer* edge of the disk because of the sharp decrease in surface density at that point. Physically, the new dependence is easy to understand. Near the disk's inner edge, accretion occurs into a large column of material, and the torque arising from the different azimuthal velocities only results in a weak inward push. The same torque provides a much stronger push at the outer edge, where there is less disk material per unit surface. In effect, the material falling onto the disk's outer edge pushes the disk inwards and limits its radial growth.

In order to quantify the size of the disk, we first have to define the outer edge R_d . Since the equations allow an infinitesimal part of the disk to spread to an infinitely large distance, we cannot simply use the full radial extent of the disk as its outer edge. Instead, we define R_d as the radius that contains 90% of the disk's mass.

With the new method, the disk's outer edge initially lies beyond the centrifugal radius (R_c). It grows more or less linearly in time as the disk spreads out to conserve the angular momentum of the entire system. The centrifugal radius grows as t^3 , so the ratio R_d/R_c decreases as the collapse goes on. If the rotation rate is high enough, the centrifugal radius overtakes the outer edge of the disk before the end of the collapse. For the remainder of the collapse phase, R_d equals R_c , because the disk cannot be smaller than the centrifugal radius (Cassen & Moosman 1981). If the rotation rate is low enough that the centrifugal radius does not overtake the outer edge of the disk before the end of the collapse, R_d continues its near-linear growth until t_{acc} . After accretion from the envelope has ceased and the inward push from the accreting material is no longer present, the disk is free to expand more rapidly. Its outer edge again grows linearly in time in both the high- and low-rotation cases, and does so at a higher rate than in the initial linear-growth regime.

Figure 4.1 shows the outer edge as a function of time for the standard model from Chapter 2, which has a low initial rotation rate Ω_0 of 10^{-14} s^{-1} . The disk grows to about 40 AU at the end of the collapse phase at $t_{\text{acc}} = 2.5 \times 10^5 \text{ yr}$, and it spreads to ten times that size over the next $7.5 \times 10^5 \text{ yr}$. The method from Chapter 2 (labelled "old" in Fig. 4.1) provides a more rapid growth during the collapse phase, giving an R_d of 230 AU at t_{acc} . The post-infall spreading occurs at the same rate as in the new method. We find the same qualitative differences and similarities between the old and the new method for the rest of the parameter grid from Chapter 2.

Is the smaller disk from the new method a realistic scenario? Our model necessarily assumes u_R to be the same at all heights above the midplane. In reality, one might expect the infalling material to interact mostly with the surface of the disk, exerting its torque on only a fraction of the total surface density. This pushes the surface material radially inwards, while material near the midplane is unaffected. Indeed, the hydrodynamical simulations of Brinch et al. (2008a) show such behaviour, with material near the surface moving inwards and material at the midplane moving outwards. However, as this

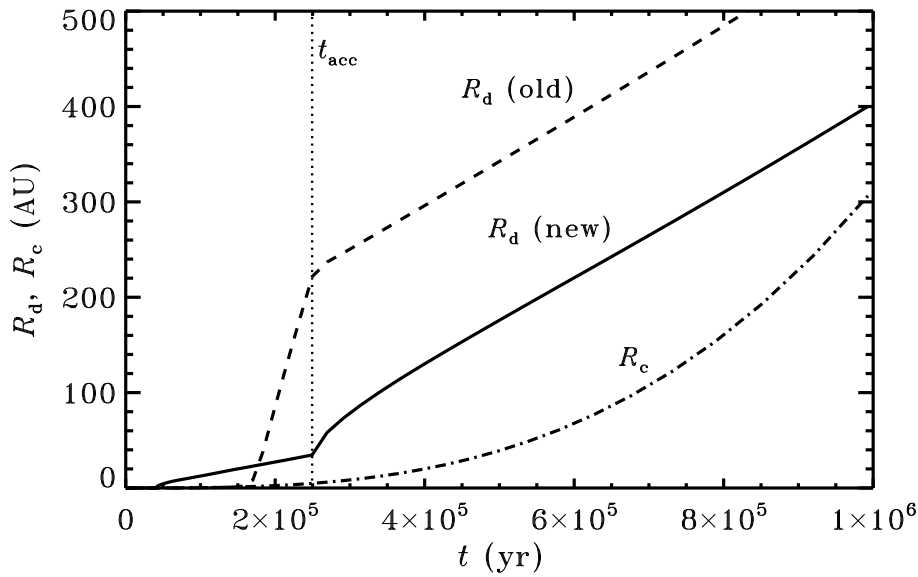


Figure 4.1 – Outer disk radius as a function of time for the standard model from Chapter 2. Solid: method from the current chapter; dashed: method from Chapter 2. The dash-dotted curve shows the centrifugal radius, and the dotted line indicates the end of the envelope accretion phase. Note that R_c is a physical quantity only up to t_{acc} ; for larger t , we simply plot the same mathematical function.

midplane material moves out beyond the outer edge, it becomes surface material itself, and is in turn exposed to the inward push from the envelope material. The new method may underestimate the outer radius by a factor of two or three because of the altitude-independence of u_R , but it produces a more realistic value than does the old method.

Although the disks are smaller with the new method, they are not necessarily less massive. In fact, we find a rather large mass increase for the standard model from Chapter 2: from 0.05 to $0.13 M_{\odot}$ at the end of the collapse phase. There are three causes for this, each of which accounts for 0.02 – $0.03 M_{\odot}$: (1) the new definition of the disk-envelope boundary (Eq. (4.6)); (2) the new sub-Keplerian correction (Eq. (4.5)); and (3) an improved integration scheme in the computational code. The effects are smaller for more rapidly rotating clouds. For example, the disk mass obtained for the reference model from Chapter 2 ($\Omega_0 = 10^{-13} \text{ s}^{-1}$) is unchanged at $0.43 M_{\odot}$.

4.4 Gas-ice ratios

During the collapse of the pre-stellar core to form a protostar and circumstellar disk, large changes occur in both density and temperature. Many molecular species are frozen out

onto dust grains before the onset of collapse (Bergin & Langer 1997, Lee et al. 2004). The warm-up phase during the collapse causes some of them to evaporate, and they may freeze out again once material settles near the disk’s relatively cold midplane. In Chapter 2, we modelled these processes for carbon monoxide (CO) and water (H₂O). Here, we investigate whether our new sub-Keplerian accretion correction affects these results.

The model consists of several steps. First, it computes the 2D axisymmetric density and velocity structure at regular intervals from the onset of collapse ($t = 0$) to the point where the entire envelope has accreted onto the star and disk ($t = t_{\text{acc}}$). Dust temperatures are computed at the same time intervals with the radiative transfer code RADMC (Dullemond & Dominik 2004a), and the gas temperature is assumed equal to the dust temperature. Using the velocity structure, the model then computes infall trajectories from a grid of initial positions in the envelope. Each trajectory represents an individual parcel of gas and dust, for which we now know the density and temperature as a function of time and position. This allows us to compute the adsorption and desorption rates of CO and H₂O, and solve for their gas and ice abundances in a Lagrangian frame. Finally, the parcels’ abundances are transformed back into 2D axisymmetric abundance profiles for the disk and remnant envelope.

As discussed in Sect. 4.3, the main difference between the disk properties from Chapter 2 and the new method is the size of the disk. Because the mass has increased or stayed the same (depending on the model parameters), the density of the disk is now higher. Hence, the dust temperature along the midplane decreases more rapidly. For example, at $t = t_{\text{acc}}$ in the reference model from Chapter 2 ($\Omega_0 = 10^{-13} \text{ s}^{-1}$), the temperature at 30 AU is 45 K. With the new method applied to the same initial conditions, the temperature is down to 31 K at that point. The midplane temperature decreases further with radius until it reaches 21 K at 160 AU with the new method. At larger radii, photons scattering off the surface of the disk begin to reach the midplane again and the temperature gradually increases to 25 K at the outer edge at 500 AU.

If all CO is taken to desorb at 18 K, as it would for a pure CO ice, the new temperature profile does not allow for any solid CO to exist in this particular model at t_{acc} . At later times, when the disk has spread to larger sizes and the protostar has become less luminous (Chapter 2), there appears a region around the midplane where the temperature does go below 18 K and CO freezes out again. In reality, solid CO forms a mixture with solid H₂O, and some of the CO remains trapped in the ice matrix at temperatures above 18 K (Collings et al. 2004, Viti et al. 2004, Fayolle et al. in prep.). When the gas-ice ratios are computed accordingly, the mass fraction of solid CO averaged over the entire disk at t_{acc} goes from 33% with the old method to 20% with the new method.

The gas-ice ratios for pure CO in the standard model from Chapter 2 ($\Omega_0 = 10^{-14} \text{ s}^{-1}$) are unchanged. With both the old and the new method, the entire disk is warmer than 18 K at t_{acc} , so there is no solid CO. If we allow part of the CO to be trapped in the H₂O ice, the disk-averaged solid fraction is 15% with both the old and the new methods.

In summary, the new treatment of the sub-Keplerian accretion results in disks that are a few degrees colder in the inner parts and a few degrees warmer in the outer parts. Overall, the new CO ice abundances are up to 50% smaller than those obtained with the old method. In all cases, H₂O remains solid in the entire disk except for the inner few AU.

4.5 Crystalline silicates

4.5.1 Observations and previous model results

Infrared spectroscopic observations have shown that about 1–30% of the silicate dust in the disks around Herbig Ae/Be and classical T Tauri stars occurs in crystalline form (Bouwman et al. 2001, 2008, van Boekel et al. 2005). Even larger fractions (up to 100%) are found in the inner 1 AU of some sources (Watson et al. 2009). The interstellar medium, from which this dust originates, has a crystalline fraction of at most 1–2% (Kemper et al. 2004, 2005). Two mechanisms are thought to dominate the conversion of amorphous silicates into crystalline form during the formation and evolution of a circumstellar disk. At temperatures above ~ 1200 K, the original grains evaporate (Petaev & Wood 2005). When the gas cools down again, the silicates recondense in crystalline form (Davis & Richter 2003, Gail 2004). Alternatively, amorphous dust can be thermally annealed into crystalline dust at temperatures above ~ 800 K (Wooden et al. 2005). As the disk is formed out of the parent envelope, part of the infalling material accretes close enough to the star that it is heated to more than 800 or 1200 K and can be crystallised. However, the observations show significant fractions of crystalline dust at least out to radii corresponding to a temperature of 100 K. Crystalline dust is also found in comets, which are formed in regions much colder than 800 K (Wooden et al. 1999, Keller et al. 2006). This suggests an efficient radial mixing mechanism to transport crystalline material from the hot inner disk to the colder outer parts (Nuth 1999, Bockelée-Morvan et al. 2002, Keller & Gail 2004).

An argument against large-scale radial mixing was recently provided by spatially resolved observations with the Spitzer Space Telescope. Bouwman et al. (2008) found a clear radial dependence in the relative abundances of forsterite and enstatite, two common specific forms of crystalline silicate. If both are formed in the hot inner disk and then transported outwards, one would expect the same relative abundances throughout the entire disk. Hence, the observed radial dependence argues in favour of a localised crystallisation mechanism such as heating by shock waves triggered by gravitational instabilities (Harker & Desch 2002, Desch et al. 2005). However, the observations do not completely rule out the possibility of crystallisation in the hot inner disk followed by radial mixing; at best, they provide an upper limit to how much crystalline dust can be formed that way.

In another set of Spitzer observations, crystalline spectroscopic features in the 20–30 μm region were detected three times more frequently than the crystalline feature at 11.3 μm (Olofsson et al. 2009). This is unexpected, because shorter wavelengths trace warmer material at shorter distances from the protostar, where all models predict the crystalline fractions to be larger. The 11.3 μm feature may be partially shielded by the amorphous 10 μm feature, but Olofsson et al. showed that this alone cannot explain the observations. A full compositional analysis (Olofsson et al. in prep.) is required to shed more light on this “crystallinity paradox”.

In the model of DAW06, crystallisation occurs right from the time when the disk is first formed. Indeed, because the disk is still very small at that time, its dust is hot and nearly fully crystalline. As the collapse proceeds and the disk’s outer radius grows, an ever

larger fraction of the infalling material does not come close enough to the star anymore to be heated above 800 K. In the absence of strong shocks, this results in amorphous dust being mixed in with the crystalline material. Hence, the crystalline fraction averaged over the entire disk is expected to decrease with time. There is tentative observational support for an age-crystallinity anticorrelation (van Boekel et al. 2005, Apai et al. 2005), but this is far from conclusive (Bouwman et al. 2008, Watson et al. 2009). One should of course consider the fact that observations do not probe the entire disk. If the model results from DAW06 are interpreted over a limited part of the disk, such as the 10–20 AU region, they show only a small difference in the crystalline fractions at 1 and 3 Myr. Add to that the uncertainties in the ages for individual objects, and it is clear that the model results cannot be said to conflict the observational data.

The crystalline fractions obtained by DAW06 were all on the high end of the observed range of 1–30%, unless unreasonably high initial rotation rates were adopted for the envelope or the disk temperature was lowered artificially. If we accept that only part of the silicates in the outer disk originate in the hot inner region – so the other part, formed in situ, can account for the observed radial abundance variations – the discrepancy between the DAW06 model and the observations becomes even larger. In the following, we show that we obtain more realistic crystalline fractions with our new method.

4.5.2 New model results

The two main differences between the old method of DAW06 and our new method are (1) the treatment of the disk as a multidimensional object instead of just a flat accretion surface and (2) the improved solution to the problem of sub-Keplerian accretion (Sect. 4.2). The former has the largest impact on the crystallisation. In case of a fully flat disk, material falls in along ballistic trajectories until it hits the midplane at or inside the centrifugal radius. If the vertical extent of the disk is taken into account, the infalling material hits the disk before it can flow all the way to the midplane. Because part of the disk often spreads beyond the centrifugal radius, especially at early times (Fig. 4.1), accretion now occurs at much larger radii. This is visualised in Fig. 4.2, which shows the mass loading onto the disk at 2.0×10^5 yr ($0.23 t_{\text{acc}}$) after the onset of collapse. The model parameters are those of the default model of DAW06: an initial envelope mass of $2.5 M_{\odot}$, a rotation rate of $1 \times 10^{-14} \text{ s}^{-1}$, and a sound speed of 0.23 km s^{-1} . The centrifugal radius at 2.0×10^5 yr is 2.2 AU, but the disk has already spread to 32 AU. Accretion occurs across the entire disk, although most mass falls in at small radii.

If the vertical structure of the disk is ignored when calculating the source function, as happened in the old method of DAW06, the infall trajectories continue along the dotted lines. They all intersect the midplane inside of R_c . In this case, that means all accretion takes place inside the “annealing radius” (R_{ann} , the radius corresponding to 800 K) and all dust is turned into crystalline form. In the new method, only 36% of the accreting material comes inside of R_{ann} , so the disk gains a much smaller amount of crystalline dust.

The crystalline fractions obtained with the new method are compared to the results from DAW06 in Fig. 4.3. In both cases, the inner part of the disk, out to a few AU, is fully crystalline. This is followed by a near-powerlaw decrease as crystalline material is mixed

Table 4.1 – Crystalline silicate fractions for a range of model parameters.^a

$\Omega_0 = 10^{-14} \text{ s}^{-1}, c_s = 0.19 \text{ km s}^{-1}$												
t	$R \text{ (AU)}$											
(Myr)	10	30	100	10	30	100	10	30	100	10	30	100
	$M: 0.20, 0.012$			$M: 0.50, 0.074$			$M: 1.0, 0.26$			$M: 5.0, 2.3$		
1.0	19.7	20.1	21.5	6.7	6.0	5.5	7.6	3.8	1.9	17.0	2.9	0.4
1.6	21.1	21.3	22.2	6.1	5.8	5.7	5.3	3.4	2.3	23.0	3.9	0.4
3.1	22.9	23.0	23.4	5.9	5.8	5.9	3.3	2.6	2.2	24.6	4.4	0.6
$\Omega_0 = 10^{-14} \text{ s}^{-1}, c_s = 0.26 \text{ km s}^{-1}$												
t	$R \text{ (AU)}$											
(Myr)	10	30	100	10	30	100	10	30	100	10	30	100
	$M: 0.20, 0^b$			$M: 0.50, 0.037$			$M: 1.0, 0.13$			$M: 5.0, 1.9$		
1.0				32.1	32.3	33.8	17.4	16.0	15.1	54.1	9.3	1.2
1.6				33.3	33.5	34.4	16.4	15.7	15.4	37.5	9.7	2.2
3.1				35.1	35.3	35.7	16.0	15.8	15.8	16.5	6.1	3.3
$\Omega_0 = 10^{-13} \text{ s}^{-1}, c_s = 0.19 \text{ km s}^{-1}$												
t	$R \text{ (AU)}$											
(Myr)	10	30	100	10	30	100	10	30	100	10	30	100
	$M: 0.20, 0.051$			$M: 0.50, 0.23$			$M: 1.0, 0.58$			$M: 5.0, 4.1$		
1.0	2.1	1.9	1.6	2.6	1.3	0.6	4.4	1.3	0.3	5.4	1.1	0.2
1.6	1.8	1.7	1.6	1.7	1.0	0.5	2.9	1.1	0.4	5.1	1.2	0.2
3.1	1.6	1.5	1.5	1.0	0.6	0.4	1.5	0.6	0.3	8.5	0.5	0.02
$\Omega_0 = 10^{-13} \text{ s}^{-1}, c_s = 0.26 \text{ km s}^{-1}$												
t	$R \text{ (AU)}$											
(Myr)	10	30	100	10	30	100	10	30	100	10	30	100
	$M: 0.20, 0.019$			$M: 0.50, 0.13$			$M: 1.0, 0.43$			$M: 5.0, 3.5$		
1.0	12.1	12.0	12.0	5.3	4.4	3.6	6.2	3.3	1.7	19.3	3.9	0.6
1.6	12.0	12.0	12.0	4.5	4.0	3.6	4.5	2.6	1.6	14.6	3.3	0.7
3.1	12.1	12.1	12.2	3.7	3.5	3.3	2.7	1.7	1.3	8.6	2.4	0.8

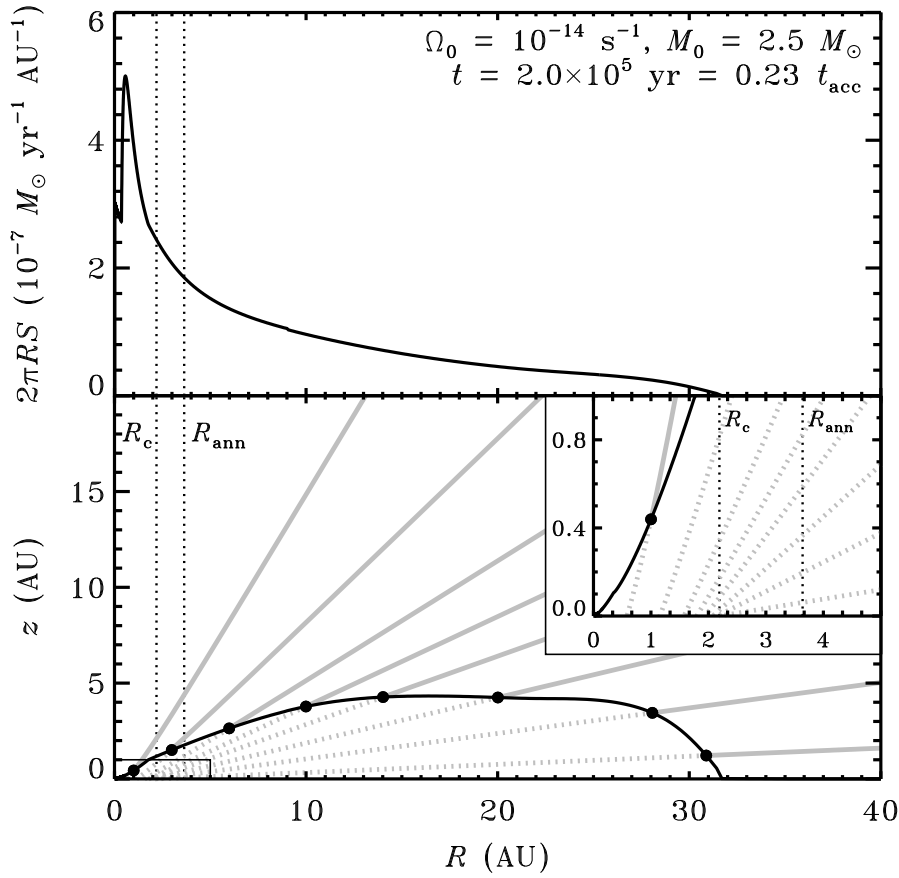


Figure 4.2 – Accretion at 2.0×10^5 yr ($0.23 t_{\text{acc}}$) for the default model of DAW06. The vertical dotted lines indicate the current values of R_c (2.2 AU) and R_{ann} (3.6 AU). Top: mass-loading as a function of radius. Bottom: infall trajectories (solid grey) from the envelope onto the surface of the disk (black). In the absence of the disk, the trajectories would extend to the midplane along the dotted lines. The inset in the bottom panel shows a blow-up of the inner 5×1 AU.

Table 4.1 – footnotes.

^a The fractions are given in per cent of the total silicate dust abundance at the indicated distance from the star (R) and time after the onset of collapse (t). The two masses (M , in units of M_\odot) listed for each combination of parameters are the initial cloud core mass and the disk mass at the end of the accretion phase.

^b No disk is formed at all for this combination of parameters.

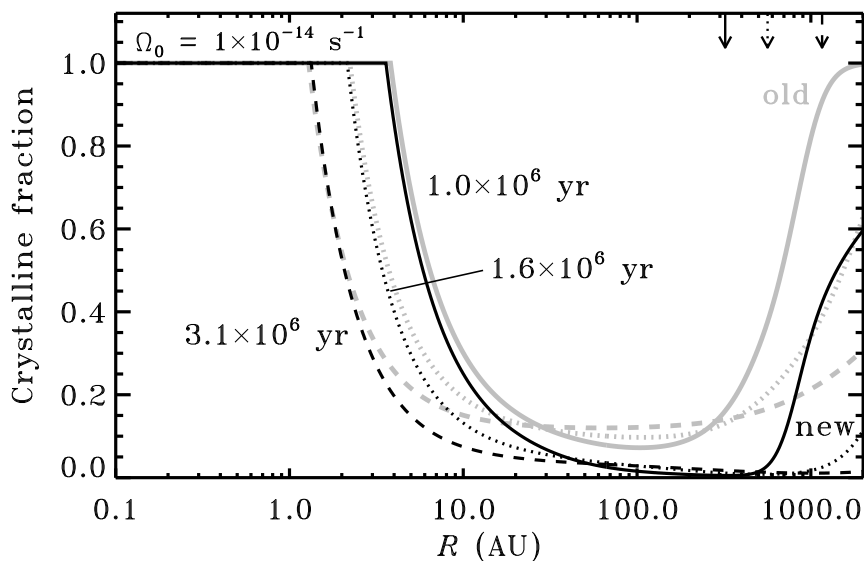


Figure 4.3 – Fraction of crystalline silicates for the default model of DAW06 at 1.0 (solid), 1.6 (dotted) and 3.1 Myr (dashed). The grey lines show the results from DAW06; the black lines show our new results. The arrows on the top axis indicate the outer disk radius for the new method.

to larger radii. At a few tens of AU, the crystallinity levels off to a base value that remains roughly constant to the outer edge of the disk, indicated by the arrows on the top axis in Fig. 4.3. The increase in crystallinity beyond that point should not be attributed much significance because, in reality, this material is mixed with the fully amorphous remnant envelope. At each of the three time steps plotted, the new crystallinity outside of a few AU is lower than the old one. For example, at 10 AU and 3.1 Myr, the fraction is down from 15.1 to 7.4%. At the outer edge of the disk, the new method produces crystalline fractions down to 1%. The differences between the old and the new method become even more pronounced when we take a slightly lower initial rotation rate of $3 \times 10^{-15} \text{ s}^{-1}$ (Fig. 4.4). The crystalline fraction at 10 AU and 3.1 Myr is now down from 72.6 to 11.3%.

The amount of crystallisation that takes place during the formation and evolution of the disk depends on the initial conditions. DAW06 already discussed the effect of the rotation rate (Ω_0) of the collapsing envelope. The more rapid the rotation, the larger the radius at which the bulk of the accretion takes place. This results in less material being heated above 800 K, so the disk becomes less crystalline. This effect also occurs in our new model. Two other conditions that can easily be changed are the initial mass (M_0) and the effective sound speed (c_s). In order to get a first understanding of their effects, we computed the crystalline fractions for the parameter grid from Chapter 2, as well as for models with initial masses of 0.2 and $5.0 M_\odot$. Table 4.1 lists the relevant model

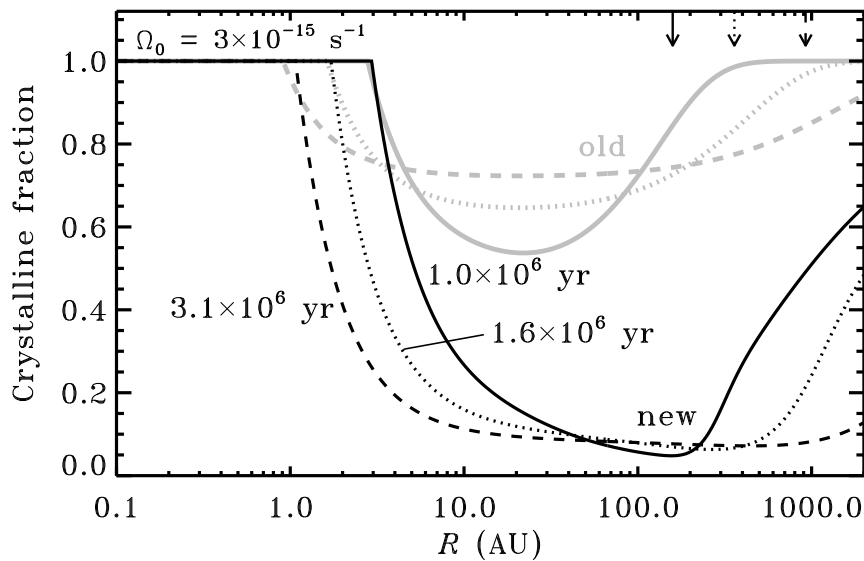


Figure 4.4 – As Fig. 4.3, but for $\Omega_0 = 3 \times 10^{-15} \text{ s}^{-1}$.

parameters together with the fraction of crystalline silicates at three different positions and three different times. The first of the three positions (10 AU) is representative of the region probed by the recent Spitzer observations, while the other two positions (30 and 100 AU) contain colder material that can be studied with the Herschel Space Observatory.

The models with a low sound speed all have a lower crystallinity than the models with a high sound speed. As noted in Chapter 2, a low sound speed results in a lower accretion rate. The accretion time becomes longer, so the disk grows larger and more massive. A lower accretion rate also gives a lower stellar luminosity, so the region where silicates can be crystallised is smaller. These effects combine to give smaller fractions of crystalline material throughout the entire disk.

Changing the initial mass of the cloud core has a more complicated effect on the crystallinity. Table 4.1 shows several cases where, for models that differ only in the initial mass, the crystalline fractions increase towards larger M_0 , and several cases where they decrease in that direction. Due to the inside-out nature of the Shu (1977) collapse, models of different mass initially evolve in exactly the same way. However, the accretion phase of the higher-mass models in our grid lasts longer ($t_{\text{acc}} \propto M_0$) than that of the lower-mass models. This affects the crystallinity in two opposing ways. First, the protostar becomes more luminous for the higher-mass models (D’Antona & Mazzitelli 1994), so the region in which crystallisation takes place is larger. Second, the disk grows larger, so the bulk of the accretion occurs farther from the star. The first effect results in higher crystalline abundances in the inner parts of the disk in the higher-mass models, while the

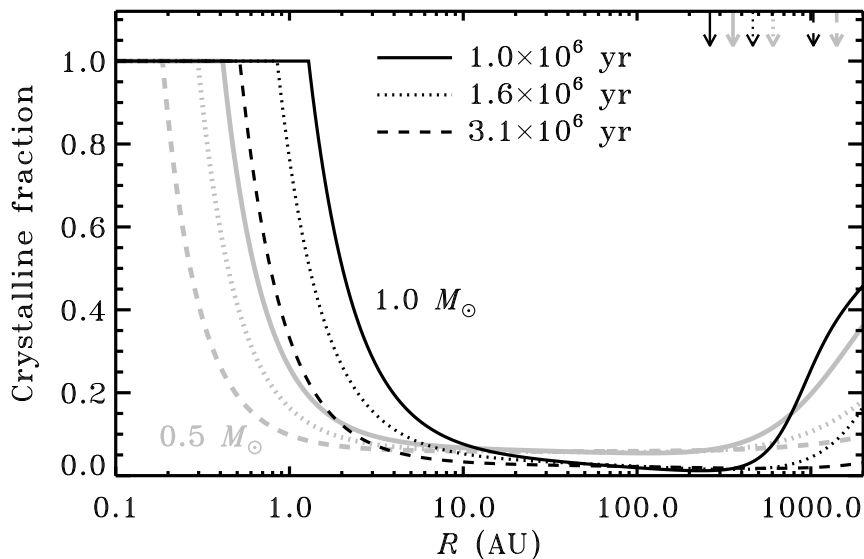


Figure 4.5 – As Fig. 4.3, but for two of the models from Table 4.1 with $\Omega_0 = 10^{-14} \text{ s}^{-1}$ and $c_s = 0.19 \text{ km s}^{-1}$. Grey: $M_0 = 0.5 M_\odot$; black: $M_0 = 1.0 M_\odot$.

second effect eventually results in *lower* crystalline abundances in the *outer* parts (Fig. 4.5). Depending on the exact initial conditions, the transition from the inner to the outer disk in this context may lie inwards or outwards of the 10–100 AU region given in Table 4.1, or even within that region. Example of two of these three possibilities can be found in the series of models with $\Omega_0 = 10^{-14} \text{ s}^{-1}$ and $c_s = 0.19 \text{ km s}^{-1}$ (top part of Table 4.1). Going from $M_0 = 0.2$ to $0.5 M_\odot$, the fraction of material accreting close enough to the star to be crystallised is reduced, so we find smaller crystalline fractions at 10, 30 and 100 AU: $\sim 6\%$ for the $0.5 M_\odot$ model versus $\sim 20\%$ for the $0.2 M_\odot$ model. Increasing the initial mass to $1.0 M_\odot$, the higher stellar luminosity increases the crystallinity at 10 AU to 7.6%. However, the crystallinity at larger radii suffers from the larger fraction of dust that remained amorphous during the accretion phase because the larger disk prevented it from getting closer to the protostar. At 30 AU, the crystalline fraction at 1.0 Myr decreases from 6.0 to 3.8% when the initial mass goes from 0.5 to $1.0 M_\odot$. The decrease in crystallinity at 100 AU is even larger: from 5.5 to 1.9%. The differences in the other three series of models can all be explained in similar fashion.

4.5.3 Discussion and future work

The goal of this chapter is to show how treating the disk as a multidimensional object and correctly solving the problem of sub-Keplerian accretion affect the results of DAW06. As

shown in Figs. 4.3 and 4.4, we obtain smaller fractions of crystalline silicates throughout the disk. This is an improvement over the old model, which was noted to overpredict crystallinity compared with observations.

A detailed parameter study is required to judge how well our current model reproduces all available observations. One complicating factor in such a procedure is the observed lack of correlation between crystallinity and other systemic properties such as the stellar luminosity, the accretion rate and the masses of the star and the disk (Watson et al. 2009). The observed absence of a correlation between two observables usually translates to a lack of a physical correlation, but this is not always the case. For example, Kessler-Silacci et al. (2007) showed why the crystallinity is not observed to be correlated with the stellar luminosity. The disk around a brighter protostar is warmer throughout, so the region from which most of the silicate emission originates lies at a larger distance from the star, where the crystallinity is lower. At the same time, though, the higher temperatures mean that more material can be thermally annealed, so the crystallinity at all radii goes up. The two effects cancel each other, so the observed crystalline fraction is not correlated with the stellar luminosity. Likewise, care must be taken when interpreting other observed non-correlations or correlations.

The best starting point for a more detailed comparison between model and observations appears to be the observed radial dependence of the relative abundances of specific types of crystalline silicates, such as enstatite and forsterite. Our model can be expanded to track multiple types of silicates, each with their own formation temperature and mechanism. First of all, this may help in explaining the “crystallinity paradox” identified by Olofsson et al. (2009; see also Sect. 4.5.1). Second, it can address the question whether crystalline silicates are predominantly formed by condensation from hot gas (~ 1200 K), by thermal annealing at slightly lower temperatures (~ 800 K), or by shock waves outside the hot inner disk. At the moment, neither the observations nor the models can rule out any of these mechanisms. The crystalline fractions obtained with our model suggest that thermal annealing followed by radial mixing must be taking place and must therefore be responsible for part of the observed crystalline silicates. A scenario in which *all* crystalline material is formed where it is observed, according to the model of Bouwman et al. (2008), appears unlikely.

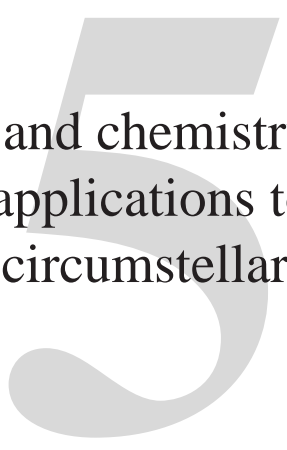
In addition to tracking multiple types of silicates, it may be worthwhile to investigate different collapse scenarios. The Shu (1977) collapse starts with a cloud core with an r^{-2} density profile, but observations of pre-stellar cores usually show an $r^{-1.5}$ density profile instead (Alves et al. 2001, Motte & André 2001, Harvey et al. 2003, André et al. 2004, Kandori et al. 2005). Bonnor-Ebert (BE) spheres have such a density profile (Ebert 1955, Bonnor 1956), so they have been proposed as an alternative starting point for collapse models (Whitworth et al. 1996). The collapse of a BE sphere results in different densities, velocities and temperatures than those obtained with the Shu collapse (Foster & Chevalier 1993, Matsumoto & Hanawa 2003, Banerjee et al. 2004, Walch et al. 2009), leading in turn to different crystalline silicate abundances. However, no analytical solutions exist for the collapse of a rotating BE sphere, so we are currently unable to pursue this point in any more detail.

4.6 Conclusions

This chapter presents a new method of correcting for the sub-Keplerian velocity of envelope material accreting onto an axisymmetric two-dimensional circumstellar disk. Unlike the previous corrections of Hueso & Guillot (2005) and from Chapter 2, this new method properly conserves angular momentum and produces infall trajectories without discontinuities. The latter is important for tracing changes in the chemical contents and dust properties during the evolution of the envelope and disk.

The disks produced with the new method are smaller than those produced with the old method by up to a factor of ten. Depending on the initial conditions, the disk masses are between 100 and 200% of previously computed values (Sect. 4.3). The new disks are a few degrees colder in the inner regions and a few degrees warmer in the outer regions, resulting in lower abundances of CO ice (Sect. 4.4). By the time the system reaches the classical T Tauri stage, at about 1 Myr, the global ice abundances still agree well with observations. Overall, there are no major changes in the gas-ice ratios compared with Chapter 2.

The disk was treated as geometrically flat by Dullemond et al. (2006a). As in Chapter 2, we now also take into account the vertical structure when computing the infall trajectories. This results in the bulk of the accretion occurring at larger radii. A smaller fraction of the infalling material now comes close enough to the star to be heated above 800 K, the temperature required for thermal annealing of amorphous silicates into crystalline form. Therefore, the new method produces crystalline abundances that are lower by a few per cent to more than a factor of five compared to the old model. We now obtain a better match with observations and we argue that thermal annealing followed by radial mixing is responsible for at least part of the crystalline silicates observed in disks. An expanded model, which tracks specific forms of crystalline silicate, is required to establish in more detail the importance of this and other possible crystallisation mechanisms.



The photodissociation and chemistry
of CO isotopologues: applications to
interstellar clouds and circumstellar
disks

R. Visser, E. F. van Dishoeck and J. H. Black
Astronomy & Astrophysics, 2009, 503, 323

Abstract

Aims. Photodissociation by UV light is an important destruction mechanism for carbon monoxide (CO) in many astrophysical environments, ranging from interstellar clouds to protoplanetary disks. The aim of this work is to gain a better understanding of the depth dependence and isotope-selective nature of this process.

Methods. We present a photodissociation model based on recent spectroscopic data from the literature, which allows us to compute depth-dependent and isotope-selective photodissociation rates at higher accuracy than in previous work. The model includes self-shielding, mutual shielding and shielding by atomic and molecular hydrogen, and it is the first such model to include the rare isotopologues $C^{17}O$ and $^{13}C^{17}O$. We couple it to a simple chemical network to analyse CO abundances in diffuse and translucent clouds, photon-dominated regions, and circumstellar disks.

Results. The photodissociation rate in the unattenuated interstellar radiation field is $2.6 \times 10^{-10} \text{ s}^{-1}$, 30% higher than currently adopted values. Increasing the excitation temperature or the Doppler width can reduce the photodissociation rates and the isotopic selectivity by as much as a factor of three for temperatures above 100 K. The model reproduces column densities observed towards diffuse clouds and PDRs, and it offers an explanation for both the enhanced and the reduced $N(^{12}CO)/N(^{13}CO)$ ratios seen in diffuse clouds. The photodissociation of $C^{17}O$ and $^{13}C^{17}O$ shows almost exactly the same depth dependence as that of $C^{18}O$ and $^{13}C^{18}O$, respectively, so ^{17}O and ^{18}O are equally fractionated with respect to ^{16}O . This supports the recent hypothesis that CO photodissociation in the solar nebula is responsible for the anomalous ^{17}O and ^{18}O abundances in meteorites. Grain growth in circumstellar disks can enhance the $N(^{12}CO)/N(C^{17}O)$ and $N(^{12}CO)/N(C^{18}O)$ ratios by a factor of ten relative to the initial isotopic abundances.

5.1 Introduction

Carbon monoxide (CO) is one of the most important molecules in astronomy. It is second in abundance only to molecular hydrogen (H_2) and it is the main gas-phase reservoir of interstellar carbon. Because it is readily detectable and chemically stable, CO and its less abundant isotopologues are the main tracers of the gas properties, structure and kinematics in a wide variety of astrophysical environments (for recent examples, see Dame et al. 2001, Najita et al. 2003, Wilson et al. 2005, Greve et al. 2005, Leroy et al. 2005, Huggins et al. 2005, Bayet et al. 2006, Oka et al. 2007 and Narayanan et al. 2008). In particular, the pure rotational lines at millimetre wavelengths are often used to determine the total gas mass. This requires knowledge of the CO- H_2 abundance ratio, which may differ by several orders of magnitude from one object to the next (Lacy et al. 1994, Burgh et al. 2007, Panić et al. 2008). If isotopologue lines are used, the isotopic ratio enters as an additional unknown.

CO also controls much of the chemistry in the gas phase and on grain surfaces, and is a precursor to more complex molecules. In photon-dominated regions (PDRs), dark cores and shells around evolved stars, the amount of carbon locked up in CO compared with that in atomic C and C^+ determines the abundances of small and large carbon-chain molecules (Millar et al. 1987, Jansen et al. 1995, Aikawa & Herbst 1999, Brown & Millar 2003, Teyssier et al. 2004, Cernicharo 2004, Morata & Herbst 2008). CO ice on the surfaces of grains can be hydrogenated to more complex saturated molecules such as CH_3OH (Charnley et al. 1995, Watanabe & Kouchi 2002, Fuchs et al. 2009), so the partitioning of CO between the gas and grains is important for the overall chemical composition as well (Caselli et al. 1993, Rodgers & Charnley 2003, Doty et al. 2004, Garrod & Herbst 2006).

A key process in controlling the gas-phase abundance of ^{12}CO and its isotopologues is photodissociation by ultraviolet (UV) photons. This is governed entirely by discrete absorptions into predissociative excited states; any possible contributions from continuum channels are negligible (Hudson 1971, Fock et al. 1980, Letzelter et al. 1987, Cooper & Kirby 1987). Spectroscopic measurements in the laboratory at increasingly high spectral resolution have made it possible for detailed photodissociation models to be constructed (Solomon & Klemperer 1972, Bally & Langer 1982, Glassgold et al. 1985, van Dishoeck & Black 1986, Viala et al. 1988, van Dishoeck & Black 1988 (hereafter vDB88), Warin et al. 1996, Lee et al. 1996). The currently adopted photodissociation rate in the unattenuated interstellar radiation field is $2 \times 10^{-10} \text{ s}^{-1}$.

Because the photodissociation of CO is a line process, it is subject to self-shielding: the lines become saturated at a ^{12}CO column depth of about 10^{15} cm^{-2} , and the photodissociation rate strongly decreases (vDB88, Lee et al. 1996). Bally & Langer (1982) realised this is an isotope-selective effect. Due to their lower abundance, isotopologues other than ^{12}CO are not self-shielded until much deeper into a cloud or other object. This results in a zone where the abundances of these isotopologues are reduced with respect to ^{12}CO , and the abundances of atomic ^{13}C , ^{17}O and ^{18}O are enhanced with respect to ^{12}C and ^{16}O . For example, the C^{17}O - ^{12}CO and C^{18}O - ^{12}CO column density ratios towards X Per are a factor of five lower than the elemental oxygen isotope ratios (Sheffer et al. 2002). The ^{13}CO - ^{12}CO ratio along the same line of sight is unchanged from the elemental

carbon isotope ratio, indicating that ^{13}CO is replenished through low-temperature isotope-exchange reactions. A much larger sample of sources shows $N(^{13}\text{CO})/N(^{12}\text{CO})$ column density ratios both enhanced and reduced by up to a factor of two relative to the elemental isotopic ratio (Sonnentrucker et al. 2007, Burgh et al. 2007, Sheffer et al. 2007). The reduced ratios have so far defied explanation, as all models predict that isotope-exchange reactions prevail over selective photodissociation in translucent clouds.

CO self-shielding has been suggested as an explanation for the anomalous ^{17}O - ^{18}O abundance ratio found in meteorites (Clayton et al. 1973, Clayton 2002, Lyons & Young 2005, Lee et al. 2008). In cold environments, molecules such as water (H_2O) may be enhanced in heavy isotopes. This so-called isotope fractionation process is due to the difference in vibrational energies of H_2^{16}O , H_2^{17}O and H_2^{18}O , and is therefore mass-dependent. It results in ^{18}O being about twice as fractionated as ^{17}O . However, ^{17}O and ^{18}O are nearly equally fractionated in the most refractory phases in meteorites (calcium-aluminium-rich inclusions, or CAIs), hinting at a mass-independent fractionation mechanism. Isotope-selective photodissociation of CO in the surface of the early circumstellar disk is such a mechanism, because it depends on the relative abundances of the isotopologues and the mutual overlap of absorption lines, rather than on the mass of the isotopologues. The enhanced amounts of ^{17}O and ^{18}O are subsequently transported to the planet- and comet-forming zones and eventually incorporated into CAIs. Recent observations of ^{12}CO , C^{17}O and C^{18}O in two young stellar objects support the hypothesis of CO photodissociation as the cause of the anomalous oxygen isotope ratios in CAIs (Smith et al. 2009). A crucial point in the Lyons & Young model is the assumption that the photodissociation rates of C^{17}O and C^{18}O are equal. Our model can test this at least partially.

Detailed descriptions of the CO photodissociation process are also important in other astronomical contexts. The circumstellar envelopes of evolved stars are widely observed through CO emission lines. The measurable sizes of these envelopes are limited primarily by the photodissociation of CO in the radiation field of background starlight (Mamon et al. 1988). Finally, proper treatment of the line-by-line contributions to the photodissociation of CO may affect the analysis of CO photochemistry in the upper atmospheres of planets (Fox & Black 1989).

In this chapter, we present an updated version of the photodissociation model from vDB88, based on laboratory experiments performed in the past twenty years (Sect. 5.2). We expand the model to include C^{17}O and $^{13}\text{C}^{17}\text{O}$ and we cover a broader range of CO excitation temperatures and Doppler widths (Sects. 5.3 and 5.4). We rederive the shielding functions from vDB88 and extend these also to higher excitation temperatures and larger Doppler widths (Sect. 5.5). Finally, we couple the model to a chemical network and discuss the implications for translucent clouds, PDRs and circumstellar disks, with a special focus on the meteoritic ^{18}O anomaly (Sect. 5.6).

5.2 Molecular data

The photodissociation of CO by interstellar radiation occurs through discrete absorptions into predissociated bound states, as first suggested by Hudson (1971) and later confirmed

by Fock et al. (1980). Any possible contributions from continuum channels are negligible at wavelengths longer than the Lyman limit of atomic hydrogen (Letzelter et al. 1987, Cooper & Kirby 1987).

Ground-state CO has a dissociation energy of 11.09 eV and the general interstellar radiation field is cut off at 13.6 eV, so knowledge of all absorption lines within that range (911.75–1117.80 Å) is required to compute the photodissociation rate. These data were only partially available in 1988, but ongoing laboratory work has filled in a lot of gaps. Measurements have also been extended to include CO isotopologues, providing more accurate values than can be obtained from theoretical isotopic relations. Table 5.1 lists the values we adopt for ^{12}CO .

5.2.1 Band positions and identifications

Eidelsberg & Rostas (1990, hereafter ER90) and Eidelsberg et al. (1992) redid the experiments of Letzelter et al. (1987) at higher spectral resolution and higher accuracy, and also for ^{13}CO , C^{18}O and $^{13}\text{C}^{18}\text{O}$. They reported 46 predissociative absorption bands between 11.09 and 13.6 eV, many of which were rotationally resolved. Nine of these have a cross section too low to contribute significantly to the overall dissociation rate. The remaining 37 bands are largely the same as the 33 bands of vDB88; bands 1 and 2 of the latter are resolved into four and two individual bands, respectively. Throughout this work, band numbers refer to our numbering scheme (Table 5.1), unless noted otherwise.

Thanks to the higher resolution and the isotopologue data, ER90 could identify the electronic and vibrational character of the upper states more reliably than Stark et al. in vDB88. The vibrational levels are required to compute the positions for those isotopologue bands that have not been measured directly. Nine of the vDB88 bands (not counting the previously unresolved bands 1 and 2) have a revised v' value.

The Eidelsberg et al. (1992) positions (ν_0 or λ_0) are the best available for most bands, with an estimated accuracy of 0.1–0.5 cm^{-1} . Seven of their ^{12}CO bands were too weak or diffuse for a reliable analysis, so their positions are accurate only to within 5 cm^{-1} . Nevertheless, we adopt the Eidelsberg et al. positions for three of these: bands 2A, 6 and 14. The former was blended with band 2B in vDB88, and the other two show a better match with the isotopologue band positions if we take the Eidelsberg et al. values. For the other four weak or diffuse bands, Nos. 4, 15, 19 and 28, we keep the vDB88 positions. Ubachs et al. (1994) further improved the experiments, obtaining an accuracy of about 0.01–0.1 cm^{-1} , so we adopt their band positions where available. Finally, we adopt the even more accurate positions (0.003 cm^{-1} or better) available for the *C1*, *E0*, *E1* and *L0* bands (Ubachs et al. 2000, Cacciani et al. 2001, 2002, Cacciani & Ubachs 2004).¹

Band positions for isotopologues other than ^{12}CO are still scarce, although many more are currently known from experiments than in 1988. The *C1* and *E1* bands have been measured for all six natural isotopologues, and the *E0* band for all but $^{13}\text{C}^{17}\text{O}$, at an accuracy of 0.003 cm^{-1} (Cacciani et al. 1995, Ubachs et al. 2000, Cacciani et al. 2001,

¹ All transitions in our model arise from the $v''=0$ level of the electronic ground state. We use a shorthand that only identifies the upper state, with *C1* indicating the $C^1\Sigma^+ v'=1$ state, etc.

Table 5.1 – New molecular data for ^{12}CO .^a

Band ^b #	ER90 ^b #	λ_0 (Å)	ν_0 (cm ⁻¹)	ID	ν'	$f_{\nu'0}$	A_{tot} (s ⁻¹)	η	B'_ν (cm ⁻¹)	D'_ν (cm ⁻¹)	ω'_e (cm ⁻¹)	$\omega_e x'_e$ (cm ⁻¹)	References & notes
1A	7A	912.70	109564.6	$^1\Pi$	0	3.4(-3)	1(10)	1.00	1.92	5.9(-5)	2170	13	1; c
1B	7B	913.40	109481.0	(5pσ) $^1\Sigma^+$	1	1.7(-3)	9(10)	1.00	1.83	1.0(-5)	2214	15	1,2; d
1C	7C	913.43	109478.0	(5pπ) $^1\Pi$	1	1.7(-3)	1(10)	1.00	1.96	1.0(-4)	2214	15	d
1D	7D	913.67	109449.0	$^1\Sigma^+$	2	2.7(-2)	9(10)	1.00	1.78	5.4(-5)	2170	13	1,2,3; c
2A	8A	915.73	109203.0	(6pπ) $^1\Pi$	0	2.0(-3)	1(11)	1.00	1.58	6.7(-6)	1563	14	e,f
2B	8B	915.97	109173.8	(6pσ) $^1\Sigma^+$	0	7.9(-3)	1(11)	1.00	1.69	1.0(-4)	2214	15	3; d
3	9A	917.27	109018.9	$^1\Pi$	2	2.3(-2)	5(11)	1.00	1.67	7.2(-5)	2170	13	2; c
4	9B	919.21	108789.1	(6sσ) $^1\Sigma^+$	0	2.8(-3)	1(11)	1.00	2.14	4.6(-5)	2214	15	4,5; d
5	9C	920.14	108679.0	I'(5sσ) $^1\Sigma^+$	1	2.8(-3)	1(11)	1.00	1.91	6.0(-6)	2291	0	g
6	10	922.76	108371.0	(5dσ) $^1\Sigma^+$	0	6.3(-3)	3(11)	1.00	1.97	6.3(-6)	2214	15	d,h
7	11	924.63	108151.3	$^1\Sigma^+$	1	5.2(-3)	1(11)	1.00	1.87	4.0(-5)	2170	13	c
8	12	925.81	108013.6	W(3sσ) $^1\Pi$	3	2.0(-2)	4(11)	1.00	1.65	1.1(-4)	1745	-4	6; g,i
9	13	928.66	107682.3	$^1\Pi$	2	6.7(-3)	4(10)	1.00	1.94	3.1(-5)	2170	13	1,2,3; c
10	14	930.06	107519.8	$^1\Pi$	2	6.3(-3)	1(11)	1.00	1.82	2.6(-5)	2170	13	c
11	15A	931.07	107402.8	$^1\Pi$	0	6.0(-3)	1(11)	1.00	1.65	1.0(-5)	2170	13	c
12	15B	931.65	107335.9	(5pπ) $^1\Pi$	0	1.2(-2)	3(11)	1.00	1.87	4.3(-5)	2214	15	2; d,j
13	15C	933.06	107174.4	(5pσ) $^1\Sigma^+$	0	2.2(-2)	3(10)	1.00	2.13	1.0(-5)	2214	15	1,2; d,i
14	16	935.66	106876.0	$^1\Sigma^+$	2	3.8(-3)	3(11)	1.00	1.95	0.0	2170	13	5; c
15	17	939.96	106387.8	I'(5sσ) $^1\Sigma^+$	0	2.1(-2)	1(12)	1.00	2.04	8.8(-5)	2291	0	4; g,j
16	18	941.17	106250.9	W(3sσ) $^1\Pi$	2	3.1(-2)	1(11)	1.00	1.62	-1.3(-5)	1745	-4	1,6; g,i,k
17	19	946.29	105676.3	(4dσ) $^1\Sigma^+$	0	7.6(-3)	1(11)	1.00	1.90	1.7(-5)	2214	15	1,2,3; d
18	20	948.39	105442.3	L(4pπ) $^1\Pi$	1	2.8(-3)	1(10)	0.99	1.96	1.0(-5)	2171	0	g
19	21	950.04	105258.4	H(4pσ) $^1\Sigma^+$	1	2.2(-2)	1(12)	1.00	1.94	4.4(-5)	2204	0	4; g,j
20	22	956.24	104576.6	W(3sσ) $^1\Pi$	1	1.6(-2)	7(11)	1.00	1.57	5.8(-5)	1745	-4	6; g
21	24	964.40	103691.7	J(4sσ) $^1\Sigma^+$	1	2.8(-3)	3(11)	1.00	1.92	9.0(-6)	2236	0	g
22	25	968.32	103271.8	L(4pπ) $^1\Pi$	0	1.4(-2)	2(9)	0.96	1.96	7.1(-6)	2171	0	7,8,9; g,i,k
23	26	968.88	103211.8	L'(3dπ) $^1\Pi$	1	1.2(-2)	2(11)	1.00	1.75	1.0(-5)	2214	15	1,2,3,9; d,k
24	27	970.36	103054.7	K(4pσ) $^1\Sigma^+$	0	3.4(-2)	2(10)	0.99	1.92	6.0(-5)	2204	0	1,2,3,9; g

Table 5.1 – continued.

Band ^b #	ER90 ^b #	λ_0 (Å)	ν_0 (cm ⁻¹)	ID	ν'	$f_{\nu'0}$	A_{tot} (s ⁻¹)	η	B'_ν (cm ⁻¹)	D'_ν (cm ⁻¹)	ω'_e (cm ⁻¹)	$\omega_e x'_e$ (cm ⁻¹)	References & notes
25	28	972.70	102806.7	$W(3s\sigma)^1\Pi$	0	1.7(-2)	1(10)	0.97	1.57	9.7(-5)	1745	-4	1,3,6; g,i,k
26	29	977.40	102312.3	$W'(3s\sigma)^3\Pi$	2	1.8(-3)	4(11)	1.00	1.54	8.0(-6)	1563	14	1,2,3; f,k
27	30	982.59	101771.7	$F(3d\sigma)^1\Sigma^+$	1	4.8(-4)	3(11)	1.00	1.85	1.4(-5)	2030	0	g
28	31	985.65	101456.0	$J(4s\sigma)^1\Sigma^+$	0	1.5(-2)	1(12)	1.00	1.92	5.1(-5)	2236	0	4; g,j
29	32	989.80	101031.0	$G(3d\pi)^1\Pi$	0	4.6(-4)	1(11)	1.00	1.96	1.1(-5)	2214	15	d
30	33	1002.59	99741.7	$F(3d\sigma)^1\Sigma^+$	0	7.9(-3)	3(11)	1.00	1.81	2.2(-4)	2030	0	g
31	37	1051.71	95082.9	$E(3p\pi)^1\Pi$	1	3.6(-3)	6(9)	0.96	1.93	6.6(-6)	2239	43	10,11,12,13; k
32	38	1063.09	94065.6	$C(3p\sigma)^1\Sigma^+$	1	3.0(-3)	2(9)	0.56	1.92	6.3(-6)	2176	15	14,15,16
33	39	1076.08	92929.9	$E(3p\pi)^1\Pi$	0	6.8(-2)	1(9)	0.80	1.95	6.3(-6)	2239	43	13,15,17,18; k

References: λ_0 , ν_0 , ID and ν' from Eidelsberg et al. (1992) and $f_{\nu'0}$, A_{tot} , B'_ν and D'_ν from ER90, except these: (1) λ_0 and ν_0 from Ubachs et al. (1994); (2) A_{tot} from Ubachs et al. (1994); (3) B'_ν and D'_ν from Ubachs et al. (1994); (4) λ_0 and ν_0 from vDB88; (5) B'_ν and D'_ν from vDB88; (6) $f_{\nu'0}$ and A_{tot} from Eidelsberg et al. (2006); (7) λ_0 , ν_0 , B'_ν and D'_ν from Cacciani et al. (2002); (8) A_{tot} from Drabbels et al. (1993); (9) $f_{\nu'0}$ from Eidelsberg et al. (2004); (10) λ_0 , ν_0 , B'_ν and D'_ν from Ubachs et al. (2000); (11) $f_{\nu'0}$ from Eidelsberg et al. (2006); (12) A_{tot} from Ubachs et al. (2000); (13) ω'_e , $\omega_e x'_e$ from Kepa (1988); (14) λ_0 , ν_0 , A_{tot} , B'_ν and D'_ν from Cacciani et al. (2001); (15) $f_{\nu'0}$ from Federman et al. (2001); (16) ω'_e , $\omega_e x'_e$ from Tilford & Vanderslice (1968); (17) λ_0 , ν_0 , B'_ν and D'_ν from Cacciani & Ubachs (2004); (18) A_{tot} from Cacciani et al. (1998).

Notes:

- ^a Many values are rounded off from higher-precision values in the references. The notation $a(b)$ in this and following tables means $a \times 10^b$.
- ^b The numbering follows vDB88. Their bands 1 and 2 are split into four and two components. The corresponding ER90 indices are also given.
- ^c ω'_e and $\omega_e x'_e$ from the CO ground state (Guelachvili et al. 1983). $\omega_e y'_e$ and $\omega_e z'_e$ (not listed) are included in the model.
- ^d ω'_e and $\omega_e x'_e$ from the CO⁺ $X^2\Sigma^+$ state (Haridass et al. 2000).
- ^e B'_ν and D'_ν from the CO⁺ $A^2\Pi$ state (Haridass et al. 2000).
- ^f ω'_e and $\omega_e x'_e$ from the CO⁺ $A^2\Pi$ state (Haridass et al. 2000). $\omega_e y'_e$ (not listed) is included in the model.
- ^g Vibrational constants derived from the different ν_0 in one of six vibrational series: bands 30–27, 28–21, 25–20–16–8, 24–19, 22–18 or 15–5.
- ^h B'_ν and D'_ν from the CO⁺ $X^2\Sigma^+$ state (Haridass et al. 2000).
- ⁱ A_{tot} depends on parity and/or rotational level (see Table 5.3). A_{tot} and η are listed here for $J'=0$ and f parity.
- ^j B'_ν and D'_ν computed from the C¹⁸O values of ER90.
- ^k B'_ν and D'_ν depend on parity (see Table 5.2); values are listed here for f parity.

Cacciani & Ubachs 2004). The positions of the $E0$ band are especially important because of its key role in the isotope-selective nature of the CO photodissociation (Sect. 5.3.3). Positions are known at lower accuracy (0.003–0.5 cm^{-1}) for an additional 25 C^{18}O , 30 ^{13}CO and 9 $^{13}\text{C}^{18}\text{O}$ bands (Eidelsberg et al. 1992, Ubachs et al. 1994, Cacciani et al. 2002); these are included throughout.

We compute the remaining band positions from theoretical isotopic relations. For band b of isotopologue i , the position is

$$\nu_0(b, i) = \nu_0(b, ^{12}\text{CO}) + [E'_v(b, i) - E''_v(X, i)] - [E'_v(b, ^{12}\text{CO}) - E''_v(X, ^{12}\text{CO})], \quad (5.1)$$

with $E'_v(b, i)$ and $E''_v(X, i)$ the vibrational energy of the excited and ground states, respectively. Hence, we need the vibrational constants ($\omega'_e, \omega_e x'_e, \dots$) for all the excited states other than the $C^1\Sigma^+$. These have only been determined experimentally for the $E^1\Pi$ state (Keřpa 1988). For the other states, we employ this scheme:

- if it is part of a vibrational series (such as band 30, for which the corresponding $v'=1$ band is No. 27), we can derive ω'_e from the difference in ν_0 ;
- else, if it is part of a Rydberg series converging to the $X^2\Sigma^+$ or $A^2\Pi$ state of CO^+ , we take those constants (Haridass et al. 2000);
- else, we take the constants of ground-state CO (Guelachvili et al. 1983).

The choice for each band and the values of the constants are given in Table 5.1.

5.2.2 Rotational constants

The rotational constants (B'_v and D'_v) for each excited state are needed to compute the positions of the individual absorption lines. ER90 provided B'_v values for most bands, at an estimated accuracy of better than 1%. Their D'_v values are less well constrained and may be off by more than a factor of two. However, this is of little importance for the low- J lines typically involved in the photodissociation of CO. More accurate values (B'_v to better than 0.1%, D'_v to 10% or better) are available for 12 states from higher-resolution experiments (Eikema et al. 1994, Ubachs et al. 1994, 2000, Cacciani et al. 2001, 2002, Cacciani & Ubachs 2004). Again, the data for isotopologues other than ^{12}CO are generally scarce, so we have to compute their constants from theoretical isotopic relations. This increases the uncertainty in B'_v to a few per cent. In case of bands 12, 15, 19 and 28, ER90 reported constants for C^{18}O but not for ^{12}CO , so we employ the theoretical relations for the latter. We adopt the vDB88 constants for bands 4 and 14, because they are more accurate than those of ER90. No constants are available for Rydberg bands 2A and 6, so we adopt the constants of the associated CO^+ states ($A^2\Pi$ and $X^2\Sigma^+$, respectively).

In seven cases, the rotational constants of the P and R branch (e parity) were found to differ from those of the Q branch (f parity; Ubachs et al. 1994, 2000, Cacciani et al. 2002, Cacciani & Ubachs 2004). For these bands, the f parity values are given in Table 5.1. Table 5.2 lists the difference between the f and e values, defined as $q'_v = B'_{v,e} - B'_{v,f}$ and $p'_v = D'_{v,e} - D'_{v,f}$. The uncertainties in q'_v and p'_v are on the order of 1 and 10%, respectively.

Table 5.2 – Parity-dependent rotational constants for ^{12}CO .

Band #	q'_v (cm^{-1})	p'_v ^a (cm^{-1})	Refs. ^b
16	-2.7(-3)	—	1
22	2.212(-2)	7.9(-6)	2
23	3.0(-2)	—	1
25	-7.0(-4)	—	1
26	-1.11(-2)	—	1
31	1.14(-2)	3.0(-8)	3
33	1.196(-2)	2.1(-7)	4

^a Dashes indicate that no measurement is available, so we adopt a value of zero.

^b (1) Ubachs et al. (1994); (2) Cacciani et al. (2002); (3) Ubachs et al. (2000); (4) Cacciani & Ubachs (2004)

5.2.3 Oscillator strengths

ER90 measured the integrated absorption cross sections (σ_{int}) for all their bands to a typical accuracy of 20%, but they cautioned that some values, especially for mutually overlapping bands, may be off by up to a factor of two. The oscillator strengths ($f_{v'0}$) derived from these data are different from vDB88 for most bands, sometimes by even more than a factor of two. In addition, there are differences of up to an order of magnitude between the cross sections of ^{12}CO and those of the other isotopologues for many bands shortwards of 990 Å. The isotopic differences are likely due in part to the difficulty in determining individual cross sections for strongly overlapping bands, but isotope-selective oscillator strengths in general are not unexpected. For example, they were also observed recently in high-resolution measurements of N_2 (G. Stark, priv. comm.). For CO, the oscillator strengths depend on the details of the interactions between the J' , v' levels of the excited states and other rovibronic levels. These interactions, in turn, depend on the energy levels, which are different between the isotopologues. We adopt the isotope-selective oscillator strengths where available. In case of transitions where no isotopic data exist, we choose to take the value of the isotopologue nearest in mass. This gives the closest match in energy levels and should, in general, also give the closest match in oscillator strengths, which to first order are determined by the Franck-Condon factors.

For ten of our bands, we adopt oscillator strengths from studies that aimed specifically at measuring this parameter (Federman et al. 2001, Eidelsberg et al. 2004, 2006). Their estimated accuracy is 5–15%. The oscillator strength for the *E0* band from Federman et al. (2001) is almost twice as large as that of vDB88 and ER90, which appears to be due to an inadequate treatment of saturation effects in the older work. The 2001 value corresponds well to other values derived since 1990. Federman et al. also measured the oscillator strength of the weaker *C1* band and found it to be the same, within the error margins, as that of vDB88 and ER90. Recent measurements of the *K0*, *L0* and *E1* transitions and the four *W* transitions show larger oscillator strengths than those of vDB88 and ER90 (Eidelsberg et al. 2004, 2006). The new values correspond closely to those of Sheffer et al.

(2003), who derived oscillator strengths for eight bands by fitting a synthetic spectrum to Far Ultraviolet Spectroscopic Explorer (FUSE) data taken towards the star HD 203374A. Lastly, the Eidelsberg et al. (2004) value for the $L'1$ band is 33% lower than that of vDB88, but very similar to those of ER90 and Sheffer et al. (2003), so we adopt it as well.

We compute the oscillator strengths of individual lines as the product of the appropriate Hönl-London factor and the oscillator strength of the corresponding band (Morton & Noreau 1994). Significant departures from Hönl-London patterns have been reported for many N_2 lines, sometimes even for the lowest rotational levels (Stark et al. 2005, 2008). The oscillator strength measured in one particular N_2 band for the P(22) line was twenty times stronger than that for the P(2) line, due to strong mixing of the upper state with a nearby Rydberg state. For other bands where deviations from Hönl-London factors were observed, the effect was generally less than 50% at $J'=10$. Similar deviations are likely to occur for CO, but a lack of experimental data prevents us from including this in our model. Note, however, that large deviations are only expected for specific levels that happen to be strongly interacting with another state. Many hundreds of levels contribute to the photodissociation rate, so the effect of some erroneous individual line oscillator strengths is small.

5.2.4 Lifetimes and predissociation probabilities

Upon excitation, there is competition between dissociative and radiative decay. A band's predissociation probability (η) can be computed if the upper state's total and radiative lifetimes are known: $\eta = 1 - \tau_{\text{tot}}/\tau_{\text{rad}}$. ER90 reported total lifetimes ($1/A_{\text{tot}}$) for all their bands, but many of these are no more than order-of-magnitude estimates. Higher-resolution experiments have since produced more accurate values for 17 of our bands (Ubachs et al. 1994, 2000, Cacciani et al. 1998, 2001, 2002, Eidelsberg et al. 2006). In several cases, values that differ by up to a factor of three are reported for different isotopologues. Where available, we take isotope-specific values. Otherwise, we follow the same procedure as for the oscillator strengths, and take the value of the isotopologue nearest in mass.

The total lifetimes of some upper states have been shown to depend on the rotational level (Drabbels et al. 1993, Ubachs et al. 2000, Eidelsberg et al. 2006). In case of $^1\Pi$ states, a dependence on parity was sometimes observed as well. We include these effects for the five bands in which they have been measured (Table 5.3).

Recent experiments by Chakraborty et al. (2008) suggest isotope-dependent photodissociation rates for the $E0$, $E1$, $K0$ and $W2$ bands. These have been interpreted to imply different predissociation probabilities of individual lines of the various isotopologues due to a near-resonance accidental predissociation process. Similar effects have been reported for ClO_2 and CO_2 (Lim et al. 1999, Bhattacharya et al. 2000). In this process, the bound-state levels into which the UV absorption takes place do not couple directly with the continuum of a dissociative state. Instead, they first transfer population to another bound state, whose levels happen to lie close in energy. For the CO $E1$ state, this process was rotationally resolved by Ubachs et al. (2000) for all naturally occurring isotopologues and shown to be due to spin-orbit interaction with the $k^3\Pi v'=6$ state, which in turn couples

Table 5.3 – Parity- and rotation-dependent inverse lifetimes for ^{12}CO .

Band #	$A_{\text{tot},f}^a$ (s^{-1})	$A_{\text{tot},e}^a$ (s^{-1})	Refs. ^b
8	$3.6(11)+4.0(9)x$	$1.6(11)+1.3(10)x$	1
13 ^c	$3.4(10)+7.3(10)x$	—	2
16	$1.0(11)+1.8(9)x$	$1.0(11)+3.4(9)x$	1
22	$1.83(9)$	$1.91(9)+1.20(9)x$	3
25	$1.2(10)$	$1.2(10)+2.4(9)x$	1

^a x stands for $J'(J' + 1)$.

^b (1) Eidelsberg et al. (2006); (2) Ubachs et al. (1994); (3) Drabbels et al. (1993).

^c This is a $^1\Sigma^+$ upper state, so there is no distinction between e and f parity.

with a repulsive state. The predissociation rates of the $E1$ state are found to increase significantly due to this process, but only for specific J' levels that accidentally overlap. For example, interaction occurs at $J'=7, 9$ and 12 for ^{12}CO , but at $J'=1$ and 6 for $^{13}\text{C}^{18}\text{O}$. Since the dissociation probabilities for the $E1$ state due to direct predissociation were already high, $\eta = 0.96$, this increase in dissociation rate only has a very minor effect (Cacciani et al. 1998). Moreover, under astrophysical conditions a range of J' values are populated, so that the effect of individual levels is diluted. Since Chakraborty et al. did not derive line-by-line molecular parameters, we cannot easily incorporate their results into our model. In Sect. 5.6.3, we show that our results do not change significantly when we include the proposed effects in an ad-hoc way.

The radiative lifetime of an excited state is a sum over the decay into all lower-lying levels, including the $A^1\Pi$ and $B^1\Sigma^+$ electronic states and the $v' \neq 0$ levels of the ground state. The total decay rate to the ground state is obtained by summing the oscillator strengths from Table 5.1 for each vibrational series (Morton & Noreau 1994, Cacciani et al. 1998). Theoretical work by Kirby & Cooper (1989) shows that transitions to electronic states other than the ground state contribute about 1% of the overall radiative decay rate for the C state and about 8% for the E state. No data are available for the excited states at higher energies. Fortunately, the radiative decay rate from these higher states to the ground state is small compared to the dissociation rate, so an uncertainty of $\sim 10\%$ does not affect the η values.

The predissociation probabilities thus computed are practically identical to those of vDB88: the largest difference is a 10% decrease for the $C1$ band. This is due to the larger oscillator strength now adopted.

There have been suggestions that the $C0$ state can also contribute to the photodissociation rate. Cacciani et al. (2001) measured upper-state lifetimes in the $C0$ and $C1$ states for several CO isotopologues. For the $v'=0$ state of ^{13}CO they found a total lifetime of 1770 ps, consistent with a value of 1780 ps for ^{12}CO , but different from the lifetime of 1500 ps in $^{13}\text{C}^{18}\text{O}$. Although the three values agree within the mutual uncertainties of 10–15% on each measurement, Cacciani et al. suggested that the heaviest species, $^{13}\text{C}^{18}\text{O}$, has a predissociation yield of $\eta = 0.17$ rather than zero if the measurements are taken at face value

and if the radiative lifetime of the $C0$ state is presumed to be 1780 ps for all three species. The accurate absorption oscillator strength measured by Federman et al. (2001) for the $C0$ band, 0.123 ± 0.016 , implies a radiative lifetime that can be no longer than 1658 ps at the lower bound of measurement uncertainty in f_{ν_0} . Taken together, the lifetime measurements of Cacciani et al. and the absorption measurements of Federman et al. favour a conservative conclusion that the dissociation yield is zero for each of these three isotopologues. We assume the $C0$ band is also non-dissociative in $C^{17}O$, $C^{18}O$ and $^{13}C^{17}O$; this is consistent with earlier studies (e.g., vDB88, ER90, Morton & Noreau 1994).

5.2.5 Atomic and molecular hydrogen

Lines of atomic and molecular hydrogen (H and H_2) form an important contribution to the overall shielding of CO. As in vDB88, we include H Lyman lines up to $n=50$ and H_2 Lyman and Werner lines (transitions to the $B^1\Sigma_u^+$ and $C^1\Pi_u$ states) from the $\nu''=0$, $J''=0-7$ levels of the electronic ground state. We adopt the line positions, oscillator strengths and lifetimes from Abgrall et al. (1993a,b), as compiled for the freely available MEUDON PDR code (Le Bourlot et al. 1993, Le Petit et al. 2002, 2006).² Ground-state rotational constants, required to compute the level populations, come from Jennings et al. (1984).

5.3 Depth-dependent photodissociation

5.3.1 Default model parameters

The simplest way of modelling the depth-dependent photodissociation involves dividing a one-dimensional model of an astrophysical object, irradiated only from one side, into small steps, in which the photodissociation rates can be assumed constant. We compute the abundances from the edge inwards, so that at each step we know the columns of CO, H, H_2 and dust shielding the unattenuated radiation field.

Following vDB88, Le Bourlot et al. (1993), Lee et al. (1996) and Le Petit et al. (2006), we treat the line and continuum attenuation separately. For each of our 37 CO bands, we include all lines originating from the first ten rotational levels ($J''=0-9$) of the $\nu''=0$ level of the electronic ground state. That results in 855 lines per isotopologue. In addition, we have 48 H lines and 444 H_2 lines, for a total of 5622. We use an adaptive wavelength grid that resolves all lines without wasting computational time on empty regions. For typical model parameters, the wavelength range from 911.75 to 1117.80 Å is divided into $\sim 47\,000$ steps.

We characterise the population distribution of CO over the rotational levels by a single temperature, $T_{\text{ex}}(\text{CO})$. The H_2 population requires a more detailed treatment, because UV pumping plays a large role for the $J''>4$ levels (van Dishoeck & Black 1986). We populate the $J''=0-3$ levels according to a single temperature, $T_{\text{ex}}(\text{H}_2)$, and adopt fixed columns of 4×10^{15} , 1×10^{15} , 2×10^{14} and $1 \times 10^{14} \text{ cm}^{-2}$ for $J''=4-7$. This reproduces observed translucent cloud column densities to within a factor of two (van Dishoeck &

² <http://aristote.obspm.fr/MIS/pdr/pdr1.html>

Black 1986 and references therein). The $J'' > 4$ population scales with the UV intensity, so we re-evaluate this point for PDRs and circumstellar disks in Sects. 5.6.2 and 5.6.3.

The line profiles of CO, H₂ and H are taken to be Voigt functions, with default Doppler widths (b) of 0.3, 3.0 and 5.0 km s⁻¹, respectively. We adopt Draine (1978) as our standard unattenuated interstellar radiation field.

5.3.2 Unshielded photodissociation rates

We obtain an unshielded CO photodissociation rate of 2.6×10^{-10} s⁻¹. This rate is 30% higher than that of vDB88, due to the generally larger oscillator strengths in our data set. The new data for bands 33 and 24 (the $E0$ and $K0$ transitions) have the largest effect: they account for 63 and 21% of the overall increase. Clearly, the rate depends on the choice of radiation field. If we adopt Habing (1968), Gondhalekar et al. (1980) or Mathis et al. (1983) instead of Draine (1978), the photodissociation rate becomes 2.0, 2.0 or 2.3×10^{-10} s⁻¹, respectively. The same relative differences between these three fields were reported by vDB88.

5.3.3 Shielding by CO, H₂ and H

Self-shielding, shielding by H, H₂ and the other CO isotopologues, and continuum shielding by dust all reduce the photodissociation rates inside a cloud or other environment relative to the unshielded rates. For a given combination of column densities (N) and visual extinction (A_V), the photodissociation rate for isotopologue i is

$$k_i = \chi k_{0,i} \Theta_i \exp(-\gamma A_V), \quad (5.2)$$

with χ a scaling factor for the UV intensity and $k_{0,i}$ the unattenuated rate in a given radiation field. The shielding function Θ_i accounts for self-shielding and shielding by H, H₂ and the other CO isotopologues; tabulated values for typical model parameters are presented in Table 5.5. The dust extinction term, $\exp(-\gamma A_V)$, is discussed in Sect. 5.3.4. Equation (5.2) assumes the radiation is coming from all directions. If this is not the case, such as for a cloud irradiated only from one side, $k_{0,i}$ should be reduced accordingly.

For now, we ignore dust shielding and compute the depth-dependent dissociation rates due to line shielding only. Our test case is the centre of the diffuse cloud towards the star ζ Oph. The observed column densities of H, H₂, ¹²CO and ¹³CO are 5.2×10^{20} , 4.2×10^{20} , 2.5×10^{15} and 1.5×10^{13} cm⁻² (van Dishoeck & Black 1986, Lambert et al. 1994), and we take C¹⁷O, C¹⁸O, ¹³C¹⁷O and ¹³C¹⁸O column densities of 4.1×10^{11} , 1.6×10^{12} , 5.9×10^9 and 2.3×10^{10} cm⁻², consistent with observational constraints. For the centre of the cloud, we adopt half of these values. We set $b(\text{CO}) = 0.48$ km s⁻¹ and $T_{\text{ex}}(\text{CO}) = 4.2$ K (Sheffer et al. 1992), and we populate the H₂ rotational levels explicitly according to the observed distribution. The cloud is illuminated by three times the Draine field ($\chi = 3$).

Table 5.4 lists the relative contribution of the most important bands at the edge and centre for each isotopologue, as well as the overall photodissociation rate at each point. The column densities are small, but isotope-selective shielding already occurs: the ¹²CO rate at the centre is lower than that of the other isotopologues by factors of three to six.

Table 5.4 – Relative and absolute shielding effects for the ten most important bands in the ζ Oph cloud.^a

Band	33	28	24	23	22	20	19	16	15	13	Total ^c
λ_0 (Å) ^b	1076.1	985.6	970.4	968.9	968.3	956.2	950.0	941.2	940.0	933.1	
¹² CO											
Edge (%) ^d	32.2	4.7	8.7	3.0	3.6	3.4	4.3	5.1	3.5	3.1	7.8(-10)
Centre (%) ^d	2.8	0.4	5.7	9.3	0.8	12.1	13.8	6.1	11.0	7.0	7.5(-11)
Shielding ^e	0.0084	0.0072	0.063	0.30	0.022	0.34	0.31	0.12	0.30	0.22	0.10
¹⁷ C ¹⁸ O											
Edge (%)	32.0	4.7	8.7	3.0	3.6	3.4	4.3	5.1	3.5	3.1	7.8(-10)
Centre (%)	22.0	0.1	5.3	3.5	0.8	8.7	10.3	14.2	9.1	2.4	2.4(-10)
Shielding	0.21	0.0067	0.19	0.36	0.065	0.79	0.74	0.85	0.81	0.23	0.31
¹⁸ C ¹⁸ O											
Edge (%)	31.5	5.1	6.2	1.5	4.9	3.7	4.7	5.2	3.8	3.4	7.2(-10)
Centre (%)	35.3	0.1	4.7	2.6	7.8	3.3	7.7	8.1	5.9	3.0	3.7(-10)
Shielding	0.58	0.0067	0.39	0.88	0.82	0.46	0.83	0.80	0.81	0.45	0.52
¹³ CO											
Edge (%)	28.1	6.5	8.3	1.8	5.2	3.4	4.3	4.9	3.9	2.4	7.8(-10)
Centre (%)	18.5	0.0	5.3	4.4	11.2	4.1	10.7	4.4	9.1	0.8	2.8(-10)
Shielding	0.23	0.0007	0.23	0.87	0.76	0.42	0.87	0.32	0.83	0.13	0.35
¹³ C ¹⁷ O											
Edge (%)	28.0	6.3	8.3	1.8	5.2	3.4	4.3	4.9	3.9	2.4	7.8(-10)
Centre (%)	32.5	0.0	7.4	2.9	7.5	5.0	7.2	8.5	6.1	1.0	4.2(-10)
Shielding	0.63	0.0007	0.48	0.88	0.79	0.78	0.91	0.94	0.85	0.24	0.54
¹³ C ¹⁸ O											
Edge (%)	30.1	7.0	5.9	1.5	4.7	3.6	4.4	5.0	4.0	2.4	7.5(-10)
Centre (%)	39.0	0.0	5.8	2.4	5.7	1.7	7.5	8.5	6.3	1.7	4.1(-10)
Shielding	0.71	0.0007	0.54	0.87	0.67	0.26	0.92	0.94	0.85	0.38	0.55

The $E0$ band is the most important contributor at the edge. This was also found by vDB88, and the higher oscillator strength now adopted makes it even stronger. Going to the centre, it saturates rapidly for ^{12}CO : its absolute contribution to the total dissociation rate decreases by two orders of magnitude, and it goes from the strongest band to the 12th strongest band. The five strongest bands at the centre are the same as in vDB88: Nos. 13, 15, 19, 20 and 23.

Figure 5.1 illustrates the isotope-selective shielding. The left panel is centred on the R(1) line of the $E0$ band (No. 33 from Table 5.1). This line is fully saturated in ^{12}CO and the relative intensity of the radiation field (I/I_0 , with I_0 the intensity at the edge of the cloud) goes to zero. ^{13}CO and C^{18}O also visibly reduce the intensity, to $I/I_0 = 0.50$ and 0.72 , but the other three isotopologues are not abundant enough to do so. Consequently, these three are not self-shielded in the ζ Oph cloud, but they are shielded by ^{12}CO , ^{13}CO and C^{18}O . The weaker shielding of $^{13}\text{C}^{17}\text{O}$ and $^{13}\text{C}^{18}\text{O}$ in the $E0$ band compared to C^{17}O is due to their lines having less overlap with the ^{12}CO lines.

The right panel of Fig. 5.1 contains the R(0) line of the $W1$ band (No. 20), with the R(1) line present as a shoulder on the red wing. Also visible is the saturated B13 R(2) line of H_2 at 956.58 \AA . The $W1$ band is weaker than the $E0$ band, so ^{12}CO is the only isotopologue to cause any appreciable reduction in the radiation field and to be (partially) self-shielded. The shielding of the other five isotopologues is dominated by overlap with the ^{12}CO and H_2 lines. This figure also shows the need for accurate line positions: if the $^{13}\text{C}^{18}\text{O}$ line were shifted by 0.1 \AA in either direction, it would no longer overlap with the H_2 line and be less strongly shielded. Note that the position of the $W1$ band has only been measured for ^{12}CO , ^{13}CO and C^{18}O , so we have to compute the position for the other isotopologues from theoretical isotopic relations. This causes the C^{17}O line to appear longwards of the C^{18}O line.

5.3.4 Continuum shielding by dust

Dust can provide a very strong attenuation of the radiation field. This effect is largely independent of wavelength for the $912\text{--}1118 \text{ \AA}$ radiation available to dissociate CO, so it affects all isotopologues to the same extent. It can be expressed as an exponential function of the visual extinction, as in Eq. (5.2). For typical interstellar dust grains (radius of $0.1 \mu\text{m}$ and optical properties from Roberge et al. 1991), the extinction coefficient γ is 3.53 for CO (van Dishoeck et al. 2006). Larger grains have less opacity in the UV and do not shield CO as strongly. For ice-coated grains with a mean radius of $1 \mu\text{m}$, appropriate for circumstellar disks (Jonkheid et al. 2006), the extinction coefficient is only 0.6. The effects of dust shielding are discussed more fully in Sect. 5.6.

Table 5.4 – footnotes.

- ^a See the text for the adopted column densities, Doppler widths, excitation temperatures and radiation field.
- ^b ^{12}CO band head position.
- ^c Total photodissociation rate in s^{-1} at the edge and the centre, and the shielding factor at the centre.
- ^d Relative contribution per band to the overall photodissociation rate at the edge and the centre of the cloud.
- ^e Shielding factor per band: the absolute contribution at the centre divided by that at the edge.

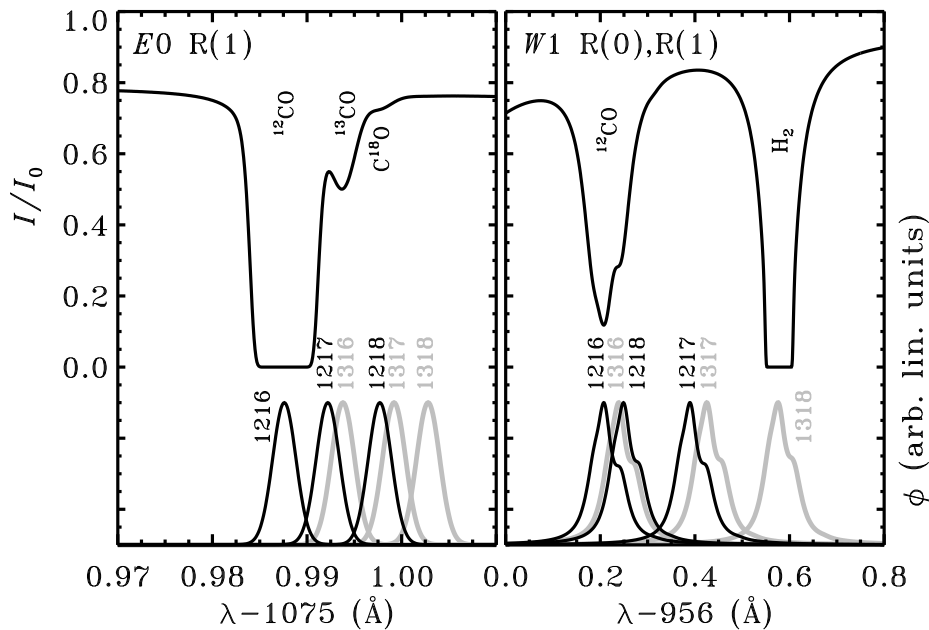


Figure 5.1 – Relative intensity of the radiation field (I/I_0) and intrinsic line profiles for the six CO isotopologues (ϕ , in arbitrary linear units) at the centre of the ζ Oph cloud in two wavelength ranges.

Photodissociation of CO may still take place even in highly extinguished regions. Cosmic rays or energetic electrons generated by cosmic rays can excite H_2 , allowing it to emit in a multitude of bands, including the Lyman and Werner systems (Prasad & Tarafdar 1983). The resulting UV photons can dissociate CO at a rate of about 10^{-15} s^{-1} (Gredel et al. 1987), independent of depth. That is enough to increase the atomic C abundance by some three orders of magnitude compared to a situation where the photodissociation rate is absolutely zero. The cosmic-ray-induced photodissociation rate is sensitive to the spectroscopic constants of CO, especially where it concerns the overlap between CO and H_2 lines, so it would be interesting to redo the calculations of Gredel et al. with the new data from Table 5.1. However, that is beyond the scope of this chapter.

5.3.5 Uncertainties

The uncertainties in the molecular data are echoed in the model results. When coupled to a chemical network, as in Sect. 5.6, the main observables produced by the model are the column densities of the CO isotopologues for a given astrophysical environment. The accuracy of the photodissociation rates is only relevant in a specific range of depths; in the average interstellar UV field, this range runs from an A_V of ~ 0.2 to ~ 2 mag. Photo-

processes are so dominant at lower extinctions and so slow at higher extinctions that the exact rate does not matter. In the intermediate regime, both the absolute photodissociation rates and the differences between the rates for individual isotopologues are important. The oscillator strengths are the key variable in both cases and these are generally known rather accurately. Taking account of the experimental uncertainties in the band oscillator strengths and of the theoretical uncertainties in computing the properties for individual lines, and identifying which bands are important contributors (Table 5.4), we estimate the absolute photodissociation rates to be accurate to about 20%. This error margin carries over into the absolute CO abundances and column densities for the $A_V \approx 0.2\text{--}2$ mag range when the rates are put into a chemical model. The accuracy on the rates and abundances of the isotopologues relative to each other is estimated to be about 10% when summed over all states, even when we allow for the kind of isotope effects suggested by Chakraborty et al. (2008).

5.4 Excitation temperature and Doppler width

The calculations of vDB88 were only done for low excitation temperatures of CO and H₂. Here, we extend this work to higher temperatures, as required for PDRs and disks, and we re-examine the effect of the Doppler widths of CO, H₂ and H on the photodissociation rates. We first treat four cases separately, increasing either $T_{\text{ex}}(\text{CO})$, $b(\text{CO})$, $T_{\text{ex}}(\text{H}_2)$ or $b(\text{H}_2)$. At the end of this section we combine these effects in a grid of excitation temperatures and Doppler widths. As a template model we take the centre of the ζ Oph cloud, with column densities and other parameters as described in Sect. 5.3.3.

5.4.1 Increasing $T_{\text{ex}}(\text{CO})$

As the excitation temperature of CO increases, additional rotational levels are populated and photodissociation is spread across more lines. Figures 5.2 and 5.3 visualise this for band 13 of ¹²CO. At 4 K, only four lines are active: the R(0), R(1), P(1) and P(2) lines at 933.02, 932.98, 933.09 and 933.12 Å. The R(0) and P(1) lines are both fully self-shielded at the line centre. Going to 16 K, the R(0) line loses about 70% of its intrinsic intensity and ceases to be self-shielding. In addition, the R(2), P(3) and higher- J lines start to absorb. The combination of less saturated low- J lines and more active higher- J lines yields a 39% higher photodissociation rate at 16 K compared to 4 K.

A higher CO excitation temperature has the same favourable effect for ¹³CO, which is partially self-shielded at the centre of the ζ Oph cloud. Its photodissociation rates increase by 16% when going from 4 to 16 K. C¹⁸O is also partially self-shielded, but less so than ¹³CO, so the favourable effect is smaller. At the same time, it suffers from increased overlap by ¹²CO. The net result is a small increase in the photodissociation rate of 0.2%.

The two heaviest isotopologues, ¹³C¹⁷O and ¹³C¹⁸O, are not abundant enough to be self-shielded. Their $J'' < 2$ lines generally have little overlap with the corresponding ¹²CO lines, especially in the E0 band near 1076 Å. This band, whose lines are amongst the narrowest in our data set, is the strongest contributor to the photodissociation rate at the

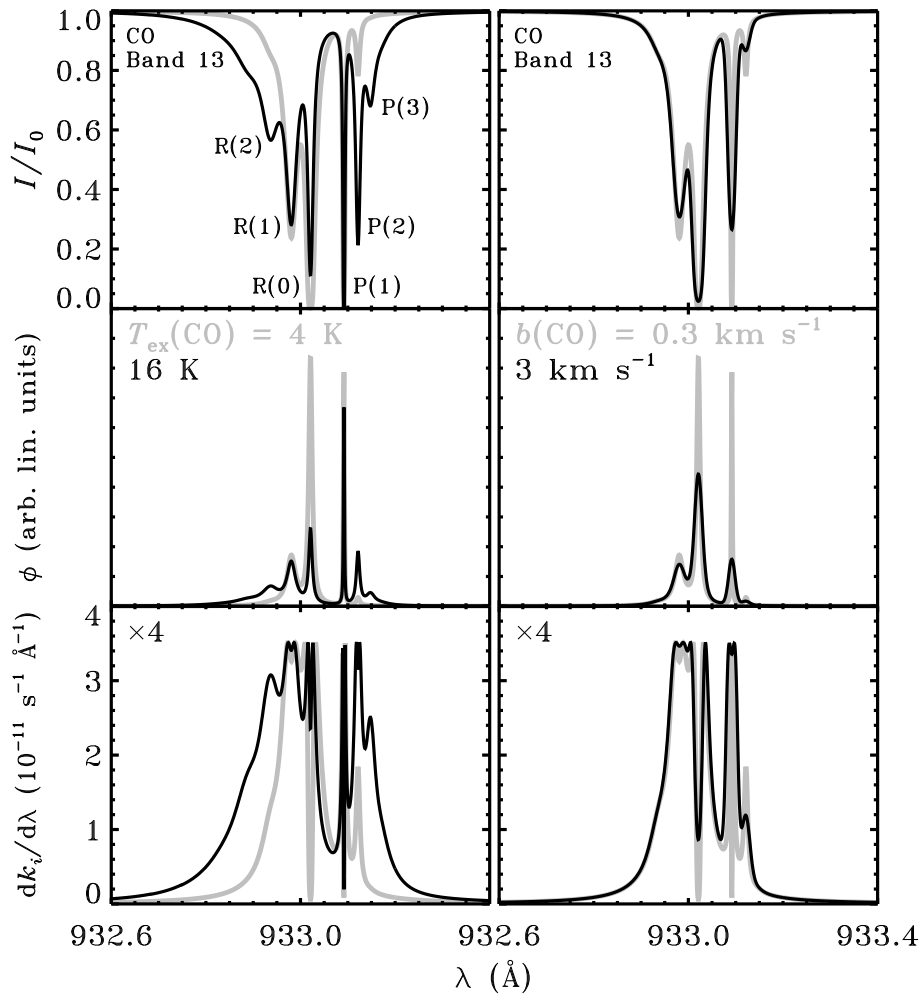


Figure 5.2 – Illustration of the effect of increasing $T_{\text{ex}}(\text{CO})$ (left) or $b(\text{CO})$ (right) in our ζ Oph cloud model (Sect. 5.3.3). Top: relative intensity of the radiation field, including absorption by ^{12}CO only. Middle: intrinsic line profile for band 13 (933.1 Å) of ^{12}CO . Bottom: photodissociation rate per unit wavelength, multiplied by a constant as indicated.

centre of the cloud for $^{13}\text{C}^{17}\text{O}$ and $^{13}\text{C}^{18}\text{O}$ (Table 5.4). In fact, its narrow lines are part of the reason it is the strongest contributor. The $J''=3$ and 4 lines that become active at 16 K do have some overlap with ^{12}CO . Without the favourable effect of less self-shielding, this causes the photodissociation rate for $^{13}\text{C}^{17}\text{O}$ and $^{13}\text{C}^{18}\text{O}$ to decrease for higher excitation

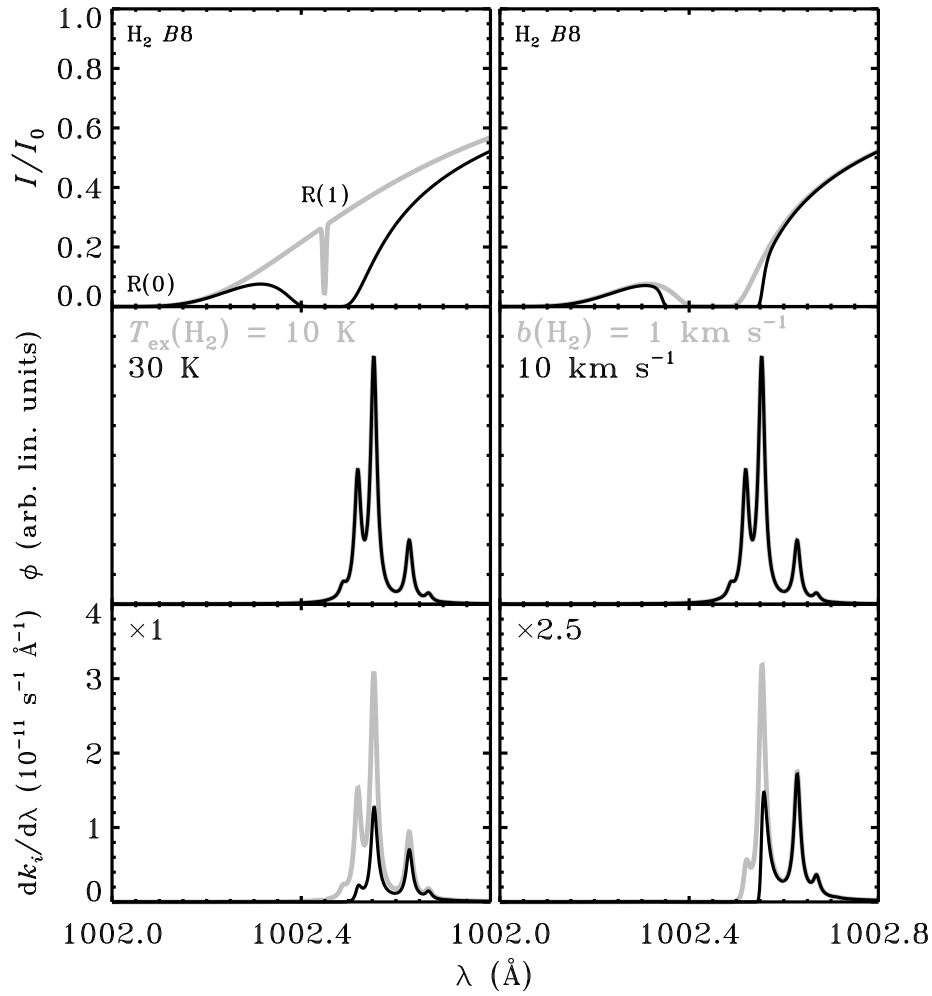


Figure 5.3 – Illustration of the effect of increasing $T_{\text{ex}}(\text{H}_2)$ (left) or $b(\text{H}_2)$ (right) in our ζ Oph cloud model (Sect. 5.3.3). Top: relative intensity of the radiation field, including absorption by H_2 only. Middle: intrinsic line profile for band 30 (1002.6 \AA) of ^{12}CO . Bottom: photodissociation rate per unit wavelength, multiplied by a constant as indicated.

temperatures. The change is only small, though: 0.4% for $^{13}\text{C}^{17}\text{O}$ and 2% for $^{13}\text{C}^{18}\text{O}$.

Finally, C^{17}O experiences an increase of 18% in its photodissociation rate. Its lines lie closer to those of ^{12}CO than do the $^{13}\text{C}^{17}\text{O}$ and $^{13}\text{C}^{18}\text{O}$ lines, so it is generally more strongly shielded. At 4 K, most of the shielding is due to the saturated R(0) lines of ^{12}CO .

These become partially unsaturated at higher $T_{\text{ex}}(\text{CO})$, so the corresponding R(0) lines of C^{17}O become a stronger contributor to the photodissociation rate, even though the shift towards higher- J lines make them intrinsically weaker. Overall, increasing $T_{\text{ex}}(\text{CO})$ from 4 to 16 K thus results in a higher C^{17}O photodissociation rate.

5.4.2 Increasing $b(\text{CO})$

The width of the absorption lines is due to Doppler broadening and natural (or lifetime) broadening. The integrated intensity in each line remains the same when $b(\text{CO})$ increases, so a larger width is accompanied by a lower peak intensity. The resulting reduction in self-shielding then causes a higher ^{12}CO photodissociation rate, as shown in Fig. 5.2 for band 13. However, the effect is rather small because the Doppler width is smaller than the natural width for most lines at typical b values. Natural broadening is the dominant broadening mechanism up to $b(\text{CO}) \approx 6 \times 10^{-12} A_{\text{tot}}$, with both parameters in their normal units. The R(0) line of band 13 has an inverse lifetime of $1.8 \times 10^{11} \text{ s}^{-1}$ (Tables 5.1 and 5.3), so Doppler broadening becomes important at about 1 km s^{-1} . From 0.3 to 3 km s^{-1} , as in Fig. 5.2, the line width only increases by a factor of 1.9. Integrated over all lines, the ^{12}CO photodissociation rate becomes 26% higher.

The rates of the other five isotopologues decrease along this $b(\text{CO})$ interval due to increased shielding by the $E0$ lines of ^{12}CO . With an inverse lifetime of only $1 \times 10^9 \text{ s}^{-1}$, Doppler broadening is this band's dominant broadening mechanism in the regime of interest. A tenfold increase in the Doppler parameter from 0.3 to 3 km s^{-1} results in a nearly tenfold increase in the line widths. At 0.3 km s^{-1} , the $E0$ lines of ^{12}CO are still sufficiently narrow that they do not strongly shield the lines of the other isotopologues. This is no longer the case at 3 km s^{-1} . ^{13}CO still benefits somewhat from reduced self-shielding in other bands, but it is not enough to overcome the reduced strength of the $E0$ band, and its photodissociation rates decrease by 2%. The decrease is 13% for C^{17}O and 26–28% for the remaining three isotopologues. The relatively small decrease for C^{17}O is due to its $E0$ band being already partially shielded by ^{12}CO at 0.3 km s^{-1} , so the stronger shielding at 3 km s^{-1} has less of an effect.

5.4.3 Increasing $T_{\text{ex}}(\text{H}_2)$ or $b(\text{H}_2)$

Increasing the excitation temperature of H_2 , while keeping the CO parameters constant, results in a decreased photodissociation rate for all six isotopologues. The cause, as illustrated in Fig. 5.3, is the activation of more H_2 lines. At $T_{\text{ex}}(\text{H}_2) = 10 \text{ K}$, the R(1) line of the B8 band at 1002.45 \AA is very narrow and does not shield the F0 band (No. 30) of the CO isotopologues. (The continuum-like shielding visible in Fig. 5.3 is due to the strongly saturated B8 R(0) line at 1001.82 \AA .) It becomes much more intense at 30 K and widens due to being saturated, thereby shielding part of the F0 band. The same thing happens to other CO bands, resulting in an overall rate decrease of 0.6–2.5%. There is no particular trend visible amongst the isotopologues; the magnitude of the rate change depends purely on the chance that a given CO band overlaps with an H_2 line.

Similar decreases of one or two percent in the CO photodissociation rates are seen when the H₂ Doppler width is changed from 1 to 10 km s⁻¹. As the H₂ lines become broader, the amount of overlap with CO increases across the entire wavelength range. As an example, Fig. 5.3 shows again the 1002.0–1002.8 Å region, where the B8 R(1) line of H₂ further reduces the contribution of the F0 band to the ¹²CO photodissociation rate.

5.4.4 Grid of T_{ex} and b

We now combine the four individual cases into a grid of excitation temperatures and Doppler widths to see how they influence each other. $T_{\text{ex}}(\text{CO})$ is raised from 4 to 512 K in steps of factors of two. The $v''=1$ vibrational level of ¹²CO lies at 2143 cm⁻¹ above the $v''=0$ level, so it starts to be thermally populated at ~500 K. No data are available on dissociative transitions out of this level, so we choose not to go to higher excitation temperatures. We increase the range of rotational levels up to $J''=39$, at 2984 cm⁻¹ above the $J''=0$ level for ¹²CO. At $T_{\text{ex}}(\text{CO}) = 512$ K, the normalised population distribution peaks at $J''=9$ and decreases to 9.7×10^{-5} at $J''=39$. The H₂ excitation temperature is set to $[T_{\text{ex}}(\text{CO})]^{1.5}$ to take account of the fact that its critical densities for thermalisation are lower than those of CO. Where necessary, absorption by rotational levels above our normal limit of $J''=7$ and by non-zero vibrational levels is taken into account (Dabrowski 1984, Abgrall et al. 1993a,b). All H₂ rovibrational levels are strictly thermally populated; no UV pumping is included. The grid is run for CO Doppler widths of 0.1, 0.3, 1.0 and 3.2 km s⁻¹; we set $b(\text{H}_2) = \sqrt{14}b(\text{CO})$ and $b(\text{H}) = \sqrt{28}b(\text{CO})$, corresponding to the differences appropriate for thermal broadening.

The top set of panels in Fig. 5.4 shows the photodissociation rate of the six isotopologues at the centre of the ζ Oph cloud as a function of excitation temperature for the different Doppler widths. The rates are normalised to the rate at 4 K. The ¹²CO rate increases from 4 to 16 K, as described in Sect. 5.4.1. At higher temperatures the increased overlap with H₂ lines takes over and the rate goes down. As long as the CO excitation temperature is less than ~100 K, the ¹²CO rate remains constant up to $b(\text{CO}) = 0.3$ km s⁻¹ and increases as $b(\text{CO})$ goes from 0.3 to 3.2 km s⁻¹ (bottom part of Fig. 5.4). At higher temperatures there is so much shielding by H₂ that reduced self-shielding in the CO lines has no discernible effect on the rate. Instead, the rate goes down with b due to stronger shielding by the broadened H₂ lines.

The ¹³CO rate also increases initially with $T_{\text{ex}}(\text{CO})$ and then goes down as H₂ shielding takes over. The rate increases from $b(\text{CO}) = 0.1$ to 0.3 km s⁻¹, but decreases for higher values as described in Sect. 5.4.2. For the remaining four isotopologues, the plotted curves likewise result from a combination of weaker shielding by ¹²CO and stronger shielding by H₂. At CO excitation temperatures between 4 and 8 K, the rates typically change by a few per cent either way. Going to higher temperatures, all rates decrease monotonically. Likewise, the rates generally decrease towards higher $b(\text{CO})$ values.

A change in behaviour is seen when increasing $T_{\text{ex}}(\text{CO})$ from 256 to 512 K. It is at this point that the $v''>0$ levels of H₂ become populated. Less energy is now needed to excite H₂ to the B and C states, so absorption shifts towards longer wavelengths. This causes even stronger shielding in the heavy CO isotopologues, for whom the E0 band at 1076 Å

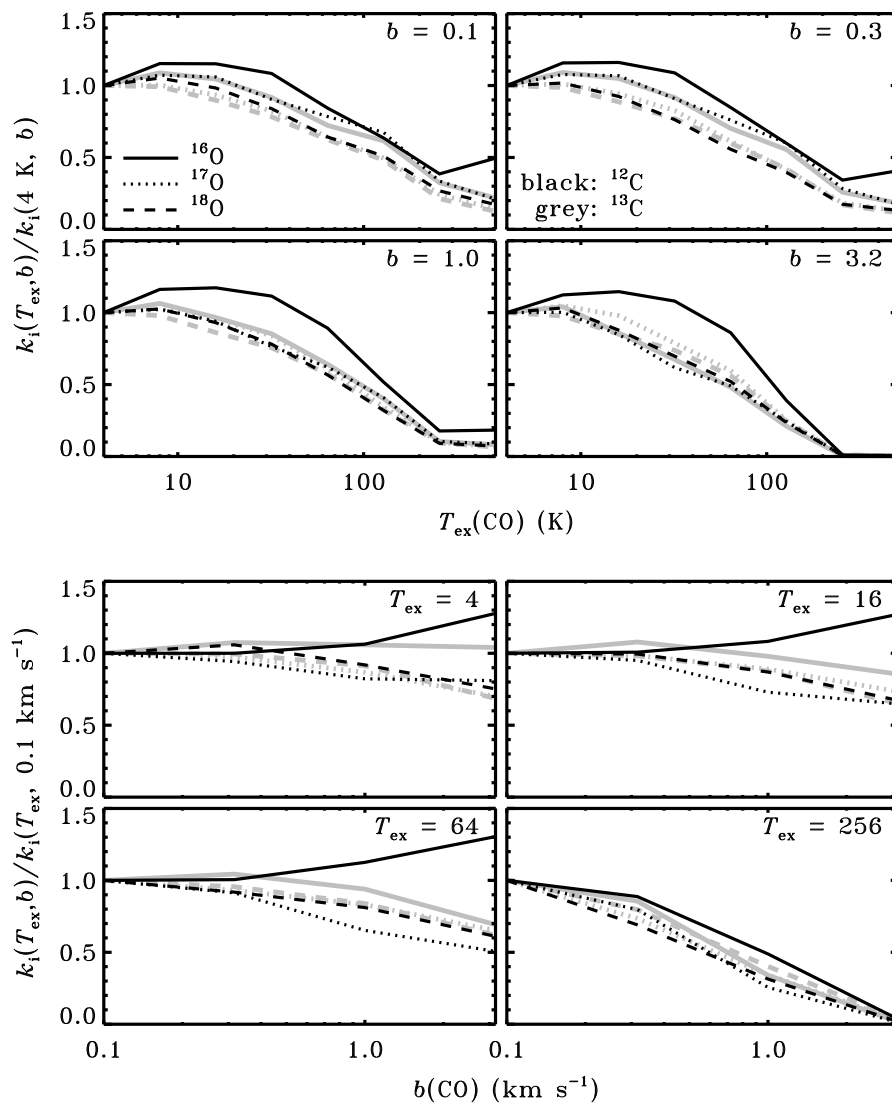


Figure 5.4 – Top: photodissociation rate of the CO isotopologues as a function of excitation temperature, normalised to the rate at 4 K, at four different Doppler widths, for parameters corresponding to the centre of the ζ Oph diffuse cloud. Bottom: photodissociation rates as a function of Doppler width, normalised to the rate at 0.1 km s⁻¹, at four different excitation temperatures. The other model parameters are as in Sect. 5.3.3, except $b(\text{H}_2) = \sqrt{14}b(\text{CO})$, $b(\text{H}) = \sqrt{28}b(\text{CO})$ and $T_{\text{ex}}(\text{H}_2) = [T_{\text{ex}}(\text{CO})]^{1.5}$.

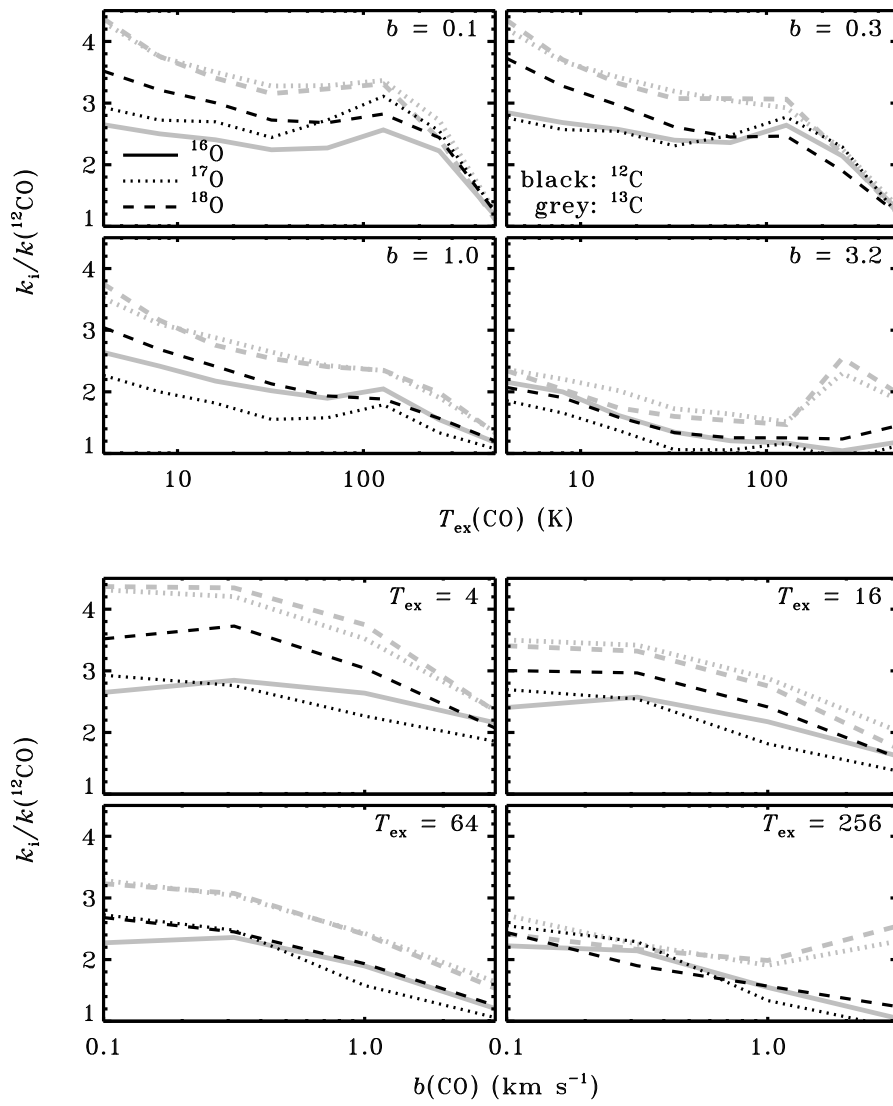


Figure 5.5 – As Fig. 5.4, but with all rates normalised to the ^{12}CO rate.

is still an important contributor to the photodissociation rate, at least as long as $b(\text{CO})$ does not exceed 0.3 km s^{-1} . The $E0$ band is strongly self-shielded in ^{12}CO (Table 5.4), so the shift of the H_2 absorption to longer wavelengths does not reduce its contribution by much. In fact, the weaker H_2 absorption at shorter wavelengths allows for an increased contribution of bands like Nos. 13 and 16 at 933 and 941 Å, causing a net increase in the ^{12}CO photodissociation rate from 256 to 512 K. The situation changes somewhat when the CO Doppler width increases to 1.0 km s^{-1} or more. The $E0$ band of the heavy isotopologues is now much less of a contributor, because it is shielded by the broader ^{12}CO lines. The shifting H_2 absorption does not cause any additional shielding, so the rates remain almost the same. Furthermore, the H_2 lines are also broader and continue to shield the ^{12}CO bands at shorter wavelengths, preventing its photodissociation rate from increasing like it does in the low- b cases.

The main astrophysical consequence becomes clear when we look at the dissociation rates of the five heavier isotopologues with respect to that of ^{12}CO . Figure 5.5 shows this $k_i/k(^{12}\text{CO})$ ratio as a function of $T_{\text{ex}}(\text{CO})$ and $b(\text{CO})$. The ratios generally decrease with both parameters: a higher excitation temperature and a larger Doppler width both cause less self-shielding in ^{12}CO , so the rate differences between the isotopologues become smaller. Shielding by H_2 increases at the same time, further reducing the differences between the isotopologues. This means that photodissociation of CO is more strongly isotope-selective in cold sources than in hot sources.

5.5 Shielding function approximations

It is unpractical for many astrophysical applications to do the full integration of all 5622 lines in our model every time a photodissociation rate is required. Therefore, we present approximations to the shielding functions Θ introduced in Eq. (5.2). The approximations are derived for several sets of model parameters and are valid across a wide range of astrophysical environments (Sect. 5.5.2).

5.5.1 Shielding functions on a grid of $N(\text{CO})$ and $N(\text{H}_2)$

The transition from atomic to molecular hydrogen occurs much closer to the edge of the cloud than the $\text{C}^+ - \text{C} - \text{CO}$ transition, so the column density of atomic H is roughly constant at the depths where shielding of CO is important. In addition, H shields CO by only a few per cent. Therefore, it is a good approximation to compute the shielding functions on a grid of CO and H_2 column densities, while taking a constant column of H. It is sufficient to express the shielding of all CO isotopologues as a function of $N(^{12}\text{CO})$, because self-shielding of the heavier CO isotopologues is a small effect compared to shielding by ^{12}CO .

Table 5.5 presents the shielding functions in the same manner as vDB88 did, but for somewhat different model parameters: $b(\text{CO}) = 0.3$ instead of 1.0 km s^{-1} , $T_{\text{ex}}(\text{CO}) = 5$ instead of 10 K, and $T_{\text{ex}}(\text{H}_2) = 5^{1.5}$ instead of $10^{1.5}$ K. The present parameters correspond more closely to what is observed in diffuse and translucent clouds. The column density

ratios for the six isotopologues are kept constant at the elemental isotope ratios from Wilson (1999): $[^{12}\text{C}]/[^{13}\text{C}] = 69$, $[^{16}\text{O}]/[^{18}\text{O}] = 557$ and $[^{18}\text{O}]/[^{17}\text{O}] = 3.6$. A small column of $5.2 \times 10^{15} \text{ cm}^{-2}$ of H_2 at $J''=4-7$ is included throughout (except at $\log N(\text{H}_2) = 0$) to account for UV pumping (Sect. 5.3.1).³ Shielding functions for larger values of b and T_{ex} and for other isotope ratios are given in the online appendix to the paper that this chapter is based on (Visser et al. 2009). For ease of use, we have also set up a webpage⁴ where the shielding functions can be downloaded in plain text format. This webpage offers shielding functions for a wider variety of parameters than is possible to include in this chapter or the paper. In addition, it uses a grid of $N(^{12}\text{CO})$ and $N(\text{H}_2)$ values that is five times finer than the grid in Table 5.5, allowing for more accurate interpolation.

For column densities of up to 10^{17} cm^{-2} of CO and 10^{21} cm^{-2} of H_2 , our shielding functions are generally within a few per cent of the vDB88 values when corrected for the difference in b and T_{ex} . Larger differences occur for larger columns: we predict the shielding to be five times weaker at $N(\text{CO}) = 10^{19} \text{ cm}^{-2}$ and more than a hundred times stronger at $N(\text{H}_2) = 10^{23} \text{ cm}^{-2}$. The 912-1118 Å wavelength range was divided into 23 bins by vDB88, and most lines were included only in one bin to speed up the computation. We integrate all lines over all wavelengths. As the lines get strongly saturated at high column depths, absorption in the line wings becomes important. Thus, H_2 lines can cause substantial shielding over a range of more than 10 Å, while CO lines may still absorb several Å away from the line centre. The binned integration method of vDB88 did not take these effects into account, so they underpredicted shielding at large H_2 columns and overpredicted shielding at large CO columns (Fig. 5.6). It should be noted, however, that photodissociation at these depths is typically already so slow a process that it is no longer the dominant destruction pathway for CO. In addition, a large CO column is usually accompanied by a large H_2 column, so the two effects partially cancel each other.

5.5.2 Comparison between the full model and the approximations

Despite being computed for a limited number of model parameters, the shielding functions from Table 5.5 and the online appendix to Visser et al. (2009) provide a good approximation to the rates from the full model for a wide range of astrophysical environments. Section 5.6.1 presents a grid of translucent cloud models, where the photodissociation model is coupled to a chemical network and CO is traced as a function of depth. This presents a large range of column densities, with the ratios between the isotopologues deviating from the fixed values adopted for Table 5.5. The grid covers gas densities from 100 to 1000 cm^{-3} and gas temperatures from 15 to 100 K, while keeping the excitation temperatures and Doppler widths constant at the values used for Table 5.5. Altogether, the grid contains 2880 points per isotopologue where the photodissociation rate is computed. Here, we compare the photodissociation rates from the approximate method to the full integration for each of these points. The sensitivity of $k(^{13}\text{CO})$ to the $N(^{12}\text{CO})/N(^{13}\text{CO})$ ratio can be corrected for in a simple manner: we use the shielding functions from Table

³ Although not mentioned explicitly by vDB88, their tabulated shielding functions also include this extra column of $J''=4-7 \text{ H}_2$.

⁴ <http://www.strw.leidenuniv.nl/~ewine/photo>

Table 5.5 – Two-dimensional shielding functions $\Theta[N(^{12}\text{CO}), N(\text{H}_2)]^a$

log $N(\text{H}_2)$ (cm^{-2})	log ^{12}CO (cm^{-2})							
	0	13	14	15	16	17	18	19
^{12}CO : unattenuated rate $k_{0,i} = 2.592 \times 10^{-10} \text{ s}^{-1}$								
0	1.000	8.080(-1)	5.250(-1)	2.434(-1)	5.467(-2)	1.362(-2)	3.378(-3)	5.240(-4)
19	8.176(-1)	6.347(-1)	3.891(-1)	1.787(-1)	4.297(-2)	1.152(-2)	2.922(-3)	4.662(-4)
20	7.223(-1)	5.624(-1)	3.434(-1)	1.540(-1)	3.515(-2)	9.231(-3)	2.388(-3)	3.899(-4)
21	3.260(-1)	2.810(-1)	1.953(-1)	8.726(-2)	1.907(-2)	4.768(-3)	1.150(-3)	1.941(-4)
22	1.108(-2)	1.081(-2)	9.033(-3)	4.441(-3)	1.102(-3)	2.644(-4)	7.329(-5)	1.437(-5)
23	3.938(-7)	3.938(-7)	3.936(-7)	3.923(-7)	3.901(-7)	3.893(-7)	3.890(-7)	3.875(-7)
C^{17}O : unattenuated rate $k_{0,i} = 2.607 \times 10^{-10} \text{ s}^{-1}$								
0	1.000	9.823(-1)	8.911(-1)	6.149(-1)	3.924(-1)	2.169(-1)	4.167(-2)	2.150(-3)
19	8.459(-1)	8.298(-1)	7.490(-1)	5.009(-1)	3.196(-1)	1.850(-1)	3.509(-2)	1.984(-3)
20	7.337(-1)	7.195(-1)	6.481(-1)	4.306(-1)	2.741(-1)	1.556(-1)	2.645(-2)	1.411(-3)
21	3.335(-1)	3.290(-1)	3.039(-1)	2.293(-1)	1.685(-1)	9.464(-2)	1.460(-2)	6.823(-4)
22	1.193(-2)	1.191(-2)	1.172(-2)	1.095(-2)	9.395(-3)	5.644(-3)	1.183(-3)	2.835(-5)
23	3.959(-7)	3.959(-7)	3.959(-7)	3.959(-7)	3.958(-7)	3.954(-7)	3.924(-7)	3.873(-7)
C^{18}O : unattenuated rate $k_{0,i} = 2.392 \times 10^{-10} \text{ s}^{-1}$								
0	1.000	9.974(-1)	9.777(-1)	8.519(-1)	5.060(-1)	1.959(-1)	2.764(-2)	1.742(-3)
19	8.571(-1)	8.547(-1)	8.368(-1)	7.219(-1)	4.095(-1)	1.581(-1)	2.224(-2)	1.618(-3)
20	7.554(-1)	7.532(-1)	7.371(-1)	6.336(-1)	3.572(-1)	1.372(-1)	1.889(-2)	1.383(-3)
21	3.559(-1)	3.549(-1)	3.477(-1)	3.035(-1)	1.948(-1)	7.701(-2)	1.071(-2)	6.863(-4)
22	1.214(-2)	1.212(-2)	1.199(-2)	1.105(-2)	8.233(-3)	3.324(-3)	6.148(-4)	3.225(-5)
23	4.251(-7)	4.251(-7)	4.251(-7)	4.251(-7)	4.249(-7)	4.233(-7)	4.180(-7)	4.142(-7)

Table 5.5 – continued.

log $N(\text{H}_2)$ (cm^{-2})	log ^{12}CO (cm^{-2})							
	0	13	14	15	16	17	18	19
^{13}CO : unattenuated rate $k_{0,i} = 2.595 \times 10^{-10} \text{ s}^{-1}$								
0	1.000	9.824(-1)	9.019(-1)	6.462(-1)	3.547(-1)	9.907(-2)	1.131(-2)	7.591(-4)
19	8.447(-1)	8.276(-1)	7.502(-1)	5.113(-1)	2.745(-1)	7.652(-2)	8.635(-3)	6.747(-4)
20	7.415(-1)	7.266(-1)	6.581(-1)	4.451(-1)	2.360(-1)	6.574(-2)	7.187(-3)	5.429(-4)
21	3.546(-1)	3.502(-1)	3.270(-1)	2.452(-1)	1.398(-1)	3.750(-2)	3.973(-3)	2.703(-4)
22	1.180(-2)	1.177(-2)	1.153(-2)	1.023(-2)	6.728(-3)	1.955(-3)	2.665(-4)	1.471(-5)
23	2.385(-7)	2.385(-7)	2.385(-7)	2.384(-7)	2.379(-7)	2.348(-7)	2.310(-7)	2.292(-7)
$^{13}\text{C}^{17}\text{O}$: unattenuated rate $k_{0,i} = 2.598 \times 10^{-10} \text{ s}^{-1}$								
0	1.000	9.979(-1)	9.820(-1)	8.832(-1)	5.942(-1)	3.177(-1)	1.523(-1)	3.885(-2)
19	8.540(-1)	8.520(-1)	8.374(-1)	7.469(-1)	4.901(-1)	2.677(-1)	1.302(-1)	3.135(-2)
20	7.405(-1)	7.387(-1)	7.254(-1)	6.439(-1)	4.198(-1)	2.333(-1)	1.142(-1)	2.607(-2)
21	3.502(-1)	3.494(-1)	3.434(-1)	3.076(-1)	2.214(-1)	1.386(-1)	6.941(-2)	1.195(-2)
22	1.279(-2)	1.278(-2)	1.267(-2)	1.198(-2)	1.045(-2)	7.743(-3)	4.088(-3)	4.581(-4)
23	2.370(-7)	2.370(-7)	2.370(-7)	2.370(-7)	2.369(-7)	2.368(-7)	2.359(-7)	2.312(-7)
$^{13}\text{C}^{18}\text{O}$: unattenuated rate $k_{0,i} = 2.503 \times 10^{-10} \text{ s}^{-1}$								
0	1.000	9.988(-1)	9.900(-1)	9.329(-1)	7.253(-1)	3.856(-1)	1.524(-1)	2.664(-2)
19	8.744(-1)	8.734(-1)	8.656(-1)	8.164(-1)	6.403(-1)	3.441(-1)	1.347(-1)	2.491(-2)
20	7.572(-1)	7.562(-1)	7.492(-1)	7.047(-1)	5.518(-1)	3.006(-1)	1.185(-1)	2.224(-2)
21	3.546(-1)	3.542(-1)	3.506(-1)	3.283(-1)	2.638(-1)	1.666(-1)	6.887(-2)	1.149(-2)
22	1.561(-2)	1.560(-2)	1.550(-2)	1.475(-2)	1.235(-2)	7.850(-3)	3.416(-3)	5.290(-4)
23	2.490(-7)	2.490(-7)	2.490(-7)	2.489(-7)	2.487(-7)	2.482(-7)	2.471(-7)	2.421(-7)

^a These shielding functions were computed for the Draine (1978) radiation field ($\chi = 1$) and the following set of parameters: $b(\text{CO}) = 0.3 \text{ km s}^{-1}$, $b(\text{H}_2) = 3.0 \text{ km s}^{-1}$ and $b(\text{H}) = 5.0 \text{ km s}^{-1}$; $T_{\text{ex}}(\text{CO}) = 5 \text{ K}$ and $T_{\text{ex}}(\text{H}_2) = 5^{1.5} \text{ K}$; $N(\text{H}) = 5 \times 10^{20} \text{ cm}^{-2}$; $N(^{12}\text{CO})/N(^{13}\text{CO}) = 69$, $N(^{12}\text{CO})/N(\text{C}^{18}\text{O}) = N(^{13}\text{CO})/N(^{13}\text{C}^{18}\text{O}) = 557$ and $N(\text{C}^{18}\text{O})/N(\text{C}^{17}\text{O}) = N(^{13}\text{C}^{18}\text{O})/N(^{13}\text{C}^{17}\text{O}) = 3.6$. Self-shielding is mostly negligible for the heavier isotopologues, so all shielding functions are expressed as a function of the ^{12}CO column density. Continuum attenuation by dust is not included in this table (see Eq. (5.2)).

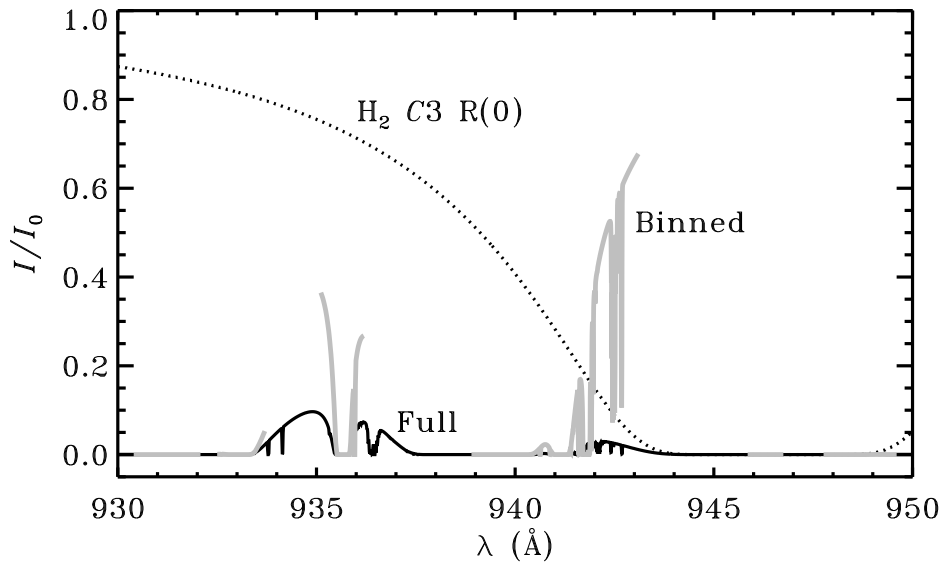


Figure 5.6 – Illustration of the effect of limited integration ranges. Solid black curve: relative intensity of the radiation field at $N(\text{CO}) = 10^{18}$ and $N(\text{H}_2) = 10^{22} \text{ cm}^{-2}$ for the parameters of Table 5.5, computed with a full integration of all lines over all wavelengths. Grey curve: the same, but computed with the binned integration method of vDB88. Dotted curve: attenuation due to the C3 R(0) line of H_2 , centred on 946.42 Å. This line was not included by vDB88 when computing the shielding in the 938.9–943.1 Å bin, thus overestimating the photodissociation rate in the W2 band at 941.1 Å.

8 of Visser et al. (2009) when the ratio is closer to 35 than to 69, and those from Table 5.5 (this chapter) otherwise.

The rate from our approximate method is within 10% of the “real” rate in 98.3% of all points (Fig. 5.7). In no cases is the difference between the approximate rates and the full model more than 40%. Perhaps even more important than the absolute photodissociation rates are the ratios, Q , between the rates of ^{12}CO and the other five isotopologues $^x\text{C}^y\text{O}$:

$$Q_i = \frac{k(^x\text{C}^y\text{O})}{k(^{12}\text{CO})}. \quad (5.3)$$

The shielding functions from Table 5.5 and Visser et al. (2009) together reproduce the ratios from the full method to the same accuracy as the absolute rates. At 98.4% of all points in the grid of translucent clouds, the ratios are off by less than 10% (Fig. 5.7). Similar scores can be obtained for models of PDRs or other environments if one uses shielding functions computed for the right combination of parameters. Otherwise, the accuracy goes down. For example, the shielding functions from Table 5.5 can easily give rates off by a factor of two when applied to a high-density, high-temperature PDR.

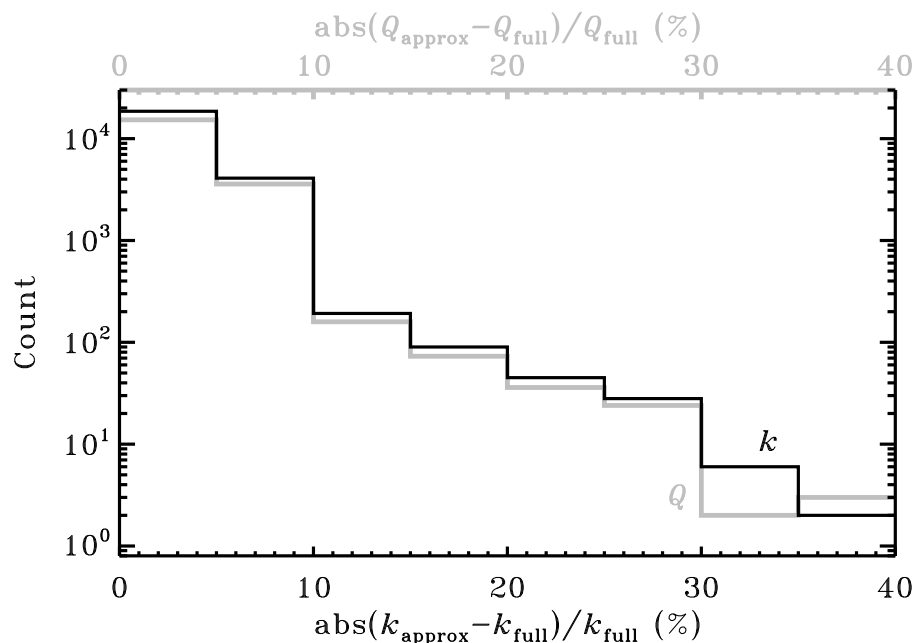


Figure 5.7 – Histogram of the absolute relative difference between the approximate method (see text for details) and the full computation for the absolute photodissociation rates (k , black line) and the isotopologue rate ratios (Q , grey line) in a grid of translucent cloud models. The data for all six isotopologues are taken together, but the Q values for ^{12}CO (which are unity regardless of the method) are omitted.

5.6 Chemistry of CO: astrophysical implications

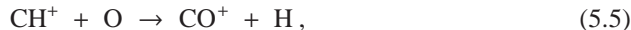
Photodissociation is an important destruction mechanism for CO in many environments. In this section, we couple the photodissociation model to a small chemical network in order to explore abundances and column densities. Specifically, we model the CO chemistry in translucent clouds, PDRs and circumstellar disks, and we compare our results to observations of such objects. The photodissociation rates are computed with our full model throughout this section.

5.6.1 Translucent clouds

5.6.1.1 Model setup

Translucent clouds, with visual extinctions between 1 and 5 mag, form an excellent test case for our CO photodissociation model. Two recent studies of several dozen lines of sight through diffuse ($A_V < 1$ mag) and translucent clouds provide a set of CO and H₂

column densities for comparison (Sonnentrucker et al. 2007, Sheffer et al. 2008). These surveys show a clear correlation between $N(\text{H}_2)$ and $N(^{12}\text{CO})$, with distinctly different slopes for H_2 columns of less and more than $2.5 \times 10^{20} \text{ cm}^{-2}$. Sheffer et al. attributed this break to a change in the formation mechanism of CO. Their models show that the two-step conversion from C^+ to CH^+ and CO^+ ,



followed by reaction with H (forming CO directly) or H_2 (forming HCO^+ , which then recombines with an electron to give CO) is the dominant pathway at low column densities. However, the highly endothermic Reaction (5.4) is not fast enough at gas kinetic temperatures typical for these environments to explain the observed abundances of CH^+ and CO. Suprathermal chemistry has been suggested as a solution to this problem. Sheffer et al. followed the approach of Federman et al. (1996), who argued that Alfvén waves entering the cloud from the outside result in non-thermal motions between ions and neutrals. Other mechanisms have been suggested by Joulain et al. (1998) and Pety & Falgarone (2000). The effect of the Alfvén waves can be incorporated into a chemical model by replacing the kinetic temperature in the rate equation for Reaction (5.4) and all other ion-neutral reactions by an effective temperature:

$$T_{\text{eff}} = T_{\text{gas}} + \frac{\mu v_A^2}{3k_B}. \quad (5.6)$$

Here, k_B is the Boltzmann constant, μ is the reduced mass of the reactants and v_A is the Alfvén speed. The Alfvén waves reach a depth of a few 10^{20} cm^{-2} of H_2 , corresponding to an A_V of a few tenths of a magnitude, beyond which suprathermal chemistry ceases to be important. CO can therefore no longer be formed efficiently through Reactions (5.4) and (5.5), and the reaction between C^+ and OH (producing CO either directly or via a CO^+ intermediate) takes over as the key route to CO. The identification of these two different chemistry regimes supports the conclusion of Zsargó & Federman (2003) that suprathermal chemistry is required to explain observed CO abundances in diffuse environments. Suprathermal chemistry also drives up the HCO^+ abundance, confirming the conclusion of Liszt & Lucas (1994) and Liszt (2007) that HCO^+ is the dominant precursor to CO in diffuse clouds.

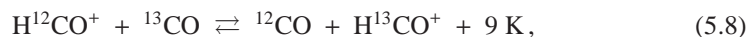
We present here a grid of translucent cloud models to see how well the new photodissociation results match the observations. We set the Alfvén speed to 3.3 km s^{-1} for $N(\text{H}_2) < 4 \times 10^{20} \text{ cm}^{-2}$ and to zero for larger column densities (Sheffer et al. 2008). The grid comprises densities ($n_{\text{H}} = n(\text{H}) + 2n(\text{H}_2)$) of 100, 300, 500, 700 and 1000 cm^{-3} , gas temperatures of 15, 30, 50 and 100 K, and relative UV intensities (χ) of 1, 3 and 10. The dust temperature is assumed to stay low for all models ($\sim 15 \text{ K}$), so the H_2 formation rate does not change. The ionisation rate of H_2 due to cosmic rays is set to a constant value of $1.3 \times 10^{-17} \text{ s}^{-1}$. Attenuation by $0.1 \mu\text{m}$ dust grains (Sect. 5.3.4) is taken into account. The Doppler widths and level populations are as described in Sect. 5.3.1, with CO and H_2

Table 5.6 – Elemental abundances.

Element	Abundance relative to n_{H}	Element	Abundance relative to n_{H}
He	1.00×10^{-1}	^{16}O	3.10×10^{-4}
^{12}C	1.40×10^{-4}	^{17}O	1.55×10^{-7}
^{13}C	2.03×10^{-6}	^{18}O	5.57×10^{-7}

excitation temperatures of 5 and $5^{1.5}$ K. Taking other b or T_{ex} values plausible for these environments does not alter our results significantly. All models are run to an A_{V} of 5 mag; results are also presented for a range of smaller extinctions.

The models require a chemical network to compute the abundances at each depth step. Since we are only interested in CO, the number of relevant species and reactions is limited. We adopt the network from a recent PDR benchmark study (Röllig et al. 2007), which includes only 31 species consisting of H, He, C and O. We duplicate all C- and O-containing species and reactions for ^{13}C , ^{17}O and ^{18}O . Freeze-out and thermal evaporation are added for all neutral species, but no grain-surface reactions are included other than H_2 formation according to Black & van Dishoeck (1987). We add ion-molecule exchange reactions such as



which can enhance the abundances of the heavy isotopologues of CO and HCO^+ (Watson et al. 1976, Smith & Adams 1980, Langer et al. 1984). The temperature dependence of the rate of these two reactions was fitted by Liszt (2007); the alternative equations from Woods & Willacy (2009) give the same results. The effective temperature from Eq. (5.6) is used instead of the kinetic temperature for all ion-neutral reactions, including Reactions (5.7) and (5.8). Altogether, the network contains 118 species and 1723 reactions. We adopt the elemental abundances of Cardelli et al. (1996) and isotope ratios appropriate for the local ISM ($^{12}\text{C}/^{13}\text{C} = 69$, $^{16}\text{O}/^{18}\text{O} = 557$ and $^{18}\text{O}/^{17}\text{O} = 3.6$; Wilson 1999); the complete list of elemental abundances is given in Table 5.6. Chemical steady state is reached at all depths after ~ 1 Myr, regardless of whether the gas starts in atomic or molecular form.

5.6.1.2 ^{12}CO

The left panel of Fig. 5.8 shows $N(^{12}\text{CO})$ versus $N(\text{H}_2)$ for all depth steps in our grid. These and other column densities are also listed for a set of selected A_{V} values in the online appendix to the paper that this chapter is based on (Visser et al. 2009). The scatter in the data is due to the different physical parameters. For a given $N(\text{H}_2)$, $N(^{12}\text{CO})$ is about two times larger at $T_{\text{gas}} = 100$ K than at 15 K. The formation rate of H_2 increases with temperature; through the chain of reactions starting with Reaction (5.4), that results in a larger CO abundance and column density. Up to $N(\text{H}_2) = 10^{21} \text{ cm}^{-2}$, increasing the

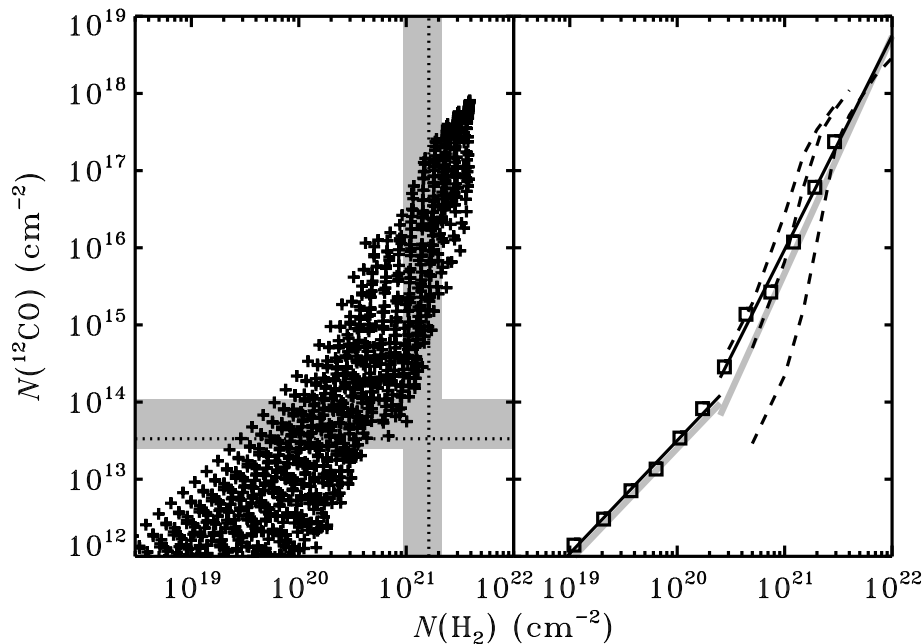


Figure 5.8 – Column densities of ^{12}CO versus those of H_2 . Left: data for all points with $A_V \leq 5$ mag from our grid of translucent cloud models. The vertical grey band indicates the range over which photodissociation ceases to be the dominant destruction mechanism of ^{12}CO ; the dotted line is the median. Likewise, the horizontal band indicates the range over which ^{12}CO becomes self-shielding. Right: 100-point means of our model results (black squares), fitted with two straight lines. Also shown are the fits to the observations by Sheffer et al. (2008, grey lines) and the results from the translucent cloud models of vDB88 for $\chi = 0.5, 1$ and 10 (dashed lines, left to right).

gas density by a factor of ten increases $N(^{12}\text{CO})/N(\text{H}_2)$ also by about a factor of ten. This is due to the photodissociation rate being mostly independent of density, while the rates of the two-body reactions forming CO are not. Photodissociation ceases to be the main destruction mechanism for CO deeper into the cloud, so increasing n_{H} has a smaller effect there. Increasing the UV intensity from $\chi = 1$ to 10 has the simple effect of decreasing $N(^{12}\text{CO})/N(\text{H}_2)$ roughly tenfold for $N(\text{H}_2) < 10^{21} \text{ cm}^{-2}$. For larger depths, changing χ only has a small effect. These dependencies on the physical parameters are consistent with the observations of Sheffer et al. (2008).

The full set of points already gives some indication that the data are not well represented by a global single-slope correlation. The right panel of Fig. 5.8 shows the 100-point means of the full set, revealing the same two distinct regimes as found by Sheffer et al. (2008). Taking the uncertainties in both the observations and the models into account, the two sets of power-law fits (indicated by the black and grey lines) are identical. The break

between the two slopes occurs at $N(\text{H}_2) = 2.5 \times 10^{20} \text{ cm}^{-2}$ and is due to the switch from suprathermal to normal chemistry. It is clearly unrelated to the switch from UV photons to He^+ or H_3^+ as the main destroyer of ^{12}CO , which does not occur until $N(\text{H}_2) = 1\text{--}2 \times 10^{21} \text{ cm}^{-2}$. When we extend the grid to higher A_V (not plotted), we quickly reach the point where the ^{12}CO abundance equals the elemental ^{12}C abundance and the plot of $N(^{12}\text{CO})$ versus $N(\text{H}_2)$ continues with a slope of unity. The model results from vDB88 (dashed lines, corresponding to $\chi = 0.5, 1$ and 10) do not extend to low enough $N(\text{H}_2)$ to show the suprathermal regime, but they do show at the upper end the transition to the regime where all gas-phase carbon is in CO.

5.6.1.3 ^{13}CO

With our model able to reproduce the observational relationship between H_2 and ^{12}CO , the next step is to look at the heavier isotopologues. Sonnentrucker et al. (2007), Burgh et al. (2007) and Sheffer et al. (2007) together presented a sample of 29 diffuse and translucent sources with derived column densities for both ^{12}CO and ^{13}CO . These data are plotted in the left panel of Fig. 5.9 (grey crosses) as $N(^{13}\text{CO})$ versus $N(\text{H}_2)$. The 100-point means from our model grid (black squares) agree with the observations to within a factor of three. The model results are again best fitted with two power laws, but the ^{13}CO observations do not extend to low enough $N(\text{H}_2)$ to confirm this.

The observations show considerable scatter in the $N(^{12}\text{CO})/N(^{13}\text{CO})$ ratio, with some sources deviating by a factor of two either way from the local elemental ^{12}C - ^{13}C ratio of 69 ± 6 (Wilson 1999). It has long been assumed that the enhanced ratios are due to isotope-selective photodissociation and that the reduced ratios are due to isotope-exchange reactions. However, no answer has been found so far to the question of why one process dominates in some sources, and the other process in other sources (Langer et al. 1980, McCutcheon et al. 1980, Sheffer et al. 1992, Lambert et al. 1994, Federman et al. 2003, Sonnentrucker et al. 2007, Sheffer et al. 2007). Chemical models consistently show that isotope exchange is more efficient than selective photodissociation for observed cloud temperatures of up to ~ 60 K. The models can easily reproduce $N(^{12}\text{CO})/N(^{13}\text{CO})$ ratios of less than 69, but they leave the ratios of more than 69 unexplained.

Our grid of models suggests that the answer lies in suprathermal chemistry. The right panel of Fig. 5.9 shows a plot of $N(^{12}\text{CO})/N(^{13}\text{CO})$ versus $N(\text{H}_2)$ for the observations (grey) and for all depth steps at $A_V \leq 5$ from our models (black plus signs). Also shown are the 100-point means from the model, offset by a factor of three for clarity. The $N(^{12}\text{CO})/N(^{13}\text{CO})$ ratio initially increases from 69 to a mean of 151 at $N(\text{H}_2) = 4 \times 10^{20} \text{ cm}^{-2}$, then decreases to a mean of 51 at $1 \times 10^{21} \text{ cm}^{-2}$, and gradually increases again for larger depths. The turnover from the initial rise to the rapid drop is due to the transition from suprathermal to normal chemistry.

At an Alfvén speed of $v_A = 3.3 \text{ km s}^{-1}$, the effective temperature for Reaction (5.7) is about 4000 K, so the forward and backward reactions are equally fast. Photodissociation is therefore the only active fractionation process and it enhances the amount of ^{12}CO relative to ^{13}CO . As we move beyond the depth to which the Alfvén waves reach ($N(\text{H}_2) = 4 \times 10^{20} \text{ cm}^{-2}$ in our model), suprathermal chemistry is brought to a halt. The forward

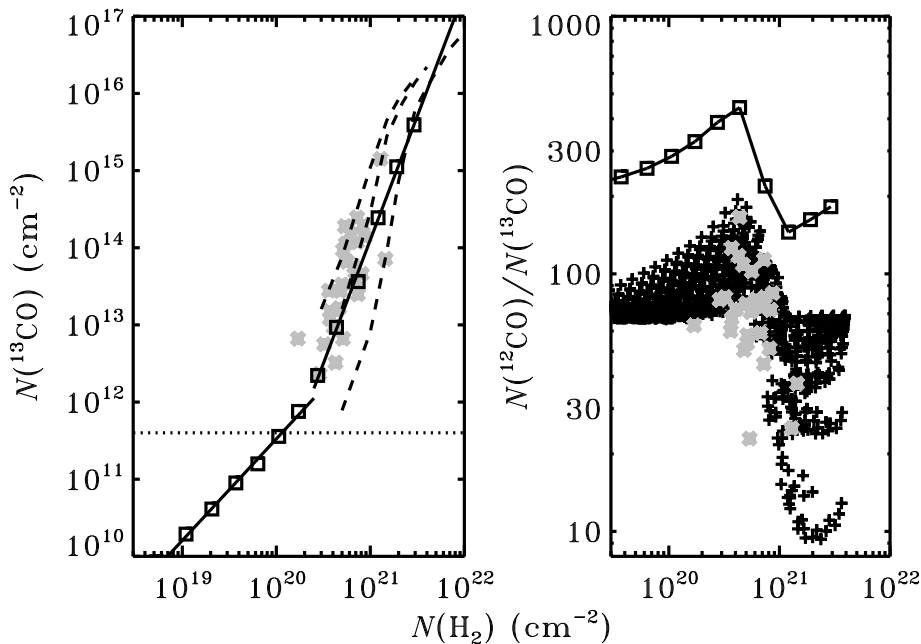


Figure 5.9 – Column densities of ^{13}CO (left) and column density ratios of ^{12}CO to ^{13}CO (right) plotted against the column density of H_2 . Grey crosses: observations of Sonnentrucker et al. (2007), Burgh et al. (2007) and Sheffer et al. (2007). Black squares and straight lines: 100-point means from our grid of translucent cloud models, offset by a factor of three in the right panel. Dotted line: median depth at which ^{12}CO becomes self-shielding. Black plus signs: model data for all points with $A_V \leq 5$ mag. Dashed lines: data from the translucent cloud models of vDB88 for $\chi = 0.5, 1$ and 10 (left to right).

channel of Reaction (5.7) becomes faster than the backward channel and isotope exchange now reverses the fractionation. When we reach a depth of $N(\text{H}_2) = 1\text{--}2 \times 10^{21} \text{ cm}^{-2}$, the $^{13}\text{C}^+$ abundance drops too low to sustain further fractionation and the $N(^{12}\text{CO})/N(^{13}\text{CO})$ ratio gradually returns to the elemental ratio of 69.

The observations show a downward trend in the $N(^{12}\text{CO})/N(^{13}\text{CO})$ ratio in the $N(\text{H}_2)$ range from 2×10^{20} to $2 \times 10^{21} \text{ cm}^{-2}$. This supports a rapid switch from selective photodissociation to isotope-exchange reactions being the dominant fractionation mechanism. A firm test of our model predictions requires observational data at both smaller and larger $N(\text{H}_2)$ than are currently available.

5.6.1.4 Other isotopologues

Moving to the next two isotopologues, C^{17}O and C^{18}O , the number of observed column densities goes down to three. Lambert et al. (1994) determined a ratio between $N(^{12}\text{CO})$

and $N(\text{C}^{18}\text{O})$ of 1550 ± 440 for the ζ Oph diffuse cloud, some three times larger than the elemental ^{16}O - ^{18}O ratio of 557 ± 30 (Wilson 1999). An even higher ratio of 3000 ± 600 was recorded by Sheffer et al. (2002) for the X Per translucent cloud, along with an $N(^{12}\text{CO})/N(\text{C}^{17}\text{O})$ ratio of 8700 ± 3600 . The elemental ^{16}O - ^{18}O ratio is about four times smaller: 2000 ± 200 .

The H_2 column density towards X Per (HD 24534) is $8.5 \times 10^{20} \text{ cm}^{-2}$ (Sonnentrucker et al. 2007, Sheffer et al. 2007). Our grid of models gives $N(^{12}\text{CO})/N(\text{C}^{18}\text{O}) = 680\text{--}3880$ (median 1080) and $N(^{12}\text{CO})/N(\text{C}^{17}\text{O}) = 2520\text{--}10\,600$ (median 3660) for that value, consistent with the observations. Out of the three parameters that we varied, χ affects the ratios most strongly. Both ratios decrease by a factor of two when χ is increased from 1 to 10. The onset of self-shielding of ^{12}CO , and with it the onset of isotopic fractionation, occurs deeper into the cloud for a stronger UV field. Therefore, $N(^{12}\text{CO})/N(\text{C}^{18}\text{O})$ and $N(^{12}\text{CO})/N(\text{C}^{17}\text{O})$ are smaller at any given depth.

In order to further explore the behaviour of C^{17}O and C^{18}O , we take a more detailed look at our results for $n_{\text{H}} = 300 \text{ cm}^{-3}$, $T_{\text{gas}} = 50 \text{ K}$ and $\chi = 1$ (model C2 α from Table 12 of Visser et al. 2009). This also allows for a comparison with $^{13}\text{C}^{17}\text{O}$ and $^{13}\text{C}^{18}\text{O}$. Both of these have been detected in interstellar clouds (Langer et al. 1980, Bensch et al. 2001), but column densities have not yet been derived.

The photodissociation rates of CO and H_2 for this combination of parameters are plotted in Fig. 5.10 as a function of depth (z) into the cloud. The isotope-selective nature of the photodissociation is clearly visible. At a depth of 4.0 pc ($A_{\text{V}} = 2.3 \text{ mag}$, $N(\text{H}_2) = 1.7 \times 10^{21} \text{ cm}^{-2}$), ^{12}CO photodissociates about 7 times slower than ^{13}CO , 15–18 times slower than C^{17}O and C^{18}O , and 23–26 times slower than $^{13}\text{C}^{17}\text{O}$ and $^{13}\text{C}^{18}\text{O}$. At depths between 0.4 and 3.4 pc ($A_{\text{V}} = 0.3\text{--}2.0 \text{ mag}$), the photodissociation of C^{18}O proceeds faster than that of C^{17}O . The lines of the latter lie closer to those of ^{12}CO and are therefore more strongly shielded, as was the case for the diffuse ζ Oph cloud (Table 5.4). As the CO column grows larger in our model cloud, C^{18}O becomes self-shielding and its rate drops below that of C^{17}O around 3.4 pc.

The extent to which each isotopologue is fractionated can easily be seen from the cumulative column density ratios when they are normalised to ^{12}CO and the isotope ratios:

$$\mathcal{R}_i(z) = \frac{N_z(^x\text{C}^y\text{O})}{N_z(^{12}\text{CO})} \frac{[^{12}\text{C}]}{[^x\text{C}]} \frac{[^{16}\text{O}]}{[^y\text{O}]}, \quad (5.9)$$

with $[Z]$ the elemental abundance of isotope Z and

$$N_z(^x\text{C}^y\text{O})(z) = \int_0^z n(^x\text{C}^y\text{O}) dz' \quad (5.10)$$

the cumulative column density. A plot of $\mathcal{R}(^{13}\text{CO})$ as function of depth (Fig. 5.11) shows the same trends as the model data in Fig. 5.9: the amount of ^{13}CO is reduced ($\mathcal{R} < 1$) up to a certain depth and is enhanced ($\mathcal{R} > 1$) farther in by isotope-exchange reactions. We only see $\mathcal{R} < 1$ for C^{17}O and C^{18}O because $^{17}\text{O}^+$ and $^{18}\text{O}^+$ never become abundant enough to convert C^{16}O in a reaction similar to Reaction (5.7). Photodissociation ceases to be the dominant destruction mechanism for C^{17}O and C^{18}O around $z = 4 \text{ pc}$ (Fig. 5.10), so it can no longer cause substantial fractionation and \mathcal{R} gradually returns to unity.

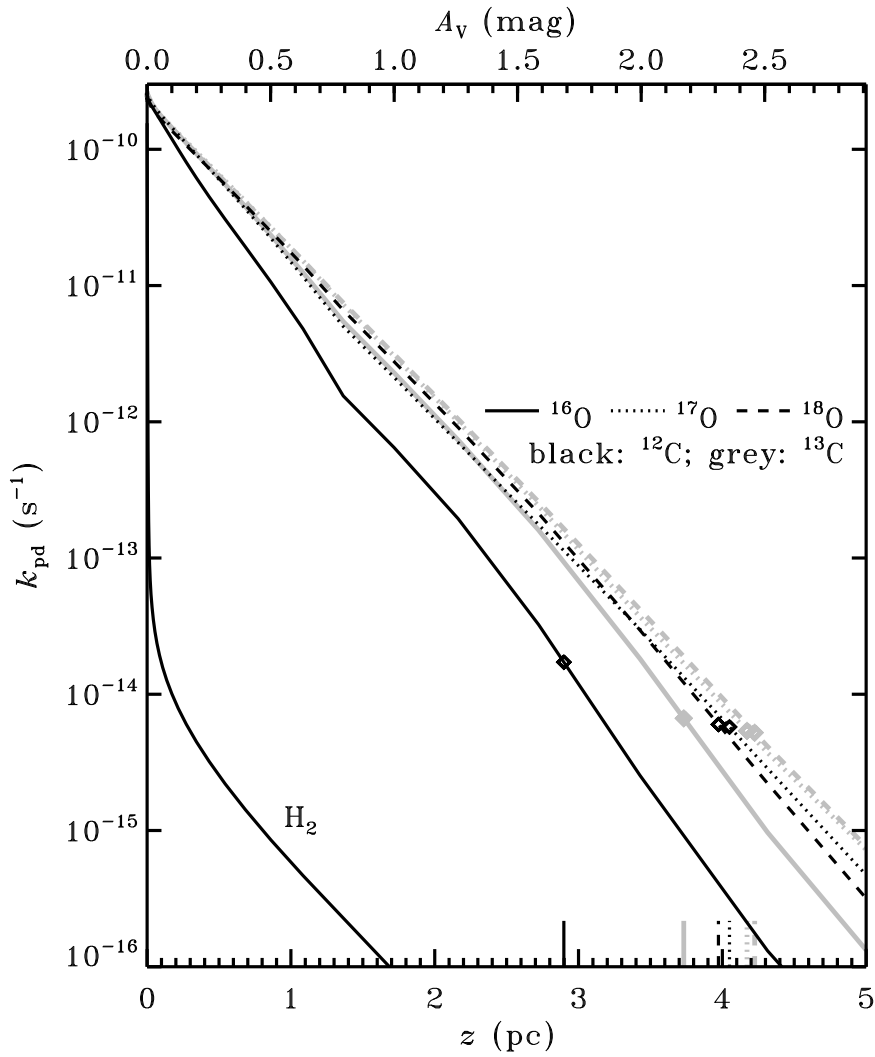


Figure 5.10 – Photodissociation rates of H_2 and the six CO isotopologues as a function of depth into translucent cloud model C2 α (Table 12 of Visser et al. 2009) with $n_{\text{H}} = 300 \text{ cm}^{-3}$, $T_{\text{gas}} = 50 \text{ K}$ and $\chi = 1$. Attenuation by dust is included. The diamonds and corresponding markers on the bottom axis indicate the depth at which He^+ takes over from UV radiation as the dominant destroyer for each isotopologue.

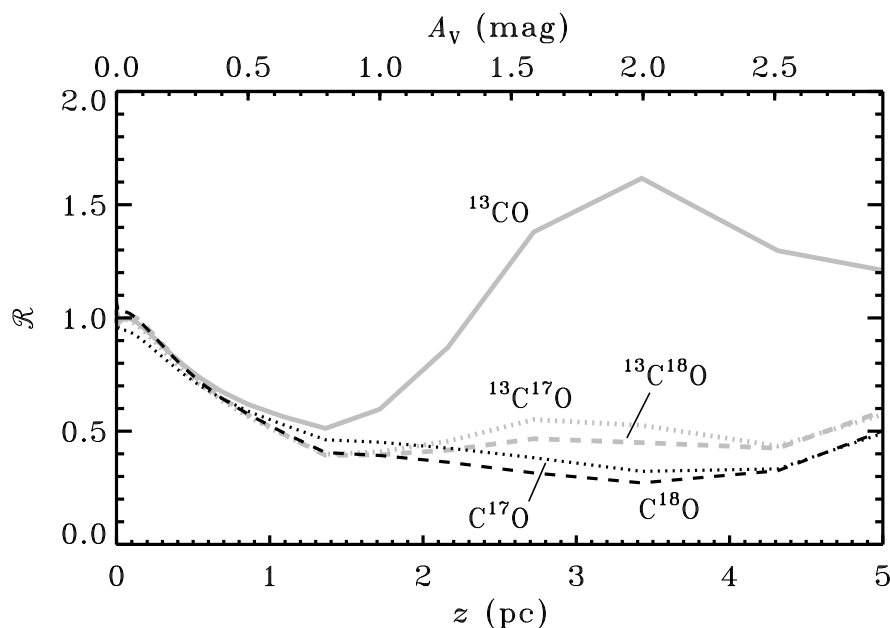


Figure 5.11 – Cumulative column densities of the CO isotopologues normalised to ^{12}CO and the elemental isotopic abundances (Eq. (5.9)) as a function of depth into translucent cloud model C2 α (Table 12 of Visser et al. 2009).

The remaining two isotopologues, $^{13}\text{C}^{17}\text{O}$ and $^{13}\text{C}^{18}\text{O}$, experience the fractionation of ^{13}C and $^{17}\text{O}/^{18}\text{O}$ simultaneously. Isotope exchange enhances their abundances relative to C^{17}O and C^{18}O , in the same manner that it enhances the abundance of ^{13}CO relative to ^{12}CO . However, isotope-selective photodissociation is a stronger effect for the two heaviest isotopologues, so \mathcal{R} remains less than unity. This result holds across our entire grid of translucent cloud models.

5.6.2 Photon-dominated regions

Photon-dominated regions (PDRs) form another type of objects where photodissociation is a key process in controlling the CO abundance. Their densities are higher (n_{H} up to $\sim 10^6 \text{ cm}^{-3}$) than those of diffuse and translucent clouds and they are exposed to stronger UV fields (χ up to $\sim 10^6$; Hollenbach & Tielens 1997). Observational efforts have mostly gone into mapping the structure of PDRs, so CO column densities are tabulated only for a small number of sources. For most of these the column density of neutral carbon has also been determined. There are no direct measurements of H_2 column densities; instead, $N(\text{H}_2)$ is usually obtained from $N(^{12}\text{CO})$ using a typical abundance ratio between the two species (e.g., Frerking et al. 1982).

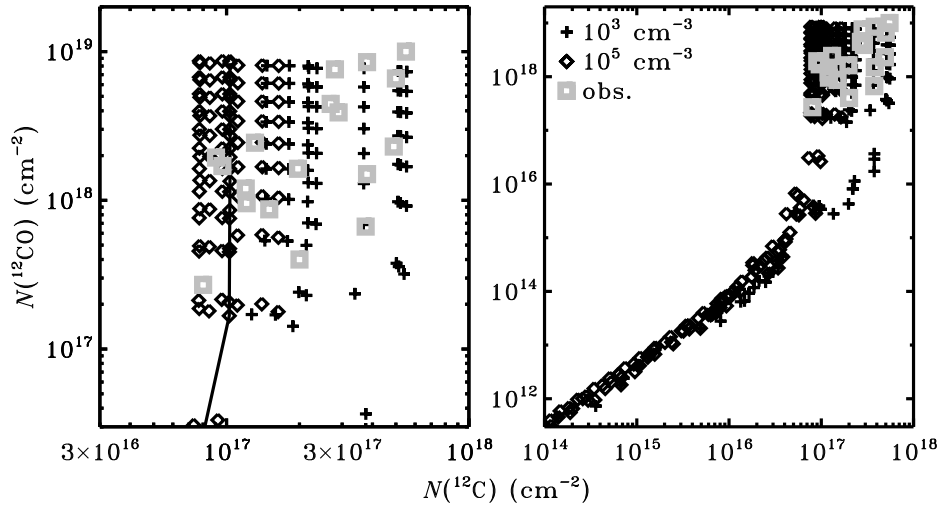


Figure 5.12 – Column density of ^{12}CO versus that of ^{12}C on two different scales. Black: results from our grid of PDR models with $n_{\text{H}} = 10^3 \text{ cm}^{-3}$ (plus signs) and 10^5 cm^{-3} (diamonds). The line traces the results for different depth steps at $n_{\text{H}} = 10^5 \text{ cm}^{-3}$, $T_{\text{gas}} = 50 \text{ K}$ and $\chi = 10^4$. Grey squares: observations of Beuther et al. (2000), Kamegai et al. (2003), Kramer et al. (2008) and Sun et al. (2008).

We present here the results from our combined photodissociation and chemistry model for a grid of physical parameters appropriate for PDRs: $T_{\text{gas}} = 50, 80$ and 100 K , $n_{\text{H}} = 10^3, 10^4, 10^5$ and 10^6 cm^{-3} , and $\chi = 10^3, 10^4$ and 10^5 . The excitation temperatures of CO and H_2 are set equal to T_{gas} . Where necessary, we expand the number of rotational levels of CO beyond the default limit of $J''=7$, and likewise for H_2 (see Sect. 5.4.4). UV pumping increases the population in the $v''=0, J''>3$ and $v''>0$ levels of H_2 . However, this does not affect the CO photodissociation rates at these temperatures, so the level population of H_2 is simply taken as fully thermal. The models are run to an A_{V} of 30 mag and are otherwise unchanged from the previous section.

Figure 5.12 shows the relationship between the column densities of ^{12}CO and ^{12}C for a large series of depths steps from our grid. The data for $n_{\text{H}} = 10^4$ and 10^6 cm^{-3} are omitted for reasons of clarity. Overplotted are column densities determined towards a number of positions in different PDRs (Beuther et al. 2000, Kamegai et al. 2003, Kramer et al. 2008, Sun et al. 2008). Figure 5a of Mookerjee et al. (2006) contains additional data for several dozen positions in the PDRs in Cepheus B. In none of these cases was the ^{12}CO column density measured directly; instead, it was derived from the ^{13}CO or C^{18}O column density using standard abundance ratios. The spread in both the model predictions and the observational data is large. The column of ^{12}C for each individual model is nearly constant for $N(^{12}\text{CO}) > 3 \times 10^{17} \text{ cm}^{-2}$, as shown by the solid line connecting the various depth steps for $n_{\text{H}} = 10^5 \text{ cm}^{-3}$, $T_{\text{gas}} = 50 \text{ K}$ and $\chi = 10^4$. The observations seem

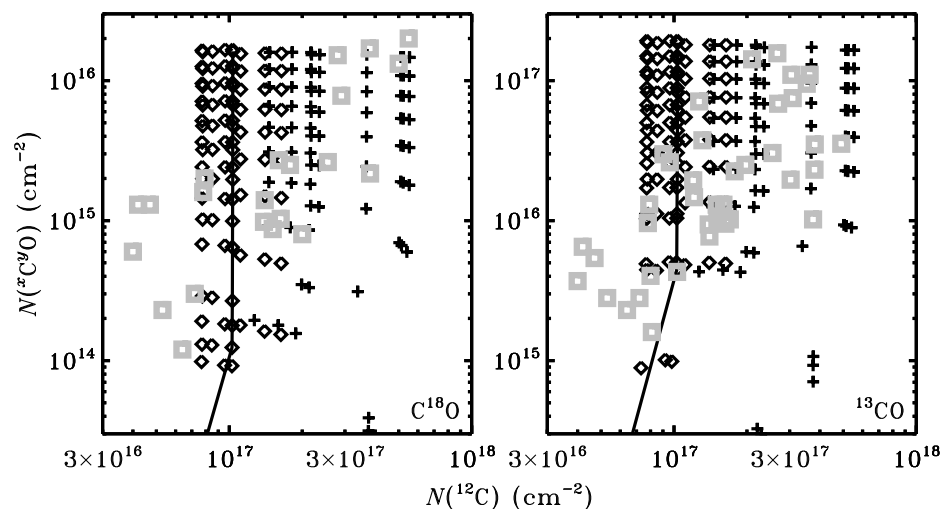


Figure 5.13 – Column densities of C^{18}O (left) and ^{13}CO (right) versus that of ^{12}C . Symbols are as in Fig. 5.12. See text for references to the observations.

to correspond more to the lower-density end of the model grid (the plus signs), but the sample is too small and is too scattered to be conclusive.

The onset of shielding is seen to occur around $N(^{12}\text{CO}) = 10^{15} \text{ cm}^{-2}$ in the models. From that point onwards, the low-density models gain more atomic carbon than do the high-density models. For a given column of ^{12}CO , the photodissociation rates (or, in other words, the ^{12}C formation rates) are roughly independent of density, but the destruction of ^{12}C occurs faster in higher densities. The same argument explained the density dependence of the $N(^{12}\text{CO})/N(\text{H}_2)$ ratio in the translucent clouds.

The two isotopologues for which column densities have been determined directly are C^{18}O and ^{13}CO (Loren 1989, Gerin et al. 1998, Plume et al. 1999, Beuther et al. 2000, Schneider et al. 2003, Mookerjea et al. 2006, Kramer et al. 2008, Sun et al. 2008). Again, both the observations and the models show a large spread in column densities (Fig. 5.13). It seems the observations do not trace the high-extinction ($A_V > 10$ mag), high-density ($n_{\text{H}} > 10^5 \text{ cm}^{-3}$) material shown in the upper left corner of each panel, but a more detailed study is required to draw any firm conclusions on this point. $N(^{12}\text{CO})$, $N(\text{C}^{18}\text{O})$ and $N(^{13}\text{CO})$ are mutually well correlated in both the observations and the models, but significant deviations can easily occur at specific depths due to the different photodissociation rates. When using standard abundance ratios to derive the column density of ^{12}CO from that of another isotopologue, as was done for all cases in Fig. 5.12, the result will generally be accurate to at best a factor of two.

5.6.3 Circumstellar disks

5.6.3.1 Model setup

Low-mass stars like our own Sun are formed through the gravitational collapse of a cold molecular cloud. As the young star grows at the centre, it gathers part of the remaining cloud material into a circumstellar disk. It is inside this disk that planets are formed, so its chemical composition is of great interest. The physical structure of the disk may be simplified as consisting of a cold, dense region near the midplane, covered by a warmer region of lower density. This surface layer intercepts the star’s radiation and shows many similarities to common PDRs.

We adopt the standard disk model of D’Alessio et al. (1999), whose chemistry has been studied extensively (Aikawa et al. 2002, van Zadelhoff et al. 2003, Jonkheid et al. 2004). The star, a T Tauri type, has a mass of $0.5 M_{\odot}$, a radius of $2 R_{\odot}$ and an effective temperature of 4000 K. It is surrounded by a disk of mass $0.07 M_{\odot}$ and outer radius 400 AU. The disk is accreting onto the star at a constant rate of $10^{-8} M_{\odot} \text{ yr}^{-1}$ and its viscosity is characterised by $\alpha = 0.01$. We focus on a vertical slice through the disk at a radius of 105 AU, where the surface is located at a height of $z = 120$ AU. This slice is irradiated from the top by a radiation field with an effective UV intensity of 516 times that of the interstellar radiation field. Following van Zadelhoff et al., we adopt two spectral shapes: the Draine field and a 4000 K blackbody spectrum. The latter is very weak in the wavelength range where CO is photodissociated. We adopt again the chemical network from Sect. 5.6.1.1, and we set the gas temperature equal to the dust temperature from the D’Alessio et al. model. Given the high densities ($2 \times 10^4 \text{ cm}^{-3}$ at the surface and more than 10^9 cm^{-3} at the midplane), we also use T_{gas} for $T_{\text{ex}}(\text{CO})$ and $T_{\text{ex}}(\text{H}_2)$. As in the PDR models, UV pumping of H_2 does not affect the CO photodissociation rates, so the H_2 level populations are taken as fully thermal.

In reality, disks are not irradiated by the Draine field or a pure blackbody. For example, T Tauri stars typically show UV emission in excess of these simple model spectra. Many of them also emit X-rays from accretion hotspots. As shown by van Zadelhoff et al. (2003), the photochemistry of the disk can be sensitive to the details of the radiation field. Moreover, the excess emission can be concentrated in a few specific lines such as H I Lyman- α . CO cannot be dissociated by Ly- α , but it can be by the H I Ly- γ line at 972.54 Å through overlap with the W0 band at 972.70 Å (No. 25 from Table 5.1). A detailed treatment of these effects is beyond the scope of the current work.

5.6.3.2 Isotopologue ratios

The depth dependence of the dissociation rates in the disk, illuminated by the Draine field, is qualitatively the same as in the clouds and PDRs from Sects. 5.6.1 and 5.6.2. Several quantitative differences arise because of the different UV flux and the higher densities. The profiles of the normalised column density ratios, \mathcal{R} (Eq. (5.9)), do not show any enhancement in ^{13}CO (Fig. 5.14). Moving down from the surface, suprathermal chemistry initially prevents the formation of ^{13}CO from ^{12}CO and $^{13}\text{C}^+$. The Alfvén waves penetrate to $N(\text{H}_2) = 4 \times 10^{20} \text{ cm}^{-2}$ or a height of about 50 AU. The absence of suprathermal chem-

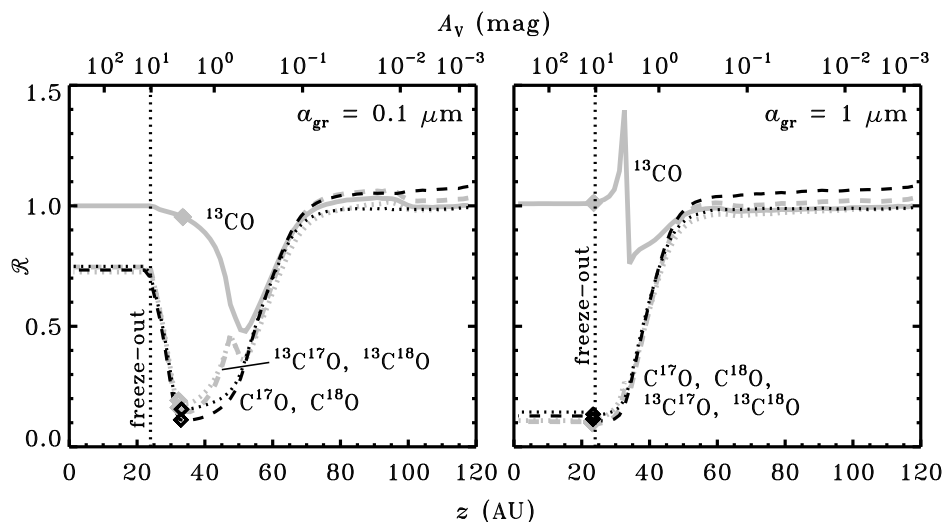


Figure 5.14 – Cumulative column densities of the CO isotopologues normalised to ^{12}CO and the elemental isotopic abundances (Eq. (5.9)) as a function of height at a radius of 105 AU in our disk model with the Draine field and dust grains of $0.1 \mu\text{m}$ (left) or $1 \mu\text{m}$ (right). CO freezes out below 24 AU. The diamond symbols indicate where H_3^+ takes over from UV photons as the main destroyer of each isotopologue.

istry below that point allows $\mathcal{R}(^{13}\text{CO})$ to increase again. However, the $^{13}\text{C}^+$ abundance decreases at the same time, and $\mathcal{R}(^{13}\text{CO})$ never gets above unity. This is consistent with the $N(^{12}\text{CO})/N(^{13}\text{CO})$ ratios of more than 69 determined for the disks around HL Tau, AB Aur and VV CrA (Brittain et al. 2005, Schreyer et al. 2008, Smith et al. 2009).

In terms of local abundances, our results show a trend opposite to the model by Woods & Willacy (2009). Moving up vertically from the midplane at a given radius, their $n(^{12}\text{CO})/n(^{13}\text{CO})$ abundance ratio initially remains nearly constant, then drops to a lower value, and finally shows a shallow rise for the remainder of the column. We also find a constant ratio at first, but then we get a *rise* (equivalent to $\mathcal{R}(^{13}\text{CO}) < 1$) and a gradual decrease back to the elemental ratio of 69. The difference is due to the absence of suprathermal chemistry in the Woods & Willacy model. Suprathermal chemistry effectively shuts down the isotope-exchange reactions, leaving photodissociation (which increases $n(^{12}\text{CO})/n(^{13}\text{CO})$) as the only fractionation mechanism. Additional observations of ^{12}CO and ^{13}CO in circumstellar disks are required to ascertain whether isotope exchange or selective photodissociation is the key process in controlling the ratio of the abundances of these two species.

For C^{17}O and C^{18}O , \mathcal{R} is ~ 1 from the disk surface down to 70 AU. It then gradually drops to ~ 0.1 due to their dissociation being faster than that of ^{12}CO . Shielding of C^{17}O and C^{18}O sets in around 32 AU, so photodissociation no longer causes isotope fractionation and \mathcal{R} increases again. However, it does not reach a value of unity. Below 24 AU,

the temperature is low enough that most of the CO freezes out onto the dust grains. The tiny amount remaining in the gas phase does not add to the column density, so \mathcal{R} is effectively frozen at 0.75 and 0.73 (Fig. 5.14). The corresponding column density ratios are $N(^{12}\text{CO})/N(\text{C}^{17}\text{O}) = 2700$ and $N(^{12}\text{CO})/N(\text{C}^{18}\text{O}) = 760$, consistent with the degree of fractionation determined for the disk around the T Tauri star VV CrA (Smith et al. 2009).

5.6.3.3 Model variations

If we illuminate the disk by a 4000 K blackbody (spectrum C from van Zadelhoff et al. 2003), it does not receive enough photons in the 912–1118 Å range to cause substantial photodissociation of CO. Instead, the non-isotope-selective reactions with He^+ and H_3^+ are the main destruction mechanisms even at the top of our vertical slice at $R = 105$ AU. The normalised column density ratios therefore remain unity at all heights. Adding the interstellar UV field at $\chi = 1$ to the 4000 K blackbody spectrum allows CO to be photodissociated again in the surface layers. The isotope fractionation returns, but only partially, because the UV field is still weaker than in the original case. Freeze-out now locks $\mathcal{R}(\text{C}^{17}\text{O})$ and $\mathcal{R}(\text{C}^{18}\text{O})$ at 0.86 and 0.85 instead of ~ 0.75 . Clearly, some UV component is required in the irradiating spectrum to get isotope fractionation through the photodissociation of CO, but it does not have to be a very strong component: the interstellar UV field already has a significant effect in this model.

Another parameter to be varied is the grain size. The disk model so far contained small dust grains, with an average size of $0.1 \mu\text{m}$. Grain growth is an inevitable step towards planet formation and is indeed known to occur in disks (van Boekel et al. 2003, Przygodda et al. 2003, Lommen et al. 2007). Larger grains cause less extinction in the UV (Shen et al. 2004), so CO can be photodissociated deeper into the disk. Grain growth also affects the H_2 formation rate: the rate is inversely proportional to approximately the square of the grain radius (Jonkheid et al. 2006). The right panel of Fig. 5.14 shows the normalised vertical column density ratios at a radius of 105 AU for an average grain size of $1 \mu\text{m}$. The onset of fractionation occurs at a lower altitude than in the $0.1 \mu\text{m}$ case: 55 AU instead of 75 AU. The slower formation rate of H_2 has a direct influence on the formation of CO through the pathway starting with Reaction (5.4). There is less H_2 and CO in the disk's surface layers when we increase the grain size, so we have to go down deeper before ^{12}CO becomes self-shielding and isotope fractionation sets in. At the same time, the weaker continuum extinction allows the UV radiation to penetrate deeper, so the isotope-selective photodissociation goes on to lower altitudes. The spike in $\mathcal{R}(^{13}\text{CO})$ to 1.4 at 30 AU is due to a narrow zone where the temperature is relatively low (35 K), the Alfvén waves do not reach, and the $^{13}\text{C}^+$ abundance is high enough to convert ^{12}CO into ^{13}CO . The model with $0.1 \mu\text{m}$ grains also has a narrow zone with a high $^{13}\text{C}^+$ abundance and no suprathreshold chemistry, but the kinetic temperature in this zone is 50 K. There is still some conversion of ^{12}CO into ^{13}CO at that temperature, but not enough to show as a spike in the normalised column density ratio.

The bigger dust grains also affect the fractionation of C^{17}O and C^{18}O . The point at which photodissociation ceases to be the main destruction mechanism now nearly coincides with the point where CO freezes out (Fig. 5.14). Both species have $\mathcal{R} \approx 0.15$ when

this happens, so the ratios are locked at that value. In the small-dust model, the ratios were locked at ~ 0.75 . Observations of face-on disks in principle probe CO all the way to the midplane, so our model predicts that grain growth from 0.1 to 1 μm can increase the observed fractionation of C^{17}O and C^{18}O by a factor of five. The fractionation in the local abundances, which is relevant for incorporating material into comets, increases by the same amount from 0.1 to 1 μm grains.

All the results so far in this section are for a T Tauri disk. Herbig Ae/Be stars are more massive and more luminous and tend to have warmer disks, where CO may not be frozen out at all. That would prevent \mathcal{R} from being locked as it is in Fig. 5.14; instead, it would rapidly return to unity for all isotopologues. Observations probing the midplane of such a disk would not find any fractionation in ^{17}O and ^{18}O relative to ^{16}O .

5.6.3.4 Implications for meteorites

Regardless of the grain size and the absence or presence of freeze-out, the model shows ^{17}O and ^{18}O to be nearly equally fractionated: \mathcal{R} has very similar values for C^{17}O and C^{18}O . The equal photodissociation rates implied by this result are partly due to our choice of molecular parameters. Spectroscopic data on C^{17}O are still very scarce, so we assume many of its oscillator strengths and predissociation probabilities to have the same value as for C^{18}O (Sects. 5.2.3 and 5.2.4). Still, two important differences remain. First, the elemental abundance of ^{18}O is higher than that of ^{17}O , resulting in some self-shielding for C^{18}O (Fig. 5.1). Second, the shifts of the C^{17}O lines with respect to ^{12}CO are generally somewhat smaller than those of the C^{18}O lines, so C^{17}O is more strongly shielded by ^{12}CO . Both effects are minor, however, and the photodissociation rates end up being nearly the same.

According to the experiments of Chakraborty et al. (2008), the photodissociation rate due to the $E0$ and $E1$ bands may be up to $\sim 40\%$ higher for C^{17}O than for C^{18}O . If we mimic this by artificially increasing the $E0$ and $E1$ oscillator strengths of C^{17}O by 40%, the overall change in $\mathcal{R}(\text{C}^{17}\text{O})$ is less than 10% at any depth. When the two oscillator strengths are doubled from their standard value, $\mathcal{R}(\text{C}^{17}\text{O})$ changes by at most 20%. In both cases, the change in $\mathcal{R}(\text{C}^{17}\text{O})$ is largest at the top of the disk and gradually decreases for lower altitudes; it is less than 1% below 50 AU.

Observational evidence for equal fractionation of ^{17}O and ^{18}O in disks was recently obtained by Smith et al. (2009) for the T Tauri star VV CrA. Their analysis points to isotope-selective photodissociation of CO as the most likely explanation, although they cautioned that more observations are needed to confirm that conclusion. Meanwhile, their observations are consistent with our model results.

A long-standing puzzle in our solar system involves the equal fractionation of ^{17}O and ^{18}O in the most refractory phases of meteorites (Clayton et al. 1973). Current evidence points at isotope-selective photodissociation of CO in the solar nebula playing a key role (Clayton 2002, Lyons & Young 2005, Lee et al. 2008). It is generally accepted that the resulting atomic oxygen eventually makes it into the refractory material to produce the observed isotope ratios, but it remains unknown how this actually happens. Any additional mass-independent fractionation during that process must be limited, because photodisso-

ciation of CO already reproduces the observed isotope abundance ratios (Young 2007). One important requirement here is to have $C^{17}O$ and $C^{18}O$ photodissociate at the same rate, an assumption that had gone untested up to now. Our model confirms they do so in many different environments – including diffuse and translucent clouds, PDRs, and circumstellar disks – even when allowing for the isotope effects suggested by Chakraborty et al. (2008).

Equal (or nearly equal) ^{17}O and ^{18}O fractionation also occurs for other oxygen-containing molecules in the model, such as water. The equal fractionation is a clear sign of CO photodissociation playing a key role in the fractionation process. Other fractionation processes, such as isotope-exchange reactions, diffusion, freeze-out and evaporation, depend on the vibrational energies of the isotopologues and are therefore mass-dependent. Specifically, such processes would lead to ^{17}O being 0.52 times as fractionated as ^{18}O (Matsuhisa et al. 1978). If mass-independent fractionation processes other than isotope-selective photodissociation play a role in circumstellar disks, they have not been discovered so far (Clayton 2002, Yurimoto & Kuramoto 2004, Lyons & Young 2005). Recently, Kimura et al. (2007) did report on a set of chemical experiments yielding mass-independently fractionated silicates, but they were unable to identify the underlying reaction mechanism. Hence, it remains unknown if this would be relevant for disks. Self-shielding in O_2 (Thiemens & Heidenreich 1983) is unimportant because O_2 never becomes abundant enough to become a significant source of atomic O.

5.7 Conclusions

This chapter presents an updated model, based on the method of van Dishoeck & Black (1988), for the photodissociation of carbon monoxide (CO) and its heavier isotopologues. It contains recent spectroscopic data from the literature and produces a photodissociation rate of $2.6 \times 10^{-10} \text{ s}^{-1}$ in the interstellar medium, 30% higher than currently adopted values. Our model is the first to include $C^{17}O$ and $^{13}C^{17}O$ and we apply it to a broader range of model parameters than has been done before. The main results are as follows:

- Self-shielding is very important for ^{12}CO and somewhat so for $C^{18}O$ and ^{13}CO . The rare isotopologues $^{13}C^{17}O$ and $^{13}C^{18}O$ have the highest photodissociation rate at most depths into a cloud or other object. The rates of $C^{17}O$ and $C^{18}O$ are very similar at all depths, but details in the line overlap and self-shielding can cause mutual differences of up to 30% (Sects. 5.3.3 and 5.6.1.4).
- When coupled to a chemical network, the model reproduces column densities observed towards diffuse clouds and PDRs. It shows that the large spread in observed $N(^{12}CO)/N(^{13}CO)$ ratios may be due to a combination of isotope-selective photodissociation and suprathermal chemistry (Sect. 5.6.1.3).
- Photodissociation of CO is more strongly isotope-selective in cold gas than in warm gas (Sect. 5.4).
- The results from the full calculation are well approximated by a grid of pre-computed shielding functions, intended for easy use in various other models. Shielding functions are provided for a range of astrophysical parameters (Sect. 5.5).

- Grain growth in circumstellar disks increases the vertical range in which CO can be photodissociated. If photodissociation is still important at the point where CO freezes out onto the grains, the observable gas-phase column density ratios $N(^{12}\text{CO})/N(\text{C}^{17}\text{O})$ and $N(^{12}\text{CO})/N(\text{C}^{18}\text{O})$ may become an order of magnitude larger than the initial isotopic abundance ratios (Sect. 5.6.3.3).
- Without a far-UV component in the irradiating spectrum, the photodissociation of CO cannot cause isotope fractionation. The interstellar radiation field can already cause substantial fractionation in disks (Sect. 5.6.3.3).
- The isotope-selective nature of the CO photodissociation results in mass-independent fractionation of ^{17}O and ^{18}O . Column density ratios computed for a circumstellar disk agree well with recent observations. Our model supports the hypothesis that the photodissociation of CO is responsible for the anomalous ^{17}O and ^{18}O abundances in meteorites (Sect. 5.6.3.4).

PAH chemistry and IR emission from circumstellar disks



R. Visser, V. C. Geers, C. P. Dullemond, J.-C. Augereau,
K. M. Pontoppidan and E. F. van Dishoeck
Astronomy & Astrophysics, 2007, 466, 229

Abstract

Aims. The chemistry of polycyclic aromatic hydrocarbons (PAHs) in disks around Herbig Ae/Be and T Tauri stars is investigated, along with the infrared emission from these species. PAHs can exist in different charge states and they can bear different numbers of hydrogen atoms. The equilibrium (steady-state) distribution over all possible charge and hydrogenation states depends on the size and shape of the PAHs and on the physical properties of the star and surrounding disk.

Methods. A chemistry model is created to calculate the equilibrium charge and hydrogenation distribution. Destruction of PAHs by ultraviolet (UV) photons, possibly in multi-photon absorption events, is taken into account. The chemistry model is coupled to a radiative transfer code to provide the physical parameters and to combine the PAH emission with the spectral energy distribution from the star+disk system.

Results. Normally hydrogenated PAHs in Herbig Ae/Be disks account for most of the observed PAH emission, with neutral and positively ionised species contributing in roughly equal amounts. Close to the midplane, the PAHs are more strongly hydrogenated and negatively ionised, but these species do not contribute to the overall emission because of the low UV/optical flux deep inside the disk. PAHs of 50 carbon atoms are destroyed out to 100 AU in the disk's surface layer, and the resulting spatial extent of the emission does not agree well with observations. Rather, PAHs of about 100 carbon atoms or more are predicted to cause most of the observed emission. The emission is extended on a scale similar to that of the size of the disk, with the short-wavelength features less extended than the long-wavelength features. The continuum emission is less extended than the PAH emission at the same wavelength. Furthermore, the emission from T Tauri disks is much weaker and concentrated more towards the central star than that from Herbig Ae/Be disks. Positively ionised PAHs are predicted to be largely absent in T Tauri disks because of the weaker radiation field.

6.1 Introduction

Polycyclic aromatic hydrocarbons (PAHs; Léger & Puget 1984, Allamandola et al. 1989) are ubiquitous in space and are seen in emission from a wide variety of sources, including the diffuse interstellar medium, photon-dominated regions, circumstellar envelopes, and (proto)planetary nebulae (Peeters et al. 2004 and references therein). The PAHs in these sources are electronically excited by ultraviolet (UV) photons. Following internal conversion to a high vibrational level of the electronic ground state, they cool by emission in the C–H and C–C stretching and bending modes at 3.3, 6.2, 7.7, 8.6, 11.3, 12.8 and 16.4 μm .

Using the Infrared Space Observatory (ISO; Kessler et al. 1996), the Spitzer Space Telescope (Werner et al. 2004a, Houck et al. 2004) and various ground-based telescopes, PAH features have also been observed in disks around Herbig Ae/Be and T Tauri stars (Van Kerckhoven et al. 2000, Hony et al. 2001, Peeters et al. 2002, Przygodda et al. 2003, van Boekel et al. 2004, Acke & van den Ancker 2004, Geers et al. 2006). Spatially resolved observations confirm that the emission comes from regions whose size is consistent with that of a circumstellar disk (van Boekel et al. 2004, Habart et al. 2006, Geers et al. 2007). Because of the optical or UV radiation required to excite the PAHs, their emission is thought to come mostly from the surface layers of the disks (Habart et al. 2004b). Acke & van den Ancker (2004) showed that PAH emission is generally stronger from flared disks (Meeus et al. 2001, Dominik et al. 2003) than from flat or self-shadowed disks.

Although the presence of such large molecules in disks and other astronomical environments is intrinsically interesting, it is also important to study PAHs for other reasons. They are a good diagnostic of the stellar radiation field and can be used to trace small dust particles in the surface layers of disks, both near the centre and farther out (Habart et al. 2004b). In addition, they are strongly involved in the physical and chemical processes in disks. For instance, photoionisation of PAHs produces energetic electrons, which are a major heating source of the gas (Bakes & Tielens 1994, Kamp & Dullemond 2004, Jonkheid et al. 2004). The absorption of UV radiation by PAHs in the surface layers influences radiation-driven processes closer to the midplane. Charge transfer of C^+ with neutral and negatively charged PAHs affects the carbon chemistry. Finally, Habart et al. (2004a) proposed PAHs as an important site of H_2 formation in photon-dominated regions, a process which is also important in disk chemistry (Jonkheid et al. 2006, 2007). Although this process is probably more efficient on grains and very large PAHs than it is on PAHs of up to 100 carbon atoms, the latter may play an important role if the grains have grown to large sizes.

Many PAHs and related species that are originally present in the parent molecular cloud, are able to survive the star formation process and eventually end up on planetary bodies (Allamandola & Hudgins 2003). They add to the richness of the organochemical “broth” on planets in habitable zones (Kasting et al. 1993), from which life may originate. Further enrichment is believed to come from the impact of comets. PAHs have now been detected in cometary material during the Deep Impact mission (Lisse et al. 2006) and returned to Earth by the Stardust mission (Sandford et al. 2006). The icy grains that constitute comets also contain a variety of other molecules (Ehrenfreund & Fraser 2003). Radiation-induced chemical reactions between frozen-out PAHs and these molecules lead

to a large variety of complex species, including some that are found in life on Earth (Bernstein et al. 1999, Ehrenfreund & Sephton 2006). These possibilities are another reason why it is important to study the presence and chemistry of PAHs in disks.

The chemistry of PAHs in an astronomical context has been studied with increasingly complex and accurate models since the 1980s (Omont 1986, Lepp et al. 1988, Bakes & Tielens 1994, Salama et al. 1996, Dartois & d’Hendecourt 1997, Vuong & Foing 2000, Le Page et al. 2001, 2003, Weingartner & Draine 2001, Bakes et al. 2001a,b); however, none of these were specifically targeted at PAHs in circumstellar disks. Disk chemistry models that do include PAHs only treat them in a very simple manner (e.g., Jonkheid et al. 2004, Habart et al. 2004b). In this chapter, an extensive PAH chemistry model is coupled to a radiative transfer model for circumstellar disks (Dullemond & Dominik 2004a, Geers et al. 2006, Dullemond et al. 2007a). The chemistry part includes ionisation (photoelectric emission), electron recombination and attachment, photodissociation with loss of hydrogen and/or carbon, and hydrogen addition. Infrared (IR) emission from the PAHs is calculated taking multi-photon excitation into account, and added to the spectral energy distribution (SED) of the star+disk system. The model can in principle also be used to examine PAH chemistry and emission in other astronomical environments.

We present the chemistry model in Sect. 6.2, followed by a brief review of the radiative transfer model in Sect. 6.3. The results are discussed in Sect. 6.4 and our conclusions are summarised in Sect. 6.5.

6.2 PAH model

The chemistry part of our model is a combination of the models developed by Le Page et al. (2001, hereafter LPSB01) and Weingartner & Draine (2001, hereafter WD01). Photodissociation is treated according to Léger et al. (1989). Where possible, theoretical rates are compared to recent experimental data. Our model employs the new PAH cross sections of Draine & Li (2007, hereafter DL07), which are an update of Li & Draine (2001) based on experimental data (Mattioda et al. 2005a,b) and IR observations (e.g., Smith et al. 2004, Werner et al. 2004b). In this section, we present the main characteristics of our model.

6.2.1 Characterisation of PAHs

The PAHs in our model are characterised by their number of carbon atoms, N_C . A PAH bears the normal number of hydrogen atoms, N_H° , when one hydrogen atom is attached to each peripheral carbon atom bonded to exactly two other carbon atoms (e.g., 12 for coronene, $C_{24}H_{12}$). The ratio between N_H° and N_C is taken as (e.g., DL07):

$$f^\circ = N_H^\circ/N_C = \begin{cases} 0.5 & N_C \leq 25, \\ 0.5\sqrt{25/N_C} & 25 < N_C \leq 100, \\ 0.25 & N_C > 100. \end{cases} \quad (6.1)$$

This formula produces values appropriate for compact (pericondensed) PAHs. Elongated (catacondensed) PAHs have a higher hydrogen coverage; however, they are believed to be less stable and to convert into a more compact geometry (Wang et al. 1997, Dartois & d'Hendecourt 1997), so only compact PAHs are assumed to be present.

Every carbon atom that bears one hydrogen atom in the normal case is assumed to be able to bear two in extreme conditions, so each PAH can exist in $2N_{\text{H}}^{\circ} + 1$ possible hydrogenation states ($0 \leq N_{\text{H}} \leq 2N_{\text{H}}^{\circ}$). Furthermore, each PAH can exist in two or more charge states Z . The maximum and minimum attainable charge depend on the radiation field and the PAH's ionisation and autoionisation potentials (Bakes & Tielens 1994, WD01). The number of accessible charge states increases with PAH size.

For a number of properties, the radius of the PAH is more important than N_{C} . The PAHs of interest are assumed to be spherically symmetric and, following e.g. Draine & Li (2001) and WD01, are assigned an effective radius a in Å:

$$a = \left(\frac{N_{\text{C}}}{0.468} \right)^{1/3}. \quad (6.2)$$

This equation does not give the actual geometric radius; rather, it gives the radius of a pure graphite sphere containing the same number of carbon atoms. Equations (6.1) and (6.2) do not apply to very small PAHs ($N_{\text{C}} \lesssim 20$), but like irregularly shaped PAHs, they are assumed not to be abundant enough to contribute to the emission (Sect. 6.2.6).

6.2.2 Photoprocesses

The absorption of a UV or visible photon of sufficient energy by a PAH causes either the emission of an electron (ionisation or detachment) or a transition to an excited electronic and vibrational state. In the second case, internal conversion and fluorescence rapidly bring the molecule to a high vibrational level of the ground electronic state. From here, several processes can take place (Léger et al. 1988, 1989): (1) dissociation with loss of atomic or molecular hydrogen; (2) dissociation with loss of a carbon-bearing fragment; or (3) cooling by infrared emission. The cooling rate constant for a PAH with internal energy E_{int} is given by Li & Lunine (2003):

$$k_{\text{cool}} = \int_{912 \text{ \AA}}^{\infty} \frac{4\pi B_{\lambda} \sigma_{\text{abs}}}{hc/\lambda} d\lambda, \quad (6.3)$$

with $B_{\lambda}(T[E_{\text{int}}])$ the Planck function at the PAH's vibrational temperature, $T[E_{\text{int}}]$ (Draine & Li 2001). The cross sections, σ_{abs} , are treated in Sect. 6.2.3.

The yield of a single dissociation process i , Y_i , depends on the rate constants, k , of all possible processes:

$$Y_i = \frac{k_i}{\sum_j k_j}. \quad (6.4)$$

To determine the rate Γ_i of dissociation process i , the yield is multiplied by the absorption rate, taking into account the possibility of electron emission, and integrated over the

relevant energy range:

$$\Gamma_i = \int_0^\infty (1 - Y_{\text{em}}) Y_i \sigma_{\text{abs}} N_{\text{ph}} dE, \quad (6.5)$$

where Y_{em} is the photoelectric emission yield (Eq. (6.8)) and N_{ph} is the number of photons in units of $\text{cm}^{-2} \text{s}^{-1} \text{erg}^{-1}$. The radiation field is treated explicitly at every point in the disk in a 2D axisymmetric geometry, i.e., the wavelength dependence is taken into account as well as the magnitude.

Photoelectric emission is the ejection of an electron from a PAH due to the absorption of a UV photon. The electron can come either from the valence band (photoionisation; possible for all charge states) or from an energy level above the valence band (photodetachment; only for negatively charged PAHs). The photoelectric emission rate is given by WD01 as

$$\Gamma_{\text{em}} = \int_{h\nu_{\text{ion}}}^\infty Y_{\text{ion}} \sigma_{\text{abs}} N_{\text{ph}} dE + \int_{h\nu_{\text{det}}}^\infty Y_{\text{det}} \sigma_{\text{det}} N_{\text{ph}} dE, \quad (6.6)$$

where h is Planck's constant. Photoelectric emission can only occur when the photon energy exceeds the threshold of $h\nu_{\text{ion}}$ or $h\nu_{\text{det}}$. The photodetachment yield, Y_{det} , is taken to be unity: every absorption of a photon with $h\nu > h\nu_{\text{det}}$ leads to the ejection of an electron. The photoionisation yield, Y_{ion} , has a value between 0.1 and 1 for $h\nu \gtrsim 8 \text{ eV}$ and drops rapidly for lower energies. For photons with $h\nu > h\nu_{\text{ion}}$, the photodetachment cross section, σ_{det} , is about two orders of magnitude smaller for $N_{\text{C}} = 50$ than the ionisation cross section, which is assumed equal to σ_{abs} .

In order to derive Y_{em} as used in Eq. (6.5), Eq. (6.6) is rewritten:

$$\Gamma_{\text{em}} = \int_0^\infty \left(Y_{\text{ion}} + \frac{\sigma_{\text{det}}}{\sigma_{\text{abs}}} Y_{\text{det}} \right) \sigma_{\text{abs}} N_{\text{ph}} dE. \quad (6.7)$$

The quantity between brackets is the electron emission yield, Y_{em} :

$$Y_{\text{em}} = Y_{\text{ion}} + \frac{\sigma_{\text{det}}}{\sigma_{\text{abs}}} Y_{\text{det}}, \quad (6.8)$$

taking Y_{ion} and Y_{det} to be zero for photon energies less than $h\nu_{\text{ion}}$ and $h\nu_{\text{det}}$, respectively. Furthermore, Y_{em} is not allowed to exceed unity: each absorbed photon can eject only one electron.

If no photoelectric emission takes place, the PAH can undergo dissociation with loss of carbon or hydrogen. Several theoretical schemes exist to calculate the dissociation rates. LPSB01 employed the Rice-Ramsperger-Kassel-Marcus quasi-equilibrium theory (RRKM-QET) and obtained hydrogen loss rates close to those determined experimentally for benzene (C_6H_6), naphthalene (C_{10}H_8) and anthracene ($\text{C}_{14}\text{H}_{10}$). Léger et al. (1989) investigated the loss of carbon as well as hydrogen, using an inverse Laplace transform of the Arrhenius law (Forst 1972) to determine the rates. In this method, the rate constant is zero when the PAH's internal energy, E_{int} , originating from one or more UV photons, is less than the critical energy, E_0 , for a particular loss channel. When E_{int} exceeds E_0 ,

$$k_{\text{diss},X} = A_X \frac{\rho(E_{\text{int}} - E_{0,X})}{\rho(E_{\text{int}})}, \quad (6.9)$$

Table 6.1 – Arrhenius parameters for the loss of carbon and hydrogen fragments from PAHs.^a

Fragment	N_{H}	Z	E_0 (eV)	A (s ⁻¹)
C	all	all	7.37	6.2×10^{15}
C ₂	all	all	8.49	3.5×10^{17}
C ₃	all	all	7.97	1.5×10^{18}
H	$\leq N_{\text{H}}^{\circ}$	all	4.65	1.5×10^{15}
H	$> N_{\text{H}}^{\circ}$	≤ 0	1.1	4×10^{13}
H	$> N_{\text{H}}^{\circ}$	> 0	2.8	1×10^{14}
H ₂	$> N_{\text{H}}^{\circ}$	≤ 0	1.5	4×10^{13}
H ₂	$> N_{\text{H}}^{\circ}$	> 0	3.1	1×10^{14}

^a E_0 and A for C, C₂ and C₃ are from Léger et al. (1989). E_0 for H and H₂ is based on the RRKM-QET parameters from Le Page et al. (2001) and modified slightly to obtain a better match with their rates. A for H is modified from Léger et al. (1989) and used also for H₂.

where A_X is the pre-exponential Arrhenius factor for channel X and $\rho(E)$ is the density of vibrational states at energy E . Léger et al. (1989) considered the loss of H, C, C₂ and C₃; LPSB01 also took H₂ loss into account for PAHs with $N_{\text{H}} > N_{\text{H}}^{\circ}$. Our model uses the method of Léger et al. (1989) for all loss channels, with values for A and E_0 given in Table 6.1.

The intensity of the UV radiation field inside the disk is characterised in our model by $G'_0 = u_{\text{UV}}/u_{\text{Hab}}$, where

$$u_{\text{UV}} = \int_{6 \text{ eV}}^{13.6 \text{ eV}} u_{\nu} d\nu = \int_{6 \text{ eV}}^{13.6 \text{ eV}} (h/c) h\nu N_{\text{ph}} d\nu \quad (6.10)$$

and $u_{\text{Hab}} = 5.33 \times 10^{-14}$ erg cm⁻³ is the UV energy density in the mean interstellar radiation field (Habing 1968). However, the radiation field inside the disk does not have the same spectral shape as the interstellar radiation field, so G'_0 is used instead of G_0 to denote its integrated intensity. The exact UV field at every point and every wavelength is calculated by a Monte Carlo code, which follows the photons from the star into the disk in an 2D axisymmetric geometry (see also Sect. 6.3.1). As a result, regions of high optical depth may not receive enough photons between 6 and 13.6 eV to calculate G'_0 . In those cases, the lower limit of the integration range is extended in 1-eV steps and the energy density of the Habing field is recalculated accordingly. If G'_0 still cannot be calculated between 1 and 13.6 eV, it is set to a value of 10^{-6} .

In the strong radiation fields present in circumstellar disks (up to $G'_0 = 10^{10}$ in the inner disk around a Herbig Ae/Be star), multiple photons are absorbed by a PAH before it can cool through emission of IR radiation. These multi-photon events result in higher dissociation rates than given by Eqs. (6.5) and (6.9). For example, a PAH of 50 carbon atoms is photodestroyed in a radiation field of $G'_0 \approx 10^5$ if multi-photon events are allowed, while $G'_0 \approx 10^{14}$ is required in a pure single-photon treatment (Sect. 6.2.6). However, the multi-photon treatment is much more computationally demanding, hence

our model is limited to single-photon treatments for all processes but photodestruction; the latter is discussed in detail in Sect. 6.2.6. The errors introduced by not including a full multi-photon treatment are discussed in Sect. 6.4.5.

As long as the internal energy of the PAH exceeds E_0 for any of the loss channels from Table 6.1, there is competition between dissociation and radiative stabilisation. Typically, the emission of a single IR photon is not sufficient to bring E_{int} below E_0 . If the emitted IR photons are assumed to have an average energy q_{IR} of 0.18 eV (6.9 μm ; LPSB01), a total of $n = (E_{\text{int}} - E_0)/q_{\text{IR}}$ photons are required to stabilise the PAH. The i th photon in this cooling process is emitted at an approximate rate (Herbst & Dunbar 1991)

$$k_{\text{rad},i} = 73 \frac{[E_{\text{int}} - (i-1)q_{\text{IR}}]^{1.5}}{s^{0.5}}, \quad (6.11)$$

with E_{int} in eV and $s = 3(N_{\text{C}} + N_{\text{H}}) - 6$ the number of vibrational degrees of freedom. The competition between dissociation and IR emission occurs for every intermediate state. Hence, the total radiative stabilisation rate is (Herbst & Le Page 1999)

$$k_{\text{rad}} = k_{\text{rad},1} \prod_{i=1}^n \frac{k_{\text{rad},i}}{k_{\text{rad},i} + k_{\text{diss,H}} + k_{\text{diss,H}_2} + k_{\text{diss,C}}}, \quad (6.12)$$

where $k_{\text{diss,C}}$ denotes the sum of all three carbon loss channels. Note that Eqs. (6.11) and (6.12) are used only in the chemical part of the code, where the details of the cooling rate function are not important (LPSB01). The radiative transfer part employs the more accurate Eq. (6.3).

Alternative stabilisation pathways such as inverse internal conversion, inverse fluorescence and Poincaré fluorescence (Leach 1987, Léger et al. 1988) are probably of minor importance. Their effect can be approximated by increasing q_{IR} , thus creating an “effective” k_{rad} that is somewhat larger than the “old” k_{rad} . However, this has no discernible effect on the rates from Eq. (6.5), so these alternative processes are ignored altogether.

6.2.3 Absorption cross sections

Li & Draine (2001) performed a thorough examination of the absorption cross sections, σ_{abs} , of PAHs across a large range of wavelengths. Following new experimental data (Mattiola et al. 2005a,b) and IR observations (e.g., Smith et al. 2004, Werner et al. 2004b), an updated model was published in DL07, providing a set of equations that can readily be used in our model. The cross sections consist of a continuum contribution that decreases towards longer wavelengths, superposed onto which are a number of Drude profiles to account for the σ - σ^* transition at 72.2 nm, the π - π^* transition at 217.5 nm, the C–H stretching mode at 3.3 μm , the C–C stretching modes at 6.2 and 7.7 μm , the C–H in-plane bending mode at 8.6 μm , and the C–H out-of-plane bending mode at 11.2–11.3 μm . Some of these primary features are split into two or three subfeatures, and several minor features are included in the 5–20 μm range to give a better agreement with recent observations (DL07). The additional absorption for ions in the near IR measured by Mattiola et al. is included as a continuum term and three Drude profiles.

The absorption properties of a PAH depend on its charge. Neutral PAHs have 6.2, 7.7 and 8.6 μm features that are a factor of a few weaker than do cations. The 3.3 μm band strength increases from cations to neutrals (Langhoff 1996, Hudgins et al. 2000, 2001, Bauschlicher 2002). The other features have similar intensities for each charge state. While the cation-neutral band ratios at 6.2, 7.7 and 8.6 μm are mostly independent of size, those at 3.3 μm decrease for larger PAHs. DL07 provide integrated band strengths, σ_{int} , for neutral and ionised PAHs, but they do not account for the size dependence of this feature in cations. Rather than taking $\sigma_{\text{int},3.3}^{Z=1} = 0.227\sigma_{\text{int},3.3}^{Z=0}$ as DL07 do, our model uses

$$\sigma_{\text{int},3.3}^{Z=1} = \sigma_{\text{int},3.3}^{Z=0} \left(1 + \frac{41}{N_C - 14} \right)^{-1}. \quad (6.13)$$

This way, the cation-neutral band ratio approaches unity for large PAHs. The theoretical ratios for $N_C = 24, 54$ and 96 from Bauschlicher are well reproduced by Eq. (6.13).

LPSB01 based their opacities on experiments by Joblin (1992) on PAHs in soot extracts. They fitted the cross section of an extract with an average PAH mass of 365 amu (corresponding to $N_C \approx 30$) with a collection of Gaussian curves, obtaining practically the same values for $\lambda \lesssim 0.25 \mu\text{m}$ ($E \gtrsim 5 \text{ eV}$) as DL07. Between 0.25 and 0.5 μm , the integrated cross section of LPSB01 is about 2.5 times stronger. Since LPSB01 were only interested in the UV opacities, their cross section throughout the rest of the visible and all of the infrared is zero. For our purposes, the different opacities in the 0.25–0.5 μm range only affect the hydrogen dissociation rates, and, as shown in Sect. 6.4.5, the effects are negligible.

The details of the IR cross sections of negatively charged PAHs are not well understood, with very different values to be found in the literature (Langhoff 1996, Bauschlicher & Bakes 2000). However, this is not a problem for our model. Because of the small electron affinities, photodetachment is a very efficient process and absorption of a photon by a PAH anion leads to ejection of an electron rather than substantial emission in the infrared. Rapid electron attachment retrieves the original anion before the transient neutral PAH can absorb a second photon. Hence, if anions are present in steady state, they are excluded altogether when the infrared emission is calculated.

Large PAHs can carry a double or triple positive charge in those regions of the disk where the radiation field is strong and the electron density is low. The differences between the cross sections of singly charged and neutral PAHs generally increase when going to multiply charged PAHs (Bauschlicher & Bakes 2000, Bakes et al. 2001a). However, no cross sections for multiply charged species exist that can be directly used in our model, so the cross sections for singly charged species are used instead. Since multiply charged species only constitute a very small part of the PAH population (Sect. 6.4.1), this approximation is not expected to cause major errors.

6.2.4 Electron recombination and attachment

Free electrons inside the disk can recombine with PAH cations or attach to PAH neutrals and anions; both processes are referred to here as electron attachment. The electron at-

attachment rate, $\Gamma_{\text{ea}} = k_{\text{ea}}n_e$, with n_e the electron number density, depends on the frequency of collisions between electrons and PAHs and on the probability that a colliding electron sticks, as expressed by WD01:

$$k_{\text{ea}} = \pi a^2 s_e \tilde{J} \sqrt{\frac{8kT}{\pi m_e}}, \quad (6.14)$$

where k is Boltzmann's constant and m_e the electron mass. The sticking coefficient, s_e , has a maximum value of 0.5 to allow for the possibility of elastic scattering. Non-scattering electrons have to be retained by the PAH before their momentum carries them back to infinity. The probability of retention is approximately $1 - e^{-a/l_e}$, where $l_e \approx 10 \text{ \AA}$ can be considered the mean free path of the electron inside the PAH. WD01 included an additional factor $1/(1 + e^{20-N_c})$ for PAH neutrals and anions to take into account the possibility that the PAH is dissociated by the electron's excess energy, but this is only important for PAHs smaller than 24 carbon atoms (see also LPSB01) and they are assumed not to be present in the disk (Sect. 6.2.6). Thus, our model uses

$$s_e = 0.5(1 - e^{-a/l_e}) \quad (6.15)$$

for all PAHs with a charge $Z > Z_{\text{min}}$.

Expressions for \tilde{J} , a dimensionless factor that takes into account the charge and size of the PAH and the temperature of the gas, can be found in Draine & Sutin (1987). For neutral PAHs, $\tilde{J} \propto T^{-1/2}$, so the attachment rate does not depend significantly on the temperature (Bakes & Tielens 1994). \tilde{J} changes as T^{-1} for PAH cations in the PAH size and gas temperature regimes of interest, leading to $\Gamma_{\text{ea}} \propto T^{-1/2}$. Finally, for PAH anions, both \tilde{J} and the attachment rate vary as $e^{-1/T}$.

Recombination rates at 300 K for PAH cations of up to sixteen carbon atoms have been determined experimentally (Abouelaziz et al. 1993, Rebrion-Rowe et al. 2003, Hassouna et al. 2003, Novotný et al. 2005, Biennier et al. 2006). The experimental and theoretical rates agree to within a factor of two for these small species, except for naphthalene (C_{10}H_8), where the theoretical value is larger by a factor of seven. Experimental data on larger PAHs are needed to ascertain the accuracy of Eq. (6.14) for the sizes used in our model.

Experimental data on electron attachment to PAH neutrals are scarce. Rates for anthracene ($\text{C}_{14}\text{H}_{10}$) have been reported from 9×10^{-10} to $4.5 \times 10^{-9} \text{ cm}^3 \text{ s}^{-1}$ (Tobita et al. 1992, Moustefaoui et al. 1998), with no apparent dependence on temperature. Equation (6.14) predicts a rate of $2 \times 10^{-10} \text{ cm}^3 \text{ s}^{-1}$, about an order of magnitude lower, for temperatures between 10 and 1000 K. For pyrene ($\text{C}_{16}\text{H}_{10}$), however, the theoretical value, $2 \times 10^{-9} \text{ cm}^3 \text{ s}^{-1}$, is 5–10 times larger than the available experimental values of 2 and $4.2 \times 10^{-10} \text{ cm}^3 \text{ s}^{-1}$ (Tobita et al. 1992). Hence, we can only estimate that Eq. (6.14) is accurate to within about an order of magnitude. No experimental data are available on electron attachment to negatively charged PAHs or on electron recombination with PAHs carrying a multiple positive charge, so the uncertainties in the theoretical rates for these reactions are at least as large.

6.2.5 Hydrogen addition

The addition of atomic hydrogen to neutral and ionised PAHs is an exothermic process requiring little or no activation energy (Bauschlicher 1998, Hiramata et al. 2004). For addition to cations, we use the temperature-independent rates from LPSB01, which are based primarily on experimental work by Snow et al. (1998). Addition to neutrals is about two orders of magnitude slower for benzene (Mebel et al. 1997, Triebert et al. 1998) and has not been measured for larger PAHs. No rates are known for the addition of hydrogen to anions or to cations with $Z > 1$. We take $k_{\text{add,H}}^{Z<1} = 10^{-2}k_{\text{add,H}}^{Z=1}$ and $k_{\text{add,H}}^{Z>1} = k_{\text{add,H}}^{Z=1}$. The rate depends on N_{H} as described by LPSB01.

It is assumed that molecular hydrogen can only attach to PAHs with $N_{\text{H}} < N_{\text{H}}^{\circ}$. Again, the rate for addition to cations from LPSB01 is used and divided by 100 for the neutral and anion rates.

For naphthalene and larger PAHs, addition of atomic hydrogen ($\text{PAH} + \text{H} \rightarrow \text{PAH}_{+1}$) is assumed to be much faster than the bimolecular abstraction channel ($\text{PAH} + \text{H} \rightarrow \text{PAH}_{-1} + \text{H}_2$; Herbst & Le Page 1999), so the latter is not included in our model.

6.2.6 PAH growth and destruction

The PAHs observed in disks are generally not believed to have been formed in situ after the collapse and main infall phases. Formation and growth of PAHs requires a high temperature (~ 1000 K), density and acetylene abundance (Frenklach & Feigelson 1989, Cherchneff et al. 1992) and, especially for the smallest PAHs, a weak UV radiation field to prevent rapid photodissociation. If these conditions exist at all in a disk, it is only in a thin slice (less than 0.1 AU) right behind the inner rim, and it is unlikely that this affects the PAH population at larger radii. Another possible method of late-stage PAH formation is in accretion shocks (Desch & Connolly 2002), but too little is known about these events to include them in the model. Hence, no in situ formation or growth of PAHs is assumed to take place.

PAH destruction is governed by the loss of carbon fragments upon absorption of one or more UV photons. C–C bonds are a few eV stronger than C–H bonds (e.g., Table 6.1), so carbon is lost only from completely dehydrogenated PAHs. In order to get an accurate destruction rate, multi-photon events have to be taken into account, as first recognised by Guhathakurta & Draine (1989) and Siebenmorgen et al. (1992). Our model uses a procedure based on Habart et al. (2004b). A PAH ensemble residing in a given radiation field assumes a statistical distribution over a range of internal energies. This distribution is represented by $P(E_{\text{int}})$, which is normalised so that $P(E_{\text{int}})dE_{\text{int}}$ is the probability to find the PAH in the energy interval from E_{int} to $E_{\text{int}} + dE_{\text{int}}$. At every E_{int} , there is competition between cooling and dissociation with loss of a carbon fragment. The probability for dissociation depends on the ratio between k_{C} (the sum of the rate constants for all carbon loss channels in Eq. (6.9)) and k_{IR} (the instantaneous IR emission rate, comparable to Eq. (6.11)) at E_{int} :

$$\eta_{\text{des}}(E_{\text{int}}) = \frac{k_{\text{C}}}{k_{\text{C}} + k_{\text{IR}}} . \quad (6.16)$$

k_{IR} is a very flat function in the relevant energy regime, while k_{C} is very steep, so η_{des} is approximately a step function.

The probability, p_{des} , that a PAH in a certain radiation field is destroyed is then found by integrating $P(E_{\text{int}})\eta_{\text{des}}(E_{\text{int}})$ over all energies:

$$p_{\text{des}} = \int_0^{\infty} P(E_{\text{int}})\eta_{\text{des}}(E_{\text{int}})dE_{\text{int}}, \quad (6.17)$$

with $P(E_{\text{int}})$ calculated according to Guhathakurta & Draine (1989). This is equal to the formula in Habart et al. (2004b) if η_{des} is replaced by a step function and the internal energy is converted to a temperature using the PAH's heat capacity (e.g., Draine & Li 2001). Destruction is assumed to take place if p_{des} exceeds a value of 10^{-8} .

We define a critical radiation intensity, G_0^* , which is the intensity required to cause photodestruction of a given PAH within a typical disk lifetime of 3 Myr, i.e., the intensity required to get $\tau_{\text{diss,C}} = 1/\Gamma_{\text{diss,C}} = 3$ Myr. The G_0^* for both single-photon and multi-photon destruction is plotted in Fig. 6.1. Knowledge of the radiation field at every point of the disk (Fig. 6.3) is required to determine where PAHs of a certain size are destroyed. An approximate approach is to trace the radiation field along the $\tau_{\text{vis}} = 1$ surface, where the intensity decreases almost as a power law (see Sect. 6.4.2). In our Herbig Ae/Be model (Sect. 6.3.2), PAHs of 50 carbon atoms ($G_0^* = 1.2 \times 10^5$) are destroyed out to 100 AU on the $\tau_{\text{vis}} = 1$ surface. The destruction radius is larger for smaller PAHs and vice versa; for example, PAHs with $N_{\text{C}} = 100$ are only destroyed in the inner 5 AU. PAHs with less than 24 carbon atoms are not taken into account at all, because they are already destroyed when $G_0' \approx 1$. There are regions inside the disk where the UV intensity is below that limit, but the PAHs in such regions do not contribute significantly to the emission spectrum. The radiation field in a T Tauri disk is much weaker than for a Herbig Ae/Be disk, so the destruction radius is smaller. In our model T Tauri disk, 50-C PAHs can survive everywhere but in the disk's inner 0.01 AU, while 100-C PAHs can survive even there (Sect. 6.4.6).

6.2.7 Other chemical processes

No reactions between PAHs and species other than H and H₂ are included in our model. Although the second-order rate coefficients for the addition of, e.g., atomic nitrogen and oxygen are comparable to that for atomic hydrogen (Snow et al. 1998, LPSB01), the abundances of these heavier elements are not high enough to affect the chemical equilibrium. Formation of dimers and clusters (Rapacioli et al. 2005 and references therein) and trapping of PAHs onto grains and ices (Gudipati & Allamandola 2003) are also left out. The midplane of the disk, where densities are high enough and temperatures low enough for these processes to play a role, does not contribute significantly to the IR emission spectrum.

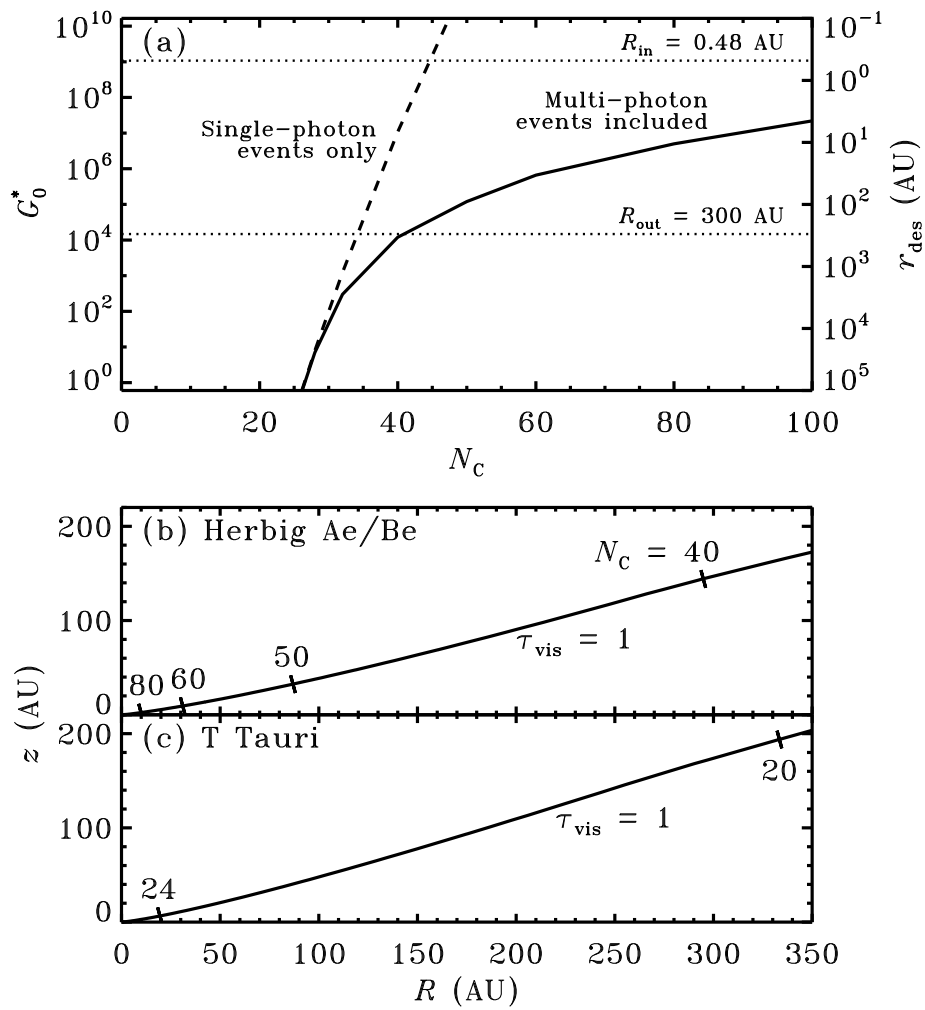


Figure 6.1 – Photodestruction of PAHs. **(a)** The UV intensity for which the destruction timescale is shorter than the disk lifetime, with (solid line) or without (dashed line) multi-photon events included. The right axis shows the corresponding “destruction radius” along the $\tau_{vis} = 1$ surface in our model Herbig Ae/Be disk. The disk’s inner and outer radius are indicated by the dotted lines. **(b,c)** The $\tau_{vis} = 1$ surface in a vertical cut through our two model disks. The tick marks denote the radius inwards of which PAHs of a given size are destroyed within the disk lifetime; for the Herbig Ae/Be model, this corresponds to the right vertical axis of panel (a).

6.3 Disk model

6.3.1 Computational code

The Monte Carlo radiative transfer code RADMC (Dullemond & Dominik 2004a) is used in combination with the more general code RADICAL (Dullemond & Turolla 2000) to produce the IR spectra from PAHs in circumstellar disks. Using an axisymmetric density structure, but following photons in all three dimensions, RADMC determines the dust temperature and radiation field at every point of the disk. RADICAL then calculates a spectrum from all or part of the disk, or an image at any given wavelength.

The calculations in RADMC and RADICAL are based on the optical properties of a collection of carbon and silicate dust grains. Recently, PAHs were added as another type of grain to model the emission from the Herbig Ae star VV Ser and the surrounding nebulosity (Pontoppidan et al. 2007), from a sample of Herbig Ae/Be and T Tauri stars (Geers et al. 2006), and to study the effects of dust sedimentation (Dullemond et al. 2007a). The PAHs are excited in a quantised fashion by UV and, to a lesser degree, visible photons (Li & Draine 2002), and cool in a classical way according to the “continuous cooling” approximation (Guhathakurta & Draine 1989), which was found by Draine & Li (2001) to be accurate even for small PAHs. A detailed description of the PAH emission module is given in Pontoppidan et al. (2007), whereas tests against other codes are described in Geers et al. (2006).

In the models used by Geers et al. (2006), Pontoppidan et al. (2007) and Dullemond et al. (2007a), no PAH chemistry was included. PAHs of a given size existed in the same charge and hydrogenation state everywhere, or in a fixed ratio between a limited number of states (e.g., 50% neutral, 50% ionised). In the current model, the chemistry is included in the following way. First, a single charge and hydrogenation state for a given N_C is included at a given abundance in the radiative transfer procedure, to calculate the disk structure and radiation field at every point. Using these physical parameters, the equilibrium distribution of the PAHs over all possible charge and hydrogenation states is then determined. After an optional second iteration of the radiative transfer to take into account the heating of thermal grains by emission from the PAHs, the spectrum or image is calculated.

Some additional chemistry is added to the model in order to determine the electron and atomic and molecular hydrogen densities, which are needed to calculate the chemical equilibrium of the PAHs. The electron abundance, $x_e = n_e/n_H$, is set equal to the C^+ abundance, based on a simple equilibrium between the photoionisation of neutral C and the recombination of C^+ (Le Teuff et al. 2000, Bergin et al. 2003, 2007). All hydrogen is in atomic form at the edges of the disk and is converted to molecular form inside the disk as the amount of dissociating photons decreases due to self-shielding and shielding by dust (Draine & Bertoldi 1996, van Zadelhoff et al. 2003). The H_2 formation rate is taken from Black & van Dishoeck (1987). For the outer parts of the disk, which receive little radiation from the star, an interstellar radiation field with $G_0 = 1$ is included.

The RADMC and RADICAL codes only treat isotropic scattering of photons. We verified with a different radiative transfer code (van Zadelhoff et al. 2003) that no significant

changes occur in the results when using a more realistic anisotropic scattering function.

Different PAHs (i.e., different sizes) can be included at the same time, and for each one, the equilibrium distribution over all charge and hydrogenation states is calculated. The abundance of each PAH with a given N_C is equal throughout the disk, except in those regions where $G'_0 > G_0^*(N_C)$; there, the abundance is set to zero. As discussed in Sect. 6.2.6, mixing processes are ignored.

6.3.2 Template disk with PAHs

For most of the calculations, a template Herbig Ae/Be star+disk model is used with the following parameters. The star has radius $2.79 R_\odot$, mass $2.91 M_\odot$ and effective temperature 10 000 K, and its spectrum is described by a Kurucz model. No UV excess due to accretion or other processes is present. The mass of the disk is $0.01 M_\odot$, with inner and outer radii of 0.48 and 300 AU. The inner radius corresponds to a dust evaporation temperature of 1700 K. The disk is in vertical hydrostatic equilibrium, with a flaring shape and a slightly puffed-up inner rim (Dullemond & Dominik 2004a). The dust temperature is calculated explicitly, whereas the gas temperature is put to a constant value of 300 K everywhere, appropriate for the upper layers from which most of the PAH emission originates. The results are not sensitive to the exact value of the gas temperature (see also Sect. 6.4.5).

The same parameters are used for a template T Tauri star+disk model, except that the star has mass $0.58 M_\odot$ and effective temperature 4000 K. The dust evaporation temperature is kept at 1700 K, so the disk's inner radius moves inwards to 0.077 AU.

$C_{50}H_{18}$ is present as a prototypical PAH, at a high abundance of 1.6×10^{-6} PAH molecules per hydrogen nucleus to maximise the effects of changes in the model parameters. This abundance corresponds to 10% of the total dust mass and to 36% of the total amount of carbon in dust being locked up in this PAH, assuming an abundance of carbon in dust of 2.22×10^{-4} with respect to hydrogen (Habart et al. 2004b). The model was also run for PAHs of 24 and 96 carbon atoms.

6.4 Results

This chapter focuses on the chemistry of the PAHs in a circumstellar disk and on its effects on the mid-IR emission, as well as on the differences between disks around Herbig Ae/Be and T Tauri stars. Geers et al. (2006) analysed the effects of changing various disk parameters, such as the PAH abundance and the disk geometry; settling of PAHs and dust was analysed by Dullemond et al. (2007a).

6.4.1 PAH chemistry

Due to the large variations in density and UV intensity throughout the disk, the PAHs are present in a large number of charge and hydrogenation states (Tables 6.2 and 6.3). When a disk containing only 50-C PAHs ($N_H^\circ = 18$) is in steady state, our model predicts that 56%

Table 6.2 – Abundances of the dominant charge and hydrogenation states for three PAHs in the model Herbig Ae/Be star+disk system.^{a,b}

N_{H}	Z	N.R.	$100\Gamma_{\text{ea}}$	$0.01\Gamma_{\text{ea}}$	$100\Gamma_{\text{diss,H}}$	$0.01\Gamma_{\text{diss,H}}$
$N_{\text{C}} = 24, N_{\text{H}}^{\circ} = 12, -1 \leq Z \leq +2$						
12	-1	6.6(+1)	9.2(+1)	3.5(+0)	6.7(+1)	6.5(+1)
12	0	2.8(+1)	6.0(-1)	8.9(+1)	2.7(+1)	2.8(+1)
23	0	1.0(-1)	6.4(-5)	6.3(-3)	1.0(-1)	1.0(-1)
24	-1	3.6(+0)	7.4(+0)	3.7(-1)	3.7(+0)	3.6(+0)
24	0	7.3(-1)	5.1(-2)	7.1(+0)	7.5(-1)	7.3(-1)
$N_{\text{C}} = 50, N_{\text{H}}^{\circ} = 18, -1 \leq Z \leq +3$						
17	0	2.2(-1)	8.1(-2)	1.6(-1)	2.1(-1)	2.2(-1)
17	+1	3.5(-2)	2.0(-3)	2.6(-2)	2.2(-2)	3.6(-2)
17	+2	4.3(-4)	8.7(-6)	9.7(-4)	1.5(-4)	6.1(-4)
18	-1	2.8(+1)	4.4(+1)	1.1(+0)	3.0(+1)	2.6(+1)
18	0	2.1(+1)	6.2(-1)	4.8(+1)	2.1(+1)	2.0(+1)
18	+1	3.3(-2)	1.3(-3)	3.7(-1)	4.9(-2)	3.1(-2)
18	+2	7.5(-4)	8.9(-6)	8.3(-3)	1.1(-3)	4.3(-4)
19	-1	9.6(-1)	1.1(+0)	7.6(-2)	3.2(-1)	5.6(-1)
19	0	1.8(-1)	3.3(-3)	1.1(+0)	5.3(-2)	2.0(-1)
19	+1	5.6(-3)	3.0(-6)	4.7(-1)	3.1(-3)	7.5(-3)
36	-1	4.5(+1)	5.3(+1)	4.2(+1)	4.5(+1)	4.8(+1)
36	0	4.0(-1)	3.0(-2)	5.6(+0)	3.8(-1)	8.3(-1)
$N_{\text{C}} = 96, N_{\text{H}}^{\circ} = 24, -2 \leq Z \leq +4$						
48	-2	2.1(+1)	2.0(+1)	2.3(+1)	2.1(+1)	2.1(+1)
48	-1	5.7(+1)	7.9(+1)	2.4(+1)	5.7(+1)	5.7(+1)
48	0	2.2(+1)	7.1(-1)	5.0(+1)	2.2(+1)	2.2(+1)
48	+1	1.3(-1)	1.0(-2)	1.1(+0)	1.3(-1)	1.3(-1)
48	+2	2.0(-2)	3.8(-4)	2.1(-1)	2.0(-2)	2.0(-2)

^a In per cent of the entire PAH population in the disk.

^b N.R.: normal rates, i.e., the rates as discussed in Sect. 6.2. $100\Gamma_X$ and $0.01\Gamma_X$: the normal rate for process X (ea: electron attachment; diss,H: photodissociation with loss of H or H₂) in/decreased by a factor of 100. The effect of increasing a certain rate is the same as decreasing the rate of the reverse process (photoelectric emission or addition of H or H₂).

of the observed PAH emission between 2.5 and 13.5 μm originates from neutral C₅₀H₁₈, with another 9% from C₅₀H₁₈⁺. PAHs missing one hydrogen atom also contribute to the emission: 22% comes from C₅₀H₁₇ and 12% from C₅₀H₁₇⁺.

A strong contribution to the observed emission does not imply a high abundance throughout the disk, because the contribution of each state to the spectrum also depends on its spatial distribution. Figure 6.2 shows a cut through the disk and indicates the abundance of the six most important states with respect to the total C₅₀H _{y} ^{Z} population. Near the surface, where the radiation field is strong, the PAHs are ionised and some of them

Table 6.3 – Emissivity contributions from 2.5 to 13.5 μm for the dominant charge and hydrogenation states for three PAHs in the model Herbig Ae/Be star+disk system.^a

N_{H}	Z	N.R.	$100\Gamma_{\text{ea}}$	$0.01\Gamma_{\text{ea}}$	$100\Gamma_{\text{diss,H}}$	$0.01\Gamma_{\text{diss,H}}$
$N_{\text{C}} = 24, N_{\text{H}}^{\circ} = 12, -1 \leq Z \leq +2$						
12	-1	–	–	–	–	–
12	0	1.0(+2)	1.0(+2)	1.0(+2)	1.0(+2)	1.0(+2)
23	0	1.2(-3)	–	2.7(-5)	1.9(-3)	1.2(-3)
24	-1	–	–	–	–	–
24	0	3.6(-2)	3.6(-1)	5.1(-2)	5.5(-2)	3.6(-2)
$N_{\text{C}} = 50, N_{\text{H}}^{\circ} = 18, -1 \leq Z \leq +3$						
17	0	2.2(+1)	5.1(+1)	2.9(+0)	1.8(+1)	2.1(+1)
17	+1	1.2(+1)	2.0(+0)	3.0(+0)	6.8(+0)	1.2(+1)
17	+2	1.3(-1)	4.9(-3)	2.4(-1)	2.4(-2)	1.9(-1)
18	-1	–	–	–	–	–
18	0	5.6(+1)	4.6(+1)	2.9(+1)	5.9(+1)	5.5(+1)
18	+1	9.0(+0)	1.2(+0)	1.0(+1)	1.5(+1)	8.3(+0)
18	+2	2.3(-1)	5.4(-3)	2.4(+0)	3.5(-1)	1.3(-1)
19	-1	–	–	–	–	–
19	0	5.3(-6)	6.9(-6)	9.1(-6)	3.9(-7)	8.2(-1)
19	+1	1.7(+0)	–	4.5(+1)	8.1(-1)	2.4(+0)
36	-1	–	–	–	–	–
36	0	5.0(-5)	3.5(-5)	6.2(-5)	5.0(-5)	5.2(-5)
$N_{\text{C}} = 96, N_{\text{H}}^{\circ} = 24, -2 \leq Z \leq +4$						
48	-2	–	–	–	–	–
48	-1	–	–	–	–	–
48	0	4.4(+1)	8.7(+1)	1.3(+1)	4.4(+1)	4.4(+1)
48	+1	4.2(+1)	1.2(+1)	2.9(+1)	4.2(+1)	4.2(+1)
48	+2	1.4(+1)	5.0(-1)	5.6(+1)	1.4(+1)	1.4(+1)

^a See footnotes to Table 6.2.

have lost a hydrogen atom. Going to lower altitudes, the PAHs first become neutral and then negatively ionised. Still lower, the increasing density and optical depth lead to further hydrogenation, resulting in a high abundance of the completely hydrogenated anion, $\text{C}_{50}\text{H}_{36}^-$, around the midplane.

Normally hydrogenated and positively ionised states occur in more strongly irradiated regions than do completely hydrogenated and negatively ionised states, so the former emit more strongly. For example, the state responsible for more than half of the emission, $\text{C}_{50}\text{H}_{18}$, constitutes only 21% of all PAHs in the entire disk (Tables 6.2 and 6.3). About half of the PAHs (45%) are expected to be in the form of $\text{C}_{50}\text{H}_{36}^-$. This state, which is assumed not to emit at all (Sect. 6.2.3), dominates the high-density regions close to the midplane. The normally hydrogenated anion, $\text{C}_{50}\text{H}_{18}^-$, accounts for 28% of all PAHs,

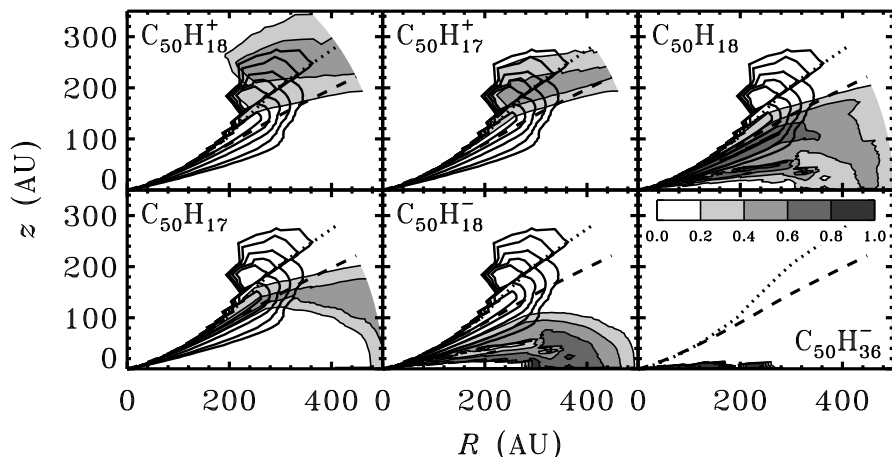


Figure 6.2 – Steady-state distribution of the most important charge and hydrogenation states of $C_{50}H_y$ ($N_H^c = 18$) in a disk around a Herbig Ae/Be star (10^4 K). Each panel shows a cut through the disk, with the equator on the horizontal axis and the pole on the vertical axis. The grey scale denotes the fraction at which a state is present compared to all possible states. The dashed line denotes the $\tau_{\text{vis}} = 1$ surface. The dotted “emission line” connects the points where the PAH emission is strongest for a given distance $r = \sqrt{R^2 + z^2}$ from the star. The thick black contour lines denote the region responsible for most of the PAH emission; from the outside inward, the contours contain 95, 90, 76, 52 and 28% of the total emitted power between 2.5 and 13.5 μm . They are omitted from the last frame for clarity.

and the remaining PAHs are mostly present as anions with $18 < N_H < 36$. States like $C_{50}H_{17}^-$ and $C_{50}H_{36}^+$ are entirely absent: the same environmental parameters that favour dehydrogenation (strong radiation, low density), also favour ionisation.

Species with $N_H < 17$ are also predicted to be absent. They have to be formed from $C_{50}H_{17}^Z$, but wherever these states exist, the ratio between the UV intensity and the hydrogen density favours hydrogen addition. In those regions where the ratio is favourable to photodissociation with H loss, the radiation field is also strong enough to destroy the carbon skeleton. The abundance of $C_{50}H_{17}^Z$ is boosted by H_2 loss from $C_{50}H_{19}^Z$, which is a much faster process than H loss from $C_{50}H_{18}^Z$. Moving from the surface to the midplane, the increasing n_H/G'_0 ratio allows all hydrogenation states from $N_H^c + 1$ to $2N_H^c$ to exist. However, since all of them except $N_H = 19$ are negatively charged, they are assumed not to emit.

6.4.2 PAH emission

The integrated UV intensity between 6 and 13.6 eV, characterised by G'_0 (Eq. (6.10)), varies by many orders of magnitude from the disk’s surface to the midplane. The radiation

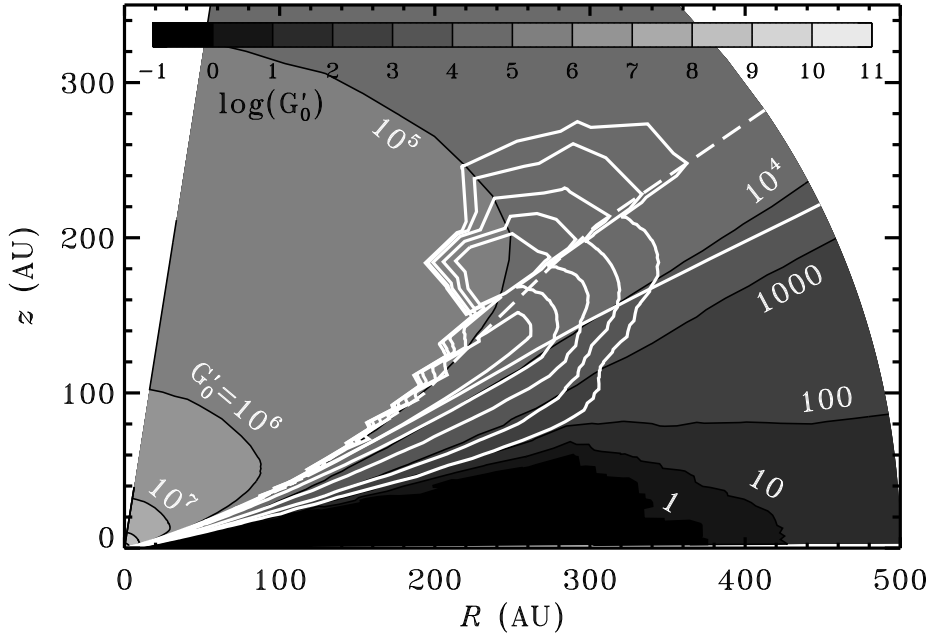


Figure 6.3 – The radiation field (characterised by G'_0 ; Eq. (6.10)) for a flaring disk around a Herbig Ae/Be star (10^4 K), containing PAHs of 50 carbon atoms. The dashed line is the “emission line” from Fig. 6.2. The white contour lines are the same as the black contour lines in Fig. 6.2.

field for the model Herbig Ae/Be system is shown in Fig. 6.3, with the region responsible for most of the 2.5–13.5 μm PAH emission indicated by contour lines. Part of this region is truncated sharply due to photodestruction of the PAHs, marking the $G'_0 = G_0^*$ line. An analysis of the disk structure shows that some 95% of the PAH emission originates from a region with $10^1 < G'_0 < 10^5$, $10^3 < n_{\text{H}} (\text{cm}^{-3}) < 10^9$, and $10^{-1} < n_{\text{e}} (\text{cm}^{-3}) < 10^4$ (see also Fig. 6.4).

When the radiation field is traced along the $\tau_{\text{vis}} = 1$ surface, and the disk’s inner 0.01 AU is disregarded, the integrated intensity decreases almost as a power law. Specifically, for any point on the $\tau_{\text{vis}} = 1$ surface a distance r_{τ} (in AU) away from the star,

$$G'_0 \approx 3.0 \times 10^8 r_{\tau}^{-1.74}. \quad (6.18)$$

The power-law exponent differs from the value of -2 expected based on geometrical considerations because of the curvature in the $\tau_{\text{vis}} = 1$ surface. This relationship allows one to predict to what radius r_{des} PAHs of a certain size are destroyed, as was done in Sect. 6.2.6 and Fig. 6.1. It should be noted, however, that this only applies to the $\tau_{\text{vis}} = 1$ surface. PAHs can survive and contribute to the emission from $r < r_{\text{des}}$ when they are at lower altitudes (e.g., Figs. 6.3 and 6.7).

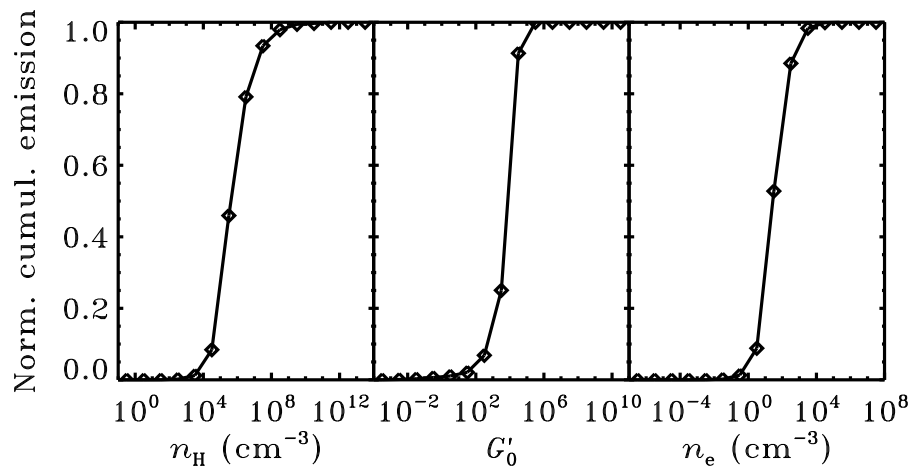


Figure 6.4 – Normalised cumulative PAH emission for the Herbig Ae/Be model as function of total hydrogen density (n_H , left panel), radiation field (G'_0 , middle panel) and electron density (n_e , right panel).

The abundances of the charge and hydrogenation states in the 95% emission region are different from those in the entire disk. Although they agree more closely to the emissivity contributions, a perfect correspondence is not achieved. For instance, only 1.0% of the PAHs in this region are in the form of $\text{C}_{50}\text{H}_{18}^+$, but they account for 8.0% of the emission (Tables 6.2 and 6.3). This is again due to the positive ions occurring in a more intense radiation field than the neutrals and negative ions.

In a vertical cut through the disk, a point exists for every distance r_{em} from the star where the PAH emission is strongest. These points form the “emission lines” in Figs. 6.2 and 6.3. The conditions along this line determine the charge and hydrogenation of the PAHs responsible for most of the observed emission. Its altitude depends mostly on two competing factors: the intensity of the UV field and the PAH number density. A strong UV field leads to stronger emission, but a strong UV field can only exist in regions of low density, where the total emission is weaker.

The variation of n_H , n_e and G'_0 along the emission line is plotted in Fig. 6.5. In the disk’s inner 100 AU (disregarding the actual inner rim), photodestruction of PAHs causes the emission line to lie below the $\tau_{\text{vis}} = 1$ surface, where n_H and n_e are relatively high (10^{11} and 10^4 cm^{-3} , respectively) and G'_0 is relatively low (10^2 – 10^3). The resulting n_e/G'_0 and n_H/G'_0 ratios favour the neutral normally hydrogenated species, $\text{C}_{50}\text{H}_{18}$. Going to larger radii, the emission line gradually moves up and crosses the $\tau_{\text{vis}} = 1$ surface at around 100 AU. As a consequence, n_H and n_e decrease while G'_0 increases. Because the electron abundance with respect to hydrogen also decreases, the PAHs first lose a hydrogen atom to become $\text{C}_{50}\text{H}_{17}$. Farther out, ionisation takes place to produce $\text{C}_{50}\text{H}_{17}^+$. At still larger

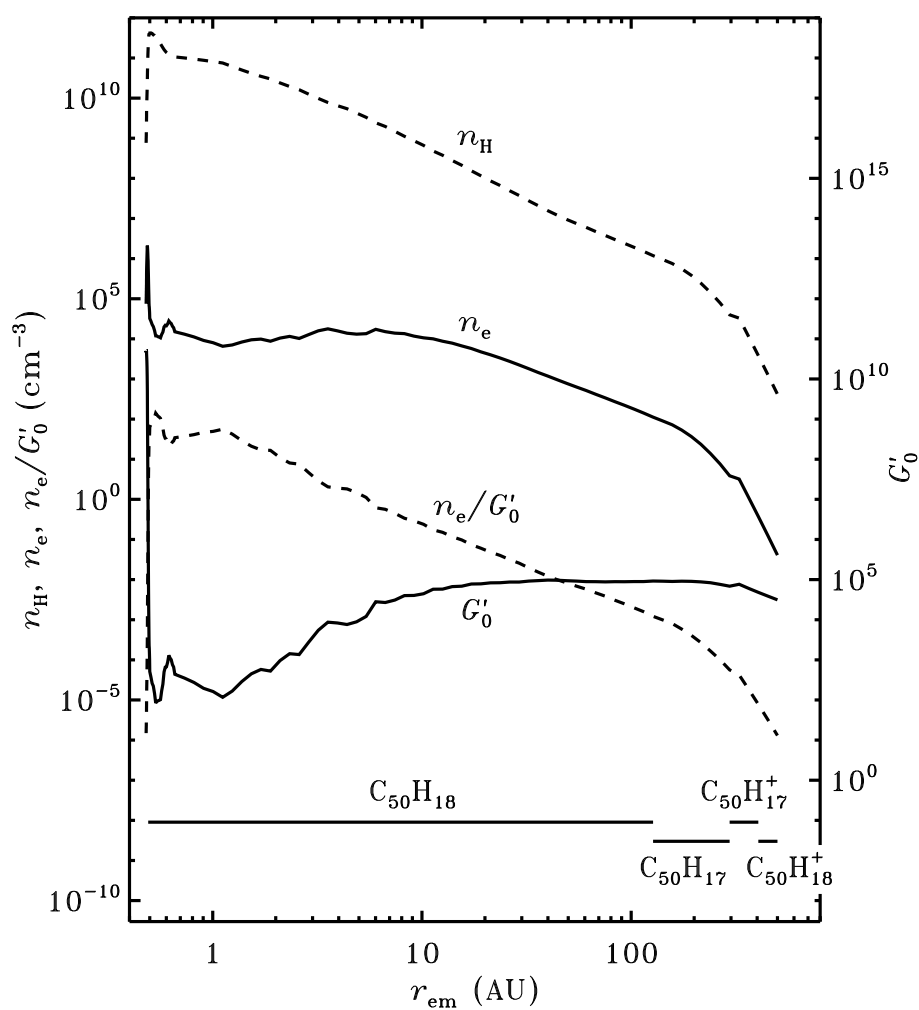


Figure 6.5 – Total hydrogen density (n_{H}), electron density (n_{e}), radiation field (G'_0) and ratio between electron density and radiation field (n_{e}/G'_0) along the emission line defined in Fig. 6.2 and Sect. 6.4.2. The bars at the bottom indicate the main emitter at each distance along the emission line. The parameters are those of the template Herbig Ae/Be model.

radii, the radiation field starts to lose intensity and $\text{C}_{50}\text{H}_{18}^+$ becomes the dominant species. The deviation from the $r^{-1.74}$ power law for the radiation field (Eq. (6.18)) is due to the emission line not following the $\tau_{\text{vis}} = 1$ surface.

It should be noted that ionised and dehydrogenated species do exist (and emit) in the

disk's inner part. However, for any given distance to the star, they only become the most abundant species at around 100 AU.

6.4.3 Other PAHs

If $C_{96}H_{24}$ is put into the disk instead of $C_{50}H_{18}$, the abundance of the dehydrogenated and normally hydrogenated states essentially goes to zero. This is due to the hydrogen addition rates being larger and the hydrogen dissociation rates being smaller for larger PAHs. Most of the 2.5–13.5 μm emission in the $N_C = 96$ case comes from $C_{96}H_{48}$ (44%), $C_{96}H_{48}^+$ (42%) and $C_{96}H_{48}^{2+}$ (14%), while the anion, $C_{96}H_{48}^-$, is the most abundant overall (Tables 6.2 and 6.3).

If only $C_{24}H_{12}$ is put in, the PAH emission becomes very weak. The critical radiation intensity for this PAH is less than 1 (Fig. 6.1), so it can only survive in strongly shielded areas. There, 66% of the PAHs are present as $C_{24}H_{12}^-$, 28% as $C_{24}H_{12}$ and 4% as $C_{24}H_{24}^-$. Only the neutral species contributes to the emission; however, since this PAH only emits from regions where $G'_0 \lesssim 1$, no PAH features are visible in the calculated spectrum, despite the high abundance used in our model. This is exemplified in Fig. 6.6, where the calculated spectra for the model star+disk system are compared for the three PAH sizes. A disk around a Herbig Ae/Be star containing PAHs of 50 or 96 carbon atoms shows strong PAH features, but the 24-C spectrum contains only thermal dust emission.

The goal of Fig. 6.6 is to show the differences arising from the photochemical modelling of the three PAH sizes in model Herbig Ae/Be and T Tauri disks, rather than to provide realistic spectra from such objects. In order to fit our model results to observations, one would need to include a range of PAH sizes in one model (Li & Lunine 2003) and execute a larger parameter study (Habart et al. 2004b, Geers et al. 2006) than was done in this work.

6.4.4 Spatial extent of the PAH emission

The top panel in Figure 6.7 presents the cumulative intensity of the five main PAH features and the continua at 3.1 and 19.6 μm as a function of radius for $N_C = 50$. In accordance with Figs. 6.2 and 6.3, more than 95% of the power radiated in the features originates from outside the inner 10 AU, and some 80% from outside 100 AU. This is largely due to these PAHs being destroyed closer to the star. The 3.3 and 11.3 μm features are somewhat less extended than the other three features. The continua are much more confined than the features, especially at 3.1 μm , where 75% comes from the disk's inner rim.

The PAH emission from a disk with $N_C = 96$ (Fig. 6.7, middle panel) is less extended than that from the same disk with $N_C = 50$, because larger PAHs can survive at smaller radii. About 80% of the integrated intensity of the 3.3 μm feature originates from within 100 AU, and so does about 60% of the other, less energetic features. The continuum at 20 μm has the same spatial behaviour as the 3.3 μm PAH feature, while the continuum at 3.1 μm is very much confined towards the centre. These results are in good agreement with the spatial extent modelled by Habart et al. (2004b). The spatial extent of the continuum

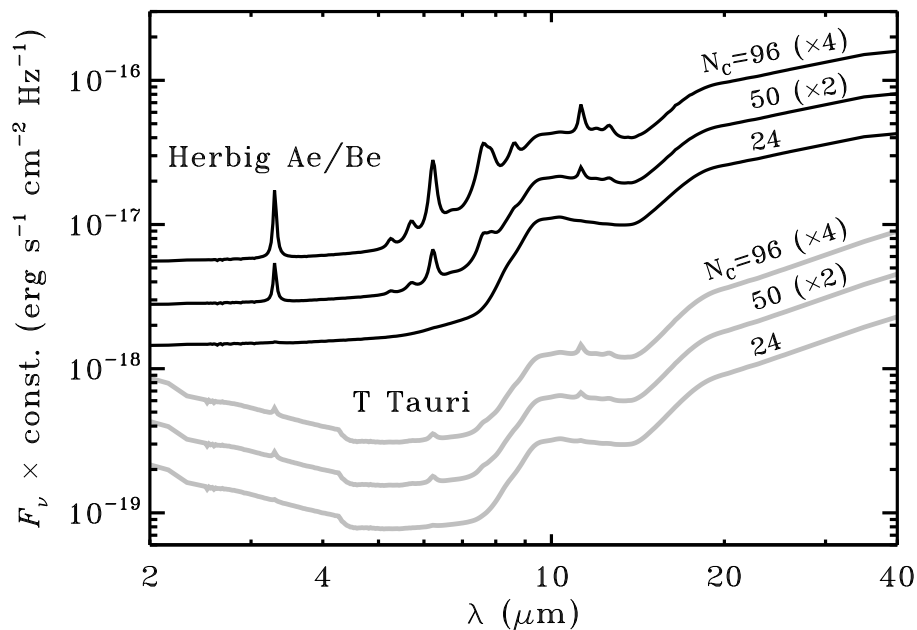


Figure 6.6 – Model spectra (flux at 1 pc) for disks around a Herbig Ae/Be (black) and a T Tauri star (grey) containing either $C_{24}H_{12}$, $C_{50}H_{18}$ (shifted by a factor of two) or $C_{96}H_{24}$ (shifted by a factor of four), with the charge and hydrogenation balance calculated by the chemistry model.

emission from the $C_{96}H_{24}$ disk is identical to that from the $C_{50}H_{18}$ disk, so the thermal dust emission appears to be unaffected by the details of the PAHs and their chemistry.

Our model also agrees well with a number of spatially resolved observations (van Boekel et al. 2004, Habart et al. 2006, Geers et al. 2007), where the PAH features were consistently found to be more extended than the adjacent continuum. Furthermore, PAH emission is typically observed on scales of tens of AU, which cannot be well explained by our model if only PAHs of 50 carbon atoms are present. Hence, the observed emission is probably due to PAHs of at least about 100 carbon atoms.

6.4.5 Sensitivity analysis

The rates for most of the chemical reactions discussed in Sect. 6.2 are not yet well known. In order to gauge the importance of having an accurate rate for a given reaction, the equilibrium distributions were calculated for rates increased or decreased by a factor of 100 from their normal model values. These results are also presented in Tables 6.2 and 6.3. Modifying the hydrogen dissociation and addition rates leads to no significant changes, so treating photodissociation with loss of hydrogen in a purely single-photon fashion likely

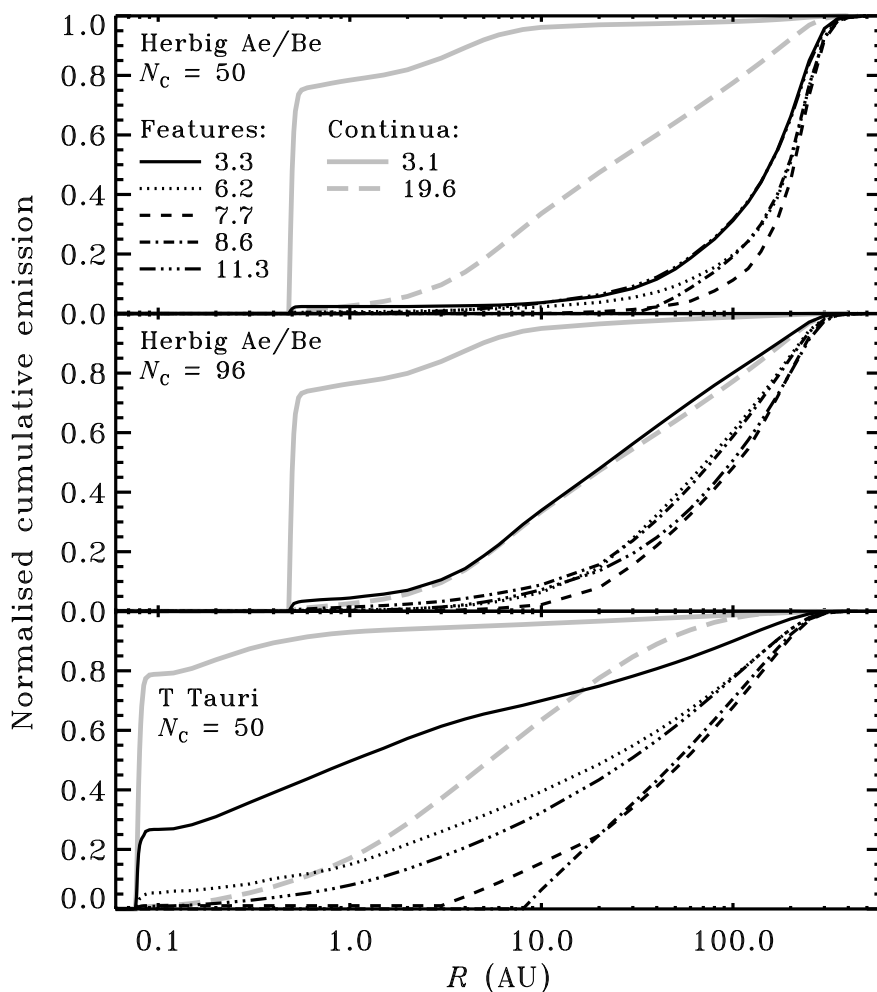


Figure 6.7 – Normalised cumulative integrated intensity of the five main PAH features (black) and the continua at 3.1 and 19.6 μm (grey) for $\text{C}_{50}\text{H}_{18}$ around a Herbig Ae/Be star (top), $\text{C}_{96}\text{H}_{24}$ around a Herbig Ae/Be star (middle) and $\text{C}_{50}\text{H}_{18}$ around a T Tauri star (bottom). In each case, the charge and hydrogenation balance are calculated by the chemistry model.

does not introduce large errors. The fact that most of the PAH emission comes from regions with a relatively weak UV field ($G'_0 < 10^5$), where multi-photon events play only a minor role, further justifies the single-photon dehydrogenation treatment.

The ionisation and electron attachment rates are more important to know accurately.

For instance, the contribution from the cations to the spectrum decreases by a factor of a few when taking an ionisation rate that is 0.01 times the normal model rate. The shift away from positively charged species also affects hydrogenation (addition of hydrogen is faster to cations than to neutrals), resulting, e.g., in a smaller emissivity contribution from $C_{50}H_{18}$ and $C_{50}H_{18}^+$ with respect to $C_{50}H_{17}$ and $C_{50}H_{17}^+$. Further laboratory work on ionisation and electron attachment rates, especially for larger PAHs, will help to better constrain this part of the model.

As shown by e.g. Kamp & Dullemond (2004) and Jonkheid et al. (2004), the gas temperature is not constant throughout the disk. The recombination rates between electrons and cations decrease for higher temperatures, whereas the attachment rates of electrons to neutrals are almost independent of temperature (Sect. 6.2.4). Taking a higher temperature would result in a slightly larger cation abundance. However, even for an extreme temperature of 5000 K, the recombination rates decrease by only a factor of four, and the effects are smaller than what is depicted in Tables 6.2 and 6.3. Hence, we believe it is justified to take a constant temperature of 300 K throughout the disk.

6.4.6 T Tauri stars

The results discussed so far are for a star with an effective temperature of 1×10^4 K, appropriate for a Herbig Ae/Be type. Colder stars, like T Tauri types, are less efficient in inducing IR emission in PAHs, as shown with both observations and models by Geers et al. (2006), unless they have excess UV over the stellar atmosphere. Hence, when the model parameters are otherwise unchanged, the continuum flux from the star+disk system and the absolute intensity of the PAH features become weaker (Fig. 6.6).

It was shown in Sect. 6.4.2 that the integrated intensity of the UV field along the $\tau_{\text{vis}} = 1$ surface of a disk around a Herbig Ae/Be star decreases approximately as a power law. This is also true for the T Tauri case, if the disk's inner 0.01 AU are again disregarded. The exponent is slightly larger:

$$G'_0 \approx 12r_\tau^{-1.93}, \quad (6.19)$$

with r_τ in AU. The UV field peaks at $G'_0 = 6 \times 10^5$ at the inner rim and drops by two orders of magnitude within 0.01 AU, so a PAH of 50 carbon atoms ($G_0^* = 1.2 \times 10^5$) can survive almost everywhere (see also Fig. 6.1).

The smaller destruction radii also lead to the PAH emission being more concentrated towards the inner disk (Fig. 6.7, bottom panel). The $3.3 \mu\text{m}$ feature is particularly confined, with 70% originating from the inner 10 AU and 25% from the inner rim. As was the case for the Herbig Ae/Be disks (Sect. 6.4.4), the inner rim contributes strongly to the continuum emission at $3.1 \mu\text{m}$. The $19.6 \mu\text{m}$ continuum also behaves very similarly to that from the Herbig Ae/Be disks, except that it is stretched inwards because of the smaller R_{in} . Thus, the spatial extent of the thermal dust emission seems to be largely unaffected by the temperature of the central star.

Cations are practically absent in the model T Tauri disk with any kind of PAH, due to the weaker radiation field. For $N_C = 24$ and 50, almost all of the PAH emission originates from the normally hydrogenated neutral species, $C_{24}H_{12}$ or $C_{50}H_{18}$. Less than 0.1%

originates from other neutral states, primarily those missing one hydrogen atom ($C_{24}H_{11}$, $C_{50}H_{17}$) or having twice the normal number of hydrogen atoms ($C_{24}H_{24}$, $C_{50}H_{36}$). If a disk around a T Tauri star contains only 96-C PAHs, all of the emission is due to $C_{96}H_{48}$. The absence of cations could help explain the weak 7.7 and 8.6 μm features in observed spectra (Geers et al. 2006), because these two features are weaker in neutral PAHs.

Anions are abundant for all three PAH sizes, accounting for about half of the entire PAH population. However, they are again assumed not to contribute to the emission.

6.4.7 Comparison with observations

Acke & van den Ancker (2004) performed a comprehensive analysis of the PAH features in a large sample of Herbig Ae/Be stars observed with ISO, measuring line fluxes and comparing them to each other. Figure 6.8 recreates their Fig. 9, plotting the ratio of the integrated fluxes in the 8.6 and 6.2 μm bands against the ratio of the integrated fluxes in the 3.3 and 6.2 μm bands. In order to gauge the plausibility of the numerous charge and hydrogenation states a PAH can in principle attain, the same ratios are also plotted for a sample of models containing one PAH in one specific state only.

The 3.3-6.2 ratio from the model is very sensitive to the charge of the PAH and increases by an order of magnitude when going from ionised to neutral species. The 3.3 and 8.6 μm features are due to C–H vibrational modes, while the 6.2 μm feature is due to a C–C mode (Sect. 6.2.3), so both ratios in Fig. 6.8 increase with N_H . The observations fall mostly in between the model points for neutral and ionised PAHs, so both charge states appear to contribute to the observed emission. This strengthens the model results presented in this work, although the observed emissivity contribution from neutral species seems to be somewhat less than the predicted $\sim 50\%$. Most of the observations agree with the model prediction that the emission originates from multiple hydrogenation states, with a lower limit of $N_H = N_H^\circ - 1$.

6.5 Conclusions

We studied the chemistry of polycyclic aromatic hydrocarbons (PAHs) in disks around Herbig Ae/Be and T Tauri stars, as well as the infrared (IR) emission from these species. We created an extensive PAH chemistry model, based primarily on the models of Le Page et al. (2001) and Weingartner & Draine (2001), with absorption cross sections from Draine & Li (2007). This model includes reactions affecting the charge (ionisation, electron recombination, electron attachment) and hydrogen coverage (photodissociation with hydrogen loss, hydrogen addition) of PAHs in an astronomical environment. Destruction of PAHs by UV radiation is also taken into account, including destruction by multi-photon absorption events. By coupling the chemistry model to an existing radiative transfer model, we obtained equilibrium charge and hydrogenation distributions throughout the disks. The main results are as follows:

- Very small PAHs (24 carbon atoms) are destroyed within a typical disk lifetime of 3 Myr even in regions of low UV intensity ($G'_0 \approx 1$). No features are seen in the

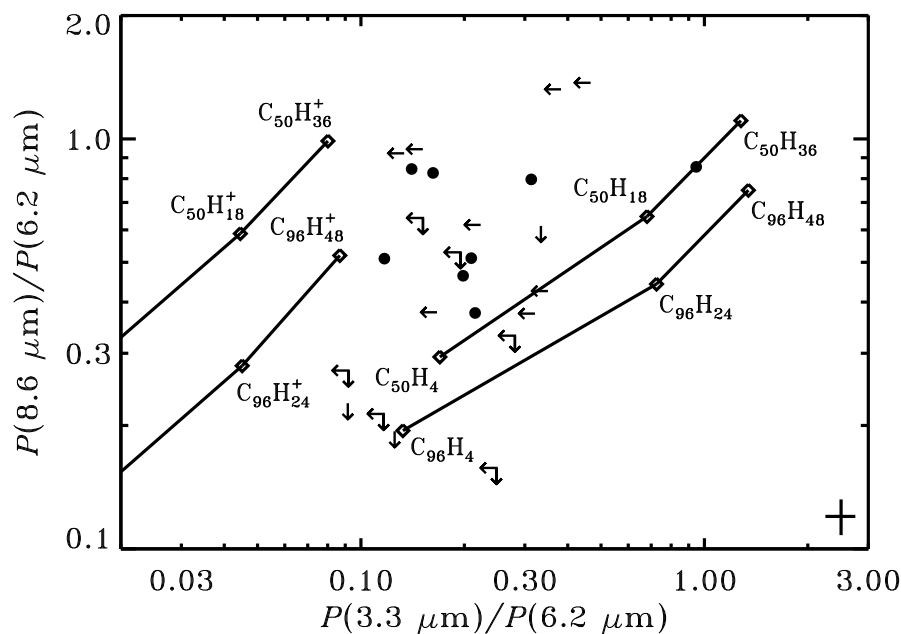


Figure 6.8 – The ratio of the fluxes of the 8.6 and 6.2 μm bands against the ratio of the fluxes of the 3.3 and 6.2 μm bands. Filled circles and arrows are detections and upper limits from Acke & van den Ancker (2004). Open diamonds and lines are predictions from the template Herbig Ae/Be model. The cross in the lower right shows the typical error bars for both the observations and the model results.

calculated spectrum for either a Herbig Ae/Be or a T Tauri disk, despite a high PAH abundance.

- PAHs of intermediate size (50 carbon atoms) do produce clearly visible features, even though they are still photodestroyed out to about 100 AU in the surface layers of a disk around a Herbig Ae/Be star. The model predicts that most of the emission arises from the surface layers and from large radii (more than 100 AU). Neutral and positively ionised species, bearing the normal number of hydrogen atoms or one less, contribute in roughly equal amounts. Negatively charged species are also present, but are assumed not to contribute to the emission.
- Going to still larger PAHs (96 carbon atoms), photodestruction becomes a slower process and the PAHs can survive down to 5 AU from a Herbig Ae/Be star. The slower photodissociation rates also mean that these PAHs are fully hydrogenated everywhere in the disk. Neutral and ionised species still contribute in comparable amounts to the emission, with some 15% originating from doubly ionised PAHs.
- The PAH emission is predicted to be extended on a scale similar to the size of the

disk, with the features at longer wavelengths contributing more in the outer parts and the features at shorter wavelengths contributing more in the inner parts. The continuum emission is less extended than the emission from the PAH features at the same wavelength.

- Disks around T Tauri stars show weaker PAH features than do disks around Herbig Ae/Be stars because of the weaker radiation from T Tauri stars, assuming they have no excess UV over the stellar atmosphere. The PAH emission from T Tauri disks is considerably more confined towards the centre than that from disks around Herbig Ae/Be stars, because PAHs can survive much closer to the star. For instance, a 50-C PAH survives everywhere but in the disk's innermost 0.01 AU. Furthermore, the radiation field is no longer strong enough to ionise the PAHs, and all the PAH emission originates from neutral species for all three PAH sizes. This could help explain the weak 7.7 and 8.6 μm features in observed spectra. About half of all PAHs in a T Tauri disk are predicted to be negatively ionised.
- Comparing the model results to spatially resolved observations (van Boekel et al. 2004, Habart et al. 2006, Geers et al. 2007) for Herbig Ae/Be stars, it appears that PAHs of at least about 100 carbon atoms are responsible for most of the emission. The emission from smaller species is predicted to be too extended. Other observations (Acke & van den Ancker 2004) support the conclusion that the emission is due to a mixture of neutral and singly positively ionised species.

Nederlandse samenvatting:

Chemische evolutie van kernen tot schijven

Astrochemie: scheikunde in de ruimte

Chemie is overal. Auto's worden aangedreven door de chemische reactie tussen benzine en zuurstof. Planten en bomen zetten koolstofdioxide en water met behulp van zonlicht om in zuurstof en glucose. In ons eigen lichaam vindt het omgekeerde proces plaats om energie te leveren voor onze spieren. Zo zijn er nog talloze chemische reacties die de Aarde en het leven daarop maken wat ze zijn. De leus "chemie is overal" beperkt zich echter niet tot de Aarde. De rode kleur van Mars is bijvoorbeeld afkomstig van ijzeroxides, een groep chemische verbindingen bestaande uit ijzer- en zuurstofatomen. De verschillende kleuren in de atmosfeer van Jupiter worden veroorzaakt door allerlei stikstof-, zwavel- en fosforhoudende verbindingen. Zelfs in de schijnbaar lege ruimte tussen de planeten en de sterren blijkt zich een scala aan chemische verbindingen te bevinden.

De wetenschap die zich bezighoudt met deze verbindingen – met deze scheikunde in de ruimte – is de astrochemie. Zij is ontstaan in de jaren twintig van de vorige eeuw, toen langzaam maar zeker duidelijk werd dat de ruimte tussen de sterren niet geheel leeg is. Er bevindt zich een zeer ijl gas, ook wel het interstellair medium genoemd, dat op de meeste plaatsen een dichtheid heeft van minder dan één atoom per kubieke centimeter (cc). Ter vergelijking: een kubieke centimeter van de lucht om ons heen bevat ruim 10.000.000.000.000.000 (10 triljoen) atomen. Een klein deel van het interstellair medium – ongeveer 1% van het totale volume – bestaat uit zogeheten moleculaire wolken. Dit zijn gebieden met een dichtheid van ongeveer 100 atomen per cc. De toevoeging "moleculair" slaat op het feit dat bij deze dichtheid de atomen elkaar al vaak genoeg tegenkomen om chemische bindingen te vormen en zo moleculen te maken.

Het eerste molecuul in de ruimte werd pas in 1937 gevonden: CH, een combinatie van één atoom koolstof (C) en één atoom waterstof (H). Inmiddels zijn er zo'n 150 interstellair moleculen ontdekt, en ieder jaar komen er nog nieuwe bij. Op de lijst staan heel gewone verbindingen zoals H₂O (water), CH₄ (methaan, het hoofdbestanddeel van aardgas) en CH₃CH₂OH (ethanol, de bekendste vorm van alcohol), maar ook exotische moleculen zoals C₆H⁻ en HC₁₁N. Een van de uitdagingen voor astrochemici is om te begrijpen hoe al deze stoffen in de ruimte worden gevormd, en waarom de ene stof in veel

hogere concentratie voorkomt dan de andere. In dit proefschrift zijn deze vragen vooral gericht op moleculen die we waarnemen in de omgeving rond pas gevormde sterren.

De vorming van sterren en planeten

De moleculaire wolken uit de vorige paragraaf zijn tot enkele tientallen lichtjaren groot en hebben dus, ondanks hun enorm lage dichtheid, een aanzienlijke massa: 1000 à 10.000 keer de massa van de Zon.^{1,2} Ze bevatten kleinere gebieden met hogere dichtheid. De dichtste hiervan worden kernen genoemd; zij zijn rond de 10.000 astronomische eenheden (AE) groot,³ een paar zonsmassa's zwaar, en hebben een dichtheid van ongeveer een miljoen atomen of moleculen per cc. De wolk en de kernen bestaan voor 99 massa-% uit gas met een betrekkelijk eenvoudige chemische samenstelling (zie de paragraaf "Chemische evolutie"). Voor de rest bestaan ze uit stof: minuscule zandkorreltjes van ongeveer 0,1 micrometer (of 0,0001 millimeter), omgeven met een dun laagje ijs.

Sterren zoals de Zon ontstaan uit kernen. In figuur 1 is schematisch aangegeven hoe dit proces verloopt. Paneel a toont een moleculaire wolk met daarin een aantal kernen van hogere dichtheid, aangegeven met een donkerdere tint grijs. Paneel b zoomt in op één zo'n kern, met een typische afmeting van 10.000 AE. Voor het gemak doen we hier alsof de kern mooi bolvorming is, zodat we een cirkelvormige dwarsdoorsnede zien. In werkelijkheid zijn kernen echter zelden precies rond. Ongeacht de vorm verliest de kern op een gegeven moment haar stabiliteit en begint ze onder invloed van haar eigen zwaartekracht ineens te storten. Dit moment wordt beschouwd als het begin van het stervormingsproces.

Door het instorten wordt de dichtheid in het midden van de kern steeds hoger, zoals wederom aangegeven met de verschillende grijstinten. Na ongeveer 10.000 jaar⁴ is de dichtheid zo hoog dat we kunnen spreken van een jonge ster (paneel c). De ronde vorm uit paneel b heeft nu plaatsgemaakt voor een plattere dichtheidsverdeling. Dit komt doordat de kern, net als de omringende moleculaire wolk, langzaam ronddraait. Een gevolg van deze draaiing is dat het materiaal dat van de buitenkant van de kern naar binnen valt, niet precies in het midden uitkomt. In plaats daarvan vormt het een platte schijf rond de jonge ster, meestal aangeduid als een circumstellaire schijf. Veel van het materiaal dat in de schijf terecht komt, beweegt verder naar binnen en valt uiteindelijk alsnog in de ster. Ondertussen wordt een deel van het materiaal weer uitgestoten in een sterke straalstroom, in een richting loodrecht op het vlak van de schijf. Deze straalstroom creëert een holle ruimte in het omringende materiaal, die we in paneel c zien als de witte zandlopervorm.

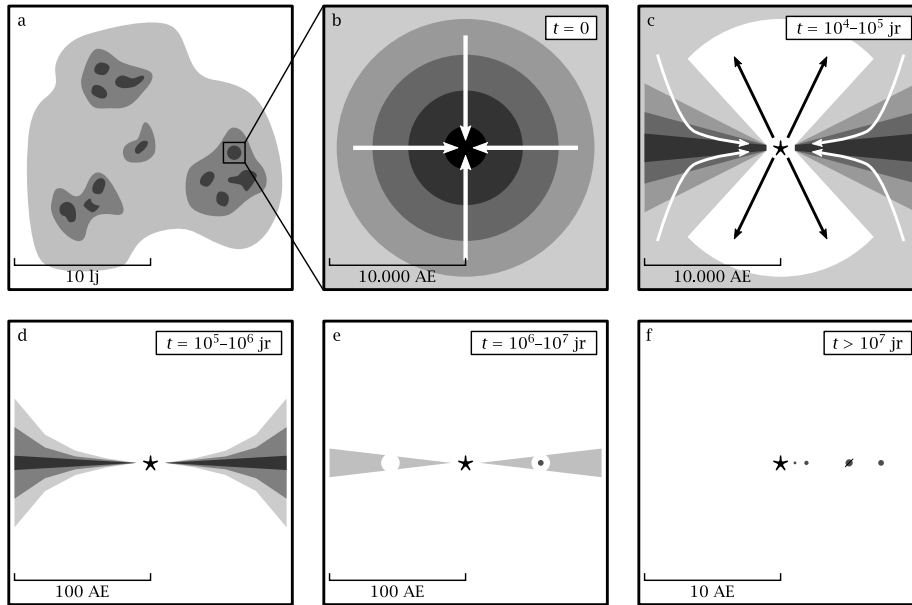
Na zo'n 100.000 jaar (10^5 jr, paneel d) is de kern volledig ingestort. Wat overblijft is een jonge ster omringd door een circumstellaire schijf van ongeveer 100 AE groot. De

¹ Een lichtjaar is de afstand die het licht in een jaar aflegt. Licht reist met een snelheid van 300.000 km per seconde, dus een lichtjaar is 10.000.000.000.000 (10 biljoen) km. Na de Zon staat de dichtstbijzijnde ster, Proxima Centauri, op 4,2 keer deze afstand.

² De massa van de Zon is 2×10^{30} kg, oftewel een 2 met 30 nullen. De Zon is ruim 300.000 keer zo zwaar als de Aarde.

³ Een astronomische eenheid is de gemiddelde afstand tussen de Zon en de Aarde, oftewel 150 miljoen km. Een afstand van 10.000 AE is gelijk aan 0,16 lichtjaar.

⁴ In wetenschappelijke notatie is dit 10^4 : een 1 met vier nullen. Een miljoen is dus bijvoorbeeld 10^6 .



Figuur 1 – Schematische weergave van de vorming van een ster met planeten. De tijd benodigd voor iedere fase is rechtsboven in de panelen aangegeven. Linksonder staan de ruimtelijke schalen; lj staat voor lichtjaar (10 biljoen km) en AE voor astronomische eenheid (150 miljoen km).

dichtheid van de schijf loopt op tot meer dan een biljoen moleculen per cc, een miljoen keer hoger dan de kern waaruit ze is ontstaan. De minuscule stofdeeltjes die in de kern aanwezig waren, beginnen zich nu te concentreren in het midden van de schijf. Ze botsen daar tegen elkaar aan en blijven soms plakken om steeds grotere stofdeeltjes te vormen. Zo krijgen we op een gegeven moment kiezels van een paar centimeter, die weer verder groeien tot rotsblokken van een paar meter, en nog verder tot planetaire embryo's van een paar kilometer. Ze zijn dan zo groot en zwaar dat hun zwaartekracht sterk genoeg is om het gas in de schijf als het ware op te zuigen. Zo belanden we na ongeveer een miljoen jaar in paneel e. De schijf is nu grotendeels verdwenen; wat er nog van over is bevat grote gaten waar het gas is opgenomen in de planeten-in-wording. Het proces van planeetgroei duurt nog enkele miljoenen jaren en resulteert tot slot in een volwassen zonnestelsel zoals getoond in paneel f.

Chemische evolutie

De rode draad in dit proefschrift is de chemische samenstelling van het gas en het stof tijdens de verschillende fases in de vorming van een jonge ster. We bestuderen deze

samenstelling met behulp van astrochemische modellen. Zoals eerder opgemerkt is de chemische samenstelling van het gas in wolkenkernen relatief eenvoudig. Dat komt omdat ze een lage temperatuur hebben (10 Kelvin⁵) en nog niet blootstaan aan het sterke stralingsveld van een ster. De lage temperatuur leidt ertoe dat veel moleculen vastvriezen op de stofdeeltjes. Zodra de kern begint in te storten loopt de temperatuur op. De vluchtigste verbindingen in het ijs verdampen weer, en de algehele chemische samenstelling van het gas en het ijs verandert. Als even later de jonge ster begint te schijnen, zorgt het stralingsveld voor nog meer veranderingen. Dankzij al deze processen, die zijn samengevat in figuur 2, ziet de circumstellaire schijf er chemisch dus heel anders uit dan de kern waarmee we begonnen. Een belangrijke reden dat we zeer geïnteresseerd zijn in de chemie van de schijf, is dat het materiaal uit de schijf in en op de planeten terecht komt. Het is nog steeds onduidelijk waar de chemische bouwstenen voor het eerste leven op Aarde vandaan komen. Als we begrijpen in wat voor omgeving de Aarde is gevormd, en uit wat voor materiaal, kunnen we die vraag in de toekomst wellicht beantwoorden.

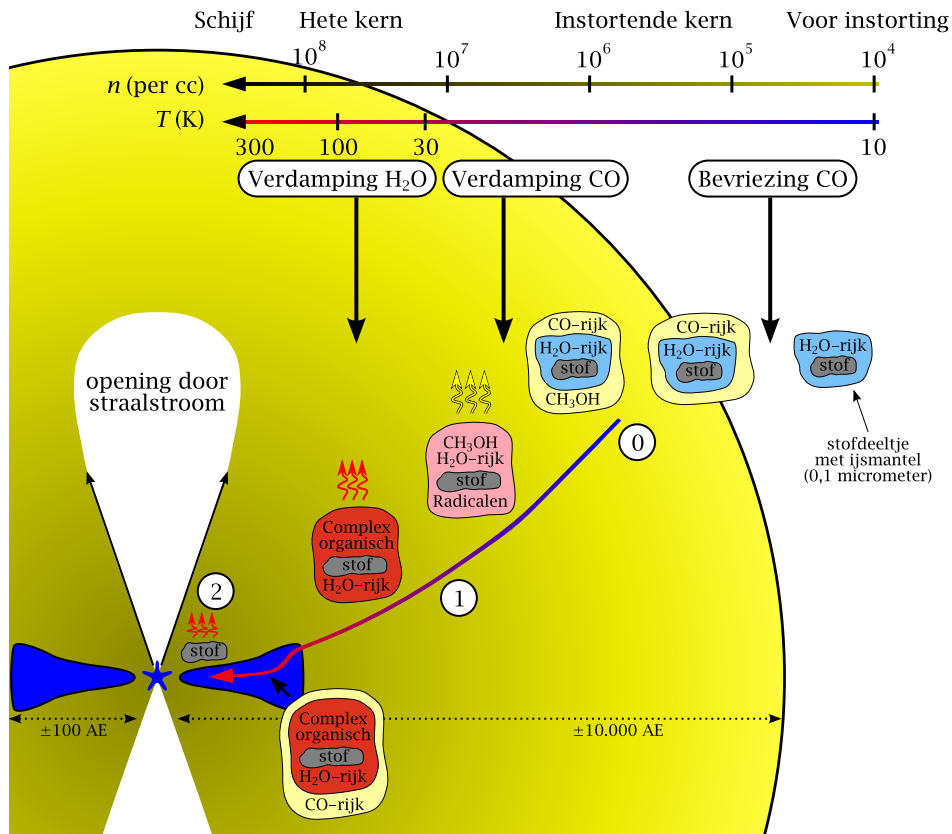
De meest directe manier om iets te weten te komen over de chemische samenstelling van moleculaire wolken en circumstellaire schijven, is door ze te bestuderen met een telescoop. Ieder molecuul, zowel op Aarde als in de ruimte, absorbeert licht en andere vormen van straling op een unieke manier. Door met telescopen te zoeken naar deze “streepjescodes” kunnen we vaststellen of een bepaalde stof wel of niet in een wolk of een schijf voorkomt. Deze methode heeft echter een aantal beperkingen. In de eerste plaats hebben we te maken met de enorme afstanden waarop stervormingsgebieden zich bevinden, waardoor we slechts weinig details kunnen onderscheiden. Een ander probleem is dat jonge sterren en schijven in het begin nog zijn ingebed in de moleculaire wolk (panelen b en c in figuur 1), zodat we ze niet rechtstreeks kunnen waarnemen. Tot slot vertellen waarnemingen ons alleen iets over de chemische samenstelling van een wolk of schijf op dit moment, en niet hoe de samenstelling vroeger was of in de toekomst zal zijn.

Een geschikte methode om de chemische evolutie in de tijd te volgen, en meteen ook om meer details te kunnen zien, is het gebruik van astrochemische modellen. Zo'n model bevat een aantal moleculen, die bepaalde reacties met elkaar aangaan. De snelheid van elke reactie hangt af van de fysische omstandigheden, zoals dichtheid, temperatuur en stralingsveld. Aan elk molecuul in het model wordt een beginconcentratie gegeven, die meestal berust op waargenomen concentraties. Vervolgens wordt een stelsel wiskundige vergelijkingen opgelost om te kijken hoe de concentraties van alle moleculen veranderen in de tijd. Dit kan gedaan worden voor constante of veranderende fysische condities. In het laatste geval kunnen we bijvoorbeeld kijken hoe de concentraties veranderen als een wolkenkern instort om een jonge ster en bijbehorende schijf te vormen.

Dit proefschrift

Zoals gezegd staat in dit proefschrift de verandering van de chemische samenstelling tijdens het stervormingsproces centraal. In het verleden is hier door anderen al veel aan-

⁵ Een temperatuur in Kelvin kan worden omgerekend in graden Celsius via $T(^{\circ}\text{C}) = T(\text{K}) - 273$. Een temperatuur van 10 K is dus -263°C .



Figuur 2 – Schematische weergave van de chemische evolutie tijdens de vorming van een ster. Bovenin zijn de dichtheid (n , in atomen per cc) en temperatuur (T , in Kelvin) aangegeven; beide nemen toe van buiten naar binnen. De grijze bol stelt de instortende kern voor, met binnenin de jonge ster en de omringende schijf. De pijl (langs de punten 0, 1 en 2) is een mogelijke baan die het materiaal kan volgen vanuit de buitendelen van de kern naar de schijf. Langs deze baan is aangegeven hoe de samenstelling van de ijslaag rond de stofdeeltjes (niet op schaal) globaal verandert. Voor de kern begint in te storten is de temperatuur laag en vriezen stoffen als water (H_2O) en koolstofmonoxide (CO) vast op het stof. Het CO wordt deels omgezet in methanol (CH_3OH). Tijdens het instorten wordt het ijs opgewarmd. Het CO verdampt, maar het minder vluchtige water en methanol blijven bevroren. In het ijs worden radicalen (instabiele verbindingen) gevormd die snel verder reageren tot complexere organische moleculen zoals azijnzuur (CH_3COOH) en ether (CH_3OCH_3). De circumstellaire schijf is relatief koud, dus als het materiaal daarin terechtkomt kan CO weer bevriezen. Dichtbij de ster is de temperatuur zo hoog dat al het ijs verdampt.

dacht aan besteed. Dit is echter altijd met eindimensionale modellen gedaan. Daarmee kan prima de chemische evolutie in de instortende kern worden gevolgd, maar voor een goede beschrijving van de circumstellaire schijf zijn tweedimensionale modellen nodig. Dit proefschrift bevat het eerste astrochemische model dat de gehele chemische evolutie vanaf de kern tot aan de schijf volgt in twee dimensies.

Na een algemene inleiding in hoofdstuk 1 geven we in hoofdstuk 2 een gedetailleerde beschrijving van het model. We gebruiken een zogeheten semi-analytische methode om de dichtheden in de kern en de schijf te berekenen, alsmede de snelheden waarmee het materiaal naar de ster toe valt. De dichtheden en snelheden komen goed overeen met wat anderen hebben berekend met een meer gedetailleerde numerieke methode. Het voordeel van onze semi-analytische methode is dat ze sneller is en dat we makkelijker het model kunnen herhalen voor bijvoorbeeld een kern met een andere massa of andere draaisnelheid. De temperatuur heeft een grote invloed op de chemische evolutie. Zij kan niet goed semi-analytisch worden berekend, dus gebruiken we hier een nauwkeurige numerieke methode.

Als een eerste voorbeeld voor de chemische evolutie volgen we de twee veel voorkomende moleculen water en koolstofmonoxide (CO). Door de lage temperatuur in de kern vriezen ze allebei vast op de stofdeeltjes voordat de instorting begint. Tijdens het instorten verdampt CO al snel omdat het een lage bindingsenergie heeft. In een later stadium kan het weer bevroren in de diepste delen van de schijf. Zij ontvangen geen directe straling van de ster en zijn dus erg koud. Water heeft een hogere bindingsenergie dan CO en verdampt pas als het binnen ongeveer 10 AE van de jonge ster komt.

In hoofdstuk 4 kijken we in meer detail naar de draaisnelheid waarmee materiaal vanuit de kern op de schijf terechtkomt. Het is al sinds de jaren tachtig bekend dat het neerkomende materiaal minder snel rond de ster draait dan het materiaal in de schijf. Hoofdstuk 2 bevat een beperkte oplossing voor dit probleem; hier leiden we een betere af, die vervolgens ook in hoofdstuk 3 gebruikt wordt. De nieuwe oplossing levert nieuwe inzichten in de kwestie van kristallijn stof in schijven. Het stof in moleculaire wolken is geheel of vrijwel geheel amorf, maar in schijven is het tot zo'n 30% kristallijn. De overgang van amorf naar kristallijn vereist een temperatuur die veel hoger is dan de temperatuur waarbij het kristallijne materiaal wordt waargenomen. Ons model laat zien dat stof dicht bij de ster op de schijf terecht kan komen, daar heet genoeg wordt om van amorf over te gaan in kristallijn, en vervolgens door de schijf heen weer van de ster af beweegt en zo in koudere gebieden belandt.

De chemie uit hoofdstuk 2 wordt in hoofdstuk 3 sterk uitgebreid tot een netwerk van ruim 400 moleculen en ruim 5200 reacties. We kijken nu niet alleen meer naar CO en water, maar naar een twintigtal belangrijke zuurstof-, koolstof- en stikstofhoudende verbindingen. Het blijkt dat de meeste veranderingen in hun concentraties het gevolg zijn van een klein aantal sleutelprocessen, zoals het verdampen van CO of de fotodissociatie van water. Deze sleutelprocessen zijn weer terug te voeren op veranderingen in bijvoorbeeld de temperatuur of de intensiteit van het stralingsveld.

In hoofdstuk 3 en 4 besteden we speciale aandacht aan kometen. Dit zijn rotsblokken ter grootte van een paar tot enkele tientallen kilometers, die tijdens de vorming van het zonnestelsel niet verder zijn gegroeid tot planeten. Op grond van de modelresultaten uit

hoofdstuk 4 en waarnemingen gedaan door anderen, concluderen we dat kometen worden gevormd uit kleinere brokken met verschillende oorsprong. Een deel van deze brokken is nooit sterk verwarmd, zodat water altijd in ijsvorm is gebleven en de gehele chemische samenstelling vrijwel hetzelfde is als die van moleculaire wolken. Een ander deel is juist wel sterk verwarmd doordat het dichtbij de ster op de schijf terecht kwam. Daarna is het naar het koudere gebied getransporteerd waar kometen worden gevormd. In dit materiaal is al het water verdampt en later weer bevroren, en het heeft een chemische samenstelling die duidelijk verschilt van die van een moleculaire wolk.

Hoofdstuk 5 beperkt zich tot CO en zijn isotoopvarianten.⁶ Onder invloed van ultraviolette straling (UV-straling) kan een molecuul CO uiteenvallen in de losse atomen C en O. We herzien een model uit 1988 met nieuwe laboratoriumdata om de snelheid van dit uiteenvallen te berekenen en om te kijken hoe de snelheid afhangt van de positie in bijvoorbeeld een moleculaire wolk of een circumstellaire schijf. De meest voorkomende isotoopvariant $^{12}\text{C}^{16}\text{O}$ blijkt in de meeste gevallen het langzaamst uiteen te vallen. Daardoor komen er relatief meer ^{13}C -, ^{17}O - en ^{18}O -atomen vrij. Dit gebeurt in een dusdanige verhouding dat we de hoeveelheden ^{17}O en ^{18}O in meteorieten kunnen verklaren.

Het laatste hoofdstuk draait om de chemie van polycyclische aromatische koolwaterstoffen (PAK's) in circumstellaire schijven. PAK's zijn een groep grote, stabiele moleculen bestaande uit een kippengaasachtig skelet van koolstofatomen omringd door een enkele rand waterstofatomen. We berekenen onder andere waar in de schijf de PAK's elektrisch geladen zijn en waar ze worden vernietigd door de UV-straling van de jonge ster. We concluderen dat waargenomen straling van PAK's in schijven in ruwweg gelijke mate afkomstig is van neutrale en geladen PAK's. De PAK's kunnen bovendien niet kleiner zijn dan honderd koolstofatomen.

⁶ Isotopen zijn verschillende atomen van hetzelfde element, maar met een afwijkende massa. Twee van nature voorkomende stabiele koolstofisotopen zijn ^{12}C en ^{13}C , met atoommassa's van respectievelijk 12 en 13. De drie natuurlijke zuurstofisotopen zijn ^{16}O , ^{17}O en ^{18}O .

Literatuur

- Abgrall, H., Roueff, E., Launay, F., Roncin, J.-Y., & Subtil, J.-L. 1993a, *A&AS*, 101, 273
- Abgrall, H., Roueff, E., Launay, F., Roncin, J.-Y., & Subtil, J.-L. 1993b, *A&AS*, 101, 323
- Abouelaziz, H., Gomet, J. C., Pasquerault, D., Rowe, B. R., & Mitchell, J. B. A. 1993, *J. Chem. Phys.*, 99, 237
- Acharyya, K., Fuchs, G. W., Fraser, H. J., van Dishoeck, E. F., & Linnartz, H. 2007, *A&A*, 466, 1005
- Acke, B. & van den Ancker, M. E. 2004, *A&A*, 426, 151
- Adams, F. C. & Shu, F. H. 1986, *ApJ*, 308, 836
- A'Hearn, M. F., Millis, R. L., Schleicher, D. G., Osip, D. J., & Birch, P. V. 1995, *Icarus*, 118, 223
- Aikawa, Y. 2007, *ApJ*, 656, L93
- Aikawa, Y. & Herbst, E. 1999, *A&A*, 351, 233
- Aikawa, Y. & Herbst, E. 2001, *A&A*, 371, 1107
- Aikawa, Y., Miyama, S. M., Nakano, T., & Umebayashi, T. 1996, *ApJ*, 467, 684
- Aikawa, Y., Ohashi, N., Inutsuka, S.-i., Herbst, E., & Takakuwa, S. 2001, *ApJ*, 552, 639
- Aikawa, Y., Umebayashi, T., Nakano, T., & Miyama, S. M. 1997, *ApJ*, 486, L51
- Aikawa, Y., van Zadelhoff, G. J., van Dishoeck, E. F., & Herbst, E. 2002, *A&A*, 386, 622
- Aikawa, Y., Wakelam, V., Garrod, R. T., & Herbst, E. 2008, *ApJ*, 674, 984
- Allamandola, L. J. & Hudgins, D. M. 2003, in *Solid State Astrochemistry*, ed. V. Pirronello, J. Krelowski, & G. Manicò (Dordrecht: Kluwer), 251
- Allamandola, L. J., Tielens, A. G. G. M., & Barker, J. R. 1989, *ApJS*, 71, 733
- Alves, J. F., Lada, C. J., & Lada, E. A. 2001, *Nature*, 409, 159
- Andersson, S., Al-Halabi, A., Kroes, G.-J., & van Dishoeck, E. F. 2006, *J. Chem. Phys.*, 124, 064715
- Andersson, S. & van Dishoeck, E. F. 2008, *A&A*, 491, 907
- André, P., Bouwman, J., Belloche, A., & Hennebelle, P. 2004, *Ap&SS*, 292, 325
- Andrews, S. M. & Williams, J. P. 2007a, *ApJ*, 671, 1800
- Andrews, S. M. & Williams, J. P. 2007b, *ApJ*, 659, 705
- Apai, D., Pascucci, I., Bouwman, J., et al. 2005, *Science*, 310, 834
- Arce, H. G. & Sargent, A. I. 2006, *ApJ*, 646, 1070
- Ashby, M. L. N., Bergin, E. A., Plume, R., et al. 2000, *ApJ*, 539, L119
- Bacmann, A., Lefloch, B., Ceccarelli, C., et al. 2002, *A&A*, 389, L6
- Bacon, F. 1653, in *The Works of Francis Bacon*, vol. X, ed. J. Spedding, R. L. Ellis, & D. D. Heath (1864; Boston: Taggard and Thompson)
- Bakes, E. L. O. & Tielens, A. G. G. M. 1994, *ApJ*, 427, 822
- Bakes, E. L. O., Tielens, A. G. G. M., & Bauschlicher, C. W. 2001a, *ApJ*, 556, 501
- Bakes, E. L. O., Tielens, A. G. G. M., Bauschlicher, C. W., Hudgins, D. M., & Allamandola, L. J. 2001b, *ApJ*, 560, 261
- Bally, J. & Langer, W. D. 1982, *ApJ*, 255, 143

- Bally, J., Reipurth, B., & Davis, C. J. 2007, in *Protostars & Planets V*, ed. B. Reipurth, D. Jewitt, & K. Keil (Tucson: Univ. of Arizona Press), 215
- Banerjee, R., Pudritz, R. E., & Holmes, L. 2004, *MNRAS*, 355, 248
- Barnard, E. E. 1919, *ApJ*, 49, 1
- Bates, D. R. & Spitzer, L. J. 1951, *ApJ*, 113, 441
- Bauschlicher, C. W. 1998, *ApJ*, 509, L125
- Bauschlicher, C. W. 2002, *ApJ*, 564, 782
- Bauschlicher, C. W. & Bakes, E. L. O. 2000, *Chem. Phys.*, 262, 285
- Bayet, E., Gerin, M., Phillips, T. G., & Contursi, A. 2006, *A&A*, 460, 467
- Beals, C. S. 1936, *MNRAS*, 96, 661
- Bensch, F., Pak, I., Wouterloot, J. G. A., Klapper, G., & Winnewisser, G. 2001, *ApJ*, 562, L185
- Benson, P. J. & Myers, P. C. 1989, *ApJS*, 71, 89
- Bergin, E. A., Aikawa, Y., Blake, G. A., & van Dishoeck, E. F. 2007, in *Protostars & Planets V*, ed. B. Reipurth, D. Jewitt, & K. Keil (Tucson: Univ. of Arizona Press), 751
- Bergin, E. A., Calvet, N., D'Alessio, P., & Herczeg, G. J. 2003, *ApJ*, 591, L159
- Bergin, E. A. & Langer, W. D. 1997, *ApJ*, 486, 316
- Bergin, E. A., Melnick, G. J., Stauffer, J. R., et al. 2000, *ApJ*, 539, L129
- Bergin, E. A. & Snell, R. L. 2002, *ApJ*, 581, L105
- Bergin, E. A. & Tafalla, M. 2007, *ARA&A*, 45, 339
- Bernstein, M. P., Sandford, S. A., Allamandola, L. J., et al. 1999, *Science*, 283, 1135
- Beuther, H., Kramer, C., Deiss, B., & Stutzki, J. 2000, *A&A*, 362, 1109
- Bhattacharya, S. K., Savarino, J., & Thiemens, M. H. 2000, *Geophys. Res. Lett.*, 27, 1459
- Biennier, L., Alsayed-Ali, M., Foutel-Richard, A., et al. 2006, *Faraday Discuss.*, 133, 289
- Birkeland, K. 1913, *The Norwegian Aurora Polaris Expedition 1902-1903* (Christiania: H. Aschehoug & Co.)
- Bisschop, S. E., Fraser, H. J., Öberg, K. I., van Dishoeck, E. F., & Schlemmer, S. 2006, *A&A*, 449, 1297
- Black, J. H. & van Dishoeck, E. F. 1987, *ApJ*, 322, 412
- Blake, G. A., Sutton, E. C., Masson, C. R., & Phillips, T. G. 1987, *ApJ*, 315, 621
- Bockelée-Morvan, D., Crovisier, J., Mumma, M. J., & Weaver, H. A. 2004, in *Comets II*, ed. M. C. Festou, H. U. Keller, & H. A. Weaver (Tucson: Univ. of Arizona Press), 391
- Bockelée-Morvan, D., Gautier, D., Hersant, F., Huré, J.-M., & Robert, F. 2002, *A&A*, 384, 1107
- Bockelée-Morvan, D., Lis, D. C., Wink, J. E., et al. 2000, *A&A*, 353, 1101
- Bohdansky, J., Roth, J., & Bay, H. L. 1980, *J. Appl. Phys.*, 51, 2861
- Bonnor, W. B. 1956, *MNRAS*, 116, 351
- Boogert, A. C. A., Pontoppidan, K. M., Knez, C., et al. 2008, *ApJ*, 678, 985
- Boogert, A. C. A., Tielens, A. G. G. M., Ceccarelli, C., et al. 2000, *A&A*, 360, 683
- Boss, A. P. & Yorke, H. W. 1995, *ApJ*, 439, L55
- Bottinelli, S., Ceccarelli, C., Lefloch, B., et al. 2004, *ApJ*, 615, 354
- Bottinelli, S., Ceccarelli, C., Williams, J. P., & Lefloch, B. 2007, *A&A*, 463, 601
- Bouwman, J., Henning, T., Hillenbrand, L. A., et al. 2008, *ApJ*, 683, 479
- Bouwman, J., Meeus, G., de Koter, A., et al. 2001, *A&A*, 375, 950
- Bowen, I. S. 1928, *ApJ*, 67, 1
- Bregman, J. D., Witteborn, F. C., Allamandola, L. J., et al. 1987, *A&A*, 187, 616

- Brinch, C., Hogerheijde, M. R., & Richling, S. 2008a, *A&A*, 489, 607
- Brinch, C., van Weeren, R. J., & Hogerheijde, M. R. 2008b, *A&A*, 489, 617
- Brittain, S. D., Rettig, T. W., Simon, T., & Kulesa, C. 2005, *ApJ*, 626, 283
- Brittain, S. D., Simon, T., Najita, J. R., & Rettig, T. W. 2007, *ApJ*, 659, 685
- Brown, J. M., Blake, G. A., Qi, C., Dullemond, C. P., & Wilner, D. J. 2008, *ApJ*, 675, L109
- Brown, J. M. & Millar, T. J. 2003, *MNRAS*, 339, 1041
- Brown, P. N., Byrne, G. D., & Hindmarsh, A. C. 1989, *SIAM J. Sci. Stat. Comp.*, 10, 1038
- Bruderer, S., Doty, S. D., & Benz, A. O. 2009, *ApJS*, 183, 179
- Burgh, E. B., France, K., & McCandliss, S. R. 2007, *ApJ*, 658, 446
- Cacciani, P., Brandi, F., Sprengers, J. P., et al. 2002, *Chem. Phys.*, 282, 63
- Cacciani, P., Brandi, F., Velchev, I., et al. 2001, *Eur. Phys. J. D*, 15, 47
- Cacciani, P., Hogervorst, W., & Ubachs, W. 1995, *J. Chem. Phys.*, 102, 8308
- Cacciani, P. & Ubachs, W. 2004, *J. Mol. Spectrosc.*, 225, 62
- Cacciani, P., Ubachs, W., Hinnen, P. C., et al. 1998, *ApJ*, 499, L223
- Cambrésy, L. 1999, *A&A*, 345, 965
- Campins, H. & Ryan, E. V. 1989, *ApJ*, 341, 1059
- Cantó, J., Raga, A. C., & Williams, D. A. 2008, *Rev. Mex. Astron. Astr.*, 44, 293
- Cardelli, J. A., Meyer, D. M., Jura, M., & Savage, B. D. 1996, *ApJ*, 467, 334
- Carr, J. S. & Najita, J. R. 2008, *Science*, 319, 1504
- Carruthers, G. R. 1970, *ApJ*, 161, L81
- Caselli, P., Benson, P. J., Myers, P. C., & Tafalla, M. 2002, *ApJ*, 572, 238
- Caselli, P., Hasegawa, T. I., & Herbst, E. 1993, *ApJ*, 408, 548
- Cassen, P. & Moosman, A. 1981, *Icarus*, 48, 353
- Ceccarelli, C. 2004, in *ASP Conf. Ser. 323: Star Formation in the Interstellar Medium: In Honor of David Hollenbach*, ed. D. Johnstone, F. C. Adams, D. N. C. Lin, D. A. Neufeld, & E. C. Ostriker (San Francisco: ASP), 195
- Ceccarelli, C., Caselli, P., Herbst, E., Tielens, A. G. G. M., & Caux, E. 2007, in *Protostars & Planets V*, ed. B. Reipurth, D. Jewitt, & K. Keil (Tucson: Univ. of Arizona Press), 47
- Ceccarelli, C., Hollenbach, D. J., & Tielens, A. G. G. M. 1996, *ApJ*, 471, 400
- Cernicharo, J. 2004, *ApJ*, 608, L41
- Chakraborty, S., Ahmed, M., Jackson, T. L., & Thiemens, M. H. 2008, *Science*, 321, 1328
- Chambers, G. F. 1889, *A Handbook of Descriptive and Practical Astronomy* (Oxford: Clarendon Press)
- Charnley, S. B., Kress, M. E., Tielens, A. G. G. M., & Millar, T. J. 1995, *ApJ*, 448, 232
- Charnley, S. B., Rodgers, S. D., & Ehrenfreund, P. 2001, *A&A*, 378, 1024
- Charnley, S. B., Tielens, A. G. G. M., & Millar, T. J. 1992, *ApJ*, 399, L71
- Cherchneff, I., Barker, J. R., & Tielens, A. G. G. M. 1992, *ApJ*, 401, 269
- Cheung, A. C., Rank, D. M., & Townes, C. H. 1969, *Nature*, 221, 626
- Cheung, A. C., Rank, D. M., Townes, C. H., Thornton, D. D., & Welch, W. J. 1968, *Phys. Rev. Lett.*, 21, 1701
- Clayton, R. N. 2002, *Nature*, 415, 860
- Clayton, R. N., Grossman, L., & Mayeda, T. K. 1973, *Science*, 182, 485
- Clerke, A. M. 1898, *Observatory*, 21, 407
- Collings, M. P., Anderson, M. A., Chen, R., et al. 2004, *MNRAS*, 354, 1133

- Cooper, D. L. & Kirby, K. 1987, *J. Chem. Phys.*, 87, 424
- Cowell, P. H. 1905, *MNRAS*, 65, 861
- Dabrowski, I. 1984, *Can. J. Phys.*, 62, 1639
- D'Alessio, P., Calvet, N., & Hartmann, L. 2001, *ApJ*, 553, 321
- D'Alessio, P., Calvet, N., Hartmann, L., Franco-Hernández, R., & Servín, H. 2006, *ApJ*, 638, 314
- D'Alessio, P., Calvet, N., Hartmann, L., Lizano, S., & Cantó, J. 1999, *ApJ*, 527, 893
- D'Alessio, P., Canto, J., Calvet, N., & Lizano, S. 1998, *ApJ*, 500, 411
- D'Alessio, P., Hartmann, L., Calvet, N., et al. 2005, *ApJ*, 621, 461
- Dalgarno, A. 2006, *Proc. Natl. Acad. Sci. USA*, 103, 12269
- Dame, T. M., Hartmann, D., & Thaddeus, P. 2001, *ApJ*, 547, 792
- D'Antona, F. & Mazzitelli, I. 1994, *ApJS*, 90, 467
- Dartois, E. & d'Hendecourt, L. B. 1997, *A&A*, 323, 534
- Davis, A. M. & Richter, F. M. 2003, in *Treatise on Geochemistry*, Vol. 1, ed. A. M. Davis, H. D. Holland, & K. K. Turekian (Amsterdam: Elsevier), 407
- Desch, S. J., Ciesla, F. J., Hood, L. L., & Nakamoto, T. 2005, in *ASP Conf. Ser. 341: Chondrites and the Protoplanetary Disk*, ed. A. N. Krot, E. R. D. Scott, & B. Reipurth (San Francisco: ASP), 849
- Desch, S. J. & Connolly, Jr., H. C. 2002, *Meteorit. Planet. Sci.*, 37, 183
- di Francesco, J., Evans, II, N. J., Caselli, P., et al. 2007, in *Protostars & Planets V*, ed. B. Reipurth, D. Jewitt, & K. Keil (Tucson: Univ. of Arizona Press), 17
- Diplas, A. & Savage, B. D. 1994, *ApJ*, 427, 274
- Disanti, M. A. & Mumma, M. J. 2008, *Space Sci. Rev.*, 138, 127
- Dominik, C., Blum, J., Cuzzi, J. N., & Wurm, G. 2007, in *Protostars & Planets V*, ed. B. Reipurth, D. Jewitt, & K. Keil (Tucson: Univ. of Arizona Press), 783
- Dominik, C., Dullemond, C. P., Waters, L. B. F. M., & Walch, S. 2003, *A&A*, 398, 607
- Doty, S. D., Schöier, F. L., & van Dishoeck, E. F. 2004, *A&A*, 418, 1021
- Doty, S. D., van Dishoeck, E. F., van der Tak, F. F. S., & Boonman, A. M. S. 2002, *A&A*, 389, 446
- Douglas, A. E. & Herzberg, G. 1941, *ApJ*, 94, 381
- Drabbers, M., Heinze, J., ter Meulen, J. J., & Meerts, W. L. 1993, *J. Chem. Phys.*, 99, 5701
- Draine, B. T. 1978, *ApJS*, 36, 595
- Draine, B. T. & Bertoldi, F. 1996, *ApJ*, 468, 269
- Draine, B. T. & Li, A. 2001, *ApJ*, 551, 807
- Draine, B. T. & Li, A. 2007, *ApJ*, 657, 810
- Draine, B. T. & Sutin, B. 1987, *ApJ*, 320, 803
- Drake, S. 1978, *Galileo at Work: His Scientific Biography* (Chicago: Univ. of Chicago Press)
- Dullemond, C. P., Apai, D., & Walch, S. 2006a, *ApJ*, 640, L67
- Dullemond, C. P. & Dominik, C. 2004a, *A&A*, 417, 159
- Dullemond, C. P. & Dominik, C. 2004b, *A&A*, 421, 1075
- Dullemond, C. P., Henning, T., Visser, R., et al. 2007a, *A&A*, 473, 457
- Dullemond, C. P., Hollenbach, D., Kamp, I., & D'Alessio, P. 2007b, in *Protostars & Planets V*, ed. B. Reipurth, D. Jewitt, & K. Keil (Tucson: Univ. of Arizona Press), 555
- Dullemond, C. P., Natta, A., & Testi, L. 2006b, *ApJ*, 645, L69
- Dullemond, C. P. & Turolla, R. 2000, *A&A*, 360, 1187
- Dunham, T. 1937a, *Nature*, 139, 246

- Dunham, Jr., T. 1937b, *PASP*, 49, 26
- Durisen, R. H., Boss, A. P., Mayer, L., et al. 2007, in *Protostars & Planets V*, ed. B. Reipurth, D. Jewitt, & K. Keil (Tucson: Univ. of Arizona Press), 607
- Dutrey, A., Guilloteau, S., & Guelin, M. 1997, *A&A*, 317, L55
- Ebert, R. 1955, *Z. Astrophys.*, 37, 217
- Eddington, A. S. 1926, *Proc. R. Soc. London Ser. A*, 111, 424
- Ehrenfreund, P., Charnley, S. B., & Wooden, D. 2004, in *Comets II*, ed. M. C. Festou, H. U. Keller, & H. A. Weaver (Tucson: Univ. of Arizona Press), 115
- Ehrenfreund, P. & Fraser, H. J. 2003, in *Solid State Astrochemistry*, ed. V. Pirronello, J. Krelowski, & G. Manicò (Dordrecht: Kluwer), 317
- Ehrenfreund, P. & Sephton, M. 2006, *Faraday Discuss.*, 133, 277
- Eidelsberg, M., Benayoun, J. J., Viala, Y., et al. 1992, *A&A*, 265, 839
- Eidelsberg, M., Lemaire, J. L., Fillion, J. H., et al. 2004, *A&A*, 424, 355
- Eidelsberg, M. & Rostas, F. 1990, *A&A*, 235, 472
- Eidelsberg, M., Sheffer, Y., Federman, S. R., et al. 2006, *ApJ*, 647, 1543
- Eikema, K. S. E., Hogervorst, W., & Ubachs, W. 1994, *Chem. Phys.*, 181, 217
- Enoch, M. L., Evans, II, N. J., Sargent, A. I., et al. 2008, *ApJ*, 684, 1240
- Evans, N. J., Dunham, M. M., Jørgensen, J. K., et al. 2009, *ApJS*, 181, 321
- Federman, S. R., Fritts, M., Cheng, S., et al. 2001, *ApJS*, 134, 133
- Federman, S. R., Lambert, D. L., Sheffer, Y., et al. 2003, *ApJ*, 591, 986
- Federman, S. R., Rawlings, J. M. C., Taylor, S. D., & Williams, D. A. 1996, *MNRAS*, 279, L41
- Fegley, B. J. 2000, *Space Sci. Rev.*, 92, 177
- Ferrière, K. M. 2001, *Rev. Mod. Phys.*, 73, 1031
- Field, G. B., Goldsmith, D. W., & Habing, H. J. 1969, *ApJ*, 155, L149
- Fock, J.-H., Gürtler, P., & Koch, E. E. 1980, *Chem. Phys.*, 47, 87
- Forbes, G. 1909, *History of Astronomy* (London: Watts & Co.)
- Forst, W. 1972, *J. Phys. Chem.*, 76, 342
- Foster, P. N. & Chevalier, R. A. 1993, *ApJ*, 416, 303
- Fox, J. L. & Black, J. H. 1989, *Geophys. Res. Lett.*, 16, 291
- Fraser, H. J., Collings, M. P., McCoustra, M. R. S., & Williams, D. A. 2001, *MNRAS*, 327, 1165
- Frenklach, M. & Feigelson, E. D. 1989, *ApJ*, 341, 372
- Frerking, M. A., Langer, W. D., & Wilson, R. W. 1982, *ApJ*, 262, 590
- Fuchs, G. W., Cuppen, H. M., Ioppolo, S., et al. 2009, *A&A*, in press (arXiv: 0906.2292)
- Gail, H.-P. 2004, *A&A*, 413, 571
- Galli, D. & Shu, F. H. 1993, *ApJ*, 417, 220
- Garrod, R. T. & Herbst, E. 2006, *A&A*, 457, 927
- Garrod, R. T., Weaver, S. L. W., & Herbst, E. 2008, *ApJ*, 682, 283
- Geers, V. C., Augereau, J.-C., Pontoppidan, K. M., et al. 2006, *A&A*, 459, 545
- Geers, V. C., van Dishoeck, E. F., Visser, R., et al. 2007, *A&A*, 476, 279
- Geppert, W. D., Thomas, R., Semaniak, J., et al. 2004, *ApJ*, 609, 459
- Gerin, M., Phillips, T. G., Keene, J., Betz, A. L., & Boreiko, R. T. 1998, *ApJ*, 500, 329
- Gerola, H. & Glassgold, A. E. 1978, *ApJS*, 37, 1
- Gibb, E. L., Whittet, D. C. B., Boogert, A. C. A., & Tielens, A. G. G. M. 2004, *ApJS*, 151, 35
- Gilbert, W. 1600, *De Magnete*, translated by P. F. Mottelay (1991; New York: Dover Publications)

- Gillett, F. C., Forrest, W. J., & Merrill, K. M. 1973, *ApJ*, 183, 87
- Glassgold, A. E., Huggins, P. J., & Langer, W. D. 1985, *ApJ*, 290, 615
- Gondhalekar, P. M., Phillips, A. P., & Wilson, R. 1980, *A&A*, 85, 272
- Goodman, A. A., Benson, P. J., Fuller, G. A., & Myers, P. C. 1993, *ApJ*, 406, 528
- Goto, M., Usuda, T., Dullemond, C. P., et al. 2006, *ApJ*, 652, 758
- Gredel, R., Lepp, S., & Dalgarno, A. 1987, *ApJ*, 323, L137
- Greve, T. R., Bertoldi, F., Smail, I., et al. 2005, *MNRAS*, 359, 1165
- Gudipati, M. S. & Allamandola, L. J. 2003, *ApJ*, 596, L195
- Guelachvili, G., de Villeneuve, D., Farrenq, R., Urban, W., & Verges, J. 1983, *J. Mol. Spectrosc.*, 98, 64
- Guhathakurta, P. & Draine, B. T. 1989, *ApJ*, 345, 230
- Habart, E., Boulanger, F., Verstraete, L., Walmsley, C. M., & Pineau des Forêts, G. 2004a, *A&A*, 414, 531
- Habart, E., Natta, A., & Krügel, E. 2004b, *A&A*, 427, 179
- Habart, E., Natta, A., Testi, L., & Carillet, M. 2006, *A&A*, 449, 1067
- Habing, H. J. 1968, *Bull. Astron. Inst. Netherlands*, 19, 421
- Hail, W. J. & Leavens, D. H. 1940, *Pop. Astron.*, 48, 292
- Haisch, Jr., K. E., Lada, E. A., & Lada, C. J. 2001, *ApJ*, 553, L153
- Haridass, C., Prasad, C. V. V., & Paddi Reddy, S. 2000, *J. Mol. Spectrosc.*, 199, 180
- Harker, D. E. & Desch, S. J. 2002, *ApJ*, 565, L109
- Hartmann, J. 1904, *ApJ*, 19, 268
- Hartmann, L., D'Alessio, P., Calvet, N., & Muzerolle, J. 2006, *ApJ*, 648, 484
- Harvey, D. W. A., Wilner, D. J., Lada, C. J., Myers, P. C., & Alves, J. F. 2003, *ApJ*, 598, 1112
- Hasegawa, T. I. & Herbst, E. 1993, *MNRAS*, 261, 83
- Hasegawa, T. I., Herbst, E., & Leung, C. M. 1992, *ApJS*, 82, 167
- Hassouna, M., Le Garrec, J.-L., Rebrion-Rowe, C., Travers, D., & Rowe, B. R. 2003, in *Dissociative Recombination of Molecular Ions with Electrons*, ed. S. L. Guberman (New York: Kluwer), 49
- Heger, M. L. 1919, *PASP*, 31, 304
- Herbig, G. H. 1968, *Z. Astrophys.*, 68, 243
- Herbst, E. & Dunbar, R. C. 1991, *MNRAS*, 253, 341
- Herbst, E. & Le Page, V. 1999, *A&A*, 344, 310
- Herbst, E. & van Dishoeck, E. F. 2009, *ARA&A*, in press
- Hersant, F., Wakelam, V., Dutrey, A., Guilloteau, S., & Herbst, E. 2009, *A&A*, 493, L49
- Hirama, M., Tokosumi, T., Ishida, T., & Aihara, J. 2004, *Chem. Phys.*, 305, 307
- Hollenbach, D., Kaufman, M. J., Bergin, E. A., & Melnick, G. J. 2009, *ApJ*, 690, 1497
- Hollenbach, D. J. & Tielens, A. G. G. M. 1997, *ARA&A*, 35, 179
- Hollenbach, D. J., Yorke, H. W., & Johnstone, D. 2000, in *Protostars & Planets IV*, ed. V. Mannings, A. P. Boss, & S. S. Russell (Tucson: Univ. of Arizona Press), 401
- Hony, S., Van Kerckhoven, C., Peeters, E., et al. 2001, *A&A*, 370, 1030
- Houck, J. R., Roellig, T. L., van Cleve, J., et al. 2004, *ApJS*, 154, 18
- Hudgins, D. M., Bauschlicher, C. W., & Allamandola, L. J. 2001, *Spectrochim. Acta A*, 57, 907
- Hudgins, D. M., Bauschlicher, C. W., Allamandola, L. J., & Fetzer, J. C. 2000, *J. Phys. Chem. A*, 104, 3655

- Hudson, R. D. 1971, *Rev. Geophys. Space Phys.*, 9, 305
- Huebner, W. F., Keady, J. J., & Lyon, S. P. 1992, *Ap&SS*, 195, 1
- Hueso, R. & Guillot, T. 2005, *A&A*, 442, 703
- Huggins, P. J., Bachiller, R., Planesas, P., Forveille, T., & Cox, P. 2005, *ApJS*, 160, 272
- Ioppolo, S., Cuppen, H. M., Romanzin, C., van Dishoeck, E. F., & Linnartz, H. 2008, *ApJ*, 686, 1474
- Ioppolo, S., Palumbo, M. E., Baratta, G. A., & Mennella, V. 2009, *A&A*, 493, 1017
- Jansen, D. J., van Dishoeck, E. F., Black, J. H., Spaans, M., & Sosin, C. 1995, *A&A*, 302, 223
- Jennings, D. E., Bragg, S. L., & Brault, J. W. 1984, *ApJ*, 282, L85
- Jessberger, E. K. & Kissel, J. 1991, in *IAU Symp. 116: Comets in the Post-Halley Era*, ed. R. L. Newburn, Jr., M. Neugebauer, & J. Rahe (Dordrecht: Kluwer), 1075
- Jijina, J., Myers, P. C., & Adams, F. C. 1999, *ApJS*, 125, 161
- Joblin, C. 1992, PhD thesis, Univ. Paris
- Jones, A. P., Tielens, A. G. G. M., Hollenbach, D. J., & McKee, C. F. 1994, *ApJ*, 433, 797
- Jonkheid, B., Dullemond, C. P., Hogerheijde, M. R., & van Dishoeck, E. F. 2007, *A&A*, 463, 203
- Jonkheid, B., Faas, F. G. A., van Zadelhoff, G.-J., & van Dishoeck, E. F. 2004, *A&A*, 428, 511
- Jonkheid, B., Kamp, I., Augereau, J.-C., & van Dishoeck, E. F. 2006, *A&A*, 453, 163
- Jørgensen, J. K. 2004, *A&A*, 424, 589
- Jørgensen, J. K., Bourke, T. L., Myers, P. C., et al. 2007, *ApJ*, 659, 479
- Jørgensen, J. K., Schöier, F. L., & van Dishoeck, E. F. 2002, *A&A*, 389, 908
- Jørgensen, J. K., Schöier, F. L., & van Dishoeck, E. F. 2004, *A&A*, 416, 603
- Jørgensen, J. K., Schöier, F. L., & van Dishoeck, E. F. 2005, *A&A*, 437, 501
- Joulain, K., Falgarone, É., Pineau des Forêts, G., & Flower, D. 1998, *A&A*, 340, 241
- Kamegai, K., Ikeda, M., Maezawa, H., et al. 2003, *ApJ*, 589, 378
- Kamp, I. & Dullemond, C. P. 2004, *ApJ*, 615, 991
- Kandori, R., Nakajima, Y., Tamura, M., et al. 2005, *AJ*, 130, 2166
- Kapteyn, J. C. 1909, *ApJ*, 29, 46
- Kasting, J. F., Whitmire, D. P., & Reynolds, R. T. 1993, *Icarus*, 101, 108
- Kastner, J. H., Zuckerman, B., Weintraub, D. A., & Forveille, T. 1997, *Science*, 277, 67
- Keller, C. & Gail, H.-P. 2004, *A&A*, 415, 1177
- Keller, L. P., Bajt, S., Baratta, G. A., et al. 2006, *Science*, 314, 1728
- Kemper, F., Vriend, W. J., & Tielens, A. G. G. M. 2004, *ApJ*, 609, 826
- Kemper, F., Vriend, W. J., & Tielens, A. G. G. M. 2005, *ApJ*, 633, 534
- Kenyon, S. J. & Hartmann, L. 1995, *ApJS*, 101, 117
- Kessler, M. F., Steinz, J. A., Anderegg, M. E., et al. 1996, *A&A*, 315, L27
- Kessler-Silacci, J. E., Dullemond, C. P., Augereau, J.-C., et al. 2007, *ApJ*, 659, 680
- Kim, J. K., Theard, L. P., & Huntress, Jr., W. T. 1975, *Chem. Phys. Lett.*, 32, 610
- Kimura, H., Mann, I., & Jessberger, E. K. 2003, *ApJ*, 582, 846
- Kimura, Y., Nuth, III, J. A., Chakraborty, S., & Thiemens, M. H. 2007, *Meteorit. Planet. Sci.*, 42, 1429
- Kirby, K. & Cooper, D. L. 1989, *J. Chem. Phys.*, 90, 4895
- Kirby, K. & van Dishoeck, E. F. 1988, *Adv. Atom. Mol. Phys.*, 25, 437
- Кęпа, R. 1988, *J. Mol. Spectrosc.*, 132, 545
- Klein, R. I., Inutsuka, S.-I., Padoan, P., & Tomisaka, K. 2007, in *Protostars & Planets V*, ed.

- B. Reipurth, D. Jewitt, & K. Keil (Tucson: Univ. of Arizona Press), 99
- Kobayashi, H., Kawakita, H., Mumma, M. J., et al. 2007, *ApJ*, 668, L75
- Kramer, C., Cubick, M., Röllig, M., et al. 2008, *A&A*, 477, 547
- Kramers, H. A. & ter Haar, D. 1946, *Bull. Astron. Inst. Netherlands*, 10, 137
- Lacy, J. H., Knacke, R., Geballe, T. R., & Tokunaga, A. T. 1994, *ApJ*, 428, L69
- Lahuis, F., van Dishoeck, E. F., Boogert, A. C. A., et al. 2006, *ApJ*, 636, L145
- Lambert, D. L., Sheffer, Y., Gilliland, R. L., & Federman, S. R. 1994, *ApJ*, 420, 756
- Langer, W. D., Goldsmith, P. F., Carlson, E. R., & Wilson, R. W. 1980, *ApJ*, 235, L39
- Langer, W. D., Graedel, T. E., Frerking, M. A., & Armentrout, P. B. 1984, *ApJ*, 277, 581
- Langhoff, S. R. 1996, *J. Phys. Chem.*, 100, 2819
- Le Bourlot, J., Pineau des Forêts, G., Roueff, E., & Flower, D. R. 1993, *A&A*, 267, 233
- Le Page, V., Snow, T. P., & Bierbaum, V. M. 2001, *ApJS*, 132, 233
- Le Page, V., Snow, T. P., & Bierbaum, V. M. 2003, *ApJ*, 584, 316
- Le Petit, F., Nehmé, C., Le Bourlot, J., & Roueff, E. 2006, *ApJS*, 164, 506
- Le Petit, F., Roueff, E., & Le Bourlot, J. 2002, *A&A*, 390, 369
- Le Teuff, Y. H., Millar, T. J., & Markwick, A. J. 2000, *A&AS*, 146, 157
- Leach, S. 1987, in *Polycyclic Aromatic Hydrocarbons and Astrophysics*, ed. A. Léger, L. B. d'Hendecourt, & N. Boccarda (Dordrecht: Reidel), 99
- Lecar, M., Podolak, M., Sasselov, D., & Chiang, E. 2006, *ApJ*, 640, 1115
- Lee, H.-H., Herbst, E., Pineau des Forêts, G., Roueff, E., & Le Bourlot, J. 1996, *A&A*, 311, 690
- Lee, J.-E., Bergin, E. A., & Evans, II, N. J. 2004, *ApJ*, 617, 360
- Lee, J.-E., Bergin, E. A., & Lyons, J. R. 2008, *Meteorit. Planet. Sci.*, 43, 1351
- Lee, L. C. 1984, *ApJ*, 282, 172
- Léger, A., Boissel, P., Désert, F. X., & d'Hendecourt, L. B. 1989, *A&A*, 213, 351
- Léger, A., Boissel, P., & d'Hendecourt, L. B. 1988, *Phys. Rev. Lett.*, 60, 921
- Léger, A. & Puget, J. L. 1984, *A&A*, 137, L5
- Lepp, S., Dalgarno, A., & Sternberg, A. 1987, *ApJ*, 321, 383
- Lepp, S., Dalgarno, A., van Dishoeck, E. F., & Black, J. H. 1988, *ApJ*, 329, 418
- Leroy, A., Bolatto, A. D., Simon, J. D., & Blitz, L. 2005, *ApJ*, 625, 763
- Letzelter, C., Eidelsberg, M., Rostas, F., Breton, J., & Thieblemont, B. 1987, *Chem. Phys.*, 114, 273
- Leung, C. M., Herbst, E., & Huebner, W. F. 1984, *ApJS*, 56, 231
- Lewis, G. C. 1862, *An Historical Survey of the Astronomy of the Ancients* (London: Parker, Son and Bourn)
- Li, A. & Draine, B. T. 2001, *ApJ*, 554, 778
- Li, A. & Draine, B. T. 2002, *ApJ*, 572, 232
- Li, A. & Lunine, J. I. 2003, *ApJ*, 594, 987
- Lim, G.-I., Lim, S.-M., Kim, S. K., & Choi, Y. S. 1999, *J. Chem. Phys.*, 111, 456
- Lissauer, J. J. & Stevenson, D. J. 2007, in *Protostars & Planets V*, ed. B. Reipurth, D. Jewitt, & K. Keil (Tucson: Univ. of Arizona Press), 591
- Lisse, C. M., VanCleve, J., Adams, A. C., et al. 2006, *Science*, 313, 635
- Liszt, H. S. 2007, *A&A*, 476, 291
- Liszt, H. S. & Lucas, R. 1994, *ApJ*, 431, L131
- Liszt, H. S. & Turner, B. E. 1978, *ApJ*, 224, L73

- Lommen, D. J. P., Jørgensen, J. K., van Dishoeck, E. F., & Crapsi, A. 2008, *A&A*, 481, 141
- Lommen, D. J. P., Maddison, S. T., Wright, C. M., et al. 2009, *A&A*, 495, 869
- Lommen, D. J. P., Wright, C. M., Maddison, S. T., et al. 2007, *A&A*, 462, 211
- Looney, L. W., Tobin, J. J., & Kwon, W. 2007, *ApJ*, 670, L131
- Loren, R. B. 1989, *ApJ*, 338, 902
- Lunine, J. I., Engel, S., Rizk, B., & Horanyi, M. 1991, *Icarus*, 94, 333
- Lynden-Bell, D. & Pringle, J. E. 1974, *MNRAS*, 168, 603
- Lyons, J. R. & Young, E. D. 2005, *Nature*, 435, 317
- Mamon, G. A., Glassgold, A. E., & Huggins, P. J. 1988, *ApJ*, 328, 797
- Masunaga, H., Miyama, S. M., & Inutsuka, S.-I. 1998, *ApJ*, 495, 346
- Mathis, J. S., Mezger, P. G., & Panagia, N. 1983, *A&A*, 128, 212
- Matsuhisa, Y., Goldsmith, J. R., & Clayton, R. N. 1978, *Geochim. Cosmochim. Acta*, 42, 173
- Matsumoto, T. & Hanawa, T. 2003, *ApJ*, 595, 913
- Matsuo, T., Shibai, H., Ootsubo, T., & Tamura, M. 2007, *ApJ*, 662, 1282
- Mattioda, A. L., Allamandola, L. J., & Hudgins, D. M. 2005a, *ApJ*, 629, 1183
- Mattioda, A. L., Hudgins, D. M., & Allamandola, L. J. 2005b, *ApJ*, 629, 1188
- McCutcheon, W. H., Shuter, W. L. H., Dickman, R. L., & Roger, R. S. 1980, *ApJ*, 237, 9
- McKee, C. F. & Ostriker, J. P. 1977, *ApJ*, 218, 148
- McKellar, A. 1940, *PASP*, 52, 187
- Mebel, A. M., Lin, M. C., Yu, T., & Morokuma, K. 1997, *J. Phys. Chem. A*, 101, 3189
- Meeus, G., Waters, L. B. F. M., Bouwman, J., et al. 2001, *A&A*, 365, 476
- Millar, T. J., Herbst, E., & Charnley, S. B. 1991, *ApJ*, 369, 147
- Millar, T. J., Leung, C. M., & Herbst, E. 1987, *A&A*, 183, 109
- Millar, T. J., Walsh, C., Cordiner, M. A., Ní Chuimín, R., & Herbst, E. 2007, *ApJ*, 662, L87
- Mitchell, J. B. A. 1990, *Phys. Rep.*, 186, 215
- Miyake, K. & Nakagawa, Y. 1995, *ApJ*, 441, 361
- Mookerjea, B., Kramer, C., Röllig, M., & Masur, M. 2006, *A&A*, 456, 235
- Morata, O. & Herbst, E. 2008, *MNRAS*, 390, 1549
- Morton, D. C. & Noreau, L. 1994, *ApJS*, 95, 301
- Motte, F. & André, P. 2001, *A&A*, 365, 440
- Motte, F., André, P., & Neri, R. 1998, *A&A*, 336, 150
- Moustefaoui, T., Rebrion-Rowe, C., Le Garrec, J.-L., Rowe, B. R., & Mitchell, J. B. A. 1998, *Faraday Discuss.*, 109, 71
- Myers, P. C., Adams, F. C., Chen, H., & Schaff, E. 1998, *ApJ*, 492, 703
- Najita, J., Carr, J. S., & Mathieu, R. D. 2003, *ApJ*, 589, 931
- Nakamoto, T. & Nakagawa, Y. 1994, *ApJ*, 421, 640
- Narayanan, G., Heyer, M. H., Brunt, C., et al. 2008, *ApJS*, 177, 341
- Natarajan, K. & Roth, P. 1987, *Combust. Flame*, 70, 267
- Natta, A., Testi, L., Calvet, N., et al. 2007, in *Protostars & Planets V*, ed. B. Reipurth, D. Jewitt, & K. Keil (Tucson: Univ. of Arizona Press), 767
- Neufeld, D. A. & Hollenbach, D. J. 1994, *ApJ*, 428, 170
- Novotný, O., Sivaraman, B., Rebrion-Rowe, C., et al. 2005, *J. Chem. Phys.*, 123, 104303
- Nuth, III, J. A. 1999, *Lunar Planet. Sci. Conf.*, 30, 1726
- Öberg, K. I., Boogert, A. C. A., Pontoppidan, K. M., et al. 2008, *ApJ*, 678, 1032

- Öberg, K. I., Fuchs, G. W., Awad, Z., et al. 2007, *ApJ*, 662, L23
- Öberg, K. I., Garrod, R. T., van Dishoeck, E. F., & Linnartz, H. 2009a, *A&A*, in press (arXiv: 0908.1169)
- Öberg, K. I., Linnartz, H., Visser, R., & van Dishoeck, E. F. 2009b, *ApJ*, 693, 1209
- Öberg, K. I., van Dishoeck, E. F., & Linnartz, H. 2009c, *A&A*, 496, 281
- Oka, T., Nagai, M., Kamegai, K., Tanaka, K., & Kuboi, N. 2007, *PASJ*, 59, 15
- Oldenberg, R. C., Loge, G. W., Harradine, D. M., & Winn, K. R. 1992, *J. Phys. Chem.*, 96, 8426
- Olofsson, J., Augereau, J. ., van Dishoeck, E. F., et al. 2009, *A&A*, in press (arXiv: 0908.4153)
- Omont, A. 1986, *A&A*, 164, 159
- Owen, T. & Bar-Nun, A. 1993, *Nature*, 361, 693
- Owen, T., Bar-Nun, A., & Kleinfeld, I. 1992, *Nature*, 358, 43
- Padgett, D. L., Brandner, W., Stapelfeldt, K. R., et al. 1999, *AJ*, 117, 1490
- Palla, F. & Stahler, S. W. 1991, *ApJ*, 375, 288
- Panić, O., Hogerheijde, M. R., Wilner, D., & Qi, C. 2008, *A&A*, 491, 219
- Peeters, E., Hony, S., van Kerckhoven, C., et al. 2002, *A&A*, 390, 1089
- Peeters, E., Mattioda, A. L., Hudgins, D. M., & Allamandola, L. J. 2004, *ApJ*, 617, L65
- Petaev, M. I. & Wood, J. A. 2005, in *ASP Conf. Ser. 341: Chondrites and the Protoplanetary Disk*, ed. A. N. Krot, E. R. D. Scott, & B. Reipurth (San Francisco: ASP), 373
- Pety, J. & Falgarone, É. 2000, *A&A*, 356, 279
- Plume, R., Jaffè, D. T., Tatematsu, K., Evans, II, N. J., & Keene, J. 1999, *ApJ*, 512, 768
- Pontoppidan, K. M. 2006, *A&A*, 453, L47
- Pontoppidan, K. M., Blake, G. A., van Dishoeck, E. F., et al. 2008a, *ApJ*, 684, 1323
- Pontoppidan, K. M., Boogert, A. C. A., Fraser, H. J., et al. 2008b, *ApJ*, 678, 1005
- Pontoppidan, K. M., Dullemond, C. P., Blake, G. A., et al. 2007, *ApJ*, 656, 991
- Pontoppidan, K. M., Fraser, H. J., Dartois, E., et al. 2003, *A&A*, 408, 981
- Prasad, S. S. & Tarafdar, S. P. 1983, *ApJ*, 267, 603
- Press, W. H., Teukolsky, S. A., Vetterling, W. T., & Flannery, B. P. 1992, *Numerical Recipes in FORTRAN. The Art of Scientific Computing* (Cambridge: Cambridge Univ. Press)
- Przygodda, F., van Boekel, R., Àbrahàm, P., et al. 2003, *A&A*, 412, L43
- Puget, J. L. & Leger, A. 1989, *ARA&A*, 27, 161
- Qi, C., Kessler, J. E., Koerner, D. W., Sargent, A. I., & Blake, G. A. 2003, *ApJ*, 597, 986
- Rapacioli, M., Calvo, F., Spiegelman, F., Joblin, C., & Wales, D. J. 2005, *J. Phys. Chem. A*, 109, 2487
- Ratzka, T., Leinert, C., Henning, T., et al. 2007, *A&A*, 471, 173
- Rawlings, J. M. C., Hartquist, T. W., Menten, K. M., & Williams, D. A. 1992, *MNRAS*, 255, 471
- Ray, T., Dougados, C., Bacciotti, F., Eisloffel, J., & Chrysostomou, A. 2007, in *Protostars & Planets V*, ed. B. Reipurth, D. Jewitt, & K. Keil (Tucson: Univ. of Arizona Press), 231
- Rebrion-Rowe, C., Le Garrec, J.-L., Hassouna, M., Travers, D., & Rowe, B. R. 2003, *Int. J. Mass Spectrom.*, 223, 237
- Roberge, W. G., Jones, D., Lepp, S., & Dalgarno, A. 1991, *ApJS*, 77, 287
- Rodgers, S. D. & Charnley, S. B. 2003, *ApJ*, 585, 355
- Röllig, M., Abel, N. P., Bell, T., et al. 2007, *A&A*, 467, 187
- Russell, H. N. 1932, in *Annual Report of the Board of Regents of the Smithsonian Institution* (Washington: Smithsonian Inst.), 133

- Russell, H. N. 1935, MNRAS, 95, 610
- Saha, M. N. 1937, Nature, 139, 840
- Salama, F., Bakes, E. L. O., Allamandola, L. J., & Tielens, A. G. G. M. 1996, ApJ, 458, 621
- Salyk, C., Pontoppidan, K. M., Blake, G. A., et al. 2008, ApJ, 676, L49
- Sandford, S. A., Aléon, J., Alexander, C. M. O., et al. 2006, Science, 314, 1720
- Sandford, S. A. & Allamandola, L. J. 1988, Icarus, 76, 201
- Sandford, S. A. & Allamandola, L. J. 1993, ApJ, 417, 815
- Schmidt-Kaler, T. & Schlosser, W. 1984, JRASC, 78, 178
- Schneider, N., Simon, R., Kramer, C., et al. 2003, A&A, 406, 915
- Schöier, F. L., Jørgensen, J. K., van Dishoeck, E. F., & Blake, G. A. 2002, A&A, 390, 1001
- Schreyer, K., Guilloteau, S., Semenov, D., et al. 2008, A&A, 491, 821
- Semenov, D., Wiebe, D., & Henning, T. 2006, ApJ, 647, L57
- Shakura, N. I. & Sunyaev, R. A. 1973, A&A, 24, 337
- Sheffer, Y., Federman, S. R., & Andersson, B.-G. 2003, ApJ, 597, L29
- Sheffer, Y., Federman, S. R., Lambert, D. L., & Cardelli, J. A. 1992, ApJ, 397, 482
- Sheffer, Y., Lambert, D. L., & Federman, S. R. 2002, ApJ, 574, L171
- Sheffer, Y., Rogers, M., Federman, S. R., et al. 2008, ApJ, 687, 1075
- Sheffer, Y., Rogers, M., Federman, S. R., Lambert, D. L., & Gredel, R. 2007, ApJ, 667, 1002
- Shen, C. J., Greenberg, J. M., Schutte, W. A., & van Dishoeck, E. F. 2004, A&A, 415, 203
- Shu, F. H. 1977, ApJ, 214, 488
- Shu, F. H., Adams, F. C., & Lizano, S. 1987, ARA&A, 25, 23
- Shu, F. H., Ruden, S. P., Lada, C. J., & Lizano, S. 1991, ApJ, 370, L31
- Sicilia-Aguilar, A., Henning, T., Juhász, A., et al. 2009, Am. Inst. Phys. Conf. Proc., 1094, 23
- Siebenmorgen, R., Kruegel, E., & Mathis, J. S. 1992, A&A, 266, 501
- Simonelli, D. P., Pollack, J. B., & McKay, C. P. 1997, Icarus, 125, 261
- Smith, D. & Adams, N. G. 1980, ApJ, 242, 424
- Smith, J. D. T., Dale, D. A., Armus, L., et al. 2004, ApJS, 154, 199
- Smith, R. L., Pontoppidan, K. M., Young, E. D., Morris, M. R., & van Dishoeck, E. F. 2009, ApJ, 701, 163
- Snell, R. L., Howe, J. E., Ashby, M. L. N., et al. 2000, ApJ, 539, L101
- Snow, T. P., Le Page, V., Keheyan, Y., & Bierbaum, V. M. 1998, Nature, 391, 259
- Snyder, L. E., Buhl, D., Zuckerman, B., & Palmer, P. 1969, Phys. Rev. Lett., 22, 679
- Solomon, P. M. & Klemperer, W. 1972, ApJ, 178, 389
- Sonnentrucker, P., Welty, D. E., Thorburn, J. A., & York, D. G. 2007, ApJS, 168, 58
- Spitzer, L. J. 1954, ApJ, 120, 1
- Stark, G., Huber, K. P., Yoshino, K., Smith, P. L., & Ito, K. 2005, J. Chem. Phys., 123, 214303
- Stark, G., Lewis, B. R., Heays, A. N., et al. 2008, J. Chem. Phys., 128, 114302
- Sun, K., Ossenkopf, V., Kramer, C., et al. 2008, A&A, 489, 207
- Swings, P. 1937, MNRAS, 97, 212
- Swings, P. & Rosenfeld, L. 1937, ApJ, 86, 483
- Tafalla, M., Myers, P. C., Caselli, P., & Walmsley, C. M. 2004, A&A, 416, 191
- Tafalla, M., Myers, P. C., Caselli, P., Walmsley, C. M., & Comito, C. 2002, ApJ, 569, 815
- Terebey, S., Shu, F. H., & Cassen, P. 1984, ApJ, 286, 529
- Teyssier, D., Fossé, D., Gerin, M., et al. 2004, A&A, 417, 135

- Thi, W.-F., van Zadelhoff, G.-J., & van Dishoeck, E. F. 2004, *A&A*, 425, 955
- Thiemens, M. H. & Heidenreich, III, J. E. 1983, *Science*, 219, 1073
- Thorndike, S. L. 1930, *PASP*, 42, 99
- Tielens, A. G. G. M. 2008, *ARA&A*, 46, 289
- Tielens, A. G. G. M., McKee, C. F., Seab, C. G., & Hollenbach, D. J. 1994, *ApJ*, 431, 321
- Tielens, A. G. G. M., Tokunaga, A. T., Geballe, T. R., & Baas, F. 1991, *ApJ*, 381, 181
- Tilford, S. & Vanderslice, J. 1968, *J. Mol. Spectrosc.*, 26, 419
- Tobita, S., Meinke, M., Illenberger, E., Christophorou, L. G., & Baumgärtel, H. 1992, *Chem. Phys.*, 161, 501
- Triebert, J., E., E. G., Olzmann, M., & Scherzer, K. 1998, *Z. Phys. Chem.*, 205, 33
- Tscharnuter, W. M. 1987, *A&A*, 188, 55
- Turner, B. E. 1992, *ApJ*, 396, L107
- Ubachs, W., Eikema, K. S. E., Levelt, P. F., et al. 1994, *ApJ*, 427, L55
- Ubachs, W., Velchev, I., & Cacciani, P. 2000, *J. Chem. Phys.*, 113, 547
- van Boekel, R., Min, M., Waters, L. B. F. M., et al. 2005, *A&A*, 437, 189
- van Boekel, R., Waters, L. B. F. M., Dominik, C., et al. 2003, *A&A*, 400, L21
- van Boekel, R., Waters, L. B. F. M., Dominik, C., et al. 2004, *A&A*, 418, 177
- van der Tak, F. F. S., van Dishoeck, E. F., & Caselli, P. 2000a, *A&A*, 361, 327
- van der Tak, F. F. S., van Dishoeck, E. F., Evans, II, N. J., & Blake, G. A. 2000b, *ApJ*, 537, 283
- van Dishoeck, E. F. 1987, in *IAU Symp. 120: Astrochemistry*, ed. M. S. Vardya & S. P. Tarafdar (Dordrecht: Reidel), 51
- van Dishoeck, E. F. 1988, in *Rate Coefficients in Astrochemistry*, ed. T. J. Millar & D. A. Williams (Dordrecht: Kluwer), 49
- van Dishoeck, E. F. 2004, *ARA&A*, 42, 119
- van Dishoeck, E. F. & Black, J. H. 1986, *ApJS*, 62, 109
- van Dishoeck, E. F. & Black, J. H. 1988, *ApJ*, 334, 771
- van Dishoeck, E. F. & Blake, G. A. 1998, *ARA&A*, 36, 317
- van Dishoeck, E. F., Blake, G. A., Draine, B. T., & Lunine, J. I. 1993, in *Protostars & Planets III*, ed. E. H. Levy & J. I. Lunine (Tucson: Univ. of Arizona Press), 163
- van Dishoeck, E. F., Jonkheid, B., & van Hemert, M. C. 2006, *Faraday Discuss.*, 133, 231
- van Helden, A. 2009, *Exp. Astron.*, 25, 3
- van Hemert, M. C. & van Dishoeck, E. F. 2008, *Chem. Phys.*, 343, 292
- Van Kerckhoven, C., Hony, S., Peeters, E., et al. 2000, *A&A*, 357, 1013
- van Weeren, R. J., Brinch, C., & Hogerheijde, M. R. 2009, *ArXiv e-prints*
- van Zadelhoff, G.-J., Aikawa, Y., Hogerheijde, M. R., & van Dishoeck, E. F. 2003, *A&A*, 397, 789
- Velusamy, T. & Langer, W. D. 1998, *Nature*, 392, 685
- Viala, Y. P., Letzelter, C., Eidelsberg, M., & Rostas, F. 1988, *A&A*, 193, 265
- Visser, R., van Dishoeck, E. F., & Black, J. H. 2009, *A&A*, 503, 323
- Viti, S., Collings, M. P., Dever, J. W., McCoustra, M. R. S., & Williams, D. A. 2004, *MNRAS*, 354, 1141
- Vorobyov, E. I. & Basu, S. 2008, *ApJ*, 676, L139
- Vuong, M. H. & Foing, B. H. 2000, *A&A*, 363, L5
- Walch, S., Burkert, A., Whitworth, A., Naab, T., & Gritschneider, M. 2009, *MNRAS*, in press (arXiv: 0901.2127)

- Walsh, C., Harada, N., Herbst, E., & Millar, T. J. 2009, *ApJ*, 700, 752
- Wang, X., Becker, H., Hopkinson, A. C., et al. 1997, *Int. J. Mass Spectrom. Ion Proc.*, 161, 69
- Warin, S., Benayoun, J. J., & Viala, Y. P. 1996, *A&A*, 308, 535
- Watanabe, N. & Kouchi, A. 2002, *ApJ*, 571, L173
- Watson, D. M., Leisenring, J. M., Furlan, E., et al. 2009, *ApJS*, 180, 84
- Watson, W. D., Anicich, V. G., & Huntress, Jr., W. T. 1976, *ApJ*, 205, L165
- Weidenschilling, S. J. 1980, *Icarus*, 44, 172
- Weingartner, J. C. & Draine, B. T. 2001, *ApJS*, 134, 263
- Weinreb, S. 1963, *Nature*, 200, 829
- Werner, M. W., Roellig, T. L., Low, F. J., et al. 2004a, *ApJS*, 154, 1
- Werner, M. W., Uchida, K. I., Sellgren, K., et al. 2004b, *ApJS*, 154, 309
- Westley, M. S., Baragiola, R. A., Johnson, R. E., & Baratta, G. A. 1995a, *Nature*, 373, 405
- Westley, M. S., Baragiola, R. A., Johnson, R. E., & Baratta, G. A. 1995b, *Planet. Space Sci.*, 43, 1311
- White, R. J., Greene, T. P., Doppmann, G. W., Covey, K. R., & Hillenbrand, L. A. 2007, in *Protostars & Planets V*, ed. B. Reipurth, D. Jewitt, & K. Keil (Tucson: Univ. of Arizona Press), 117
- Whitney, B. A., Wood, K., Bjorkman, J. E., & Wolff, M. J. 2003, *ApJ*, 591, 1049
- Whittet, D. C. B., Gerakines, P. A., Hough, J. H., & Shenoy, S. S. 2001, *ApJ*, 547, 872
- Whitworth, A. P., Bhattal, A. S., Francis, N., & Watkins, S. J. 1996, *MNRAS*, 283, 1061
- Willacy, K. & Langer, W. D. 2000, *ApJ*, 544, 903
- Williams, J. P., de Geus, E. J., & Blitz, L. 1994, *ApJ*, 428, 693
- Wilson, B. A., Dame, T. M., Masheder, M. R. W., & Thaddeus, P. 2005, *A&A*, 430, 523
- Wilson, R. W., Jefferts, K. B., & Penzias, A. A. 1970, *ApJ*, 161, L43
- Wilson, T. L. 1999, *Rep. Prog. Phys.*, 62, 143
- Woitke, P., Kamp, I., & Thi, W.-F. 2009, *ArXiv e-prints*
- Woodall, J., Agúndez, M., Markwick-Kemper, A. J., & Millar, T. J. 2007, *A&A*, 466, 1197
- Wooden, D. H., Harker, D. E., & Brearley, A. J. 2005, in *ASP Conf. Ser. 341: Chondrites and the Protoplanetary Disk*, ed. A. N. Krot, E. R. D. Scott, & B. Reipurth (San Francisco: ASP), 774
- Wooden, D. H., Harker, D. E., Woodward, C. E., et al. 1999, *ApJ*, 517, 1034
- Woods, P. M. & Willacy, K. 2009, *ApJ*, 693, 1360
- Woon, D. E. 2009, *Interstellar & Circumstellar Molecules* (<http://www.astrochymist.org>)
- Wyckoff, S., Tegler, S. C., & Engel, L. 1991, *ApJ*, 367, 641
- Yorke, H. W. & Bodenheimer, P. 1999, *ApJ*, 525, 330
- Yorke, H. W., Bodenheimer, P., & Laughlin, G. 1993, *ApJ*, 411, 274
- Young, C. H. & Evans, II, N. J. 2005, *ApJ*, 627, 293
- Young, E. D. 2007, *Earth Planet. Sc. Lett.*, 262, 468
- Yurimoto, H. & Kuramoto, K. 2004, *Science*, 305, 1763
- Zhukovska, S., Gail, H.-P., & Tieloff, M. 2008, *A&A*, 479, 453
- Zsargó, J. & Federman, S. R. 2003, *ApJ*, 589, 319

Publicaties

Refereed papers

1. *The chemical history of molecules in circumstellar disks. II. Gas-phase species*
R. Visser, S. D. Doty and E. F. van Dishoeck
Astronomy & Astrophysics, to be submitted (Chapter 3)
2. *Sub-Keplerian accretion onto circumstellar disks*
R. Visser and C. P. Dullemond
Astronomy & Astrophysics, to be submitted (Chapter 4)
3. *PROSAC: a Submillimeter Array survey of low-mass protostars. II. The mass evolution of envelopes, disks and stars from the Class 0 through I stages*
J. K. Jørgensen, E. F. van Dishoeck, **R. Visser**, T. L. Bourke, D. J. Wilner, D. J. P. Lommen, M. R. Hogerheijde and P. C. Myers
Astronomy & Astrophysics, in press
4. *The photodissociation and chemistry of CO isotopologues: applications to interstellar clouds and circumstellar disks*
R. Visser, E. F. van Dishoeck and J. H. Black
Astronomy & Astrophysics, 2009, 503, 323–343 (Chapter 5)
5. *The steric nature of the bite angle*
W.-J. van Zeist, **R. Visser** and F. M. Bickelhaupt
Chemistry: A European Journal, 2009, 15, 6112–6115
6. *Photodesorption of ices. II. H₂O and D₂O*
K. I. Öberg, H. V. J. Linnartz, **R. Visser** and E. F. van Dishoeck
The Astrophysical Journal, 2009, 693, 1209–1218
7. *The chemical history of molecules in circumstellar disks. I. Ices*
R. Visser, E. F. van Dishoeck, S. D. Doty and C. P. Dullemond
Astronomy & Astrophysics, 2009, 495, 881–897 (Chapter 2)
8. *Spatially extended PAHs in circumstellar disks around T Tauri and Herbig Ae stars*
V. C. Geers, E. F. van Dishoeck, **R. Visser**, K. M. Pontoppidan, J.-C. Augereau, E. Habart and A. M. Lagrange
Astronomy & Astrophysics, 2007, 476, 279–289
9. *Dust sedimentation in protoplanetary disks with PAHs*
C. P. Dullemond, T. Henning, **R. Visser**, V. C. Geers, E. F. van Dishoeck and K. M. Pontoppidan
Astronomy & Astrophysics, 2007, 473, 457–466

10. *PAH chemistry and IR emission from circumstellar disks*
R. Visser, V. C. Geers, C. P. Dullemond, J.-C. Augereau, K. M. Pontoppidan and E. F. van Dishoeck
Astronomy & Astrophysics, 2007, 466, 229–241 (Chapter 6)
11. *Polycyclic benzenoids: Why kinked is more stable than straight*
J. Poater, **R. Visser**, M. Solà and F. M. Bickelhaupt
Journal of Organic Chemistry, 2007, 1134–1142
12. *c2d Spitzer-IRS spectra of disks around T Tauri stars. II. PAH emission features*
V. C. Geers, J.-C. Augereau, K. M. Pontoppidan, C. P. Dullemond, **R. Visser**, J. E. Kessler-Silacci, N. J. Evans, II, E. F. van Dishoeck, G. A. Blake, A. C. A. Boogert, J. M. Brown, F. Lahuis, B. M. Merín
Astronomy & Astrophysics, 2006, 459, 545–556
13. *Oxidative addition to main group versus transition metals: insights from the Activation Strain model*
G. T. de Jong, **R. Visser** and F. M. Bickelhaupt
Journal of Organometallic Chemistry, 2006, 691, 4341–4349

Conference proceedings

1. *Chemical changes during transport from cloud to disk*
R. Visser, E. F. van Dishoeck and S. D. Doty
IAU Symposium 251: Organic Matter in Space, 2008, 111–115
2. *PAH chemistry and IR emission from circumstellar disks*
R. Visser, V. C. Geers, C. P. Dullemond, J.-C. Augereau, K. M. Pontoppidan and E. F. van Dishoeck
Molecules in Space and Laboratory, 2007, 102–105

Curriculum vitae

Ik ben geboren op 15 januari 1983, tien dagen voor de lancering van de Infrared Astronomical Satellite (IRAS), de eerste ruimtetelescoop ooit die volledig in het infrarood werkte. Na negen maanden verhuisde ik met mijn ouders van Amersfoort naar Uithoorn, waar later ook mijn broer en zus zijn geboren. In Uithoorn behaalde ik in 2000 mijn gymnasiumdiploma aan het Alkwin Kollege. Dat najaar begon ik met een studie scheikunde aan de Vrije Universiteit Amsterdam. In augustus 2003 behaalde ik mijn bachelor, twee jaar later gevolgd door mijn master; beide waren cum laude. Mijn hoofdvakonderzoek voerde ik uit in de sectie Theoretische Chemie onder begeleiding van dr. Matthias Bickelhaupt (sindsdien benoemd tot hoogleraar) en drs. Theodoor de Jong. De resultaten hebben geleid tot twee wetenschappelijke publicaties. Een vijfweeks bezoek aan prof. dr. Miquel Solà op de Universitat de Girona in Spanje vormde de basis voor een derde publicatie.

Tijdens mijn bachelor was ik op een studentensymposium aanwezig bij de lezing “Astrochemie: Van exotische ionen tot ‘geladen’ vragen”. Tot dan toe had ik sterrenkunde altijd wel leuk gevonden, maar afgedaan als te natuurkundig om me er professioneel in te verdiepen. Nu bleek sterrenkunde opeens een stuk scheikundiger te zijn! Deze hernieuwde kennismaking mondde in 2004 uit in een bijvakonderzoek op de Sterrewacht Leiden. Na mijn afstuderen in september 2005 keerde ik daar terug voor een promotieplaats.

De Sterrewacht Leiden is een internationaal georiënteerd instituut, en daar heb ik dankbaar gebruik van gemaakt. Ik ben op werkbezoek geweest bij Denison University in Granville, Ohio, het MPIA in Heidelberg, het MPE in Garching, en de ETH in Zürich. Een bijzondere ervaring was de waarneemsessie met de Very Large Telescope in Chili in 2006. Ik heb mijn werk gepresenteerd op congressen in St. Jacut de la Mer (Frankrijk), Vidago (Portugal), Belfast, Parijs, Hong Kong, Amsterdam, Dalfsen (Nederland), Londen en Rolduc (Nederland). Ook tijdens de werkbezoeken aan Granville en Zürich heb ik lezingen gehouden over mijn onderzoek. Tevens heb ik publiekslezingen gegeven op de Oude Sterrewacht in Leiden en op volkssterrenwachten in Amersfoort en Overveen. Als werkcollegeassistent was ik tweemaal betrokken bij het college stralingsprocessen.

Als ik niet met astrochemie bezig ben, ben ik vaak te vinden op het honkbalveld van de Keytown Hitters in Leiden of op een van de andere velden in Nederland. Ik honkbal sinds mijn zevende, afgezien van een onderbreking van een paar jaar tijdens mijn bachelor. In 2006 heb ik mijn scheidsrechterslicentie behaald en sindsdien ben ik steeds vaker actief als scheidsrechter en minder als speler. Ik heb inmiddels wedstrijden geleid tot en met de eerste klasse. In oktober hoop in een tweede licentie te behalen waarmee ik kan doorstromen naar de hoofdklasse, het hoogste niveau dat we in Nederland hebben. Mijn wens is om het uiteindelijk te schoppen tot internationale toernooien als EK's en WK's.

Na mijn promotie blijf ik als postdoc nog een jaar in Leiden. Ik zal dan betrokken zijn bij het project *Water in Star-Forming Regions with Herschel* (WISH) op de in mei gelanceerde Herschel-ruimtetelescoop.

Nawoord

Hoewel er maar één naam op de kaft van dit proefschrift staat, is het geenszins het werk van slechts één persoon. Deze laatste pagina is een dankwoord aan iedereen die iets heeft bijgedragen. Om te beginnen is er natuurlijk de Sterrewacht Leiden als geheel. De Sterrewacht is een groot instituut, maar dankzij de vele gezamenlijke activiteiten blijft het prettig kleinschalig. De computergroep, het secretariaat en het andere ondersteunend personeel staan altijd klaar om te helpen en zorgen ervoor dat alles soepel blijft draaien.

De astrochemiegroep is een mix van waarnemers, theoretici en experimentalisten, en biedt daarmee een geweldige omgeving voor wetenschappelijk onderzoek. Vincent and Jean-Charles, when I first arrived in Leiden, I couldn't tell a T Tauri star from a supernova. You turned me from a chemist into a proper astrochemist. Bastiaan, jouw hulp met de chemische modellen – ook nog lang na je vertrek – heb ik zeer gewaardeerd. Lars, the hot water and all the *merde* helped keep me sane during the final months. Edith, the same goes for all the laughs we shared at coffee, lunch and other occasions. Karin, I enjoyed our collaboration on the water photodesorption paper. Christian, Dave, meneer Dominic, Elena, Guido, Herma, Isa, Jeanette, Nadine, Olja and all other Sterrewachters past and present, it was a pleasure to share these corridors with you. To the staff at the MPE, the MPIA, Denison and the ETH: the hospitality during my visits is much appreciated.

Steve, your name deserves to be printed here in capitals. If it weren't for you, the model never would have worked. I look back fondly on our many long discussions in Granville and elsewhere. Kees, ook jij verdient een eervolle vermelding. Mijn tweede bezoek aan Heidelberg vormde de basis voor het stervormingsmodel zoals het uiteindelijk is geworden. Daarnaast ben ik je zeer erkentelijk voor de vele hulp met RADMC.

In de sectie Theoretische Chemie van de Vrije Universiteit Amsterdam leerde ik voor het eerst hoe leuk wetenschappelijk onderzoek is. Matthias en Theodoor, jullie begeleiding was onmisbaar bij die eerste stappen. Aan mijn studietijd op de VU heb ik een aantal goede vrienden overgehouden. Petra, Dianne, Galvin, Philip, Michiel, Danièle, Maaïke en Nanda, alle etentjes, bioscoopbezoeken en potjes Kolonisten hebben de afgelopen jaren voor de broodnodige afleiding gezorgd. Carlos, Els, Gideon, Jeroen, Manon, Petra, Mike, Bart, Bart, Lennart, Robin en alle andere Keytown Hitters, met jullie beleefde ik vele uren plezier op het honkbalveld. Fred, Henk, Jeroen, Rinus, Renée en alle collega-scheidsrechters, jullie zorgden voor nog vele uren meer honkbalplezier.

Rolf, Tom, ik ben blij dat ik jullie al zo lang tot mijn vrienden mag rekenen. Onze vakanties waren ieder jaar iets om naar uit te kijken en zorgden ervoor dat ik daarna weer met nieuwe energie verder kon. Martin, Suzanne, ik bof dat ik zo'n geweldige broer en zus heb. Zonder al die potjes Kolonisten, Carcassonne en Fase 10, zonder al dat bowlen, poolen, PSone'en en PS3'en, zonder al die wederzijdse etentjes – kortom: zonder jullie – zou het leven maar saai zijn. Papa, mama, bij jullie kon ik altijd terecht om de goede en minder goede momenten te delen. Jullie zijn geweldig.

“If you have an apple and I have an apple and we exchange these apples then you and I will still each have one apple. But if you have an idea and I have an idea and we exchange these ideas, then each of us will have two ideas.”

– George Bernard Shaw

